SULEIMAN, RIAD S., Ph.D., DECEMBER, 1999 PHYSICS

MEASUREMENT OF THE ELECTRIC AND MAGNETIC ELASTIC STRUCTURE FUNCTIONS OF THE DEUTERON AT LARGE MOMENTUM TRANSFERS (244 pp.)

Director of Dissertation: Professor Gerassimos G. Petratos

The deuteron elastic structure functions, $A(Q^2)$ and $B(Q^2)$, have been extracted from cross section measurements of elastic electron-deuteron scattering in coincidence using the Continuous Electron Beam Accelerator and Hall A Facilities of Jefferson Laboratory. Incident electrons were scattered off a high-power cryogenic deuterium target. Scattered electrons and recoil deuterons were detected in the two High Resolution Spectrometers of Hall A. $A(Q^2)$ was extracted from forward angle cross section measurements in the squared four-momentum transfer range $0.684 \leq Q^2 \leq 5.90$ $(\mathrm{GeV/c})^2$. $B(Q^2)$ was determined by means of a Rosenbluth separation in the range $0.684 \leq Q^2 \leq 1.325$ $(\mathrm{GeV/c})^2$. The data are compared to theoretical models based on the impulse approximation with the inclusion of meson-exchange currents and to predictions of quark dimensional scaling and perturbative quantum chromodynamics. The results are expected to provide insights into the transition from meson-nucleon to quark-gluon descriptions of the nuclear two-body system.

Measurement of the Electric and Magnetic Elastic Structure Functions of the Deuteron at Large Momentum Transfers

A dissertation submitted
to Kent State University in partial
fulfillment of the requirements for the
degree of Doctor of Philosophy

by

Riad S. Suleiman

December, 1999

Dissertation written by

Riad S. Suleiman

B.S., Yarmouk University - Jordan, 1993

M.A., Kent State University, 1997

Ph.D., Kent State University, 1999

Approved by

Gerassimos Petratos , Chair, Doctoral Dissertation Committee

Bryon Anderson , Members, Doctoral Dissertation Committee

Jian-Ping Chen ,

Javier Gomez ,

Declan Keane ,

Paul Wang ,

Philip Westerman ,

Accepted by

David Allender , Chair, Department of Physics

John Watson , Associate Dean, College of Arts and Sciences

Table of Contents

List of Figures vii

List of Tables xiv

1 Introduction 1

1.1 Introduction 1

1.2 Kinematics 3

1.3 Deuteron Elastic Structure Functions and Form Factors 4

1.4 This Experiment 6

1.5 Previous Data 7

2 Experimental Apparatus 12

2.1 Overview 12

2.2 Accelerator 12

2.3 Hall A 15

2.4 Hall A Arc and Beamline 15

2.4.1 Beam Position Monitors 17

2.4.2 Beam Current Monitors 18

2.4.3 Beam Rastering System 21

2.4.4 Beamline Magnetic Elements 22

2.4.5 Scattering Chamber 23

2.4.6 Exit Beamline and Beam Dump 23

2.5 Targets 24

2.5.1 Cryotargets 24

2.5.1.1 Heat Exchanger 28
2.5.1.2 Loop Pump 29
2.5.1.3 Cells and Cell Block 31
2.5.1.4 Heaters 33
2.5.1.5 Thermometry 33
2.5.1.6 Loop One Collimator 35
2.5.1.7 Control System 36
2.5.1.8 Target Density 38
2.5.1.9 Gas Purity 40
2.5.1.10 Luminosity and Heat Deposition 40
2.5.2 Dummy and Solid Targets 40
2.6 High Resolution Spectrometers 42
2.7 Detector Packages 50
2.7.1 Vertical Drift Chambers 52
2.7.2 Scintillators 54
2.7.3 Gas Čerenkov Detector 55
2.7.4 Lead-Glass Calorimeter 58
2.8 Trigger Setup 62
2.8.1 Trigger Supervisor 67
2.8.2 Latched Trigger Word 70
2.8.3 Data Rates 74
2.8.4 Electronics and Computer Dead Time 75
2.8.5 Inclusive Measurement with a Single Spectrometer 77
2.8.6 Hadron Arm Delays 80
2.9 Data Acquisition 80
2.9.1 CODA Overview 82

2.9.2 CODA Data File 82

3 Data Analysis 84

3.1 Overview 84

3.2 ESPACE 84

3.3 Accumulated Charge 86

3.4 Beam Energy Study 88

3.5 Detector Calibrations 92

3.5.1 Vertical Drift Chamber Calibration 92

3.5.2 Scintillator Timing Corrections 94

3.5.3 Čerenkov Calibration 95

3.5.4 Lead-Glass Calorimeter Calibration 99

3.6 Coincidence Time-of-Flight 109

3.7 Particle Identification 117

3.8 Corrections to the Experimental Data 119

3.8.1 Trigger Inefficiencies 120

3.8.2 Detector Inefficiencies 128

3.8.3 Recoil Nuclear Interactions 132

3.8.4 Target Density Correction 135

3.9 Monte Carlo Simulation 138

3.9.0.1 Solid Angle 140

3.10 Radiative Corrections 143

3.11 Empty-Cell Subtraction 145

3.12 Electron-Proton Elastic Cross Section Calibration 145

4 Results 152

4.1 Electron-Deuteron Elastic Cross Sections 152

4.2 Rosenbluth Separation of $A(Q^2)$ and $B(Q^2)$ at Low Q^2 155
4.3 $A(Q^2)$ at Large Q^2 160

5 Theoretical Overview 164
5.1 Introduction 164
5.2 Non-Relativistic Impulse Approximation 164
5.2.1 Isobar Configurations 171
5.3 Relativistic Impulse Approximation 174
5.3.1 Light-Front Dynamics 178
5.3.2 Manifestly Covariant Dynamics 188
5.3.2.1 Quasi-Potential Approximation 188
5.3.2.2 Equal Time Approximation 198
5.4 Meson-Exchange Currents 201
5.5 Dimensional Scaling Laws 208
5.6 Perturbative Quantum Chromodynamics 211

6 Summary and Outlook 220

A Full Trigger Electronics Diagrams 223

B Spectrometer Setup Kinematics 227

C Input for Cross Section Calculations 231

References 239

List of Figures

1-1 Feynman Diagram of Elastic Electron-Deuteron Scattering 3

1-2 Deuteron Elastic Form Factors 6

1-3 Existing $A(Q^2)$ Data up to 1.9 (GeV/c)^2 8

1-4 Existing $A(Q^2)$ Data 9

1-5 Existing $B(Q^2)$ Data 10

1-6 Existing $A(Q^2)$ and $B(Q^2)$ Data 11

2-1 Schematic of the Jefferson Lab Accelerator 13

2-2 Schematic of Hall A 16

2-3 First Section of Hall A Beamline 16

2-4 Second Section of Hall A Beamline 17

2-5 Diagram of Hall A Current Monitoring System 19

2-6 Beam Profile with the Fast Raster 22

2-7 Side View of Cryotarget with the Attached Solid Target Ladder 25

2-8 Downstream View of the Three Cryotarget Loops 26

2-9 Diagram of a Single Target Loop 27

2-10 Diagram of a Single Target Loop 29

2-11 Diagram of a Target Cell Block 31

2-12 Absolute Calibration of Cernox Compared to Liquid Helium Temperature . 34

2-13 The Difference Between the Cernox Temperature Readings and Their Average Temperature 35

2-14 Collimator Dimensions 36

2-15 Physical and Logical Architecture of an EPICS Control System 37

2-16 Schematic of the Hall A High Resolution Spectrometer 43

2-17 SNAKE Simulation of Set of Rays Traced from the Target to the First Scintillator Plane 47
2-18 The Relative Momenta Settings of the Electron and Hadron Spectrometers 48
2-19 Schematic of the Procedure Used to Set the Spectrometer Angle 49
2-20 Schematic of the Electron Arm Detector Package 51
2-21 Schematic of the Hadron Arm Detector Package 51
2-22 VDC Schematic 52
2-23 Schematic Layout of the VDC Assembly 53
2-24 The Cross Section View of a VDC 54
2-25 Schematic Display of a Scintillator Plane 55
2-26 Electron Arm CO_2 Gas Čerenkov Detector 57
2-27 Preshower Detector Map 59
2-28 Preshower Detector Block 60
2-29 Shower Detector Map 61
2-30 Simplified Diagram of the Spectrometer Trigger Circuit 63
2-31 Widths and Delays of Electron Arm S1 Trigger and Hadron Arm S3 Trigger at the Coincidence Logic AND 65
2-32 An Event in the Scintillator Planes 65
2-33 Nominal Delays for Electron Arm S1 Trigger and Hadron Arm S3 Trigger at the Input of the Trigger Supervisor Relative to S5 69
2-34 Latched Trigger Pattern versus Event Type 71
2-35 The TDC Channel of the Latched Trigger for Trigger Type 1 72
2-36 The TDC Channel of the Latched Trigger for Trigger Type 2 72
2-37 The TDC Channel of the Latched Trigger for Trigger Type 3 73
2-38 The TDC Channel of the Latched Trigger for Trigger Type 4 73
2-39 The TDC Channel of the Latched Trigger for Trigger Type 5 74

2-40 Measured Computer Dead Time 76
2-41 Electron and Hadron Arm Relative Momentum Spectra 79
2-42 Schematic of the Hall A DAQ 81
3-1 Current Calibration Schematic 86
3-2 Calibration Coefficients of Upstream and Downstream BCMs versus Run Number (Time) 88
3-3 Incident Beam Energy as Determined from $H(e, e'p)$ with Nominal Beam Energy 4424.0 MeV 90
3-4 Incident Beam Energy Offset as a Function of Time for $B(Q^2)$ Kinematics . 91
3-5 Incident Beam Energy Offset as a Function of Time for $A(Q^2)$ Kinematics . 92
3-6 A Typical Trajectory in the Vertical Drift Chambers 93
3-7 Electron Arm β for Electrons from Time-of-Flight Between the Two Scintillator Planes 96
3-8 Hadron Arm β from Time-of-Flight Between the Two Scintillator Planes . . 96
3-9 ADC Spectrum of a PMT of the Electron Arm Čerenkov Detector 97
3-10 Čerenkov Detector ADC Sum 98
3-11 Čerenkov Detector Photoelectron Spectrum 99
3-12 Energy Deposition in the Preshower Detector versus Energy Deposition in the Shower Detector 101
3-13 Energy Measured by the Calorimeter Divided by the Particle Momentum . 102
3-14 Energy Measured by the Calorimeter Divided by the Particle Momentum after a Cut on the Čerenkov Detector 102
3-15 Energy Deposition in the Preshower Detector versus Energy Deposition in the Shower Detector from an *e-p* Calibration Run for $B(Q^2)$ 103
3-16 Energy Measured by the Calorimeter Divided by the Particle Momentum from an *e-p* Calibration Run for $B(Q^2)$ 104

3-17 The Centroid of the Electron Arm Calorimeter Energy Ratio for all e-p Calibration Runs versus Scattered Electron Energy 105
3-18 Electron Arm Calorimeter Resolution versus Scattered Electron Energy . . 105
3-19 Preshower Block 23 Coefficient versus Scattered Electron Energy 106
3-20 Shower Block 21 Coefficient versus Scattered Electron Energy 107
3-21 Preshower Block 23 Coefficient versus Run Number 107
3-22 Shower Block 21 Coefficient versus Run Number 108
3-23 The Coefficients of Preshower and Shower Blocks Used in the Analysis . . . 108
3-24 Simplified Schematic of the Coincidence Trigger Setup 109
3-25 Raw Coincidence Time-of-Flight 110
3-26 The x Coordinate Along the Hadron Arm Scintillator Plane S1 versus Raw Coincidence Time-of-Flight 112
3-27 The x Coordinate Along the Hadron Arm Scintillator Plane S1 versus Corrected Coincidence Time-of-Flight 112
3-28 Electron Arm θ_{tra} versus Corrected Coincidence Time-of-Flight 115
3-29 The Electron Arm θ_{tra} versus Final Corrected Coincidence Time-of-Flight . 115
3-30 The Final Corrected Coincidence Time-of-Flight 116
3-31 Corrected Coincidence Time-of-Flight 116
3-32 Hadron Arm Scintillator Pulse Height 117
3-33 Hadron Arm scintillator Pulse Height versus Hadron Arm β 118
3-34 Coincidence Time-of-Flight versus Hadron Arm Scintillators Pulse Height . 119
3-35 Electron Arm Trigger Inefficiency versus Run Number 122
3-36 Electron Arm Trigger Inefficiency versus Electron Arm Rate 122
3-37 Hadron Arm Trigger Inefficiency versus Run Number 123
3-38 Hadron Arm Trigger Inefficiency versus Hadron Arm Rate 123
3-39 Electron Arm S1 Inefficiency versus Run Number 125

3-40 Electron Arm S2 Inefficiency versus Run Number 126
3-41 Hadron Arm S1 Inefficiency versus Run Number 126
3-42 Hadron Arm S2 Inefficiency versus Run Number 127
3-43 Hadron Arm S2 Inefficiency versus Recoil Proton Momentum 127
3-44 Electron Arm VDC Efficiency versus Scattered Electron Energy 128
3-45 Hadron Arm VDC Efficiency versus Recoil Proton Momentum 129
3-46 Electron Arm ϕ_{tra} versus θ_{tra} 130
3-47 Electron Arm y_{tra} versus x_{tra} 130
3-48 Electron Arm Čerenkov Inefficiency versus Scattered Electron Energy . . . 131
3-49 Electron Arm Calorimeter Inefficiency versus Scattered Electron Energy . . 132
3-50 Proton-Proton, Proton-Neutron, and Proton-Deuteron Total Cross Sections 136
3-51 Normalized Yield versus Current for the 15 cm LH_2 Target 137
3-52 Normalized Yield versus Current for the 15 cm LD_2 Target 137
3-53 Data versus Monte Carlo Comparison 141
3-54 Data versus Monte Carlo Comparison 142
3-55 Measured Elastic *e-p* Cross Sections Compared to the World Data for the $B(Q^2)$ Kinematics 148
3-56 Measured Elastic *e-p* Cross Sections Compared to the World Data for the $A(Q^2)$ Kinematics 148
4-1 The Corrected *e-d* Coincidence Time-of-Flight Spectra for all $B(Q^2)$ Kinematics 153
4-2 The Corrected *e-d* Coincidence Time-of-Flight Spectra for Selected $A(Q^2)$ Kinematics 154
4-3 The 12 Events Detected at $Q^2 = 5.90$ (GeV/c)^2 with Beam Energy of 4.397 GeV 155
4-4 Schematic of the Rosenbluth Separation of $A(Q^2)$ and $B(Q^2)$ 159
4-5 JLab Hall A $A(Q^2)$ Measurements up to $Q^2 = 1.5$ (GeV/c)^2 161

4-6 JLab Hall A $B(Q^2)$ Measurements up to $Q^2 = 1.5$ (GeV/c)^2 161

4-7 JLab Hall A $A(Q^2)$ Measurements up to $Q^2 = 6$ (GeV/c)^2 162

5-1 IA Diagrams with Meson-Exchange Currents and Isobar Configuration . . . 165

5-2 Deuteron Wave Function 168

5-3 $A(Q^2)$ in the Non-Relativistic Impulse Approximation Using the Argonne v_{18} Potential 170

5-4 $B(Q^2)$ in the Non-Relativistic Impulse Approximation Using the Argonne v_{18} Potential 170

5-5 $B(Q^2)$ in the Models C' and D' of Blunden *et al.* 173

5-6 $A(Q^2)$ in the Models C' and D' of Blunden *et al.* 173

5-7 $A(Q^2)$ for the Deuteron Wave Function of Model $W1$ of Dymarz and Khanna with Δ-Isobars 175

5-8 $B(Q^2)$ for the Deuteron Wave Function of Model $W1$ of Dymarz and Khanna with Δ-Isobars 176

5-9 The Approaches that can be Used for a Relativistic Description of the Deuteron 177

5-10 Electromagnetic Vertex of the Deuteron in Light-Front Dynamics 181

5-11 Contact Term Contribution to the Electromagnetic Interaction with the Deuteron 186

5-12 The $A(Q^2)$ Data Compared to the Model of Carnobell and Karmanov . . . 186

5-13 The $B(Q^2)$ Data Compared to the Model of Carnobell and Karmanov . . . 187

5-14 The Four Relativistic Wave Functions of the Deuteron 191

5-15 Feynman Diagrams Representing the Gross Current Matrix Element 193

5-16 The $A(Q^2)$ Data Compared to the CIA of Van Orden *et al.* and to the RIA of Hummel and Tjon 195

5-17 The $B(Q^2)$ Data Compared to the CIA of Van Orden *et al.* and to the RIA of Hummel and Tjon 195

5-18 One Example of a Two-body Current which Becomes Necessary in order to Satisfy Current Conservation when Retardation Effects are Included 199
5-19 The $A(Q^2)$ Data Compared to the ET Calculation of Phillips *et al.* 199
5-20 The $B(Q^2)$ Data Compared to the ET Calculation of Phillips *et al.* 200
5-21 RIA Feynman Diagram 202
5-22 Theoretical Predictions of the $\rho\pi\gamma$ Form Factor 205
5-23 The $A(Q^2)$ Data Compared to the CIA of Van Orden *et al.* and to the RIA of Hummel and Tjon with the Inclusion of Meson-Exchange Currents 206
5-24 The $B(Q^2)$ Data Compared to the CIA of Van Orden *et al.* and to the RIA of Hummel and Tjon with the Inclusion of Meson-Exchange Currents 207
5-25 n-Point "Decomposition" of $AB \longrightarrow CD$ 208
5-26 Elastic Electromagnetic Form Factors of Hadrons at Large Q^2 210
5-27 The General Structure of the Deuteron Form Factor at Large Q^2 in QCD . 211
5-28 The Deuteron Form Factor $F_d(Q^2)$ Times $(Q^2)^5$ 213
5-29 Two Possible Quark-Constituent Views of Elastic *e-d* Scattering 215
5-30 The Reduced Deuteron Form Factor $f_d(Q^2)$ 216
5-31 Perturbative QCD Predictions for the Ratio B/A Compared with Experiment 219
6-1 Existing and Projected Data from a Planned $A(Q^2)$ JLab Experiment with a 10 GeV Beam 221
6-2 Existing and Projected Data from a Planned $B(Q^2)$ JLab Experiment . . . 221
6-3 Present and Projected Data from a Planned $B(Q^2)$ JLab Experiment Compared to pQCD Calculations 222
A-1 Diagram of the Electron Arm Trigger 224
A-2 Diagram of the Hadron Arm Trigger 225
A-3 Diagram of the Coincidence Trigger 226

List of Tables

2-1 The Operating Parameters of the Fans for Hydrogen and Deuterium 30

2-2 Cryotarget Dimensions 32

2-3 Upstream and Downstream Target Windows Material 32

2-4 Target Density (Para H_2 and Normal D_2) 39

2-5 Luminosity and Heat Deposition in the Target at 100 μA Beam Current . . 41

2-6 Dummy Target Thicknesses and Materials 41

2-7 Dummy Target z Positions and Lengths 42

2-8 Solid Target Thicknesses and Materials 42

2-9 HRS Design Goals and Present Performance 44

2-10 TRANSPORT Model of the Two Hall A HRS 45

2-11 Properties of the Lead-Glass Blocks 60

2-12 Trigger Types 64

2-13 The Outputs of the First MLU 66

2-14 The Relation Between the Event Type and the Latched Trigger Word . . . 70

3-1 Path Difference Correction Coefficients 114

3-2 Classification of the Inefficient Events in Each Arm 120

3-3 Trigger Inefficiency Corrections 124

3-4 Detector Inefficiency Corrections 132

3-5 Summary of the Recoil Nuclear Interactions Corrections 134

3-6 Measured Elastic e-p Cross Sections for $B(Q^2)$ Kinematics 147

3-7 Measured Elastic e-p Cross Sections for $A(Q^2)$ Kinematics 150

3-8 Systematic Uncertainties of the Measured e-p Elastic Cross Sections 151

4-1 Measured Elastic e-d Cross Sections for $B(Q^2)$ Kinematics 156

4-2 Measured Elastic *e*-*d* Cross Sections for $A(Q^2)$ Kinematics 157
4-3 Systematic Uncertainties of the Measured *e*-*d* Elastic Cross Sections 158
4-4 Breakdown of Relative Systematic Errors Between the Backward and Forward Elastic *e*-*d* Cross Section Measurements 158
4-5 Table of the Extracted $A(Q^2)$ and $B(Q^2)$ Values from the Rosenbluth Separation 160
4-6 Table of Extracted $A(Q^2)$ Values at Large Q^2 162
5-1 Static Properties of the Deuteron 168
5-2 Deuteron Properties of the Models C' and D' of Blunden *et al.* 171
5-3 Properties of Mesons Used in One-Boson-Exchange Models of the NN Potential 190
B-1 *e*-*p* Elastic Kinematics for the Backward Angle Calibration 227
B-2 *e*-*d* Elastic Kinematics for $B(Q^2)$ 228
B-3 *e*-*p* Elastic Kinematics for the Forward Angle Calibration 229
B-4 *e*-*d* Elastic Kinematics for $A(Q^2)$ 230
C-1 Input for *e*-*p* Elastic Cross Section Calculations for the Backward Angle Calibration 232
C-2 Input for *e*-*d* Elastic Cross Section Calculations for $B(Q^2)$ 233
C-3 Input for *e*-*p* Elastic Cross Section Calculations for the Forward Angle Calibration 236
C-4 Input for *e*-*d* Elastic Cross Section Calculations for $A(Q^2)$ 238

Acknowledgments

I have had the good fortune to have Makis Petratos as my advisor. I would like to thank him for being generous with his time, attention, patience, and encouragement throughout this project. Thanks to the other members of my committee: Bryon Anderson, Declan Keane, Paul Wang, Philip Westerman, Jian-Ping Chen, and Javier Gomez for all of their suggestions on this work.

I would like to thank my friends at Kent State University, especially Shan Wang, Lu Qian, Charles Johnson, and Michael Olson. I would like to thank my professors at Kent State University: Bryon Anderson, Mark Manley, Michael Lee, George Fai, Peter Tandy, and Richard Madey. Thanks to Reyad Sawafta and Abdellah Ahmidouch for their help and support.

I want to thank the past and present Hall A staff: Larry Cardman, Eugene Chudakov, Ron Gilman, Ole Hansen, Kees de Jager, Meme Liang, John LeRose, Bob Michaels, Sirish Nanda, Eddy Offermann, Arun Saha, Bogdan Wojtsekhowski, Jian-Ping Chen, Javier Gomez, Michael Kuss, and Jack Segal for making CEBAF such a rewarding place for me to work and learn. We built one of the best cryogenic targets in the world, thanks to all who worked on this project. I want to thank the Hall A Cryogenic Target System Group: Jian-Ping Chen, Natalie Degrande, Alexandre Deur, Fraser Duncan, Lars Ewell, Christophe Jutier, Kathy McCormick, Larry Weinstein, and Gary Rutledge. I want to thank David Griffith, Mark Hoegerl, Steven Knight, Mike Seely, Ronald Zarobinski of the JLab Polarized and Cryogenic Target Group, and Paul Brindza and Joyce Miller of the Hall A Engineering Group. I want to thank the members of the E91-026 analysis group for giving me such a pleasant working environment. Thanks to Dave Prout, Kathy McCormick, Michael Kuss, Lars Ewell, Paul Ulmer, Javier Gomez, and Mina Katramatou. Without the Hall A technical staff, this experiment would never have been so successful. Thanks to Ed Folts, Mark

Stevens, James Proffitt, and Scot Spiegel. Thanks to the other Hall A graduate students and post-docs for all of their hard work. Many things in the Hall work today because of the efforts of Amra Serdarevic, Wilson Miller, Lars Ewell, Nilanga Liyanage, Krishni Wijesooriya, Juncai Gao, Kevin Fissum, Fraser Duncan, Bill Kahl, Christophe Jutier, Gary Rutledge, Kathy McCormick, Dave Prout, Alexandre Deur, Luminita Todor, Gilles Quemener, Sergey Malov, and Mark Jones. Thanks to the Hall A collaboration especially John Calarco and George Chang. Thanks to all other Hall A experimenters who took the time to sit on shifts in E91-026.

Last but not least, I want to thank my family and especially my wife Hanadi, to whom this work is dedicated.

Chapter 1

Introduction

1.1 Introduction

Electron scattering provides a powerful tool for studying the structure of the nucleus. Because the electron-photon interaction is well described by quantum electrodynamics (QED), electron scattering provides a well understood probe of nuclear structure. The deuteron is the simplest nucleus made up of only a proton and a neutron. This makes it one of the best cases for studying the structure of the nucleus.

The nuclear force is a manifestation of a fundamental force, the strong force, acting among the quarks and gluons. The nuclear force holds the nucleus together. It acts among the nucleons in a nucleus, with a range that is of the same order of magnitude as the nucleon radius ($\sim$1 fm). The form of the nucleon-nucleon (NN) potential is studied by analyzing two-body systems such as nucleon-nucleon scattering and the only two nucleon bound system, the deuteron.

The ground state properties of the deuteron yield information about the character of the nuclear force. Some deuteron properties, such as its binding energy (2.225 MeV), provide inputs which are used to constrain free parameters in models of the nucleon-nucleon interaction. Measurements of the deuteron magnetic dipole and charge quadrupole moments have yielded $\mu_d = 0.857406\ \mu_N$ and $Q_d = 0.2859$ fm^2, respectively. The value of the electric quadrupole moment reveals information about the deformation of the deuteron, which in turn reveals information about the nuclear tensor force. Since the deuteron is a relatively simple system, it has been the subject of many theoretical studies, using both relativistic and non-relativistic approaches.

Non-relativistically, the Schrödinger equation can be solved with a high degree of accuracy for few nucleon systems, and predictions for the deuteron static properties such as the D/S ratio (where D and S denote the angular momentum states present in the deuteron wave function), the charge radius and the magnetic and quadrupole moments exist in all recent NN interaction models (see Section 5.2). In most cases, the models are able to provide accurate predictions for the static properties. The exceptions are the magnetic and quadrupole moments, which are underestimated in the non-relativistic treatment, even with the latest state of the art models, so they provide evidence that relativistic and two-body exchange corrections must be taken into account.

The electromagnetic structure of the deuteron is described in terms of three form factors: the charge monopole, the charge quadrupole, and the magnetic dipole form factors, which are discussed in the sections that follow. These form factors are combined, along with some kinematical factors, into two structure functions known as the elastic electric and magnetic structure functions, $A(Q^2)$ and $B(Q^2)$, respectively. These structure functions, and therefore the three form factors, can be studied by elastic electron-deuteron (e-d) scattering. Many non-relativistic predictions of the structure functions exist, but these predictions usually have to be augmented with corrections (such as relativistic corrections and meson-exchange current (MEC) contributions) before they are able to describe the available data. Relativistically, deuteron wave functions can be derived from realistic NN interaction models via solution of the Bethe-Salpeter and Gross Equations (see Section 5.3). The deuteron structure functions $A(Q^2)$ and $B(Q^2)$ have been calculated using a variety of relativistic models, but they tend to underestimate the data. The relativistic theory of elastic electron-deuteron scattering is considered to be reliable, so the failure of one-body calculations to describe the data then gives an estimate of the contributions that two-body effects can make to the deuteron elastic structure functions (see Section 5.4).

At sufficiently large momentum transfers, the deuteron form factors should be calculable

in terms of only quarks and gluons within the framework of quantum chromodynamics (QCD). There are predictions of perturbative QCD and dimensional scaling laws which predict the Q^2 dependence of the form factors, but comparison with the available data (see References [1] and [2]) indicates that these calculations are not applicable below a Q^2 of 3 $(\mathrm{GeV/c})^2$.

This work describes a new set of measurements of the deuteron electric and magnetic elastic structure functions, $A(Q^2)$ and $B(Q^2)$. The next two sections of this chapter describe the kinematics of elastic electron-deuteron scattering and the extraction of the structure functions. Section 1.5 gives an overview of the existing data.

1.2 Kinematics

The Feynman diagram for elastic electron-deuteron scattering, in the one-photon-exchange approximation, is shown in Figure 1-1. This diagram represents an electron with energy E incident on a stationary deuteron of mass M_d.

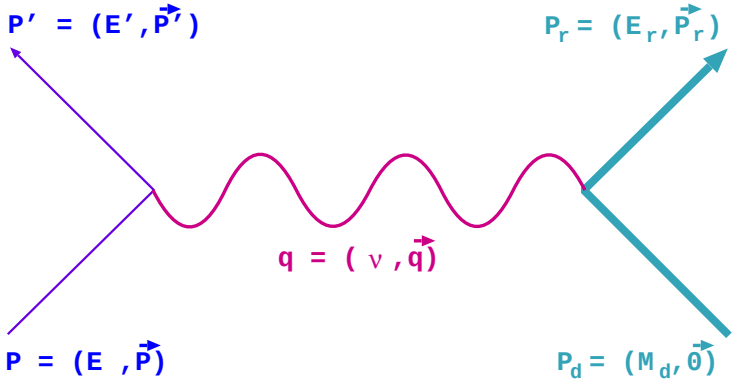

Fig. 1-1: Feynman diagram of elastic electron-deuteron scattering. The four-momenta of the interacting particles and the exchanged virtual photon are defined.

The four-momentum transfer squared is given by:

$$Q^2 = -q^2 = 4EE' \sin^2 \frac{\theta}{2} \,, \tag{1-1}$$

where E is the incident beam energy, E' is the energy of the scattered electron and θ is the electron scattering angle. In the derivation of Equation 1-1, the electron rest mass has been neglected. The energy transfered to the target nucleus, ν, is $\nu = E - E'$. The energy of the scattered electron is given in terms of E and θ as:

$$E' = \frac{E}{1 + \frac{2E}{M_d}\sin^2\frac{\theta}{2}} \ . \tag{1-2}$$

1.3 Deuteron Elastic Structure Functions and Form Factors

The cross section for unpolarized elastic electron-deuteron scattering is described, in the one-photon-exchange approximation, by the Rosenbluth formula:

$$\frac{d\sigma}{d\Omega} = \sigma_M[A(Q^2) + B(Q^2)\tan^2(\theta/2)] \ , \tag{1-3}$$

where the Mott cross section, σ_M, describes the cross section for scattering from a structure-less and spinless target:

$$\sigma_M = \frac{\alpha^2 E' \cos^2\frac{\theta}{2}}{4E^3\sin^4\frac{\theta}{2}} \ , \tag{1-4}$$

with $\alpha = 1/137$ being the fine-structure constant. The form of the Mott cross section shown in Equation 1-4 includes a factor that accounts for the recoil of the target nucleus. It is evident from Equation 1-3 that $A(Q^2)$ and $B(Q^2)$ can be separated by measuring the cross section at two different electron scattering angles while keeping Q^2 constant (Rosenbluth separation technique).

The elastic structure functions $A(Q^2)$ and $B(Q^2)$ can be expressed in terms of the charge monopole (F_C), the charge quadrupole (F_Q) and the magnetic dipole (F_M) form factors of the deuteron:

$$A(Q^2) = F_C^2(Q^2) + \frac{8}{9}\eta^2 F_Q^2(Q^2) + \frac{2}{3}\eta F_M^2(Q^2) \ , \tag{1-5}$$

$$B(Q^2) = \frac{4}{3}\eta(1+\eta)F_M^2(Q^2) \ , \tag{1-6}$$

where $\eta = Q^2/4M_d^2$. The kinematic factors of F_Q and F_M are chosen so that in the static limit ($Q^2 = 0$):

$$\begin{aligned} F_C(0) &= 1 \ , \\ F_Q(0) &= M_d^2 Q_d = 25.84 \ , \\ F_M(0) &= \frac{M_d}{M_N}\mu_d = 1.714 \ , \end{aligned} \tag{1-7}$$

where $F_C(0)$ is the electric charge of the deuteron, normalized to the elementary charge e, and M_N is the nucleon mass.

A measurement of the deuteron elastic structure functions, $A(Q^2)$ and $B(Q^2)$, allows only the extraction of F_M, since $B(Q^2)$ depends on F_M alone. To separate F_C and F_Q, a measurement of another observable is required, and this is necessarily a polarization observable. One must either measure the asymmetries induced by a tensor polarized target, or measure the tensor polarization or the vector polarization of the recoil deuterons. Usually, the t_{20} moment of the deuteron tensor polarization is measured which is given by:

$$t_{20}(Q^2) = -\frac{1}{\sqrt{2}}\left[\frac{\frac{8}{3}\eta F_C(Q^2)F_Q(Q^2) + \frac{8}{9}\eta^2 F_Q^2(Q^2) + \frac{1}{3}\eta\left[1 + 2(1+\eta)\tan^2(\theta/2)\right]F_M^2(Q^2)}{A(Q^2) + B(Q^2)\tan^2(\theta/2)}\right] . \tag{1-8}$$

Figure 1-2 shows the individual contribution of the three form factors to $A(Q^2)$ as calculated in the relativistic impulse approximation by Hummel and Tjon [3].

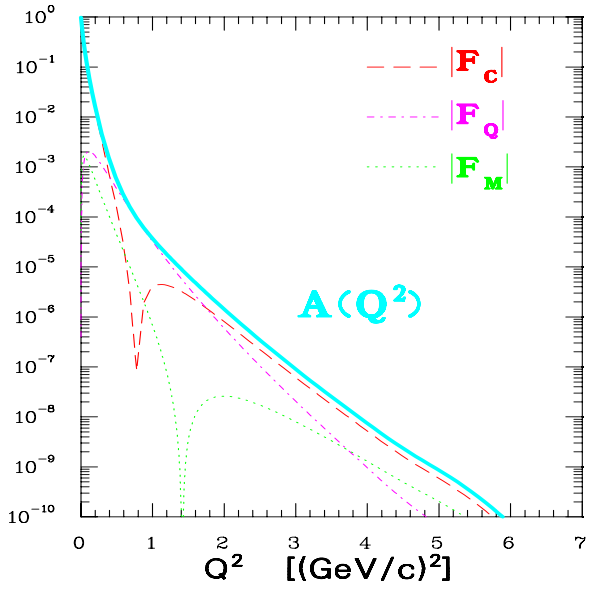

Fig. 1-2: The contribution of the deuteron form factors to $A(Q^2)$ as calculated by Hummel and Tjon [3].

1.4 This Experiment

This experiment, referred to as E91-026 [4], was performed in Hall A at Jefferson Laboratory (JLab) in Newport News, Virginia. $A(Q^2)$ and $B(Q^2)$ were measured using the JLab electron beam and a high power liquid deuterium target. The elastic electron-deuteron data taking was divided into two periods: the first period was dedicated to measurements at a fixed backward electron scattering angle (144.5°) where the contribution from the magnetic structure function to the cross section is maximized. Data were taken at $Q^2 = 0.684$, 0.813, 0.941, 1.069, 1.197 and 1.325 (GeV/c)^2. The second period of data taking was dedicated to measurements of $A(Q^2)$ up to the largest possible Q^2. Data were taken at $Q^2 = 0.685$, 0.811, 0.938, 1.063, 1.188, 1.314, 1.53, 1.76, 2.35, 3.01, 3.41, 3.92, 4.40, 4.91, 5.30, and 5.90 (GeV/c)^2. Interspersed in the two month running period were elastic electron-proton (e-p) cross section measurements, which were used for calibration purposes.

The experimental apparatus, including the JLab accelerator and the Hall A equipment,

are discussed in Chapter 2. The analysis method is discussed in Chapter 3. The results of both $A(Q^2)$ and $B(Q^2)$ measurements are given in Chapter 4. A discussion of several applicable theories and a comparison to the data is given in Chapter 5.

1.5 Previous Data

The first objective of this experiment was to obtain a precise measurement of $A(Q^2)$ from $Q^2 = 0.7$ to 6 $(\mathrm{GeV/c})^2$. The measurement of $A(Q^2)$ at low momentum transfers (below 2 $(\mathrm{GeV/c})^2$) was motivated by the disagreement between the SLAC $A(Q^2)$ [1] data and the data from Saclay [5], CEA [6] and Bonn [7] in the region where they overlap, as shown in Figure 1-3. Prior to this experiment, the deuteron $A(Q^2)$ structure function had been measured up to a maximum momentum transfer of $Q^2 = 4$ $(\mathrm{GeV/c})^2$ in SLAC Experiment 101 (Figure 1-4). Measurements at high momentum transfers are important because they probe the short distance structure of the deuteron, hence, they are sensitive to the presence of quark degrees of freedom in the deuteron. Therefore, our goal was to extend the measured $A(Q^2)$ range to a maximum of $Q^2 = 6$ $(\mathrm{GeV/c})^2$.

The second objective of this experiment was to provide a precise measurement of $B(Q^2)$ from $Q^2 = 0.7$ to 1.3 $(\mathrm{GeV/c})^2$. It is also extremely desirable to measure $B(Q^2)$ around its minimum at $Q^2 \sim 2$ $(\mathrm{GeV/c})^2$. The Rosenbluth technique is limited by the magnitude of $B(Q^2)$ compared to $A(Q^2)$. Thus, to do a measurement around the minimum, the electron scattering angle should be close to 180°, which was not feasible in this experiment. Figure 1-5 shows the $B(Q^2)$ measurements available prior to this experiment [2, 8, 7]. Figure 1-6 shows the existing world data on $A(Q^2)$ and $B(Q^2)$ indicating the relative size of the two elastic structure functions.

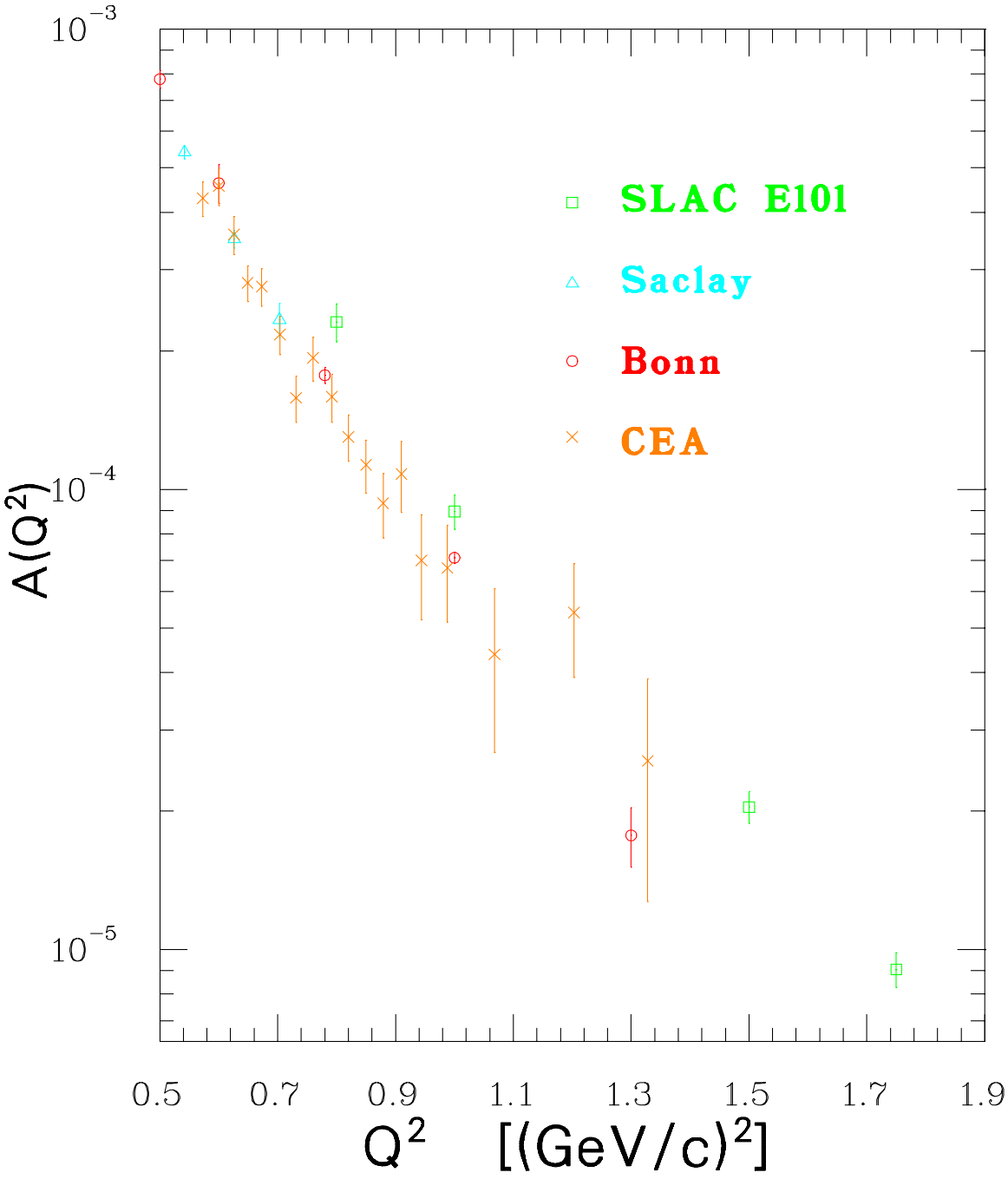

Fig. 1-3: Existing $A(Q^2)$ data in the range of $0.5 \leq Q^2 \leq 1.9$ (GeV/c)^2. Shown are data from experiments performed at SLAC [1], Saclay [5], CEA [6] and Bonn [7].

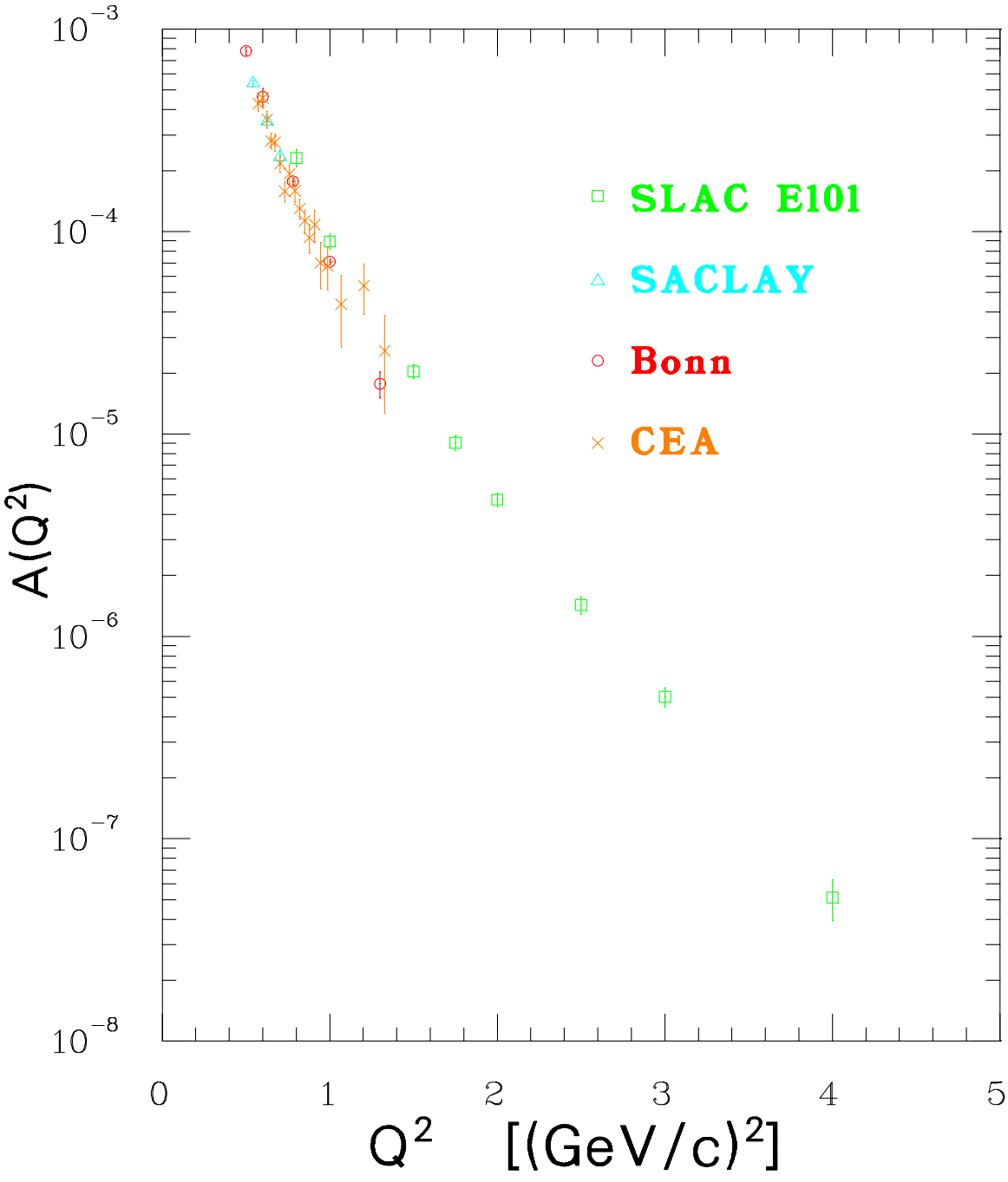

Fig. 1-4: Existing $A(Q^2)$ data. Shown are data from experiments performed at SLAC [1], Saclay [5], CEA [6] and Bonn [7].

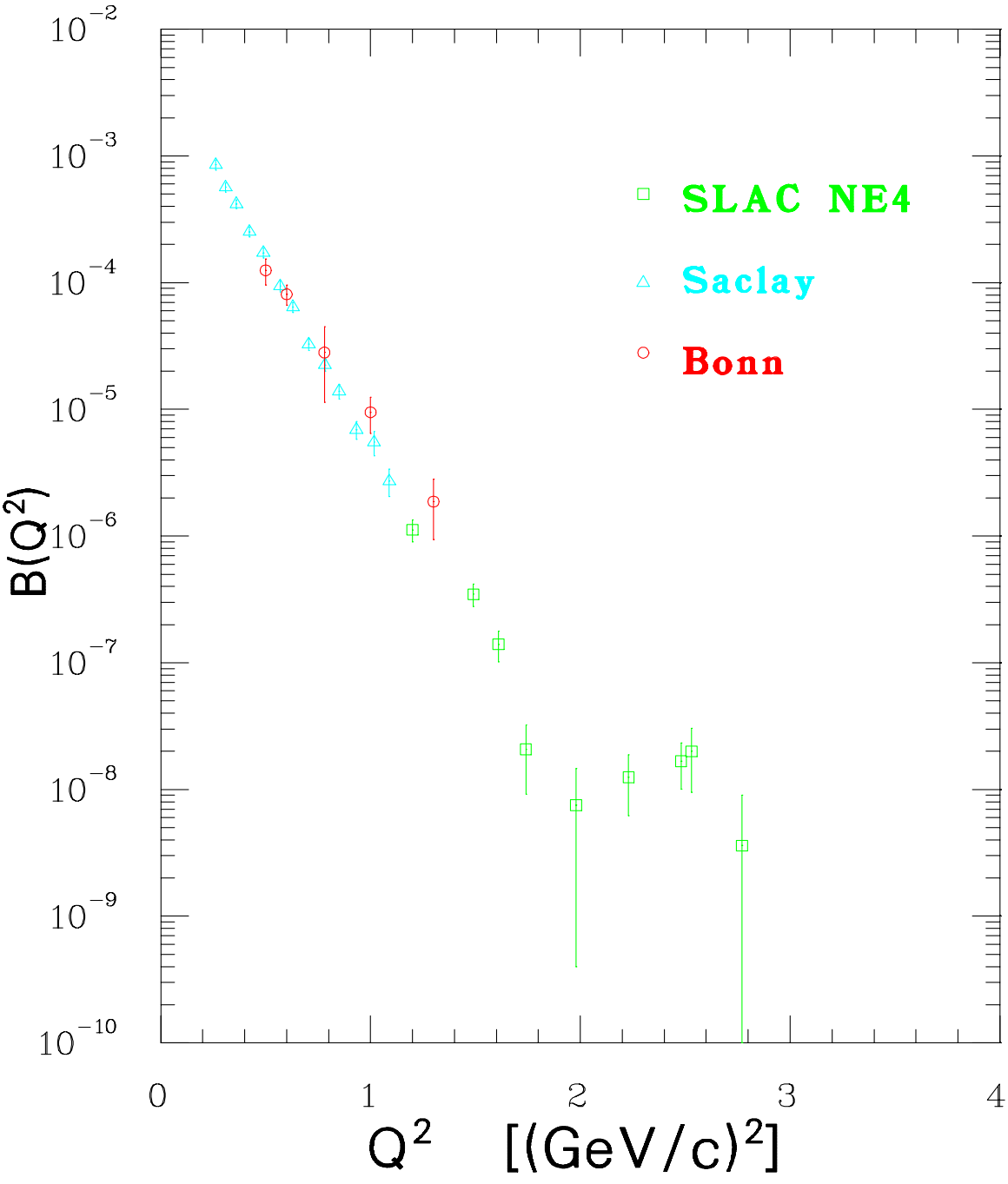

Fig. 1-5: Existing $B(Q^2)$ data. Shown are data from experiments performed at SLAC [2], Saclay [8], and Bonn [7].

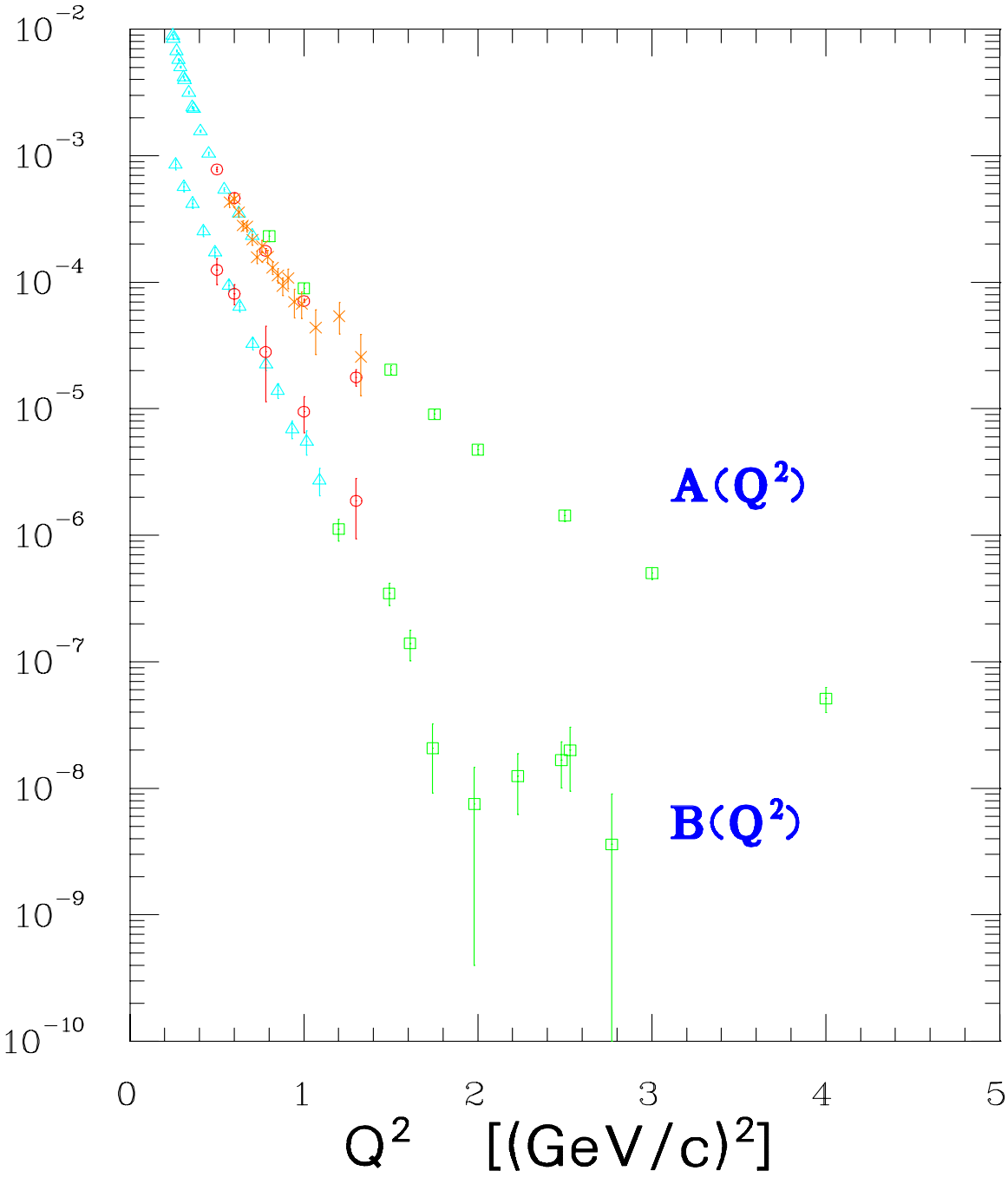

Fig. 1-6: Existing $A(Q^2)$ and $B(Q^2)$ data. Shown are data from previous experiments [1, 2, 5, 6, 7, 8] indicating the relative size of the two elastic structure functions.

Chapter 2

Experimental Apparatus

2.1 Overview

Experiment E91-026, "Measurement of the Deuteron Elastic Structure Functions at Large Momentum Transfers", took place in experimental Hall A of JLab. The data taking phase took place in the period October 13 to December 17, 1997, during which the other two JLab experimental halls, Hall B and Hall C, were also running experiments. The goal of E91-026 was to measure the elastic electric and magnetic structure functions of the deuteron. This was a coincidence experiment, with the scattered electrons detected in the Electron Arm High Resolution Spectrometer (HRSE) and the recoil deuterons detected in the Hadron Arm High Resolution Spectrometer (HRSH). Elastic *e-p* calibration data were also taken. The data taking required a range of beam energies (0.539–4.399 GeV) and beam currents (5–120 μA).

2.2 Accelerator

The Continuous Electron Beam Accelerator (CEBA) of JLab was designed to deliver a continuous beam of electrons simultaneously to three experimental end-stations. A diagram of the racetrack shaped accelerator is given in Figure 2-1. The source of the injector is a 100 keV thermionic emission gun with a maximum beam current of a few mA. Next, the beam is incident on a chopping aperture which contains slits of different sizes, one for each of the experimental Halls A, B and C. The width of these slits determines the beam current that is delivered to each Hall. The chopper sweeps the beam over the slits with a rotating electric field with a frequency of 1497 MHz. The beam then enters the first superconducting

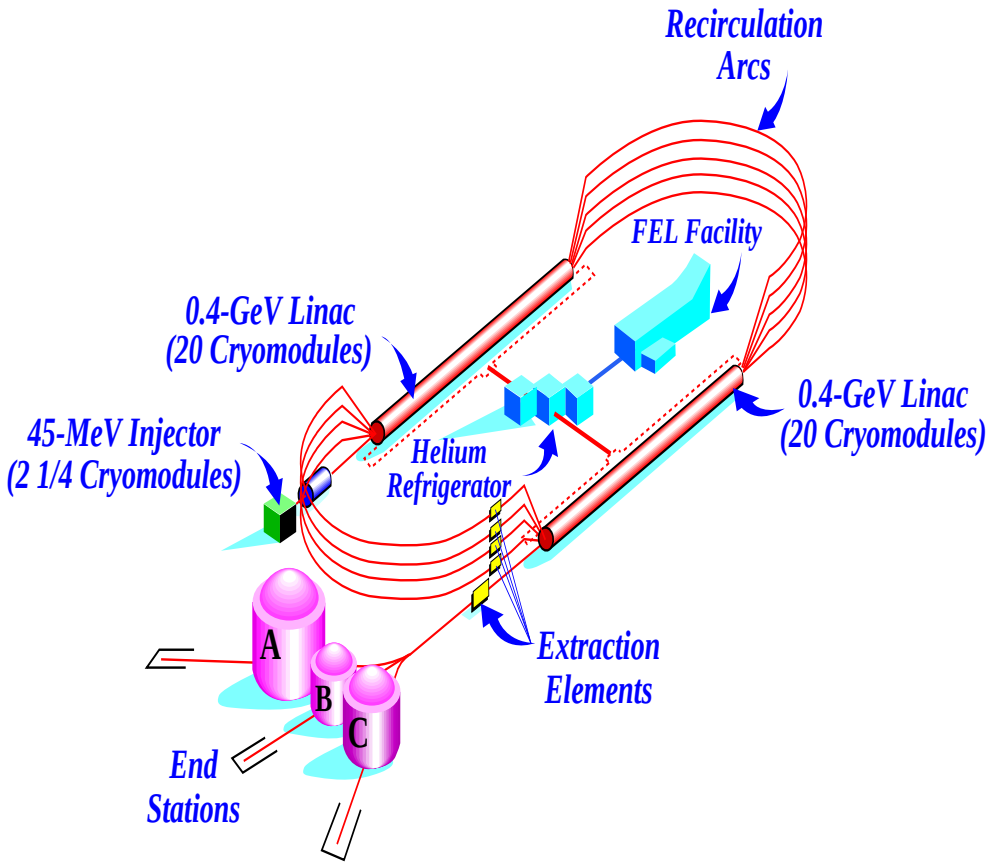

Fig. 2-1: Schematic of the Jefferson Lab accelerator.

accelerator section, 2 1/4 cryomodules, where it is accelerated to 45 MeV and then injected into the North Linac.

The North Linac is a string of 20 cryomodules, with each cryomodule containing eight super-conducting niobium cavities. These cavities are kept super-conducting by 2 K Helium coolant from the Central Helium Liquefier (CHL). The niobium cavities contain electric fields which accelerate the electrons as they travel through them. At the end of the North Linac, the electron beam has a nominal energy of 445 MeV (45 MeV from the injector and 400 MeV from the Linac), although by careful tuning of the accelerating electric field of the cavities, this energy can be raised or lowered, as was the case several times during E91-026. Next, the beam enters the east magnetic recirculation arcs, where it is bent in a semi-circle to the South Linac. Here again the beam is accelerated through a string of 20 cryomodules. At the end of the South Linac, the beam can be extracted for use in any of the experimental halls or it can proceed around the west recirculation arcs for another pass around the accelerator. The beam can traverse the accelerator a maximum of five times, gaining a nominal 800 MeV of energy with each pass around the machine. In the North and South Linacs the different energy beams, resulting from each pass around the accelerator, travel in the same beamline. However, the different energy beams require different bending fields in the recirculation arcs. When the beams reach the arcs they are separated by momentum and each one goes through a different arc (as seen in Figure 2-1). At the end of the arcs, the beams are recombined into the same beamline again. When the beam is of the energy requested by the experimental halls, it is extracted from the accelerator to the Beam Switch Yard (BSY). There the three sets of beam bunches are separated into the appropriate experimental hall beamline by deflecting cavities operating at 499 MHz. Each hall receives a short (1.67 ps) train of pulses with a frequency of 499 MHz.

The beam has a very small transverse size ($\lesssim$200 μm (FWHM) at 845 MeV). The fractional energy spread (ΔE/E) is at the 10^{-4} level. The beam energy is known absolutely

to 0.2% from the analysis of $H(e, e'p)$ scattering data taken in Hall A (see section 3.4).

2.3 Hall A

The Hall A facility is the largest of the three JLab experimental halls, with a diameter of 53 m. It contains two nominally identical high resolution magnetic spectrometers, respectively known as the Electron and the Hadron Spectrometer. Either spectrometer can be configured for positive or negative particle detection by changing the polarity of its magnetic elements. The spectrometers can be moved clockwise or counter-clockwise around the hall. The Electron spectrometer has a minimum angle of 12.5° with respect to the beamline and a maximum central angle of 165.0°, while the Hadron spectrometer has a minimum angle of 12.5° and a maximum central angle of 130.0°.

A schematic of Hall A is shown in Figure 2-2. At the pivot point of the two spectrometers sits the cryotarget, encased within a cylindrical aluminum scattering chamber. The electron beam is incident on the target through the beamline. There are elements along the beamline for measurement of the beam current, beam position, beam energy and beam polarization. The primary target for this experiment was a high power liquid deuterium target. Scattered electrons and recoil deuterons traverse the magnetic elements of the spectrometers and are detected by an array of detectors located in the shield house at the top of each spectrometer. The primary beam continues along the path of the beamline to the beam dump (not shown in Figure 2-2).

2.4 Hall A Arc and Beamline

When the beam has reached the requested energy, it is directed into the appropriate experimental hall. Beam bound for the Hall A target is bent into the hall through an arc containing eight magnets. A knowledge of the magnetic field strength of these magnets and the path of the beam through them allows determination of the incident beam energy. The arc energy measurement was not available during this experiment. After entering the

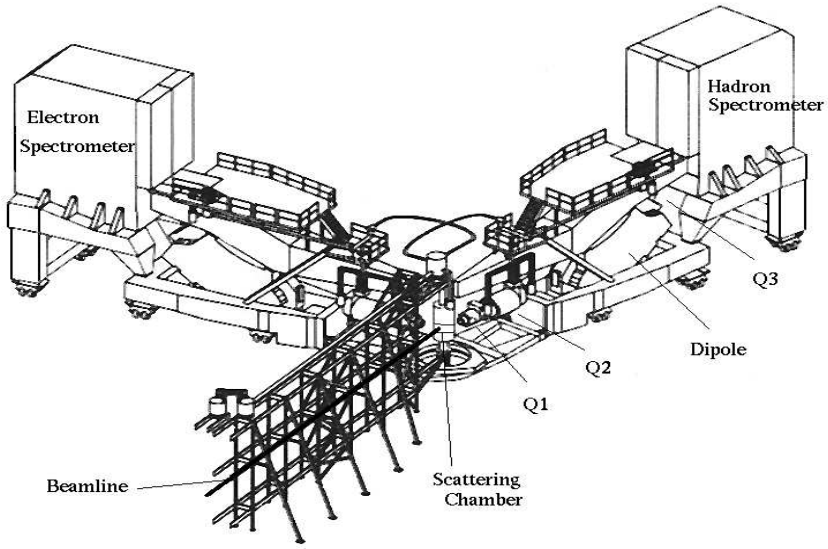

Fig. 2-2: Schematic of Hall A. Shown are the two high resolution spectrometers, the scattering chamber and the beamline.

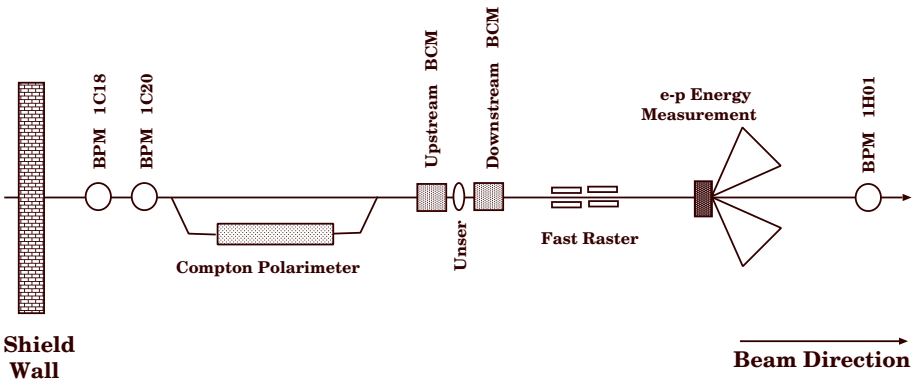

Fig. 2-3: The Hall A beamline from the shield wall through the *e-p* energy measurement system (not to scale). This section of the beamline spans approximately 26 m.

hall, the beam travels in a straight section of beamline until the target. This straight section contains the major beamline elements, including a Compton polarimeter, an "*e-p* energy measurement" device and a Møller polarimeter. None of these devices were directly employed during E91-026, although the magnetic elements of the Møller polarimeter were used for beam tuning (see section 2.4.4 for more details). More details on all of these devices can be found on the Hall A web page [9]. The beamline also contains many smaller elements, such as the Beam Position Monitors (BPMs), used to measure the beam position, the Beam Current Monitors (BCMs), used to measure the charge incident on the target and a beam rastering system, used to reduce target density changes and prevent damage to the target cell.

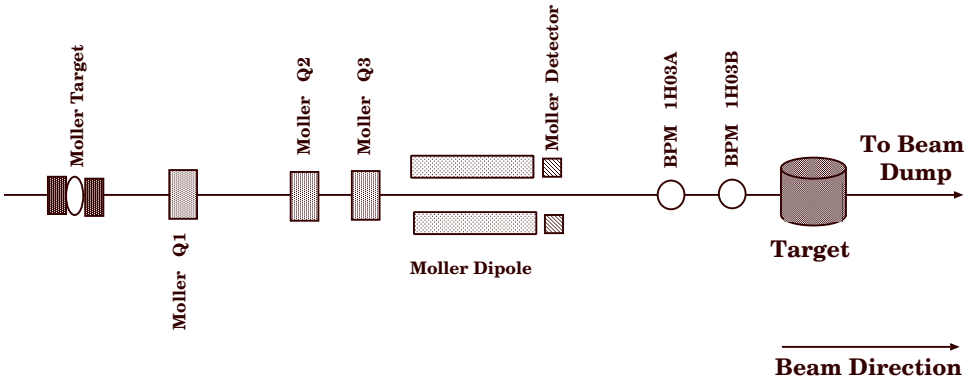

Fig. 2-4: Continuation of Figure 2-3: The Hall A beamline from the Møller target through the cryotarget. This section of beamline spans approximately 18 m. After the target, the primary beam continues to the beam dump (not shown).

2.4.1 Beam Position Monitors

There are five BPMs in the Hall A beamline between the target and the shield wall that separates Hall A from the accelerator (see Figures 2-3 and 2-4). These BPMs are used by the accelerator operators to measure the position of the electron beam inside the beam-pipe. The BPMs measure the position of the beam non-destructively, and can therefore be used

to monitor the beam position continuously.

Each BPM is a cavity with a four-wire antenna array running parallel to its axis, with two wires being used to measure the x (horizontal) position and the other two being used to measure the y (vertical) position of the beam inside the cavity. The antenna wires are positioned at $\pm 45^\circ$ from the horizontal and vertical. When the beam passes through the cavity, it induces a signal in each antenna wire, proportional to the distance from that wire. The x and y beam positions are then given by the asymmetry between the two x antenna wire signals and the two y antenna wire signals, respectively, multiplied by some calibration constants (for a complete description of the operation of the BPMs, see Reference [10]).

For the data taking phase of E91-026, the beam was steered so that its position was within ± 0.2 mm of zero, as read on the last two BPMs before the target (denoted "1H03A" and "1H03B", respectively). The BPMs have been aligned to the center of the target cell via survey, with an error of approximately 0.5 mm.

2.4.2 Beam Current Monitors

The beam current monitoring system for Hall A consists of a parametric current transformer (Unser monitor [11]) sandwiched between two resonant cavities [12]. The Unser monitor provides an absolute measurement of the current, but it drifts on the time scale of minutes, so it cannot be used to monitor the current continuously. Continuous monitoring of the current is accomplished with the resonant cavities. The cavities have a stable output signal that is proportional to the beam intensity, but they are unable to give an absolute measure of the current. To obtain an absolute current measurement that is stable over time, the outputs of the resonant cavities are calibrated to that of the Unser monitor.

A schematic of the current monitoring system is shown in Figure 2-5. The two resonant cavities, labeled Upstream and Downstream BCM, and the Unser monitor, are seen in the upper-right of this figure. The cavities are steel cylindrical waveguides, 15.48 cm in diameter

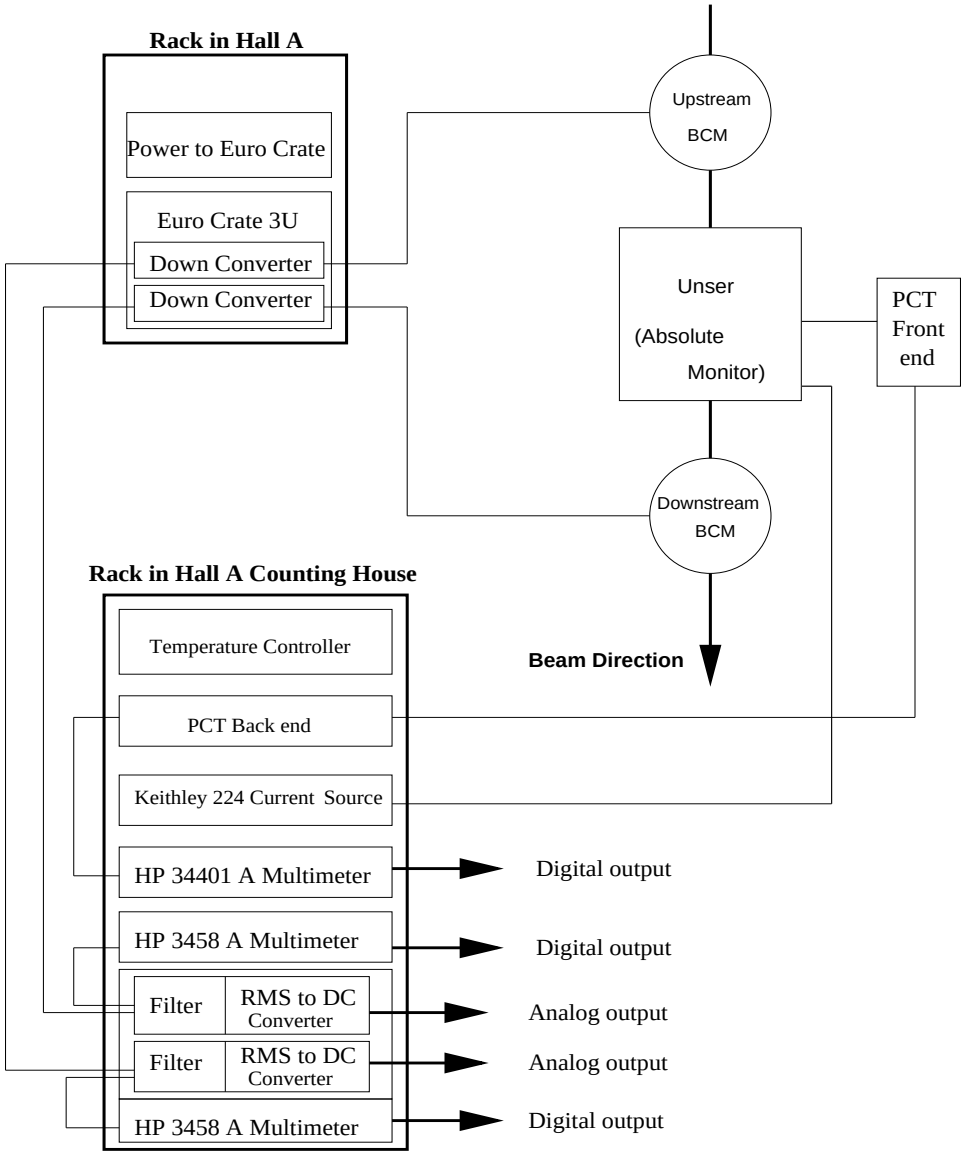

Fig. 2-5: Diagram of the Hall A current monitoring system.

and 15.24 cm long. Inside each cavity are two coaxial loop antennas. The smaller of the two loop antennas is for calibration purposes, while the larger picks up the signal from the beam. When the beam passes through the cavity, it excites the TM_{010} mode. This mode has a resonant frequency of 1497 MHz. The large loop antenna then provides an output signal whose voltage is proportional to the beam current. Two possible sources of error in this type of current measurement are temperature variations and radial beam displacements. Since the resonant frequency of the cavity is sensitive to the dimension of the cavity (and therefore to temperature), the BCMs and Unser are housed in a temperature stabilized box where the temperature is regulated to 0.2 °C. This fluctuation leads to an error of 0.07% in the measured beam current. Also, the output signal of the cavity is sensitive to the radial displacement of the beam from the cavity axis, leading to an error of about 0.06% per cm of radial displacement. In practice, the beam is kept within millimeters of the cavity axis, leading to a very small error on the measured beam current from radial displacements.

The signal from each cavity is then fed into a down-converter (top-left in Figure 2-5), where it is reduced from 1497 MHz to 1 MHz for transmission to the electronics located in the Hall A counting house (bottom-left in Figure 2-5). For each BCM signal, two outputs are available in the counting house: a digital output from a HP 3458A multi-meter and an analog output. The output from the digital multi-meter is fed into a control system developed in the EPICS environment (see Section 2.5.1.7 for EPICS information). This signal comes in one second intervals and represents a rms average of the input signal during that second. The resulting number is proportional to the average beam current (and therefore charge) during that second. To obtain the absolute value of the beam current, the multi-meter output is multiplied by a calibration constant (see section 3.3 for the measurement of the calibration constant). About each four seconds, the value of the beam current (multi-meter output times calibration constant) is written into the data stream, allowing later extraction of the charge accumulated during a data run.

The other output from the current measurement system is the analog output from the RMS to DC converters (one for each BCM) in the counting house (bottom-left in Figure 2-5). The RMS to DC converter produces a DC voltage level which is fed into a Voltage-to-Frequency (VtoF) converter whose output frequency is proportional to the input DC level. The output from the VtoF is then fed into scalers and injected into the data stream with the rest of the scaler information, leading to an accumulated scaler sum at the end of a run which is proportional to the beam charge. To obtain an absolute measure of the charge accumulated during a run, the scaler sum from the VtoF is compared to the EPICS output of the multimeter during that same run (for details on the VtoF calibration, see Reference [13]).

Both of the above methods of monitoring the beam current (sampled and integrated) should be able to yield accurate estimates of the charge accumulated during a run, as long as beam variations do not occur on the time scale with which the sampled EPICS data is recorded. During this experiment, the beam delivery was stable, so the charge accumulated during a run was extracted from the (sampled) multi-meter data which was written into the data stream.

2.4.3 Beam Rastering System

In an effort to reduce beam-induced target density changes and prevent damage from depositing too much beam power in too small an area, the beam is rastered before it impinges on the target. The hardware for the rastering system is located 23 m upstream of the cryotarget, between the beam current monitors and the *e-p* energy measurement system (see Figure 2-3). For a complete description of the raster hardware, see Reference [14].

The fast rastering system consists of two sets of steering magnets. The first set has its magnetic field oriented so as to deflect the beam horizontally and the second set has its magnetic field oriented to deflect the beam vertically. The magnetic fields of the deflecting

coils were varied sinusoidally, at 25.3 kHz in the horizontal direction and 17.7 kHz in the vertical direction. The ratio of the oscillation frequencies of the two coils was chosen so that the resulting raster pattern would sweep out a rectangular pattern at the target. The beam position on an event by event basis is shown in Figure 2-6. Since the beam rastering was sinusoidal, the beam spent more time around the edges of the raster pattern.

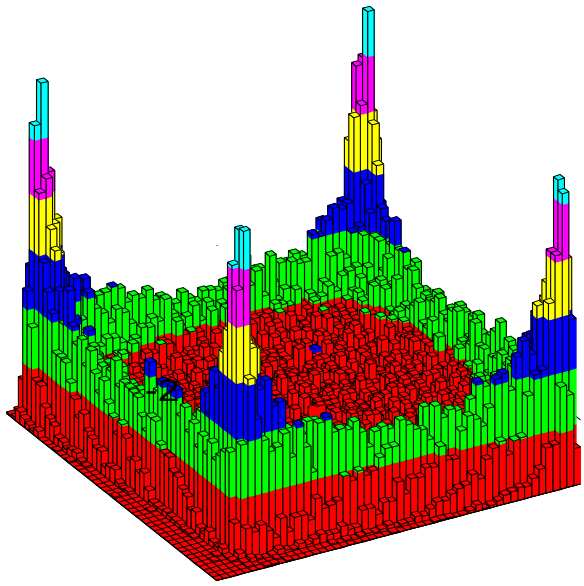

Fig. 2-6: Beam profile with the fast raster showing the position of the beam on target, taken on an event by event basis. For normal data taking, the raster size was set for ($\pm$1.7 mm) $\times$ ($\pm$1.4 mm) (x and y dimensions, respectively), while the spot in this picture is approximately ($\pm$2.5 mm) $\times$ ($\pm$2.5 mm).

2.4.4 Beamline Magnetic Elements

As seen in Figures 2-3 and 2-4, the Møller polarimeter is placed between the e-p energy measurement system and the cryotarget. The polarimeter is used to make measurements of the polarization of the incident electron beam. The beam was unpolarized for this experiment, so no Møller measurements were made, but the three quadrupole magnetic elements of the Møller polarimeter were used by the machine operators for beam tuning.

2.4.5 Scattering Chamber

The scattering chamber used in this experiment consisted of three sections. The bottom section was fixed to the pivot of the Hall. This section contained several viewports through which the targets could be visually inspected and several ports for vacuum pumps. The middle section, where the beam interacted with the target, was an aluminum cylinder with an inner diameter of 104 cm, a height of 91 cm and a wall thickness of 5 cm. The beam entrance and exit pipes were coupled directly to this central section, so the beam passed through no material before interacting with the target. Scattered particles exited the scattering chamber to the spectrometers through aluminum exit windows. Both exit windows were 18 cm tall and together these windows span about 93% of the scattering chamber's circumference, interrupted only by supports for the beam entry and exit and four additional smaller supports spaced around the circumference. The scattering chamber exit windows for both the electron and hadron spectrometer were made of 0.016 inch thick aluminum sheet (5052-H34 alloy, density: 2.68 g/cm^3). The third and uppermost section of the scattering chamber contained space for the cryogenic target plumbing and instrumentation related to its coolant.

All three sections of the scattering chamber were maintained under vacuum. Besides reducing multiple scattering, the chamber vacuum served as an insulator which helped keep the cryogenic target cold. The vacuum level was carefully maintained at the 10^{-6} Torr level. Any degradation in the scatting chamber vacuum was quickly noted, as it led to an increase in temperature of the cryogenic target.

2.4.6 Exit Beamline and Beam Dump

Attached directly to the rear of the scattering chamber is the exit beamline, which terminates at the Hall A beam dump. The exit beamline is divided into two sections which are

separated by a kapton window. In the first section after the scattering chamber (approximately 1.5 m long), the vacuum is maintained at the same level as in the primary beamline (10^{-6} Torr). In the second section, after the kapton window, the vacuum is maintained at the level of 10^{-4} Torr. This second section extends the remaining approximately 28.5 m toward the beam dump. The beam spot starts to blow up because of multiple scattering in the target. As the beam spot expands, so does the beam halo, and to contain the majority of the halo, the diameter of the exit beam pipe grows with a cone opening angle of 1.5°.

The beam terminates on the beam dump. The window of the Hall A beam dump is a sandwich of two beryllium plates with water flowing between them. After this diffuser, beam particles continue on to the main beam dump through a 20 m helium filled pipe approximately 45 cm in diameter. The main beam dump contains water-cooled aluminum plates where the beam deposits its energy. In many cases beam is delivered to the hall with raster off and empty target. The diffuser is required to guarantee that the beam spot on the surface of the aluminum plates of the main beam dump has a minimum size of 2 cm × 2 cm. This design of the exit beamline and beam dump reduces the radiation in the hall compared to other designs in which the exit beamline is filled with helium as in the case of Hall C.

2.5 Targets

A schematic of the target ladder used in this experiment is shown in Figure 2-7. Shown in this figure (from top to bottom) are the three cryogenic target loops, the three aluminum dummy targets that were used to estimate the contribution from the target cell windows and the five solid targets that were used for various calibration purposes.

2.5.1 Cryotargets

The cryogenic portion of the Hall A target consists of three target loops, each of which has two target cells (see Figure 2-8). These target cells are of lengths 15 cm and 4 cm. The

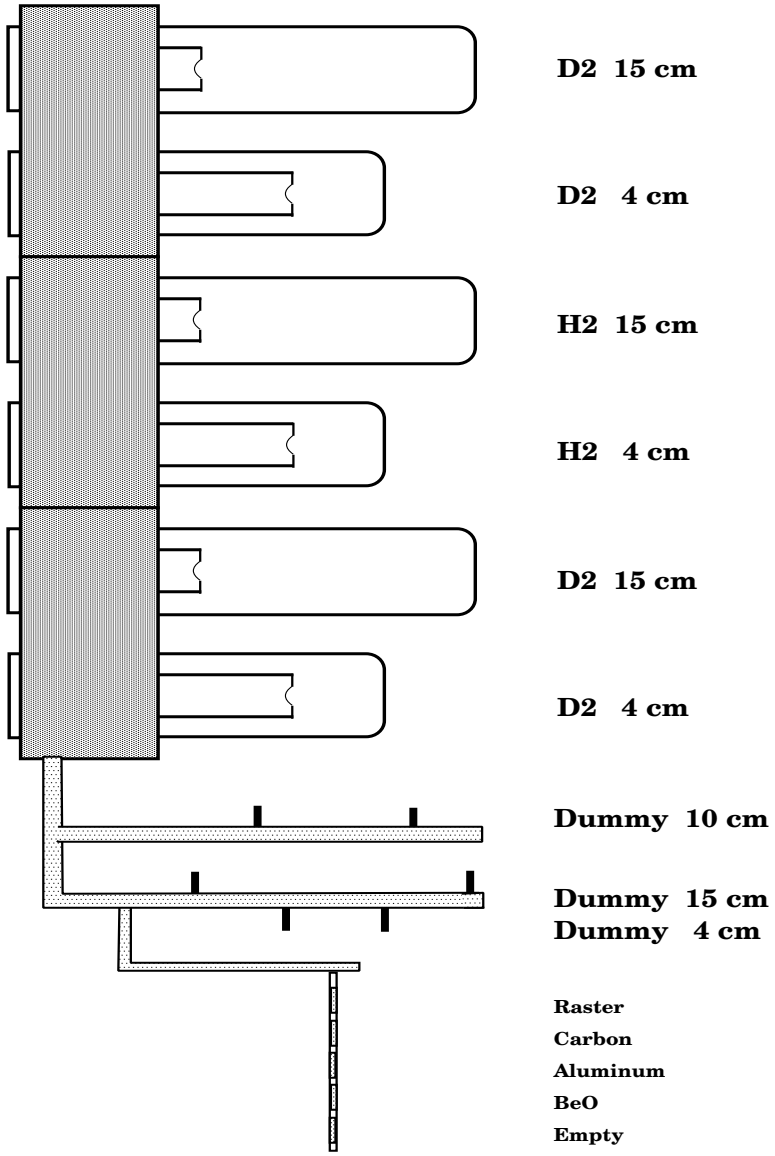

Fig. 2-7: Side view of the Hall A cryotarget with the attached solid target ladder. Shown, from top to bottom, are the three cryogenic target blocks (each block consists of two cells of lengths 15 and 4 centimeters), the three aluminum dummy targets and the five solid targets.

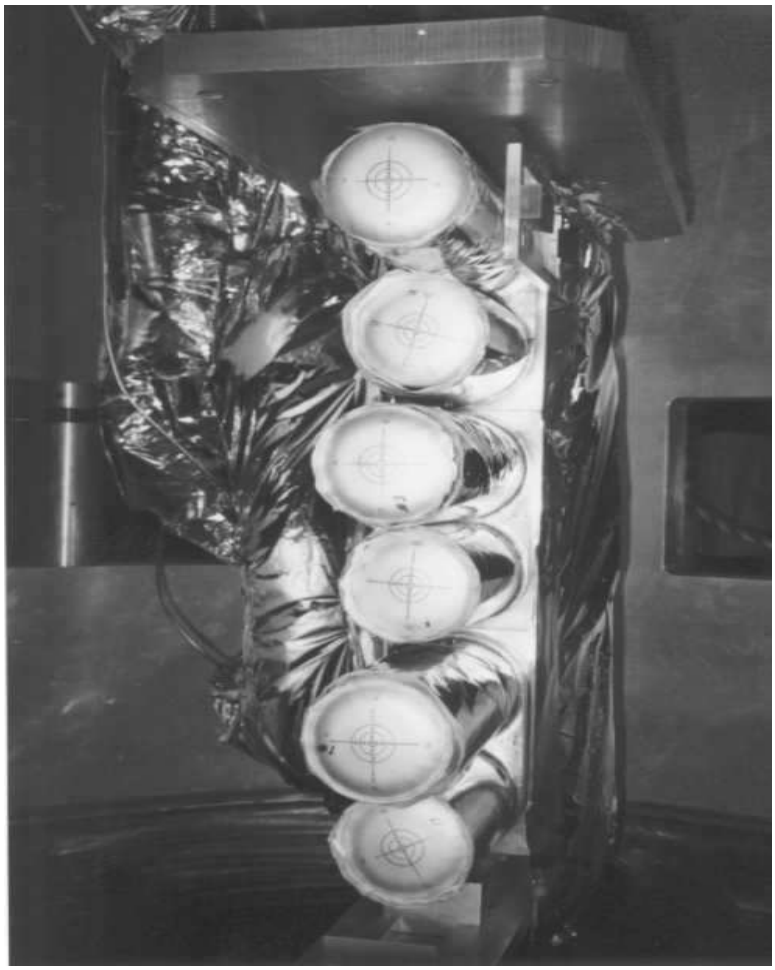

Fig. 2-8: Downstream view of the three cryotarget loops inside the scattering chamber. Some of the target wiring and insulated target plumbing can be seen on the left.

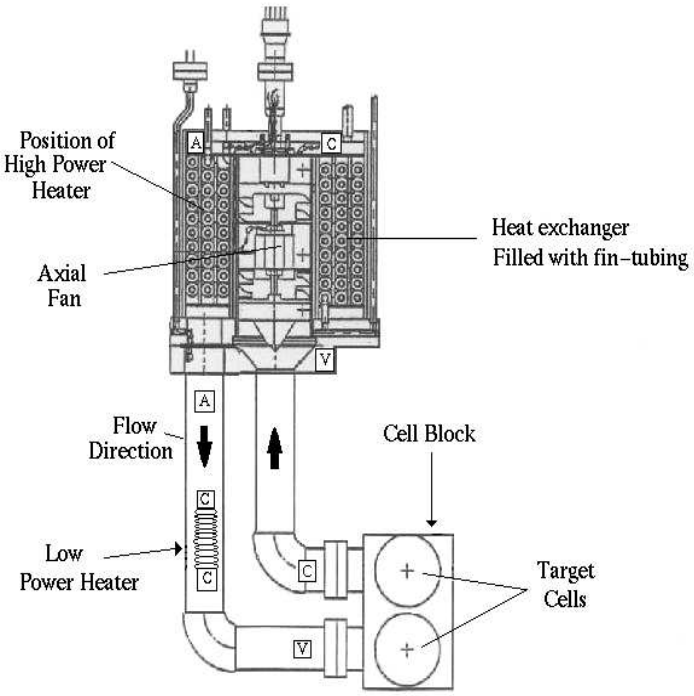

Fig. 2-9: Diagram of a single target loop. Shown are all of the main loop components. The squares represent the three types of temperature sensors: (C)ernox, (A)llen-Bradley and (V)apor pressure bulbs.

cryogen in Loop 2 (middle) is liquid hydrogen (LH_2), while the cryogen in Loops 1 (top) and 3 (bottom) can alternate between liquid deuterium (LD_2) and gaseous ^{4}He according to data taking requirements. The unused loop was filled with ^{4}He at pressure of $\sim$22 psia to protect its cells in case of catastrophic vacuum failure. During the first period of E91-026, data were taken for the $B(Q^2)$ measurement, using the 15 cm Loop 1 target cell as the deuterium target. To maximize the magnetic structure function's contribution to the cross section, the electron spectrometer was placed at a backward scattering angle (144.5°). At this scattering angle, a portion of the scattered electrons would re-scatter through the target cell block (the metal block to which the targets are attached, see Figures 2-9 and 2-11). In order to reduce this effect's contributions, a collimator was installed on the 15 cm target cell of Loop 1. The use of this collimator was unnecessary during the $A(Q^2)$ data taking (during which scattered electrons were detected at forward angles), so to minimize mechanical changes to the target, liquid deuterium was switched to Loop 3 (which had no collimator) and the cryogen in Loop 1 was changed to gaseous ^{4}He. The target remained in this configuration for the rest of the data taking. Note that the gaseous ^{4}He loop was not used as a target. It functions as a spare loop which will be used in the future. The whole target ladder shown in Figure 2-7 is connected to a vertical lifting mechanism so that the desired target cell can be placed in the path of the beam. In the target ladder's uppermost vertical position, the beam passes through the empty target, straight to the beam dump.

A diagram of one of the loops can be seen in Figures 2-9 and 2-10. The main components in each loop are the heat exchanger, the axial fan, the cell block, the heaters and the temperature thermometry.

2.5.1.1 Heat Exchanger

The heat exchanger is seen at the top of Figure 2-9. Inside the heat exchanger are three concentric cylinders filled with fin-tubing. Gaseous ^{4}He from the End Station Refrigerator

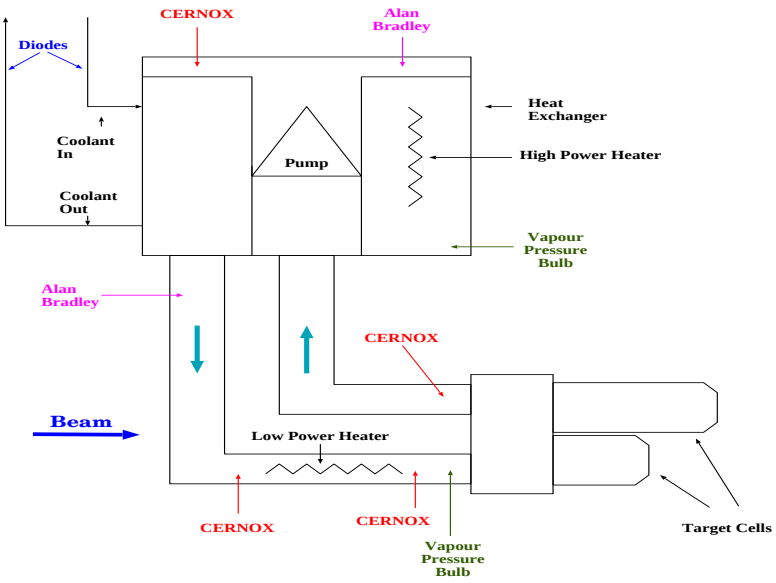

Fig. 2-10: Schematic of a single target loop. Shown are all of the main loop components.

(ESR) provides cooling for the Hall A Cryotarget at a nominal rate of 10 g/s with a temperature of 15 K and a pressure of 12 atm. The ESR can provide up to 26 g/s to the three halls. One gram of refrigerant per second supplies roughly 50 W of cooling power. The flow to each loop can be adjusted depending upon the amount of cooling power needed by partially opening or closing a Joule-Thompson Valve (J-T Valve). The coolant passing the J-T valve flows through the tubing in the heat exchanger and returns to ESR at 20 K and 2.6 atm. The temperature of the coolant was monitored using Silicon Diode temperature sensors, DT-470-SD-11. The axial fan, located at the center of the heat exchanger, pumps the target cryogen around the fin-tubing, in the direction denoted by the arrows, from the heat exchanger to the cell block and back again.

2.5.1.2 Loop Pump

The pump (also called fan) in each loop circulates the target cryogen through the target cells and then through the heat exchanger, around the fin-tubing. The pump is located

at the center of the heat exchanger and is powered by a three phase motor. Each motor is driven by a three phase variable frequency controller located in the main electronics racks for the target. Table 2-1 lists the operating parameters of the fans for hydrogen and deuterium and their dependence on the fan frequency. The fan in the hydrogen target was driven at 81.6 Hz while the fan in the deuterium target was driven at 67.2 Hz. The current and the voltage listed in the table are those drawn by the motor. The heat power deposited in each loop by the motor is also listed. The flow speed of the cryogen depends upon the rotation frequency of the axial fan that circulates the target fluid. This circulation rate was optimized during the target commissioning. The mass flow of the circulating fluid can be determined from its temperature rise across a known power source. The mass flow was measured from the temperature difference between the two Cernox before and after the cell when beam was on target. Then, the flow speed through an area can be calculated from the mass flow. The flow speed of the cryogen normal to the electron beam was measured to be 80 cm/s for hydrogen and 70 cm/s for deuterium. Both fans were ∼30% efficient.

	$F(f)$	Hydrogen Target	Deuterium Target
Fan Frequency, f (Hz)	–	81.6	67.2
Current (A)	$\sim f^1$	3.0	4.5
Voltage (V)	$\sim f^1$	37	36
Power (W)	$\sim f^3$	130	150
Differential Pressure (psi)	$\sim f^2$	0.5	1
Mass Flow (g/s)	$\sim f^1$	250	480
Flow Speed (cm/s)	$\sim f^1$	80	70
Fan Efficiency (%)	$\sim f^0$	30	30

Table 2-1: The operating parameters of the fans for hydrogen and deuterium and their dependence on the fan frequency, $F(f)$.

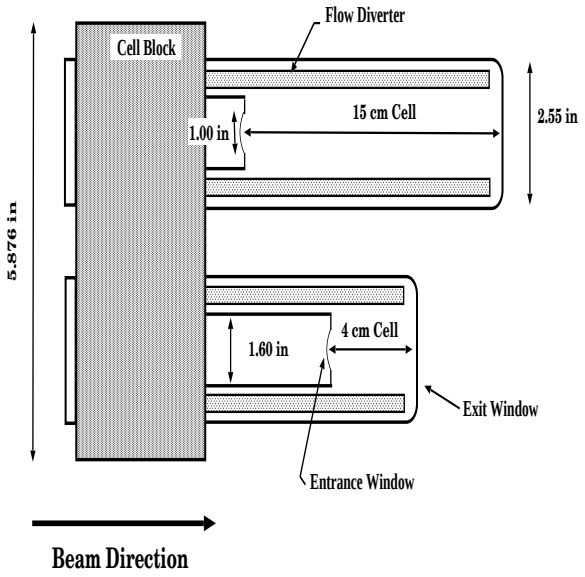

Fig. 2-11: Side view of a target cell block. Shown are the cell block's pair of target cells and their dimensions.

2.5.1.3 Cells and Cell Block

A side view of a cell block and its pair of target cells can be seen in Figure 2-11. The target cells themselves are thin cylinders made from Aluminum beer can stock. The cans have a diameter of 2.55 inch and a sidewall thickness of 0.007±0.001 inch (see Reference [15] for all target measurements). The upstream end of the target can is soldered onto the cell block. Inside each target cell is a flow diverter which forces the cryogen into the beam path through an area of ∼42 cm^2 (for the 15 cm can). The target liquid flows through the two target cans from bottom to top, *i.e.* the cryogen flows first through the 4 cm cell and then through the 15 cm and back to the heat exchanger. The nominal target lengths are 15 cm and 4 cm. The actual target lengths vary with construction and operating temperature and pressure. Table 2-2 lists the lengths of each target cell (without the windows), corrected for their operating pressure (22 psia for Loop 1 and Loop 3 and 26 psia for Loop 2) and for thermal contraction (∼0.4% at 20 K).

Target loop	Target Cell cm	Cold Length cm	Upstream Window Thickness cm	Downstream Window Thickness cm
1	15	14.91±0.02	0.0071±0.0003	0.0107±0.0005
	4	3.91±0.01	0.0071±0.0003	0.0117±0.0005
2	15	14.95±0.02	0.0071±0.0003	0.0094±0.0005
	4	3.78±0.01	0.0071±0.0003	0.0089±0.0005
3	15	14.94±0.02	0.0071±0.0003	0.0097±0.0005
	4	3.93±0.01	0.0071±0.0003	0.0091±0.0005

Table 2-2: Cryotarget dimensions.

The thickness of the target cells and downstream windows was measured using the Coordinate Measurement Machine (CMM). The thickness of the upstream window is 0.0028 inch for all the cells. The error on the target length calculation (without beam) is ∼0.1% and is due mainly to the uncertainty of the thermal contraction. The downstream window original thickness was 0.014 inch. Its thickness was reduced by etching it in a chemical bath. Table 2-3 lists the the properties of the upstream and downstream windows.

	Upstream Window	Downstream Window
Al Alloy	5052	3004
Density (g/cm^3)	2.68	2.71
Thickness (inch)	0.0028	0.0040
$X_\circ$ (g/cm^2)	23.85	24.12
Radiation Length (*r.l.*)	0.0008	0.0011

Table 2-3: Upstream and downstream target windows material. The average thickness of the downstream window is used in this table.

To reduce the heat radiated from the wall of the scattering chamber to the cells and cell blocks, each target cell was wrapped on the side with 4 layers of superinsulation. Each layer consisted of one sheet of aluminum (thickness: 0.00025 inch) and three sheets of fiber glass (thickness: 0.0010 inch each).

2.5.1.4 Heaters

Two types of heaters were employed: "high" and "low" power heaters. The high power heaters (∼26 Ω each) are kapton encased wires embedded in the heat exchanger. These heaters can provide more than 700 W of power. They are used to regulate the temperature of the cryogen during periods when the electron beam is off. The low power heaters (∼23 Ω each) are located on the inlet side of the cell block. They can provide up to 50 W of heating power and were used to compensate for small temperature variations caused by a small change in coolant flow or temperature.

2.5.1.5 Thermometry

Each loop was monitored by several different types of temperature gauges with a particular range of temperatures to which it is calibrated. These different types of thermometers have different accuracies. The temperature sensors which are most accurate at our cryogenic temperatures are the Cernox Temperature Sensors, CX-1070-SD. There are four of them per loop; two on the cryogen inlet side, one on the outlet side, and one in the heat exchanger. The one in the heat exchanger was calibrated from 4 K to 300 K while the others from 4 K to 80 K. These sensors provide resistive temperature measurements. The resistors are calibrated by the manufacturer (LakeShore) and the calibrations are loaded into a temperature monitoring unit, Oxford Temperature Controllers Model ITC^{502}, which converts the measured resistance to temperature. There are two Allen-Bradley temperature sensors (1/8 W, 270 Ω resistors) located in each loop, one on the cryogen inlet side and one in the heat exchanger. These sensors are less accurate at our cryogenic temperatures than the Cernox sensors and are used mostly as a visual check that the temperature is in the correct range. In addition, they are used to monitor the target's temperature during cool-down periods and act like level sensors to check when the heat exchanger is filled with liquid. The third type of temperature measurement is deduced from the vapor pressure inside a hydrogen

filled bulb. There are two vapor pressure bulbs located in the target loop, with one on the cryogen inlet side and one in the heat exchanger. As with the Allen-Bradley sensors, this method is used as a visual check that the cryogen's temperature is in the correct range.

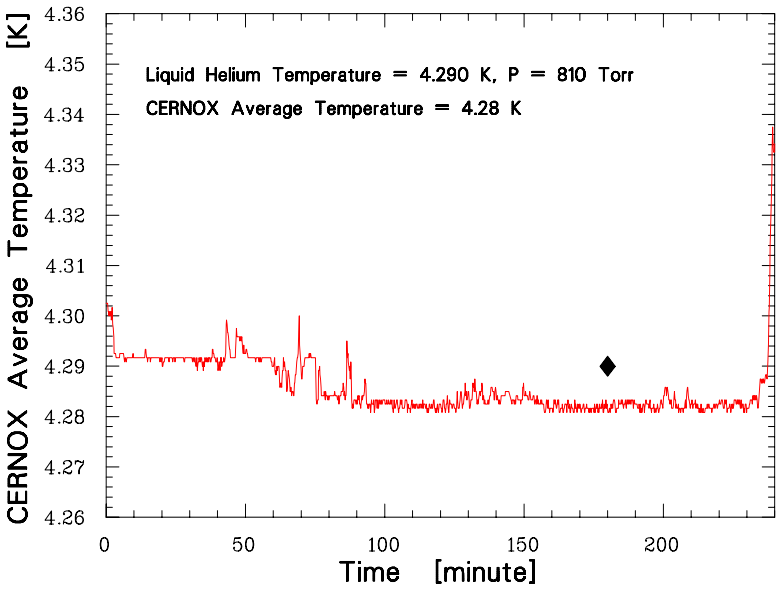

Fig. 2-12: Absolute calibration of Cernox compared to liquid helium temperature. The diamond point is the expected ^{4}He liquid temperature at 810 Torr.

The temperature sensors were tested in the Vertical Test Area (VTA) in the JLab Test Lab before installing them in the target. The sensors were mounted on an aluminum plate and put at the bottom of a vertical dewar. Liquid ^{4}He was then poured in and gradually heated (above 4.29 K it becomes gas). The readings of the sensors were continuously recorded. Figure 2-12 shows the average temperature of ^{4}He in the dewar as measured by the Cernox resistors versus time. When the sensors were completely emerged in liquid helium, their average temperature was 4.28 K. The pressure in the dewar was 810 Torr which corresponds to liquid helium temperature of 4.29 K [16]. Figure 2-13 shows the difference between the temperature reading of each Cernox sensor and the average temperature of all the Cernox sensors versus the average temperature. The Cernox sensors were absolutely

calibrated to within ±50 mK around the operating range of interest.

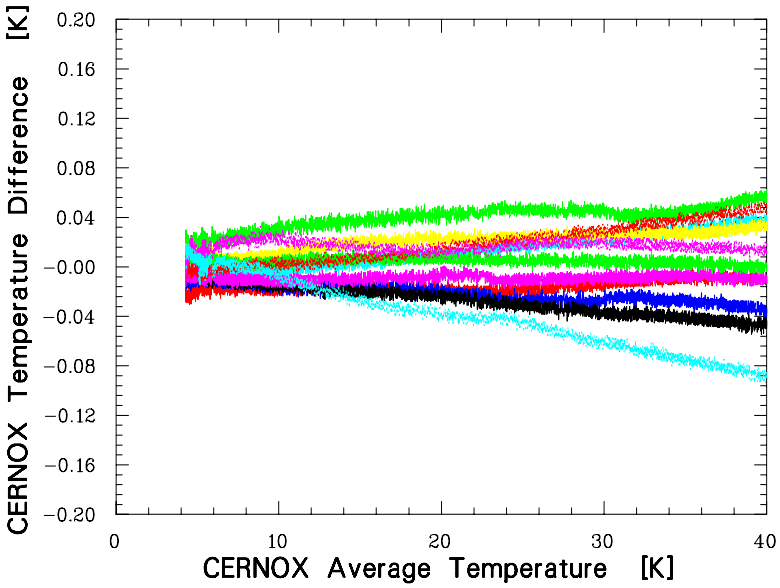

Fig. 2-13: The difference between the Cernox temperature readings (calibrated from 4 K to 80 K) and their average temperature. The Cernox sensors were absolutely calibrated to within ±50 mK around the operating range of interest.

The sensors were also emerged in liquid nitrogen and the temperature was recorded for each sensor. The average of the Cernox readings is 77.5 K. The expected liquid nitrogen temperature is 77.4 K.

2.5.1.6 Loop One Collimator

Experiment E91-026 required a 15 cm deuterium target with a collimator to collimate the cell block and the downstream window for the backward angle (144.5°) measurement of the magnetic form factor of the deuteron. Loop 1 was modified for this purpose and was used as the deuterium target form October 11 to October 27, 1997. The collimator (see Figure 2-14) reduced the 15 cm target length to 9.31 cm (3.07 cm upstream and 6.24 cm downstream). The collimator was made of two tungsten blocks of 1 cm thickness (2.86 *r.l.*) and height of 1.90 cm.

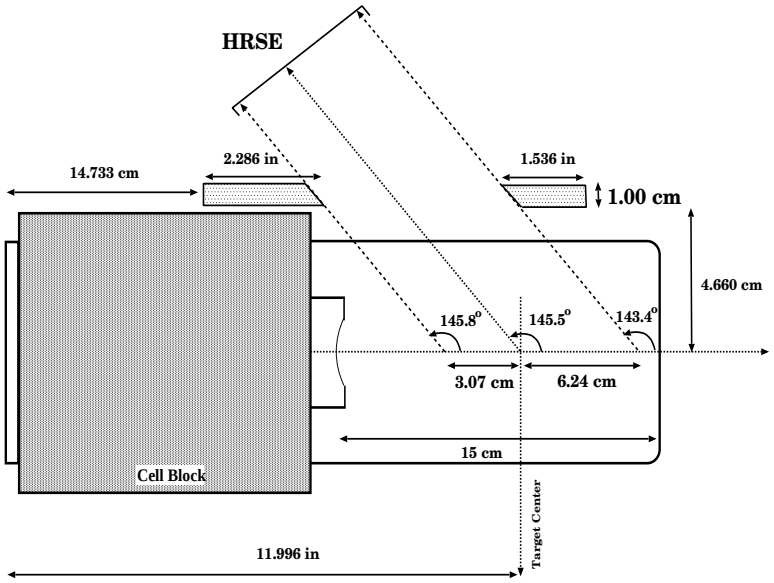

Fig. 2-14: Schematic of the collimator attached to loop 1.

2.5.1.7 Control System

The control system development environment known as EPICS (Experimental Physics and Industrial Control System) was used to develop the interfaces needed for remote control of the cryotarget hardware. The EPICS development environment consists of a collection of C codes and MOTIF programs developed by Los Alamos National Laboratory and Argonne National Laboratory.

The physical architecture of a control system developed in the EPICS environment is shown in the left half of Figure 2-15. A workstation (here an HP 745) runs the graphical user interfaces (GUIs) or other programs which communicate via Ethernet to an IOC (Input/Output Controller). The IOC for the cryotarget is a VME based Motorola MV162-532 single board computer. The communication with the hardware is through the IOC. In the right half of Figure 2-15 is a schematic of the actual software tools which make the hardware communication possible. For the cryotarget, GUI development programs such as TCL/TK were used to develop control screens for each piece of hardware to be controlled. When

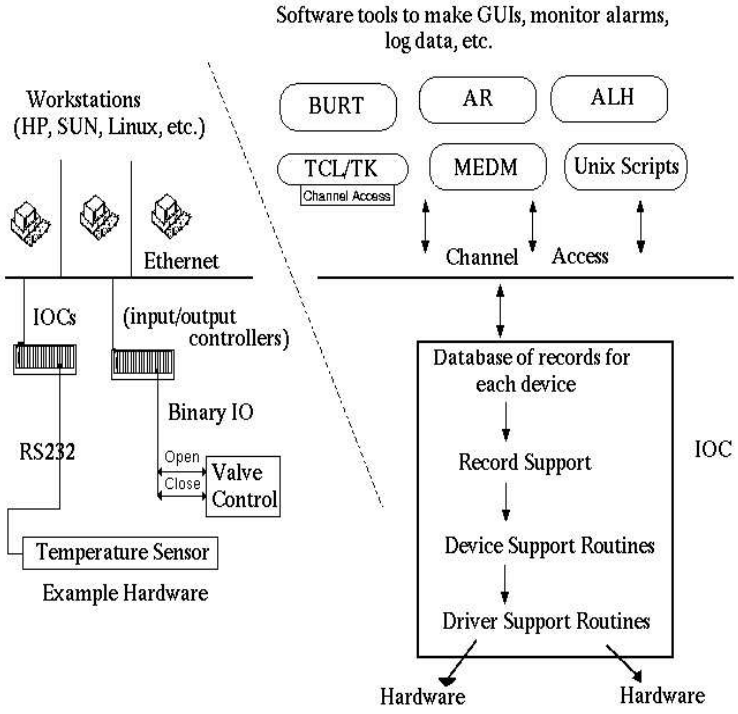

Fig. 2-15: Physical (left) and logical (right) architecture of a control system developed in the EPICS environment.

the status of a hardware device is queried or changed, the GUI communicates to the IOC via a network protocol known as channel access. Explicitly, the GUI communicates with a database which runs on the IOC. This database contains multiple records for each device that is to be controlled. Most of these records refer to a specific function to be performed by a device, such as reading the output of a temperature sensor or setting the position of a valve. The database is monitored by the record support. When a change or update of a hardware device is requested, the record support calls the device support routines necessary to query the hardware. Depending upon the complexity of the hardware, the device support may communicate directly with it or it may call a specialized driver support to do the communication. This cycle continues over and over, for each change or update of a device's status.

The control system for the Hall A target was developed entirely in the EPICS environment. There are 13 serial devices, two relay boards and five I/O boards that are queried and controlled, on time scales of 0.1 to 10 seconds. The GUI contains approximately 40 sub-screens which allow communication with the 1200 records in the IOC's database.

2.5.1.8 Target Density

The operating temperature and pressure of the hydrogen and deuterium target loops are shown in Table 2-4. The temperature is determined by the Cernox resistive temperature measurements, while the pressure is measured by two pressure transducers, one located in the target fill line and the other in the target return line. The error on the density results from three sources. The first is the error on the measured temperature and pressure. The Cernox temperature measurements have an absolute accuracy of ± 50 mK. The density (ρ) dependence on temperature (T) is $\frac{1}{\rho}\frac{d\rho}{dT} = -1.5\%/\mathrm{K}$, which leads to an error of less than 0.1% in the density from temperature uncertainty. The pressure measurement from the pressure transducers has an error of about ± 0.3 psia. The dependence of density on

pressure (P) is $\frac{1}{\rho}\frac{d\rho}{dP} = 0.01\%$/psia, which leads to an error of much less than 0.1% in the density from the pressure measurement. The additional sources of error in the density are the uncertainty in the equations of state and uncertainty in our knowledge of the relative amounts of ortho versus para molecules in the hydrogen and deuterium target fluid (because the two molecular states have different densities).

Target Liquid	Temperature K	Pressure psia	Density g/cm^3
Hydrogen	19.00	26.0	0.07230±0.00007
Deuterium	22.00	22.0	0.1670±0.0005

Table 2-4: Target density (para H_2 and normal D_2).

Different relative orientations of the two nuclear spins in the diatomic molecules H_2 and D_2 give rise to the molecular states designated by the prefixes ortho and para. The equilibrium ortho-para composition is temperature dependent. The high temperature concentration of hydrogen, closely approached at room temperature and known as "normal" hydrogen, is 75% ortho-hydrogen (nuclear spins in the same direction) and 25% para-hydrogen (nuclear spins in opposite directions). The high temperature equilibrium composition of deuterium is 67% ortho and 33% para. For D_2, no difference in P-ρ -T values for different ortho-para mixtures could be observed. On the other hand the density of ortho-para mixtures of hydrogen will vary very little and the differences in density between normal and pure para-hydrogen is about 0.5-0.7% (normal hydrogen has the larger density). At 19 K, the equilibrium concentration is almost 100% para. The assumption that the target liquid hydrogen is in equilibrium is valid since the hydrogen has some impurities which act as catalysts for ortho-para conversion and the time scale is long enough for conversion to equilibrium. Since this experiment ran for 60 days, the error in the hydrogen target density due to ortho-para states is negligible.

The error in the density calculation (without beam) is $\sim 0.1\%$ for H_2 and 0.3% for D_2

and is due mainly to the uncertainty of the equations of state. All of these factors combined lead to an operating density of 0.07230±0.00007 g/cm^3 for hydrogen and 0.1670±0.0005 g/cm^3 for deuterium in the absence of beam. With beam, there is an additional current-dependent uncertainty in the target density as will be described in Section 3.8.4.

2.5.1.9 Gas Purity

A chemical analysis of the hydrogen target gas was performed by Atlantic Analytical Laboratory. The purity of the hydrogen gas was found to be 99.8% where the largest contaminations were nitrogen (0.1%), oxygen and carbon dioxide. These gases should freeze at 19 K on the surfaces in the heat exchanger. Therefore it is assumed that the contamination in the target cell is negligible and no correction in density is applied. For the deuterium gas, a sample was sent for analysis but it was contaminated during shipping. The deuterium supplied to Jefferson Lab has the same purity as hydrogen. The purity of deuterium was assumed the same as for hydrogen and no correction was applied in the analysis.

2.5.1.10 Luminosity and Heat Deposition

Using this target system, we were able to achieve record high luminosity for both liquid hydrogen and deuterium. Table 2-5 lists the luminosity achieved at 100 μA beam current and the energy deposited in the target by the beam at this current. The energy loss for deuterium is the hydrogen value scaled by $Z/A = 1/2$.

2.5.2 Dummy and Solid Targets

Attached to the bottom of the cryotarget ladder was a solid target ladder with three aluminum dummy targets and five solid target positions (see Figure 2-7). Each dummy target consists of two flat plates of aluminum, separated by empty space. The three dummy targets, with separations of 10 cm, 15 cm and 4 cm, were used to estimate the contribution of the target aluminum windows to the cross sections. Table 2-6 lists the thicknesses and the

	Hydrogen	Deuterium
Density (g/cm^3)	0.07230	0.1670
Length (cm)	15.0	15.0
$\frac{1}{\rho}\frac{dE}{dx}$ (MeV cm^2 g^{-1})	5.4	2.7
Power (W)	586	676
Luminosity (cm^{-2} s^{-1})	4.1 $\times 10^{38}$	4.7 $\times 10^{38}$
$X_\circ$ (g/cm^2)	61.28	122.4
Radiation Length	0.0177	0.0205

Table 2-5: Luminosity and heat deposition in the target at 100 μA beam current.

material of the dummy targets. The thickness of the upstream (downstream) plate is equal to the length of the upstream (downstream) window plus half the length of the corresponding cryocell (15 cm or 4 cm cell) in radiation lengths. This minimizes the running time on the dummy target. Table 2-7 lists the position of the plates and the length of the dummy targets.

Target	10 cm Dummy		15 cm Dummy		4 cm Dummy	
	upst	dnst	upst	dnst	upst	dnst
Al Alloy	6061	6061	6061	6061	6061	6061
Density (g/cm^3)	2.71	2.71	2.71	2.71	2.71	2.71
Thickness ($\times 10^{-3}$ inch)	36.95	36.60	38.85	38.85	12.60	12.25
$X_\circ$ (g/cm^2)	24.12	24.12	24.12	24.12	24.12	24.12
Radiation Length	0.0105	0.0104	0.0111	0.0111	0.0036	0.0035

Table 2-6: Dummy target thicknesses and materials.

Below the dummy targets were the solid foil targets. On this ladder there were two aluminum targets, one carbon target, one beryllium-oxide (BeO) target and one empty target with no target foil. Each target (except the empty target) was approximately 2.54 cm high and 1.91 cm wide. Table 2-8 lists the thicknesses of each target.

At the top of the solid target ladder is an aluminum target with two small holes (1 mm and 2 mm square) in it. This target was used during the fast raster commissioning, with the idea that the dimensions of the rectangular holes were known so the dimensions of a

Dummy Target cm	z position of upstream foil mm	z position of downstream foil mm	Cold distance between center of foils cm
10	-47.77±0.2	+51.86±0.2	9.96±0.03
15	-73.15±0.2	+76.31±0.2	14.95±0.04
4	-17.79±0.2	+22.47±0.2	4.03±0.01

Table 2-7: Dummy target z positions and lengths. $+z$ is along the direction of the beam to the beam dump.

Target	C	Al	BeO
Thickness ($\times 10^{-3}$ inch)	40.0±0.1	40.0±0.5	20.0±0.5
Dimensions (inch)	1.00×0.75	1.00×0.75	1.00×0.75
Density	223.20±0.14 mg/cm^2	2.71 g/cm^3	—

Table 2-8: Solid target thicknesses and materials.

rastered beam passing through the holes could be discerned. Next are carbon and aluminum target foils. These targets can be used for spectrometer studies. Next on the solid target ladder is the beryllium-oxide target. When the beam is incident on a BeO target, it causes the target to glow brilliantly. This target is used for a visual check that the beam is present and in the correct position with a well defined shape. At the bottom of the solid target ladder is the empty target, which is essentially an aluminum foil with a circular hole cut in it. The empty target functions as the "target-out-of-beam" position, because when it is positioned in the beam's path, the beam goes through the hole, straight to the beam dump.

2.6 High Resolution Spectrometers

There are two superconducting high resolution spectrometers in Hall A which are nominally identical in terms of their magnetic properties. The spectrometer magnets are in a QQDQ (quadrupole, quadrupole, dipole, quadrupole) configuration, as shown in Figure 2-16. The dipole has focusing effects due to a 30° tilt angle of the entrance and exit pole faces and a negative first order field index, $n = -1.26$. The optical length of the spectrometer is

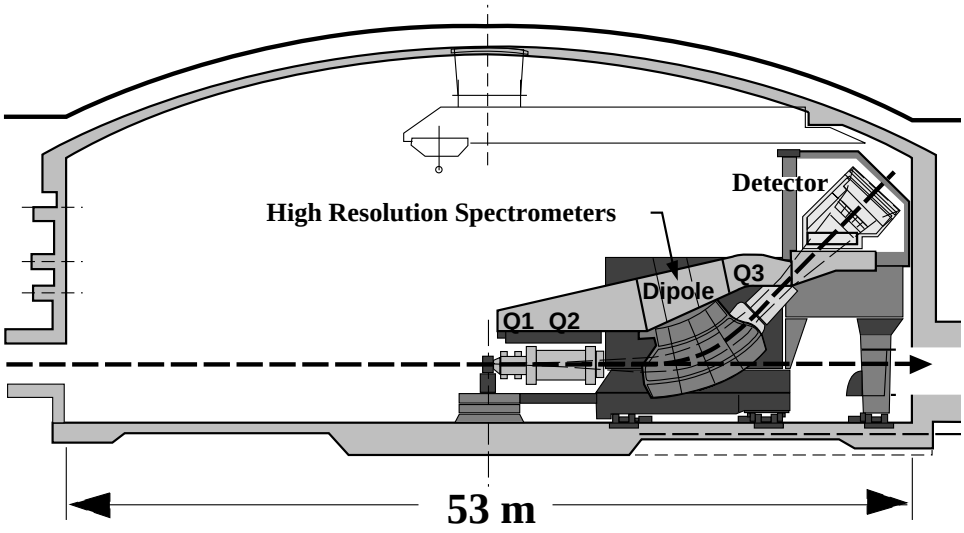

Fig. 2-16: Side view of the Hall A High Resolution Spectrometer. Shown are the scattering chamber and the spectrometer magnetic elements, including the dipole and the three quadrupole magnets (labeled Q1, Q2 and Q3). The detectors are inside the shield house at the top of the spectrometer.

23.4 m, with a 45° vertical bending angle at the dipole. Due to a short in the copper part of the superconducting coils in the Hadron dipole, the Hadron arm spectrometer is limited to a 3.2 GeV/c maximum momentum (instead of 4.0 GeV/c). Table 2-9 summarizes the design goals from the CEBAF Conceptual Design Report [20] and present performance of the HRS. The TRANSPORT [21] Model of the HRS is listed in Table 2-10.

The entrance window of each spectrometer is separated from the scattering chamber exit windows by 20 cm of air. The entrance window is covered with 0.18 mm (0.007 inch) of Kapton foil. A box containing three movable tungsten collimators [23] is located between this entrance window and the first quadrupole (Q1). The upper collimator is a sieve slit. This collimator is 5 mm thick and has a 7×7 grid of holes bored in it; two of the holes are 4 mm in diameter and the rest are 2 mm in diameter. These two holes are used to verify proper left-right and top-bottom positioning. The sieve slit collimator is used during spectrometer optics studies. The middle collimator is an 8 cm thick, 6 msr (6.29 cm wide

Characteristics	CDR	Measured Value
Bend angle (vertical)	45°	
Bend radius	8.40 m	
Optical length	23.4 m	
Momentum range	0.3 to 4.0 GeV/c	
Momentum acceptance	±5 %	
Momentum dispersion	12.4 cm / %	
Radial linear magnification	-2.5	
Range of scattering angle	12.5° to 165° (E)	
	12.5° to 130° (H)	
Horizontal angular acceptance	±30 mrad	
Vertical angular acceptance	±65 mrad	
Solid angle	7.8 msr	
Transverse length acceptance	±5 cm	
Momentum resolution (FWHM)	1×10^{-4}	2.5×10^{-4}
Horizontal angle resolution (FWHM)	0.5 mrad	2 mrad
Vertical angle resolution (FWHM)	1.0 mrad	6 mrad
Transverse position resolution (FWHM)	1 mm	3 mm

Table 2-9: HRS design goals and present performance. Design values are from the Conceptual Design Report (CDR) [20]. Measured values are from commissioning elastic data with a thin ^{12}C target at an electron beam energy of 845 MeV [22].

Characteristics	Value
Target to Q1	1.5903 m (1.6000)
Q1 Magnetic Length	0.9413 m
Q1 Field Gradient	7.7845 T/m (7.7616)
Q1 Radius	15 cm
Q1 to Q2	1.1721 m (1.1558)
Q2 Magnetic Length	1.8266 m
Q2 Field Gradient	-3.0867 T/m (-3.0789)
Q2 Radius	30 cm
Q2 to Dipole	4.4308 m (4.3474)
Dipole	
Magnetic length	6.5973 m
Field index (n)	-1.26
Central field B_0	1.5884 T
Central gap	25 cm
Effective width	90 cm
Entrance pole face rotation	-30°
Exit pole face rotation	-30°
Entrance curvature (R_1)	1.57 m
Exit curvature (R_2)	-2.80 m
Dipole to Q3	1.5925 m (1.5910)
Q3 Magnetic Length	1.8268 m
Q3 Field Gradient	-2.8559 T/m (-2.8475)
Q3 Radius	30 cm
Q3 to Focal Plane	3.4523 m (3.4538)

Table 2-10: TRANSPORT Model of the two Hall A High Resolution Spectrometers. The numbers in parenthesis are for the Hadron arm. Fields and gradients are for 4 GeV/c.

$\times$ 12.18 cm high, at a distance of 110.9 cm from the target) rectangular collimator. This collimator can be used to assure that the limits of acceptance of the spectrometer are well defined. The bottom collimator is an "empty collimator" which performs no collimation. At the top of each spectrometer is a 0.10 mm (0.004 inch) thick titanium exit window, situated between the spectrometer's last quadrupole (Q3) and the detector shield house.

The HRS was operated in its standard tune: point-to-point focusing in the dispersive plane and mixed focusing in the transverse plane. In the transverse plane a compromise is made in order to achieve both good position resolution (optimized in point to point) and good angular resolution (optimized in parallel to point). This tune provides very high momentum resolution, large momentum acceptance, large solid angle, and large extended target acceptance (see Table 2-9). In this tune, Q1 focuses in the dispersive direction while Q2 and Q3 focus in the transverse direction. The dipole field is monitored and regulated with a NMR probe. The quadrupole fields are regulated by monitoring the current in the magnets. The field of the dipole is stable at the 10^{-5} level.

The focal plane was designed to be at 45° with respect to the central ray, and coincides with the first wire plane. The true focal plane of the spectrometer is tilted forward from the "detector" focal plane (used in the software) by 71°. Figure 2-17 shows a SNAKE simulation [24] of a set of rays traced from the target to the first scintillator plane. The focal plane is shown as a dotted line.

The absolute central momentum for both spectrometers was calibrated, prior to this experiment, assuming the nominal value of the beam energy. Although the beam energy was found after this experiment to be lower than the nominal energy by $\sim$0.6% (see Section 3.4), the momenta settings of the Electron and Hadron spectrometers were set close to the desired values (see Figure 2-18). The relative momenta settings of the Electron and the Hadron arms were determined by measuring the position of the elastic peaks at the focal plane. In the dipole, two NMR probes are placed at slightly more than 0.4 m from the

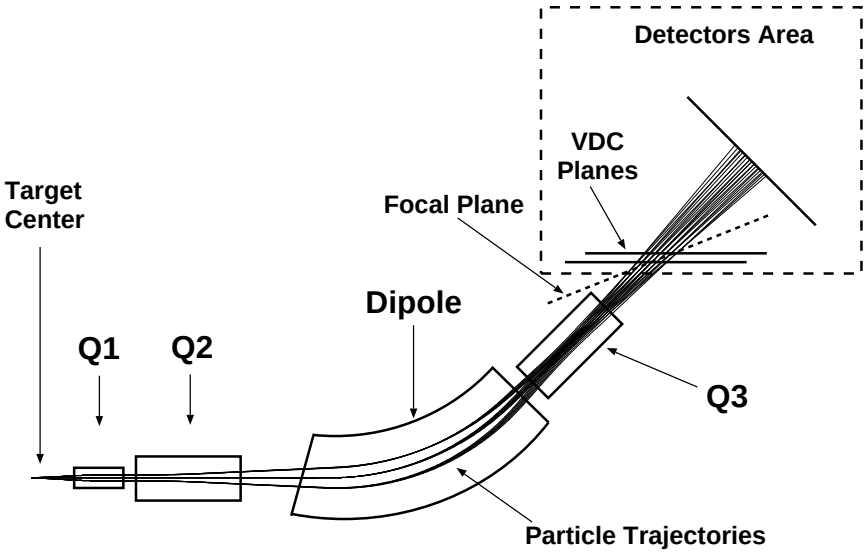

Fig. 2-17: SNAKE simulation [24] of a set of rays traced from the target to the first scintillator plane for HRS central momentum P_0 = 4 GeV/c. Rays originate from target point (0,0) with momentum $\frac{P-P_0}{P_0}$ = -3% to +3% with a 1% step and vertical angles (0,+50,-50) mrad.

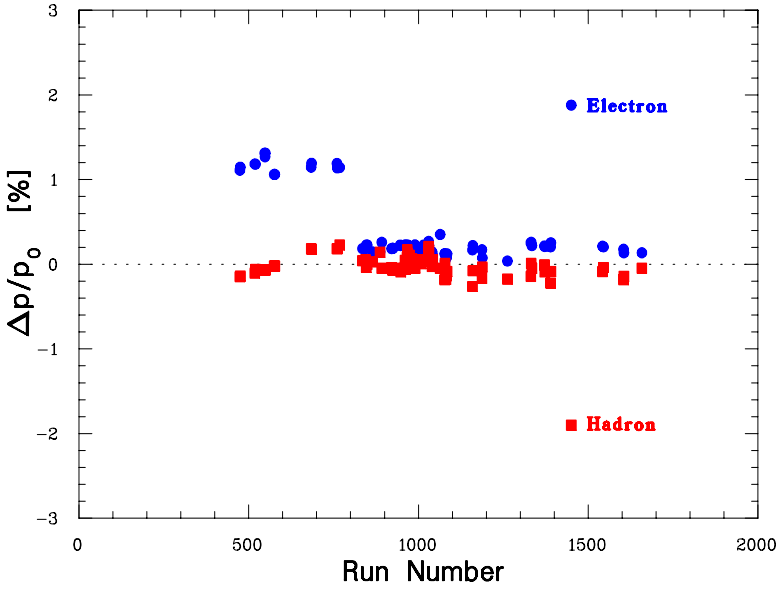

Fig. 2-18: The relative momenta settings of the Electron and Hadron spectrometers for all *e-p* runs and the high statistics *e-d* runs. The Electron spectrometer momentum was intentionally lowered by 1% for the *e-p* and *e-d* backward runs.

centerline of the magnet, one on the high field side and the other on the low field side. This second NMR probe is normally used to set and monitor the magnetic field of the Hadron dipole during experiments. In the case of the Electron arm, the magnetic field of the dipole is set by the average of the high and low field probes rather than just the low field probe. This difference in the operating procedure is rather historical. The central field B_0 is then calculated from the low field NMR for the Hadron arm and from both the low and high field NMRs for the Electron arm. Due to noise problems in the hall, the Electron arm NMRs were unable to read fields <0.16 T, therefore, the momentum in the Electron arm was set using the current in the dipole for the first half of the backward data taking where the scattered electron momentum was <400 MeV.

The angle of the spectrometer is measured by comparing the position of the back of the spectrometer to marks that have been scribed on the floor of the hall with the help of the Jefferson Lab Survey Group. The marks are at a 10 m radial distance from the center of the

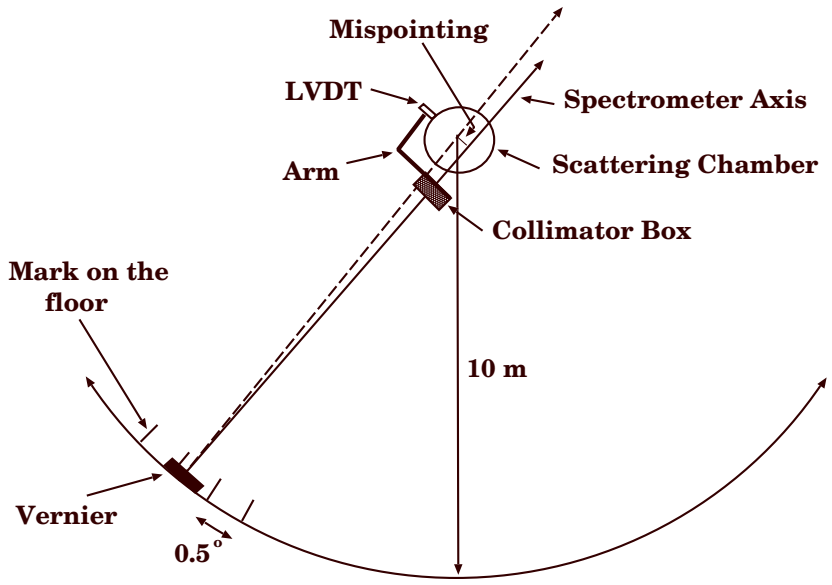

Fig. 2-19: Schematic of the procedure used to set the spectrometer angle.

hall and spaced by 0.5°. A vernier attached to the bottom of the dipole is used to interpolate between two marks (see Figure 2-19). This determination is good to better than 1 mm and gives an angular uncertainty of less than 0.1 mrad. However, the dipole is carried by a cradle which is connected to the target pivot with a link. The three quadrupoles and the detector package is supported by the "Box Beam" which is mounted on the top of the dipole. When the spectrometer is rotated, the central axis of the spectrometer may mispoint to the target. To measure the mispointing, a Linear Variable Differential Transformer (LVDT) was attached by an arm to the collimator box in the front of Q1 and made to touch the target scattering chamber. The LVDT is used to measure the off radial distance of the spectrometer axis. After rotating the spectrometer, the mispointing is measured and the angle is corrected. Before and after the experiment, the spectrometers were rotated to a set of angles using this method and the Jefferson Lab Survey Group surveyed the position and mispointing of the spectrometers. After the experiment was finished, a discrepancy of 0.25 mrad [25] was found between the survey numbers and the ones obtained using the marks

on the floor. During the experiment, mechanical work had to be done on the collimater box and Q1 which affected the angle calibration. Therefore, for determining errors in the cross section due to spectrometer angle uncertainty, we assume an uncertainty of ± 0.3 mrad.

The particles that traverse the spectrometer are detected in a detector package located in a shield house at the top of each spectrometer. The position and angle of incidence of the detected particles are measured at the spectrometer "focal plane" with a pair of vertical drift chambers. These measured coordinates can then be used to reconstruct the interaction point within the target via a set of optical traceback elements. SNAKE simulation [24] of the standard tune of the HRSE gives the following first order transport matrix from the target to the focal plane:

$$\begin{pmatrix} x \\ \theta \\ y \\ \phi \\ \delta \end{pmatrix}_{\text{tra}} = \begin{pmatrix} -2.18 & -0.02 & 0.00 & 0.00 & 11.91 \\ -1.00 & -0.47 & 0.00 & 0.00 & 19.67 \\ 0.00 & 0.00 & -0.60 & -0.13 & 0.00 \\ 0.00 & 0.00 & 3.63 & -0.90 & 0.00 \\ 0.00 & 0.00 & 0.00 & 0.00 & 1.00 \end{pmatrix} \begin{pmatrix} x_0 \\ \theta_0 \\ y_0 \\ \phi_0 \\ \delta_0 \end{pmatrix}_{\text{tgt}} . \qquad \text{(2-1)}$$

The corresponding HRSH matrix is:

$$\begin{pmatrix} x \\ \theta \\ y \\ \phi \\ \delta \end{pmatrix}_{\text{tra}} = \begin{pmatrix} -2.17 & -0.02 & 0.00 & 0.00 & 11.89 \\ -1.01 & -0.47 & 0.00 & 0.00 & 19.63 \\ 0.00 & 0.00 & -0.60 & -0.12 & 0.00 \\ 0.00 & 0.00 & 3.42 & -0.97 & 0.00 \\ 0.00 & 0.00 & 0.00 & 0.00 & 1.00 \end{pmatrix} \begin{pmatrix} x_0 \\ \theta_0 \\ y_0 \\ \phi_0 \\ \delta_0 \end{pmatrix}_{\text{tgt}} . \qquad \text{(2-2)}$$

2.7 Detector Packages

The detector package for each spectrometer is mounted in a steel frame. During data taking, the frame and detectors sit inside a metal and concrete shield house where they are

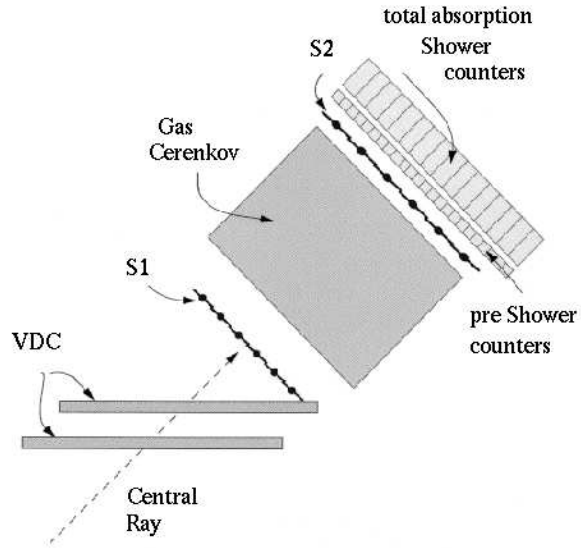

Fig. 2-20: Schematic of the Electron Arm detector package as used in this experiment.

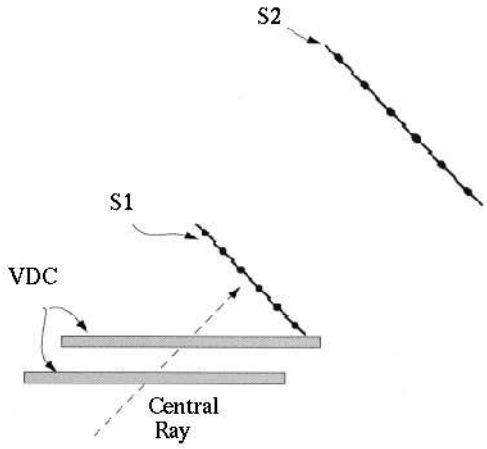

Fig. 2-21: Schematic of the Hadron arm detector package as used in this experiment.

shielded from background radiation that could cause spurious events. The detector packages for the two spectrometers are shown in Figures 2-20 and 2-21. They are similar, but not identical. Each arm has two Vertical Drift Chambers (VDCs) and two planes of scintillators (S1 and S2). For this experiment, these were the only detectors employed on the hadron spectrometer. Additionally, the electron spectrometer's detector package contained a CO_2 gas threshold Čerenkov detector and two arrays of lead-glass blocks acting as a preshower and a shower detector, respectively. In the following sections, a brief description of each detector will be given. The detector efficiencies will be discussed in Chapter 3.

2.7.1 Vertical Drift Chambers

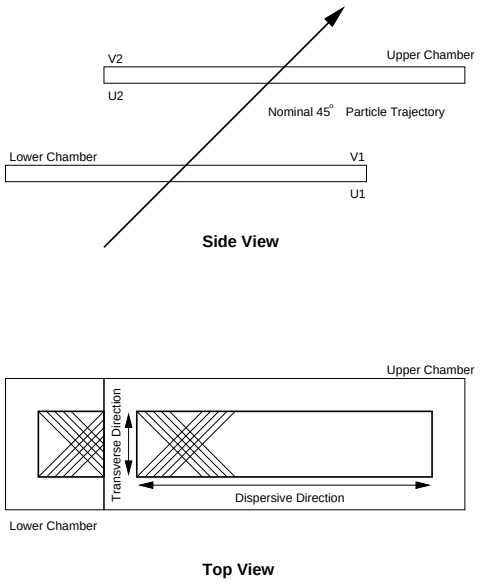

Fig. 2-22: Schematic of the two Vertical Drift Chambers of the Electron Spectrometer (the Hadron Spectrometer VDCs are identically configured).

In order to determine the position and angle of incidence of particles passing through the detector package, each spectrometer has two Vertical Drift Chambers separated by 50 cm. For a complete discussion of the VDCs, see Reference [26]. The VDCs are mounted on permanent rails on the floor of the shield house, between the spectrometer Q3 exit window

and the detector frame. As shown in Figures 2-22 and 2-23, each VDC has two wire planes, perpendicular to each other, in a standard UV configuration. The active area of each VDC is 211.8 cm × 28.8 cm in the dispersive and transverse directions, respectively. The position resolution of each plane is approximately 225 μm (FWHM). Each wire plane contains 368 signal wires. The signal wires are 20 μm in diameter and are made of gold-plated tungsten. The distance between two neighboring wires is 4.243 mm. Each wire plane is oriented at 45° with respect to the spectrometer central ray.

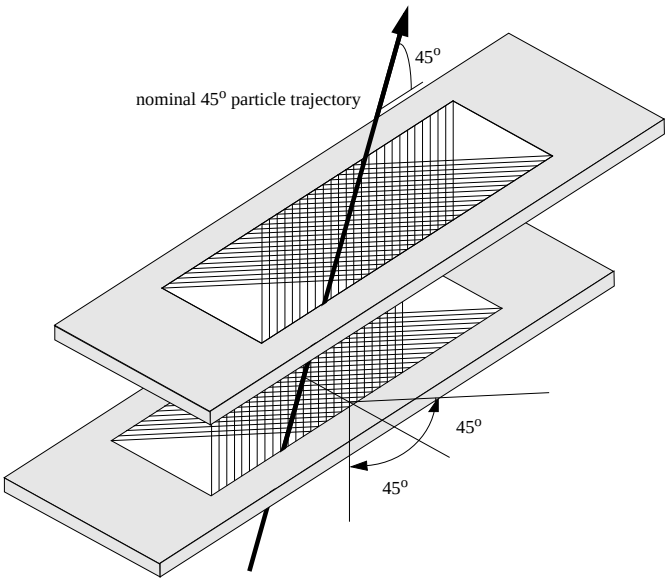

Fig. 2-23: Schematic layout of the VDC assembly.

Inside each VDC, there are three planes of negative high voltage (−4.0 kV nominal), surrounding the two planes of signal wires (see Figure 2-24). The chamber gas is a mixture of Argon (Ar) and Ethane (C_2H_6). When a charged particle passes through the VDC, it produces ions and electrons in the gas mixture. The electrons drift along the electric field lines defined by the high voltage planes to the signal wires. The drift velocity of the electrons for the argon-ethane gas mixture at −4.0 kV is roughly 50 μm/ns. The subsequent pulses on the signal wires are used to start multihit Time-to-Digital Converters (TDCs),

which are stopped by the overall event trigger.

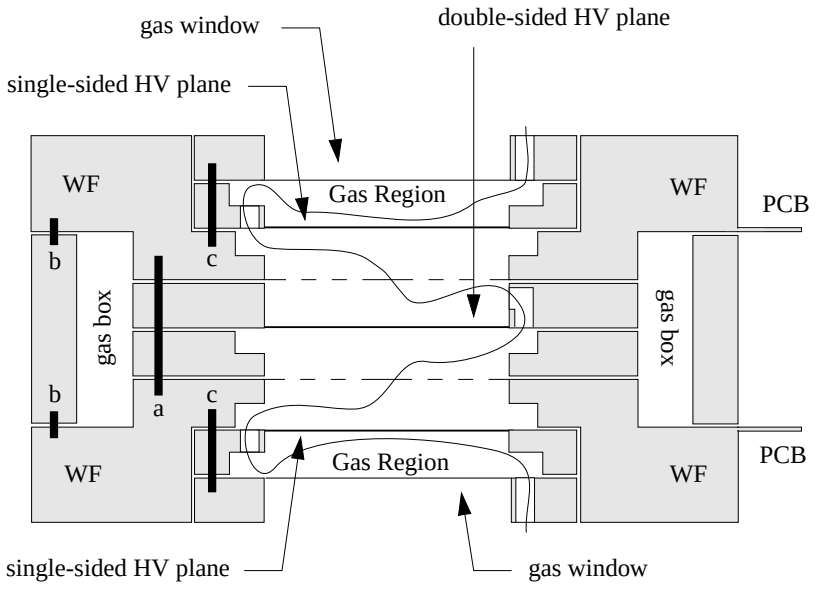

Fig. 2-24: The cross section view of a VDC (not to scale). Wire frames are labeled "WF" while "PCB" indicates printed circuit boards. The path of the gas flow is shown by the meandering line. The dashed lines indicate the location of the wire plane.

2.7.2 Scintillators

Each detector package contains two planes of trigger scintillators, S1 and S2. The two planes are separated by 1.933 m in the Electron arm and by 1.854 m in the Hadron arm. Each plane of scintillators consists of 6 scintillator paddles, made of Bicron BC-408 plastic which has a density of 1.1 g/cm^3. Two Burle 8575 2-inch photomultiplier tubes (PMTs) view each scintillator (one on each side). The active volume of the S1 scintillator paddles is 36.0 cm (transverse) $\times$ 29.3 cm (dispersive) $\times$ 0.5 cm. The paddles in plane S2 are slightly larger, with an active volume of 60.0 cm (transverse) $\times$ 37.0 cm (dispersive) $\times$ 0.5 cm. The scintillator paddles of each plane overlap by 0.5 cm in order to insure complete coverage of the detector plane. The scintillators are oriented so that they are perpendicular to the spectrometer central ray. The scintillators are used to provide the physics event triggers.

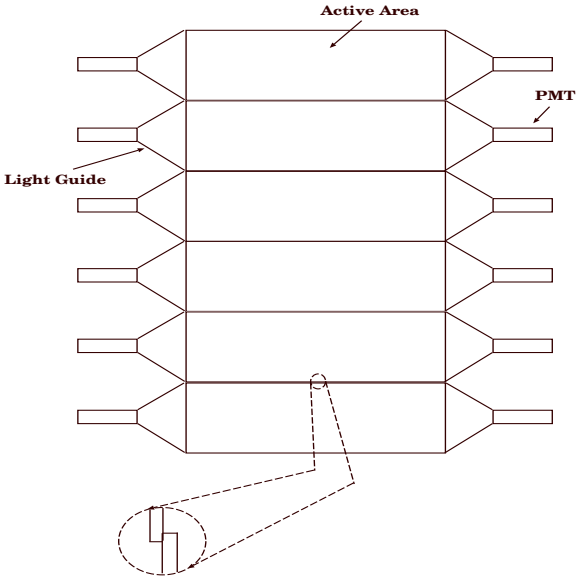

Fig. 2-25: Schematic display of a scintillator plane.

2.7.3 Gas Čerenkov Detector

To discriminate between pions and electrons, a threshold gas Čerenkov detector was employed [32]. A Čerenkov detector operates on the principle that when a charged particle travels through the detector medium, it emits Čerenkov light if it travels faster than light would in that same medium (*i.e.* $v \geq \frac{c}{n}$, where n is the index of refraction of the detector medium). The Čerenkov light is emitted about the particle's trajectory in a forward pointing cone with an opening angle, θ_c defined by:

$$\cos\theta_c = 1/n\beta. \tag{2-3}$$

The Čerenkov detector employed in the HRSE used 2780 liters of CO_2 as the detector medium. The CO_2 was at atmospheric pressure, leading to an index of refraction of $n = 1.00041$. With this index of refraction, the minimum particle momentum for the production of Čerenkov light is 0.017 GeV/c for electrons and 4.8 GeV/c for pions. Note that the threshold momentum for pions is above the maximum momentum for the spectrometer,

so pions could only give a Čerenkov signal through the production of knock-on electrons (known also as δ-ray electrons).

Mechanically, the detector was a rectangular tank. The dimensions of the sensitive area of the detector were 1.996 m in the dispersive x-direction, 0.558 m in the y-direction and 1.5 m in the z-direction (see Figure 2-26). The entrance and exit windows of the detector were made of Tedlar foils (two 37.5 μm thick films per window). The emitted Čerenkov light was reflected from ten aluminum mirrors placed just before the detector exit window. Each mirror had a spherical surface with radius of curvature of 90 cm and reflected the light to 5-inch photomultiplier tubes placed at the side of the detector box. The ten PMTs were of type Burle 8854, with a sensitive photocathode area of approximately 110 mm in diameter. The quantum efficiency of the tubes was 22.5% at 385 nm, with a lower wavelength limit of 220 nm. As a test, one of the ten PMT's of the detector was coated with p-Terphenyl ($C_{18}H_{14}$). This coating absorbed ultraviolet (UV) light in the range from 110-360 nm and re-emitted it at about 385 nm, increasing the photon yield in the sensitive range of the PMT.

Signals from the PMTs ran through a 50-50 splitter and one set of the outputs was summed in a Philips 740 linear fan-in module. The analog sum and the second set went through a LeCroy 4413 Constant Threshold Discriminator (60 mV). Then, the analog signals went through cable delay to a LeCroy 1881M Analog-to-Digital Converters (ADC). The logic outputs went to a LeCroy 4518 fan-out module. One set of outputs went to scalers and another set went to a LeCroy 1875A TDC. The discriminated analog sum went to the trigger logic.

Because the signal from the Čerenkov was used in the trigger, the high voltages were adjusted so that the height of the signal from each tube was identical to within 10%. Then a single threshold was applied to the analog signals from the PMTs. The mean number of photoelectrons is $\sim$11 and the trigger threshold corresponds to $<$1.0 photoelectron. This

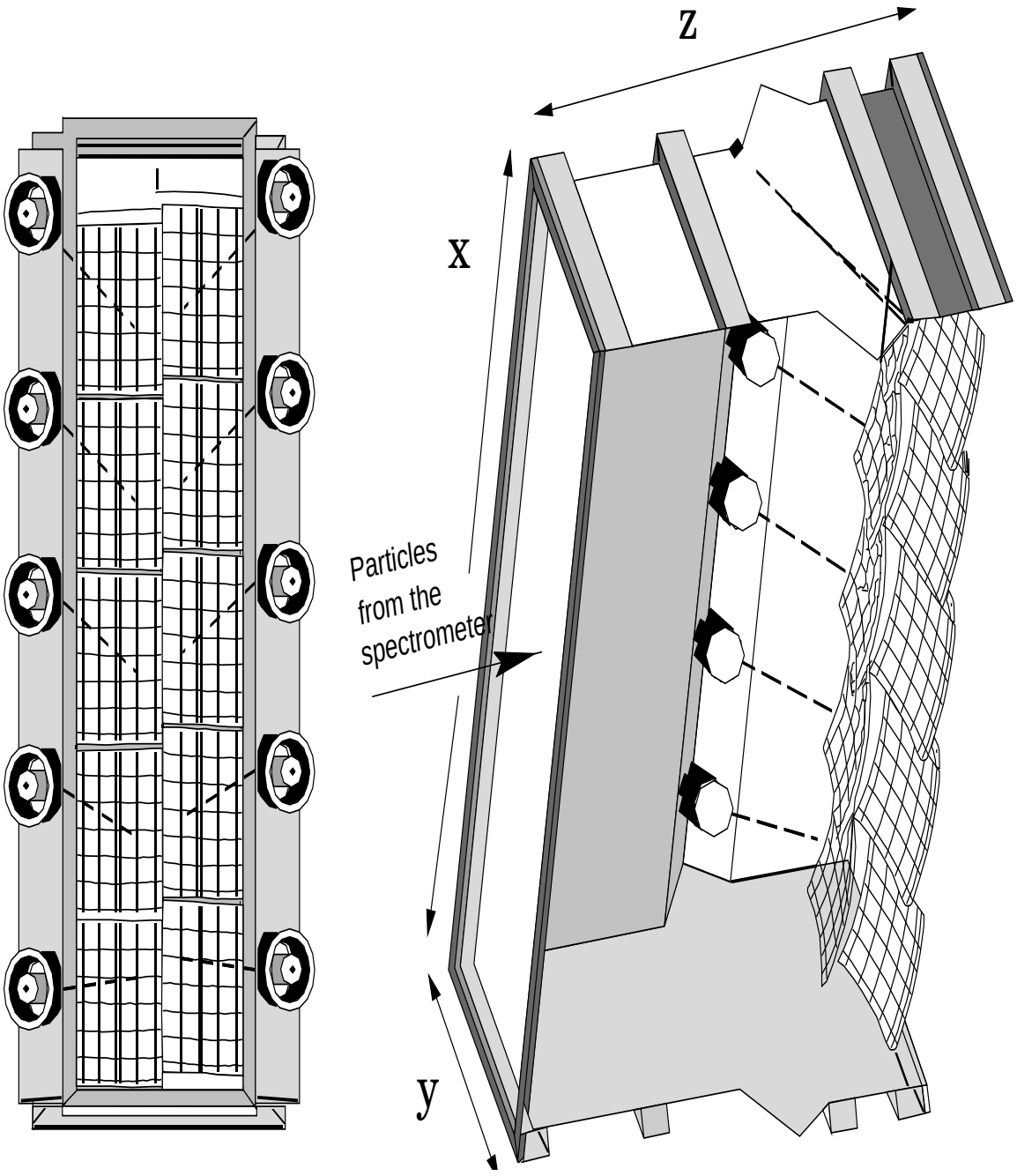

Fig. 2-26: Electron arm CO_2 gas Čerenkov detector. Front view and 3-D, partially open, view of the detector.

means that the Čerenkov trigger signal is >99.9% efficient.

2.7.4 Lead-Glass Calorimeter

The lead-glass detector is an electromagnetic calorimeter that detects the energy deposited when an electron enters the detector. A high energy electron will radiate photons through Bremsstrahlung in the calorimeter, which will, in turn, generate positron-electron pairs. These pairs will also radiate photons, and a shower of particles (photons, electrons, and positrons) will be generated. Electrons and positrons produce Čerenkov light which will be detected by the PMTs at the end of each block. Photons, electrons, and positrons will deposit their entire energy in the calorimeter giving a detected "energy ratio" of one. The energy ratio is the ratio of the energy deposited in the calorimeter to the momentum determined from VDC tracking and the spectrometer central momentum setting. Hadrons, mainly pions, usually deposit a constant energy amount due to ionization and direct Čerenkov light giving an energy ratio of much smaller than one. Unfortunately, pions can produce a charge-exchange reaction in the calorimeter, resulting in neutral pions with a significant fraction of the initial pion's momentum. The neutral pion will decay into two photons, and the full energy of the neutral pion can be deposited in the calorimeter depending where the reaction happened along the calorimeter. The resulting high energy tail is the dominant contribution to pion miss-identification.

The Hall A Electron arm HRS is equipped with a two layer, segmented total absorption lead-glass detector. The first layer, the "Preshower" detector, shown in Figure 2-27, consists of 24 identical modules in front of the shower detector. Each module, shown in Figure 2-28, consists of two lead-glass blocks each having the dimension 10 cm × 10 cm × 35 cm and made of TF-1 lead-glass. The blocks are optically isolated. Each module is viewed by a single Hammamatsu 3-inch R3036 PMT optically coupled to the side of the block by optical grease. The second layer, the "Shower" detector, shown in Figure 2-29, is made of 96 (16×6)

1L	1A4	(22 : 3)	1A1	(22 : 0)	1R
2L	1A5	(22 : 4)	1A2	(22 : 1)	2R
3L	1A6	(22 : 5)	1A3	(22 : 2)	3R
4L	1B4	(22 : 9)	1B1	(22 : 6)	4R
5L	1B5	(22 :10)	1B2	(22 : 7)	5R
6L	1B6	(22 : 11)	1B3	(22 : 8)	6R
7L	2A4	(22 : 15)	2A1	(22 : 12)	7R
8L	2A5	(22 : 16)	2A2	(22 : 13)	8R
9L	2A6	(22 : 17)	2A3	(22 : 14)	9R
10L	2B4	(22 : 21)	2B1	(22 : 18)	10R
11L	2B5	(22 : 22)	2B2	(22 : 19)	11R
12L	2B6	(22 : 23)	2B3	(22 : 20)	12R
13L	3A4	(22 : 27)	3A1	(22 : 24)	13R
14L	3A5	(22 : 28)	3A2	(22 : 25)	14R
15L	3A6	(22 : 29)	3A3	(22 : 26)	15R
16L	3B4	(22 : 33)	3B1	(22 : 30)	16R
17L	3B5	(22 : 34)	3B2	(22 : 31)	17R
18L	3B6	(22 : 35)	3B3	(22 : 32)	18R
19L	4A4	(22 : 39)	4A1	(22 : 36)	19R
20L	4A5	(22 : 40)	4A2	(22 : 37)	20R
21L	4A6	(22 : 41)	4A3	(22 : 38)	21R
22L	4B4	(22 : 45)	4B1	(22 : 42)	22R
23L	4B5	(22 : 46)	4B2	(22 : 43)	23R
24L	4B6	(22 : 47)	4B3	(22 : 44)	24R

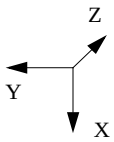

AMP#AMP-Ch (ADC Slot# : Chan #)

Fig. 2-27: Preshower detector map.

	Preshower	Shower
Type	TF-1	SF-5
Composition (by weight)	51.2% PbO 41.5% SiO_2 5.0% K_2O 2.0% Na_2O	55% PbO 38% SiO_2 5% K_2O 1% Na_2O
Radiation length (cm)	2.74	2.36
Critical energy (MeV)	17.5	15.8
Refractive index	1.647	1.673
Density (g/cm^3)	3.86	4.08
Total radiation length	3.65	14.83

Table 2-11: Properties of the lead-glass blocks.

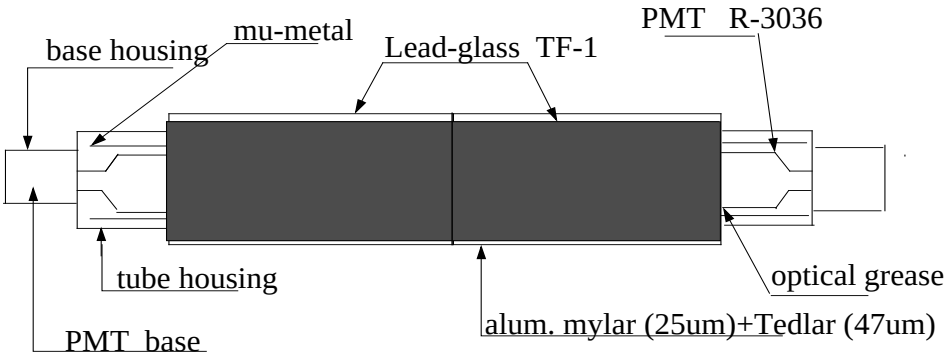

Fig. 2-28: Preshower detector block.

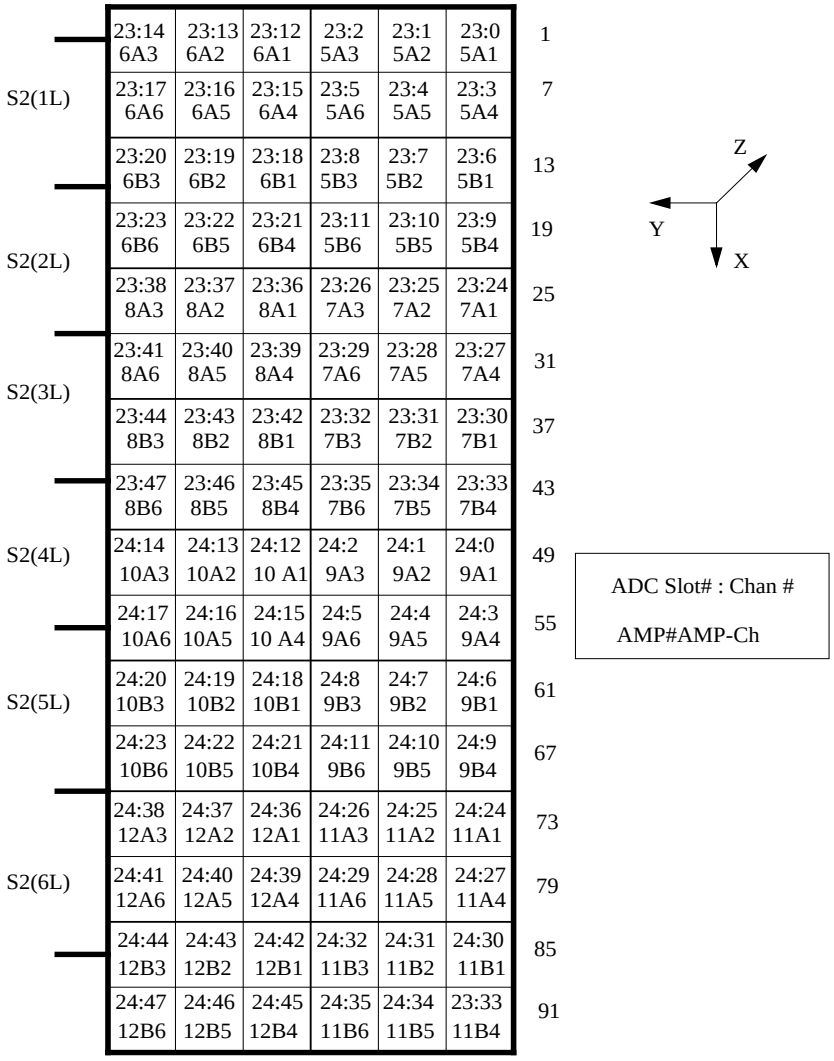

Fig. 2-29: Shower detector map.

blocks of SF-5 lead-glass. Each of the blocks is 15 cm × 15 cm × 35 cm in size and each lead-glass block is viewed by a 5-inch Philips XP2050 PMT. The properties of lead-glass are listed in Table 2-11. There was no hardware threshold on the PMT signals from preshower and shower since they were not included in the trigger. The raw PMT signals for both detectors were fed into analog amplifier modules and then sent directly through 1000 ns delay cables to Fastbus ADCs, model 1881. The preshower PMT signals were reduced by 0.8, while the shower PMT signals were transmitted without any change.

The preshower detector has a radiation length of 3.65. The shower detector has a radiation length of 14.83 and serves as a total absorption calorimeter. The detectors are divided so as to make electron-pion discrimination easier. There is a big difference in the mean free path (the mean distance traveled by a particle before suffering a collision) between electrons and hadrons, so the electron has a high probability of starting a shower in the preshower detector but the pion does not. By looking at the energy deposited in the preshower detector versus the energy deposited in the shower detector, electrons and pions can be distinguished (see Figure 3-12).

2.8 Trigger Setup

For this experiment, the trigger electronics for both spectrometers were very similar. The main difference was that for the hadron spectrometer the trigger was formed by a coincidence between its two scintillator planes S1 and S2, while the electron spectrometer contained a gas Čerenkov detector that was used as part of its trigger, in addition to its two scintillator planes S1 and S2. The coincidence trigger was an AND of the triggers from the two spectrometers.

A simplified diagram of the trigger electronics is shown in Figure 2-30. The full diagrams of the HRSE trigger circuit, the HRSH trigger circuit and the coincidence circuit is shown in Appendix A.

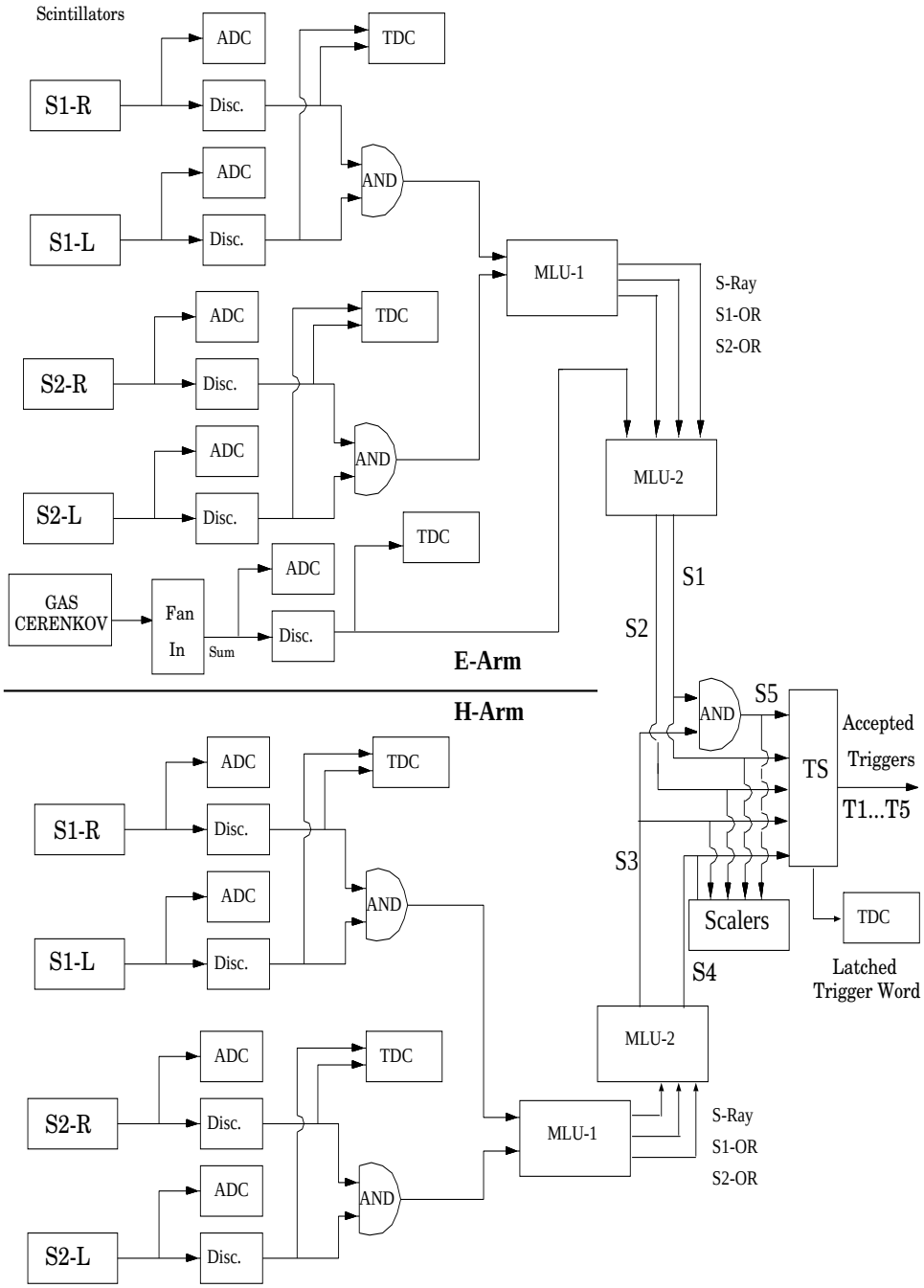

Fig. 2-30: A simplified diagram of the HRSE, HRSH and Coincidence trigger circuits used for this experiment. Note that none of the delays are shown. S1–S5 denote the raw trigger signals, while T1–T5 denote the accepted triggers.

	Trigger Type	Description
Raw Triggers	S1	HRSE S1 AND S2 (S-Ray)
	S2	Not S-Ray and one missing of HRSE S1, S2, Čerenkov
	S3	HRSH S1 AND S2 (S-Ray)
	S4	Not S-Ray and one missing of HRSH S1, S2
	S5	S1 AND S3 in coincidence
Accepted Triggers	T1	Electron Singles Trigger
	T2	Electron "Junk" Trigger
	T3	Hadron Singles Trigger
	T4	Hadron "Junk" Trigger
	T5	Coincidence Trigger

Table 2-12: Trigger types.

The trigger types for this experiment are presented in Table 2-12. An electron singles trigger, S1, was formed by a signal from the two HRSE scintillator planes S1 and S2 in coincidence and satisfies the S-Ray requirements (see below). A hadron singles trigger, S3, was formed by a signal from the the two HRSH scintillator planes S1 and S2 in coincidence and satisfies the S-Ray requirements. Each spectrometer also had a "junk" trigger. The HRSE "junk" trigger, S2, allowed one of the scintillators S1, S2 or Čerenkov signals to be missing and excluded the conditions for an S-Ray. The HRSH "junk" trigger, S4, allowed one of the scintillators S1 or S2 signals to be missing and excluded the conditions for an S-Ray. These junk triggers were used for detector efficiency studies. Their usefulness was limited because they were severely prescaled away during the experiment. The singles triggers, S1 and S3, are sent to a LeCroy logic AND module (model 4516) to form the coincidence trigger, S5. Figure 2-31 shows the timing for the coincidence trigger. The Electron arm normally defines the coincidence timing.

For the S-Ray requirements both planes must have signals. Assuming that paddle N (or 2 overlapping paddles) gave a signal in the scintillator plane S1, then in the scintillator plane S2 the signal must come from paddle N (or N-1 or N+1 or any overlap between them). If it was otherwise it will not be an S-Ray. Always both sides of the paddle must fire. There

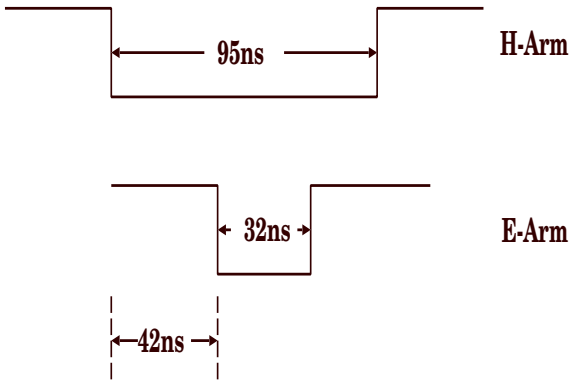

Fig. 2-31: Widths and delays of Electron arm S1 trigger and Hadron arm S3 trigger at the coincidence logic AND. The Electron arm normally defines the coincidence timing.

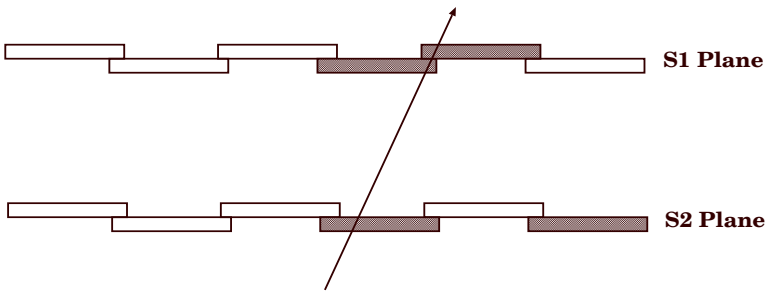

Fig. 2-32: An event in the scintillator planes. There are signals in the shaded paddles.

was a change in the programming of the Memory Lookup Unit (MLU) in the last part of the experiment. This change should affect cases like the one shown in Figure 2-32. Before the change, such an event will be registered as S2 trigger (S4 in the Hadron arm). After the change, the MLU will consider this event as an S-Ray event and will be registered as S1 trigger (S3 in the Hadron arm) regardless of the existence of other hits in paddles such that their numbers are $> |N \pm 1|$. This change was made to reduce the trigger inefficiency that was caused by background events and noise in the scintillators PMTs.

Bit 1	S-Ray
Bit 2	S1-OR
Bit 3	S2-OR

Table 2-13: The outputs of the first MLU.

The trigger logic is done using LeCroy 2373 Memory Lookup Units (MLU). There are two MLUs in each arm. The first MLU is programmed the same for both spectrometers. The first MLU is in "Strobe" mode. In this mode, the leading edge of the strobe signal latches the MLU inputs. The MLU will be busy for 45ns. There are 12 inputs from 12 scintillators (as left and right PMTs must fire). The strobe comes from the OR of S1R-OR or S2R-OR. S1R-OR is the OR of the right PMTs of the six paddles in scintillator plane S1. S2R-OR is the OR of the right PMTs of the six paddles in the scintillator plane S2. The S2R-OR signal comes $\sim$15 ns before the S1R-OR, so it defines the timing. The outputs of the first MLU are listed in Table 2-13. Bits 1, 2, 3 outputs go to the second MLU inputs 1, 2, 3. On the Electron arm the Čerenkov signal goes into input 4. On the Hadron arm nothing goes into input 4. S1-OR is the OR of the six paddles in scintillator plane S1. S2-OR is the OR of the six paddles in the scintillator plane S2. The Čerenkov signal is the discriminated sum of the 10 Čerenkov PMTs.

The second MLU is in "Transparent" mode. In this mode, latching is disabled and the

output follows the input with minimum propagation delay of 40 ns. The second MLU is programmed similarly for both spectrometers. If S-Ray is present it puts out trigger S1 (trigger S3 for the Hadron arm). If S-Ray is absent, then trigger S2 (trigger S4 for the Hadron arm) may be formed as follows: On the Electron arm, 2 out of 3 hits are required from S1-OR, S2-OR, and Čerenkov. On the hadron arm, 1 out of 2 hits are required from S1-OR, S2-OR. Trigger S1 and S2 are exclusive. Trigger S2 will not go to the coincidence circuit. Similarly for triggers S3 and S4.

Triggers S1–S5 are counted by the scalers and fed into the Trigger Supervisor (TS). The scalers simply count the number of triggers of each type which were produced by the system. Each channel of scaler is independent, and so the triggers are counted independently and with no prescaling. Note that, the scalers count a coincidence event as two single arm events. Therefore, the scaler count of S5 is included within the scaler count of S1 and S3. The Trigger output does not record a coincidence event as two single arm events. Thus event types T1, T3, and T5 are exclusive.

2.8.1 Trigger Supervisor

The interface between the trigger hardware and the computer data acquisition system is the trigger supervisor (TS). The trigger supervisor module was designed and built by the Data Acquisition Group at Jefferson Lab [28].

The trigger supervisor has a prescale function and a memory lookup function. When the signals arrive at the input, the prescale function acts *first*. A prescale factor of N for a trigger type means the trigger supervisor ignores N-1 triggers of that type until the Nth one comes along. The MLU function acts upon the prescaled trigger inputs. TS latches 10 ns after the edge of the first trigger to reach it. The trigger supervisor uses the latched trigger word as a vector in a lookup table to define the event type. When an event is accepted, a "level-1 accept" signal is generated by the TS. This signal is sent to a scaler and to the

re-timing circuit in each arm. The "level-1 accept" is re-timed with respect to the single arm S2R-OR or S1R-OR signal for that spectrometer and used to generate the start, stop, and gate signals for the Fastbus TDCs and ADCs. For every event accepted, all the Read Out Controllers (ROCs) are read out and all the variable information from the detectors in both spectrometers is passed to the CODA (CEBAF On-line Data Acquisition) file. This is especially useful in studying the trigger inefficiency. During the event read out, the trigger supervisor is dead for typically 700 μs. This is the time required to process an event which has an average size of 1 kbyte. This limits the maximum rate of the data acquisition to $\sim$1.4 kHz.

In order to reduce the event size, the sparsification feature (zero and overflow suppression) of the Fastbus ADCs and TDCs was used. The TDCs normally operate in sparsified mode, giving an event for a channel only if it received a stop signal after the common start (model 1875A) or it received a start signal after the common stop (model 1877). The LeCroy 1881M ADCs can be programmed to ignore all channels that have a signal smaller than a threshold value which can be set for each channel. However, using the sparsification means that we do not record pedestal values for each channel during normal data taking. To determine the pedestal values, a fixed number of events (usually 1000) generated by a "pulser" trigger was taken while data sparsification was disabled. This allowed us to measure the mean and the standard deviation (σ) of the pedestal values for the ADCs. The threshold was set to be 3σ higher than the mean for each channel. After determining the threshold, sparsification was enabled and normal data were taken in a pedestal suppression mode.

The prescaling for an input channel is done out-of-line. That is, the current pulse determines the pass through status of the next pulse. The prescale circuitry for each channel is composed of a count-down counter and some logic. An input pulse will pass through the circuit only if the count upon its arrival is zero. The rising edge of the input pulse serves

as a clock to count down or load the counter. If the counter is non-zero at the arrival time of this rising edge, the counter will count down. If the count is zero upon its arrival, the programmed prescale factor will be loaded into the counter. In either case the new count value is quickly resolved and its zero status is latched by the falling edge of the same pulse. This determines the pass through status of the next pulse.

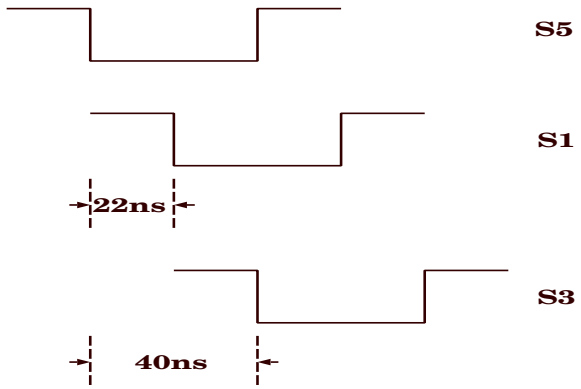

Fig. 2-33: Nominal delays for Electron arm S1 trigger and Hadron arm S3 trigger at the input of the trigger supervisor relative to S5. Triggers S1 and S3 are delayed to avoid overlaps of triggers at TS input.

When the data acquisition can accept a trigger, the first trigger to arrive at TS may trigger the system. However, if a second trigger signal (or more) arrives on a different input of the TS within 10 ns of the first, an overlap occurs and the TS in its present state of programming creates an event type 14. This 10 ns interval is the minimum simultaneous trigger resolution time. That is, if an input trigger signal on any channel has a leading edge within 10 ns of the earliest such trigger signal, it is included among those that are latched to determine the event type. To avoid overlaps of triggers, S5 is forced to arrive 22 ns before S1 and 40 ns before S3. Figure 2-33 shows the nominal delays for Electron arm trigger S1 and Hadron arm trigger S3 at the input of the trigger supervisor relative to S5. For every S5 there are also S1 and S3 triggers, but they are discarded because S5 takes precedence. This discarding occurs in addition to the prescaling away of S1 and S3.

2.8.2 Latched Trigger Word

Latched Trigger TDC Channel					Pattern	Event Type
ch1	ch2	ch3	ch4	ch5		
1	0	0	0	0	1	1
0	1	0	0	0	2	2
0	0	1	0	0	4	3
0	0	0	1	0	8	4
0	0	0	0	1	16	5
1	0	1	0	0	5	1
1	0	0	0	1	17	5
0	0	1	0	1	20	5
1	0	1	0	1	21	5
1	0	0	1	0	9	1
0	1	1	0	0	6	3
0	1	0	1	0	10	2 or 4

Table 2-14: The relation between the event type and the latched trigger word.

The latched trigger word, which TS uses to determine the event type, was put in the data stream at the beginning of $A(Q^2)$ data taking. For $B(Q^2)$ data taking, the latched word was not available in the data stream, only the final trigger type was available. The trigger supervisor had 12 outputs corresponding to 12 trigger inputs *after* prescaling. These 12 outputs represent the latched trigger word. The outputs were sent to a LeCroy TDC model 1877. If a trigger M happens, channel M gets a hit. If a T5 is accompanied by a T3, there will be a hit on channels 3 and 5. This makes it straight forward to extract the single arm triggers from the coincidence triggers. Table 2-14 shows the relation between the event type and the latched trigger word. In the analysis, the latched trigger word (12 TDC channels) were decoded into a latched trigger pattern. The pattern is calculated as the sum of 2^{ch_i}, where ch_i is the channel number where there was a hit. 1 indicates there is a hit in a channel. 0 indicates there is no hit in a channel either because there is no trigger or the trigger is prescaled away.

The event type will be 14 if any two inputs arrive within 10 ns. If trigger 5 is prescaled,

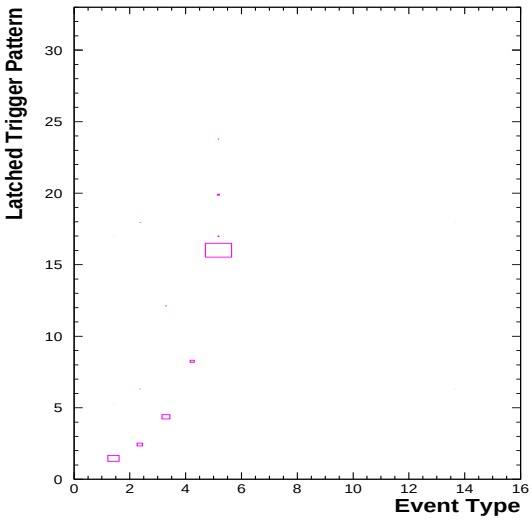

Fig. 2-34: Latched trigger pattern versus event type.

then we may have cases where the coincidence was prescaled away and T1 and T3 were not prescaled away. In this case event type 14 will be generated. This may happen if there is any problem with timing. Figure 2-34 shows the latched trigger pattern versus event type. Some combinations are illegal, for example a trigger type 2 should not be accompanied by a trigger type 1, since they are exclusive; however, the TDC that reads the latched trigger word has a 5 μs window. There may be a few random hits depending on the rate. Looking at the latched trigger word is very useful for trigger diagnostics. Having the latched trigger word makes it straight forward to construct the single arm spectra (see Section 2.8.5).

Figure 2-35 shows the TDC channel of the latched trigger for trigger type 1. The peak at channel 2677 is the self timing peak when there is only a hit in the first channel. The peak at channel 2633 corresponds to a hit in the first channel and a hit in the fifth channel. The stop signal comes from T5 (since it is the accepted trigger) while the start signal comes from T1 which is delayed by 22 ns (44 channels) relative to T5. Figure 2-36 shows the TDC channel of the latched trigger for trigger type 2. There is just the self timing peak. Figure

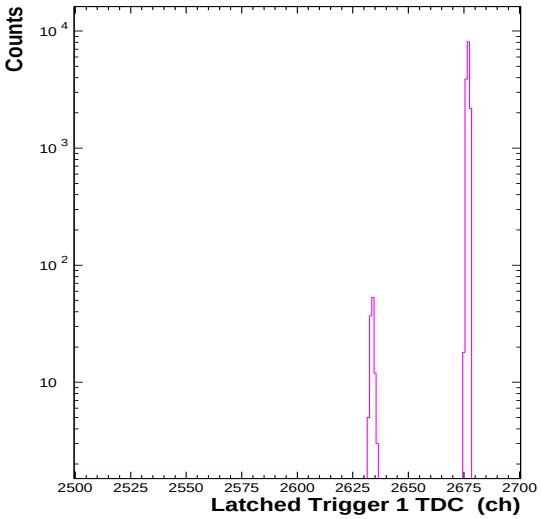

Fig. 2-35: The TDC channel of the latched trigger for trigger type 1. The peak at channel 2677 is the self timing peak when there is only a hit in the first channel. The peak at channel 2633 corresponds to a hit in the first channel and a hit in the fifth channel. The stop signal comes from T5 (since it is the accepted trigger) while the start signal comes from T1 which is delayed by 22 ns (44 channels) relative to T5.

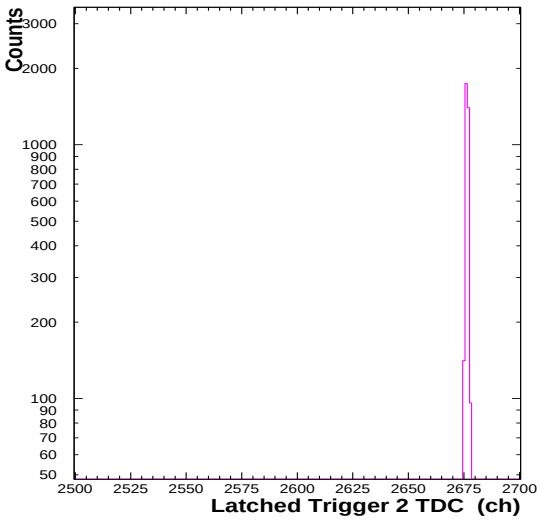

Fig. 2-36: The TDC channel of the latched trigger for trigger type 2.

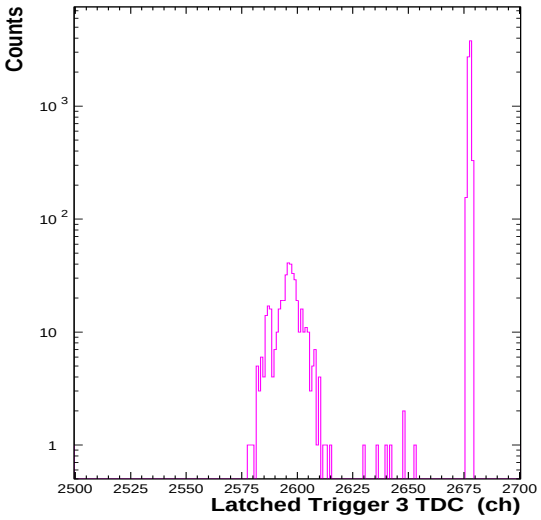

Fig. 2-37: The TDC channel of the latched trigger for trigger type 3. The description of the peaks is the same as for trigger 1 except this time trigger 3 is delayed by 40 ns (80 channels) relative to T5. The peak at channel 2597 is wider in this case since S1 defines the timing, not S3.

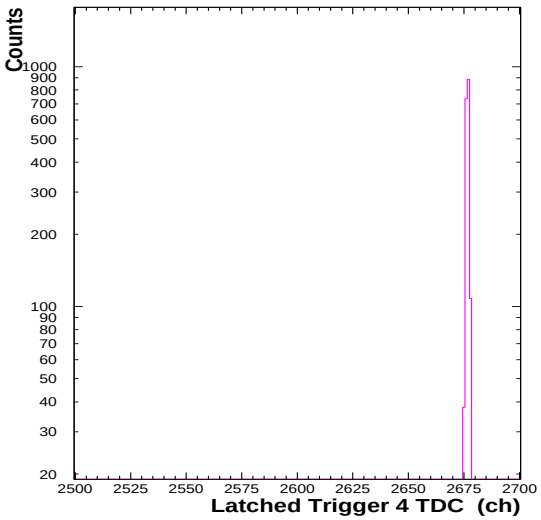

Fig. 2-38: The TDC channel of the latched trigger for trigger type 4.

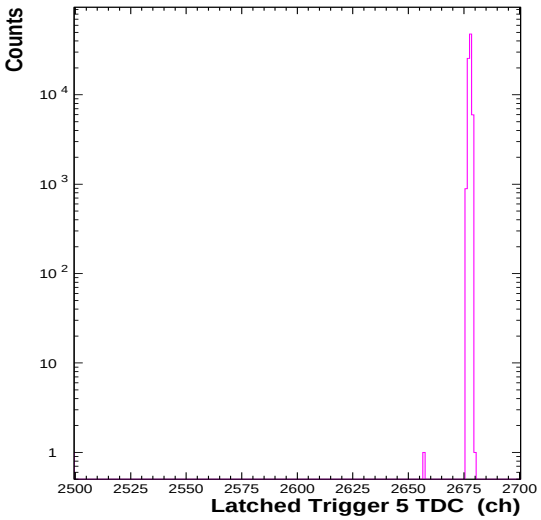

Fig. 2-39: The TDC channel of the latched trigger for trigger type 5.

2-37 shows the TDC channel of the latched trigger for trigger type 3. The description of the peaks is the same as for trigger 1 except this time trigger 3 is delayed by 40 ns (80 channels) relative to T5. The peak at channel 2597 is wider in this case since S1 defines the timing, not S3. Figure 2-38 shows the TDC channel of the latched trigger for trigger type 4. Figure 2-39 shows the TDC channel of the latched trigger for trigger type 5.

2.8.3 Data Rates

The maximum data taking rate is limited by the Fastbus conversion and data readout time. In basic data acquisition mode, the total time to process an event is just under 1 ms. The time is broken up as follows: $\sim$95 μs for Fastbus data conversion, $\sim$150 μs for the Fastbus crate controller (FSCC) to read the data from the ADC and TDC modules into its First-in First-out memory (FIFO), and $\sim$650 μs for the FSCC to take the data from its memory and send it out over ethernet. This limits data acquisition to $\sim$1.1 kHz, but gives large computer dead times even at lower rates. Several improvements have been made to

improve the data rate and decrease dead time. First, because the FSCC is inefficient at sending data over the ethernet, the readout of the Fastbus data was modified to be read out from the FSCC FIFO through a VME Struck Fastbus Interface (SFI) CPU. This reduced the processing time to ∼95 μs for Fastbus conversion, and ∼600 μs for the data readout. The fraction of events missed is equal to the fraction of the time the computer is busy which equals the rate of events taken over the maximum rate (1.4 kHz). Even at 150 Hz the computer dead time is ∼15-20%.

2.8.4 Electronics and Computer Dead Time

The main correction to the measured number of events comes from data acquisition dead times. Electronic dead time is caused when triggers are missed because the hardware is busy when an event that should generate a trigger comes in. When a logic gate in the trigger is activated, the output signal stays high for a fixed time. If another event tries to activate the gate in that time, it is ignored. The electronic dead time was measured to be ∼100 ns. Detector dead time occurs when a detector is unable to respond properly to an event because it is still responding to a previous event. The VDCs are the slowest detectors in processing an event while the scintillators are the fastest (this is why they are used in the trigger). The detector dead times are expected to be < 1 μs. Electronics and detector dead times are negligible for rates < 1 MHz as was the case in this experiment.

A more significant source of dead time for this experiment was the computer dead time. In this case, events are lost because a hardware trigger is formed when the data acquisition system is busy processing the previous event. The total processing time for an event is ∼700 μs. The computer dead time is measured by counting the number of triggers that were formed and the number of triggers that were processed by the Trigger Supervisor. The number processed over the number generated is the live time of the data acquisition system. The dead time was calculated for each run, and the cross section was corrected

for the lost triggers (this correction is denoted as C_{cdt}). No systematic error is assigned to this correction since the number of triggers that were formed is known and if a random sample of these triggers made it to the CODA file then the computer dead time correction is exactly defined.

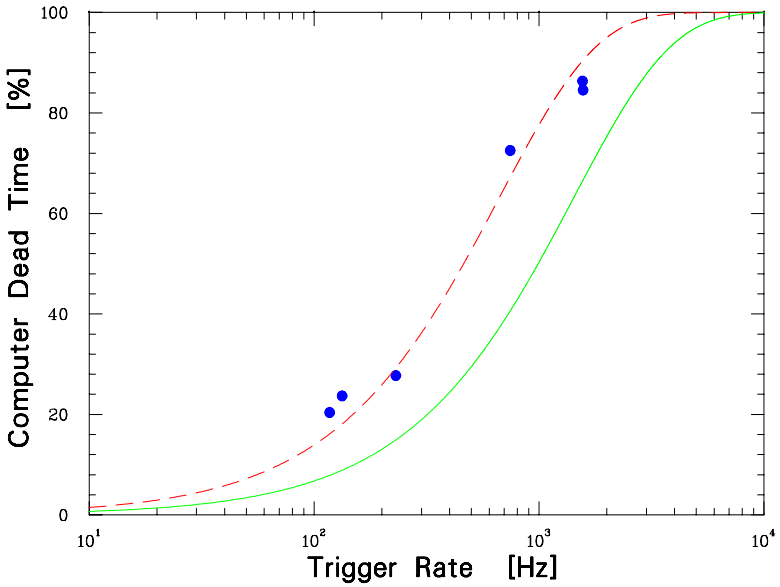

Fig. 2-40: Measured computer dead time versus trigger rate for a few runs. The solid line is the expected value for a processing time, τ, of 700 μs. The dashed line is for τ = 1500 μs. The expected value is $1 - e^{-R\tau}$, where R is the trigger rate.

Figure 2-40 shows the measured computer dead time for a few runs. The measured computer dead time is higher than that expected for a processing time, τ, of 700 μs because the contribution to the dead time from the network was larger than anticipated [29]. The network was shared by many computers and was only a 10 Mb ethernet. The measured computer dead time corresponds to a processing time of $\sim$1500 μs. The measured computer dead times for event types T1, T2, T3, T4 and T5 are approximately the same.

2.8.5 Inclusive Measurement with a Single Spectrometer

Although not required for this experiment, this section describes how to reconstruct single arm spectra, needed for determination of single arm cross sections. An example of a single arm spectrum is the relative momentum, $\Delta p/p$, of events in one arm. To construct a single arm spectrum, it is incorrect to analyze **event type 1** and **event type 5** and add the two histograms because the two contributions have different dead time corrections and the shape of the this spectrum will be different from the correct one.

With the dead time correction taken into account, an HRSE single arm (e,e') spectrum $S_E^{(e,e')}$ is given by:

$$S_E^{(e,e')} = \frac{s1 - s5/ps5}{t1} S_1^{(e,e')} + \frac{s5/ps5}{t5} S_5^{(e,e')} \ , \tag{2-4}$$

where $S_1^{(e,e')}$ is the (e,e') spectrum of events written to tape as event type 1, and $S_5^{(e,e')}$ is the (e,e') spectrum of events written to tape as event type 5. $s1$ and $s5$ are the scaler counts of triggers S1 and S5. $t1$ and $t5$ are the number of event types T1 and T5 written to tape. $ps5$ is the prescale factor for trigger 5.

Another way to obtain the HRSE single arm (e,e') spectrum $S_E^{(e,e')}$ is to use the latched trigger word:

$$S_E^{(e,e')} = \frac{S1}{tl1} S_{L1}^{(e,e')} \ , \tag{2-5}$$

where $S_{L1}^{(e,e')}$ is the (e,e') spectrum of events written to tape which have a hit in the latched trigger TDC channel 1 and $tl1$ is the number of events written to tape which have a hit in the latched trigger TDC channel 1.

Similarly, a HRSH single arm (e,p) spectrum $S_H^{(e,p)}$ (after dead time correction) is:

$$S_H^{(e,p)} = \frac{s3 - s5/ps5}{t3} S_3^{(e,p)} + \frac{t5/ps5}{t5} S_5^{(e,p)} \ , \tag{2-6}$$

where $S_3^{(e,p)}$ is the (e,p) spectrum of events written to tape as event type 3, and $S_5^{(e,p)}$ is the (e,e') spectrum of events written to tape as event type 5. $s3$ and $s5$ are the scaler counts of triggers S3 and S5. $t3$ and $t5$ are the number of event types T3 and T5 written to tape. $ps5$ is the prescale factor for trigger 5.

Another way to obtain the HRSH single arm (e,p) spectrum $S_H^{(e,p)}$ is to use the latched trigger pattern:

$$S_H^{(e,p)} = \frac{S3}{tl3} S_{L3}^{(e,p)} \ , \tag{2-7}$$

where $S_{L3}^{(e,p)}$ is the (e,p) spectrum from events written to tape which have a hit in the latched trigger TDC channel 3 and $tl3$ is the number of events written to tape which have a hit in the latched trigger TDC channel 3.

Figure 2-41 shows the Electron and Hadron arm relative momentum spectra, $(p-p_0)/p_0$, reconstructed using both the event type and the latched trigger word. If the experimenter is interested in single arm spectra, it is important to write on tape a balanced number of type 5 events and type 1 or 3 events. As seen in Figure 2-41, the Electron arm spectrum had good statistics while the Hadron arm one had poor statistics. There were fewer Hadron arm T3 events than Electron arm T1 events.

For coincidence events, the dead time is different. The total number of coincidence $(e,e'p)$ events after the dead time correction is:

$$S_{EH}^{(e,e'p)} = \frac{s5}{t5} S_5^{(e,e'p)} \equiv \frac{s5}{tl5} S_{L5}^{(e,e'p)} \ , \tag{2-8}$$

where $S_5^{(e,e'p)}$ is the $(e,e'p)$ spectrum of events written to tape as event type 5. $tl5$ is the number of events written to tape which have a hit in the latched trigger TDC channel 5, and $S_{L5}^{(e,e'p)}$ is the $(e,e'p)$ spectrum from events written to tape which have a hit in the latched trigger TDC channel 5.

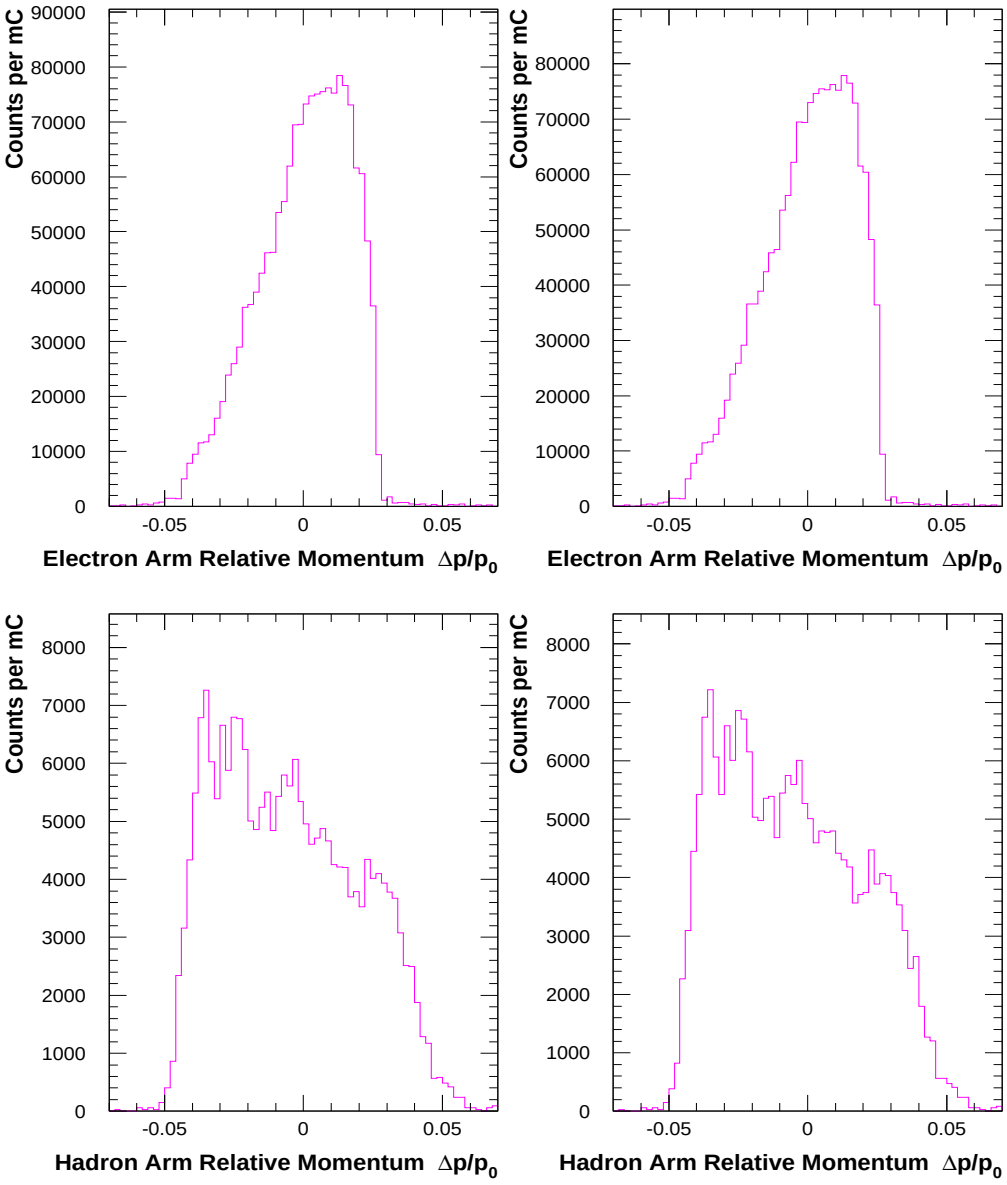

Fig. 2-41: Electron and Hadron arm relative momentum, $(p - p_0)/p_0$, reconstructed using both the event type and the latched trigger word. The spectra on the left are constructed using the event type. The spectra on the right are constructed using the latched trigger word.

2.8.6 Hadron Arm Delays

For a particle moving at the speed of light, it takes ∼80 ns to reach the HRS focal plane from the target. In the Hadron arm, the deuterons and the protons are much slower. For the slowest hadron (deuteron with P_d ∼840 MeV/c) the hadron time-of-flight (hTOF) is ∼200 ns from the target to the focal plane. The coincidence trigger electronics was setup such that the hadron coincidence delay just before the coincidence AND logic module is programmed to delay the hadron S3 trigger by an amount such that: Hadron delay 1 + hTOF = 200 ns. Consequently, the electron S1 trigger and the hadron S3 trigger arrive at the coincidence AND logic module at the same time regardless of the time-of-flight of the hadron. After the coincidence AND logic module, the second hadron delay was programmed to delay the "level-1 accept" signal by an amount such that: Hadron delay 1 + Hadron delay 2 = 120 ns. This is necessary to guarantee that the signals sent to Fastbus ADCs and TDCs have the right timing compared to the original signal from the detectors. This is illustrated in Figure A-3 in Appendix A.

2.9 Data Acquisition

The data acquired during E91-026 were a mixture of physics event data (acquired from the spectrometers with each accepted trigger), scaler data and data from the hardware slow controls systems (EPICS events). All data were acquired using a data acquisition (DAQ) system built under the CODA environment, version 1.4. CODA was developed at Jefferson Lab by the Data Acquisition Group. For a detailed explanation of CODA and its capabilities, see Reference [27]. The data acquisition system is controlled via a graphical user interface known as "RunControl". Data acquired by CODA are written to a local computer disk and copied at specified times to the Mass Storage System (MSS) in the JLab Computer Center where they are archived on data tapes.

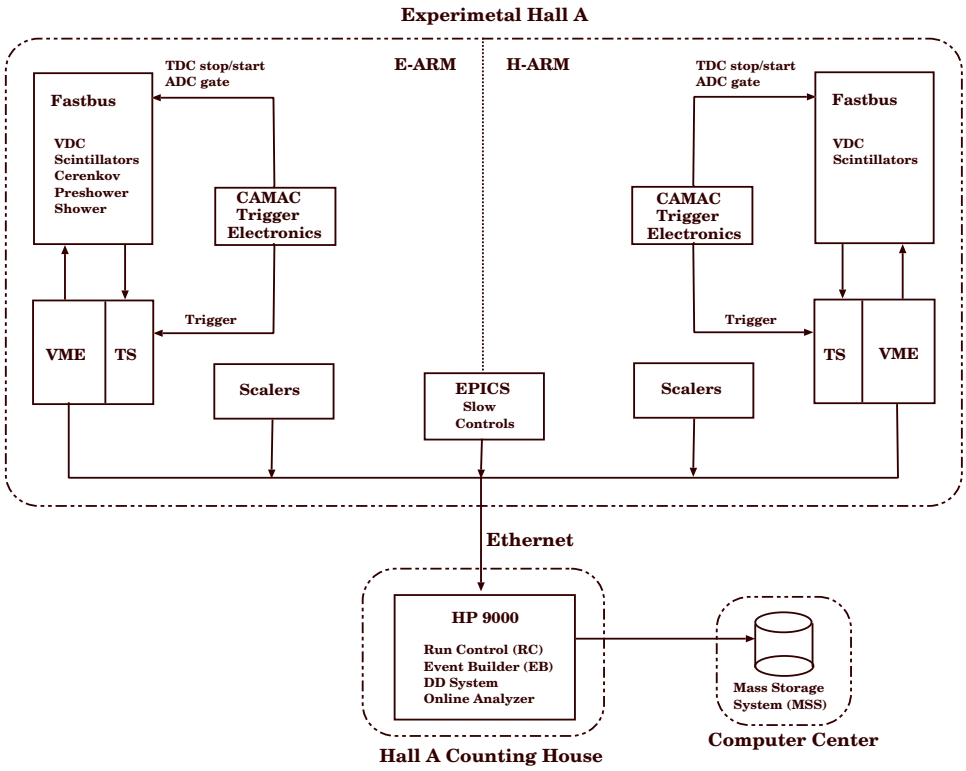

Fig. 2-42: Schematic of the Hall A DAQ.

2.9.1 CODA Overview

A schematic of the data acquisition system used in this experiment is shown in Figure 2-42. When particles pass through the detector package of either the Electron or Hadron spectrometer, they can generate signals in the scintillators and Čerenkov detector. If the pattern of detector signals is recognized by the trigger electronics as one of the allowed trigger types (see section 2.8 for allowed types), the Trigger Supervisor causes an event to be recorded by the data acquisition. First, the Read-Out Controllers are read out. There are four ROCs in the Hall A DAQ. The ROCs are single board computers in the Fastbus and VME crates. These crates contain the ADCs, TDCs and scalers which record the physics event information. The Fastbus modules are for the detectors and consist of LeCroy Model 1877 TDCs (operating in common-stop mode with 0.5 ns resolution for the VDC), LeCroy model 1875A TDC (operating in common-start mode with 0.1 ns resolution for the scintillators and Čerenkov), and LeCroy Model 1881M ADC (for scintillators, Čerenkov, preshower, and shower). The fragments of information from the ROCs are then collected by the Event Builder (EB) and put together into the CODA event format, including header and identifying information. After the event is built by the EB, it is written to disk for later analysis by the Hall A analysis program ESPACE, which is described in Section 3.2.

Incoming data were spied on using the CODA Data Distribution (DD) system. The DD system maintains a real-time event buffer which can be accessed by software tools. During this experiment, online programs [30], which utilized the DD system, were used to make real-time diagnostic histograms so that the quality of data could be monitored online.

2.9.2 CODA Data File

The data file generated by CODA is a mixture of status events, physics events and "special" events [31]. The status events are events like "prestart", "go", "pause", and "end" that are included whenever the state of the run changes.

Spread throughout the data file are the physics event data. These data come in an array of 32-bit words. The first part of the event structure is a "header" information, containing information like how long the event is, the event type (*e.g.*, T1–T5) and the run number. After the header comes the physics event information, which has been extracted from the four ROCs. Three of the ROCs provide the information from the detectors, while the fourth ROC provides BPM and raster data which can be used later to reconstruct the interaction point of an event within the target.

"Special events" are events such as scaler readouts and EPICS data from the detector and beamline elements not directly associated with the DAQ. The scalers count the raw hits on the detector phototubes, as well as the number of triggers generated by the trigger supervisor. They are monitored online, and each ten seconds they are read out and their values are inserted into the datastream. The so-called "EPICS events" provide the status of some of the experimental hardware components which can be later correlated to the physics data taken around the same time. Approximately every thirty seconds, a long list of EPICS variables is inserted into the datastream. This list contains readouts of the beam current, the beam position, the magnetic fields of the spectrometer magnets, the high voltage of the detector PMTs, etc. For hardware information needed on a more frequent time-scale, a subset of the EPICS variables are read out approximately every five seconds. This subset includes the beam position and beam current. This read out of the beam current was used to calculate the accumulated charge in each run (see Section 3.3). The archived EPICS data are used, for example, to study the magnetic fields of the spectrometer magnets as a function of time over the course of a run. These data also allows pinpointing the time during a run when a piece of equipment began to malfunction.

Chapter 3

Data Analysis

3.1 Overview

Approximately 40 Gbytes of data were collected during the two month running period of this experiment. The data were analyzed using the Hall A data analysis program ESPACE (Event Scanning Program for Hall A Collaboration Experiments). From this analysis, elastic *e-p* calibration events and elastic *e-d* events were identified. These events, along with other measured and calculated factors, were used to determine both elastic *e-p* cross sections and elastic *e-d* cross sections as a function of Q^2. The measured *e-p* cross sections were compared to the previous world data. The results of this comparison are given in Section 3.12. The deuteron elastic structure functions $A(Q^2)$ and $B(Q^2)$ were extracted from the measured elastic *e-d* cross sections. The results of our measurements for both $A(Q^2)$ and $B(Q^2)$ are presented in Chapter 4.

3.2 ESPACE

The Hall A event analyzer, ESPACE [33], was adapted from an analyzer developed at Mainz by E. Offermann, and was used to analyze all of the data taken during this experiment. ESPACE takes the raw data file (which is the output of CODA), along with a header file (which contains run-specific information such as spectrometer magnetic fields), a detector map file (which contains the correspondence between the event readout electronics and the physical detector outputs) and a database file (which contains basic calibration constants of the detectors, such as gains, offsets, physical positions, etc.) as input. Using all these, it calculates the focal plane vertex for each detected particle trajectory (x_{tra}, y_{tra}, θ_{tra},

ϕ_{tra}). Using the spectrometer magnetic matrix elements (see section 2.6), the coordinates of a particle trajectory at the focal plane are traced back through the spectrometer to the target to obtain the interaction vertex (θ_{tgt}, ϕ_{tgt}, y_{tgt}, $\delta p/p$). The output of ESPACE consists of ntuples, a type of data file, and histograms for the analyzed events, optionally cut with various logical conditions. These outputs can be produced for all levels of the analysis, *i.e.* from the raw ADC and TDC information, to the position of an event within the detectors, to the measured momentum of a particle.

The focal plane coordinate system is designed to follow the TRANSPORT [21] convention. x_{tra} is the position in the dispersive direction ($\hat{x}$ points downwards for vertical bend spectrometers), y_{tra} is the position in the non-dispersive direction ($\hat{y}$ points left when looking at the spectrometer from the target). The $\hat{z}$ direction is parallel to the central ray (such that $\hat{x} \times \hat{y} = \hat{z}$) with $z = 0$ at the focal plane. θ_{tra} and ϕ_{tra} are the slopes of the rays at the focal plane ($\frac{dx_{tra}}{dz}$ and $\frac{dy_{tra}}{dz}$). When the tracks are reconstructed to determine the location and direction of the events at the target, the same coordinate system is used. x_{tgt} is the vertical position ($\hat{x}$ points downwards), y_{tgt} is the horizontal position perpendicular to the spectrometer angle ($\hat{y}$ points left when looking at the spectrometer from the target), and z_{tgt} is the horizontal position in the direction perpendicular to y_{tgt} ($\hat{x} \times \hat{y} = \hat{z}$). θ_{tgt} and ϕ_{tgt} are the slopes of the ray at the target ($\frac{dx_{tgt}}{dz}$ and $\frac{dy_{tgt}}{dz}$). While θ and ϕ are slopes, they are nearly equal to the out-of-plane and in-plane angles for events in the spectrometer acceptance. Therefore, they are often referred to as the angle relative to the spectrometer angle and given in units of mrad. However, they are in fact the tangent of those angles, and are treated as such when calculating kinematics.

The goal of the analysis was to identify elastic electron-proton and electron-deuteron coincidence events and determine their kinematics. Events were first separated by type, *i.e.* coincidence or single arm. Next, coincidence events with a narrowly defined time difference between the triggers of the two spectrometers were identified, reducing the number of

accidental coincidence events. The events that survived these cuts were further required to pass cuts on the HRSE Čerenkov and calorimeter detectors and on the HRSH sintillators pulse height and on the velocity of the recoil nuclei, β, measured from the time-of-flight between the two HRSH planes of scintillators. The events that remained after these cuts were the elastic electron-deuteron (electron-proton) coincidence events, from which $A(Q^2)$ and $B(Q^2)$ could be extracted. Approximately 98% of the raw coincidence events in the elastic *e-p* runs passed all the applied cuts.

3.3 Accumulated Charge

The discussion in Section 2.4.2 focused on charge extraction from the BCM signals, but the signal provided by a BCM is only proportional to the beam current. The absolute value of the current is provided by the Unser monitor. Unfortunately, the zero offset of the Unser monitor drifts on the scale of minutes, so the more stable BCMs are used as the continuous current monitor. A calibration procedure has been developed to calibrate the output of the BCM's to that of the Unser monitor.

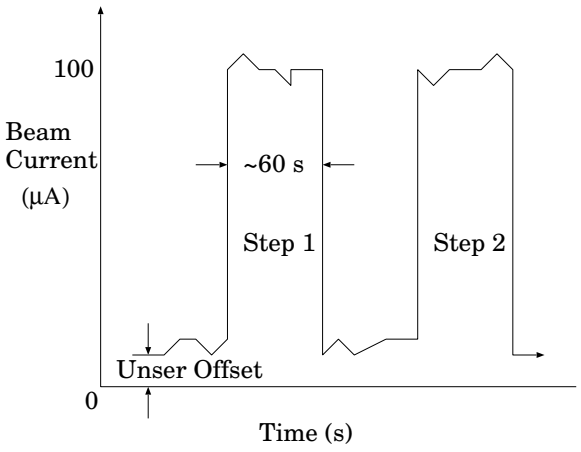

Fig. 3-1: Current calibration scheme.

The calibration procedure consists of a series of beam current steps (see Figure 3-1),

typically from 0-100 μA. During each current calibration step, the current remains at zero for one minute. During this time, the Unser monitor signal is recorded. The average of this value represents the average zero offset of the Unser monitor, denoted by I_0. Next, the current is stepped to some maximum value (typically $\geq$100 μA) as quickly as possible. The current remains at this maximum for one minute, during which time the outputs of the Unser and the two BCMs are recorded. Denoting the output of the Unser as I_u and the output of the BCM's as V_1 and V_2 (for the upstream and downstream BCM respectively), the output of the BCM's can be related to the current measured by the Unser monitor as:

$$I_u - I_0 = A_{1(2)} \times V_{1(2)} \ , \tag{3-1}$$

where $A_{1(2)}$ is the calibration coefficient for the upstream (downstream) BCM. This calibration procedure continues for four more steps in current (from zero to maximum). At the end of the procedure an average is taken of the calibration coefficients computed during each step, and this becomes the best estimate of the calibration coefficient until the next current calibration. The standard deviation is also computed for the average calibration coefficient. The calibration coefficients taken during this experiment are shown in Figure 3-2 for both BCMs as a function of run number (time) [13].

During the analysis of experiment E89-003 (the first Hall A experiment), a calculation was made of the magnitude of the expected error on the calibration coefficients A_1 and A_2 [18]. The expected error was calculated to be on the level of 0.3%, while the average standard deviation on all of the calibration coefficients taken during this experiment was on the order of 1.2%. The cause of this difference between the expected error and the measured error was found to be a problem with the algorithm used by the calibration procedure. Namely, the Unser and BCM readings were sometimes found to get out of synchronization on the part of the calibration sequence, where the current went from zero to maximum or vice versa, so

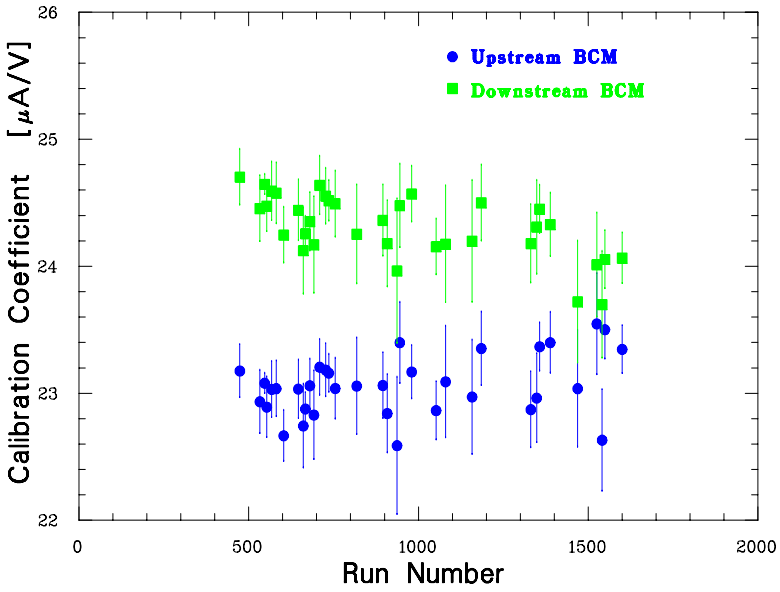

Fig. 3-2: Calibration coefficients of upstream and downstream BCMs versus run number (time). The standard deviation of the calibration coefficients of each BCM is 1.2%.

that, for example, one meter would be reading the maximum current and the other would still be reading the zero current. This error was random and occurred in both directions equally, hence, the calibration coefficients scattered around the true value. Therefore, the standard deviation of the calibration coefficients is taken to be the error on the calibration coefficient (and therefore on the beam current). A systematic error of 1.2% was assigned to the charge determination. For each run the accumulated charge was also calculated from VtoF scalers and compared with the accumulated charge calculated from the EPICS data. They were found to agree to much better than 1.0%.

3.4 Beam Energy Study

The incident electron beam energy for this experiment was determined through a study of coincidence elastic electron-proton scattering. For the $H(e, e'p)$ reaction, the incident beam energy, E, is given by:

$$E = M_p(\cot\frac{\theta}{2}\cot\theta_p - 1) + E_{loss} \ , \tag{3-2}$$

where M_p is the mass of the proton, θ_p is the proton recoil angle and E_{loss} is the ionization energy loss of the incident electron beam before scattering (*i.e.* energy loss up to the reaction vertex). The ionization energy loss is given by:

$$E_{loss} = \frac{1}{\rho}\frac{dE}{dx}(\beta\gamma)\rho l \ , \tag{3-3}$$

where $\frac{1}{\rho}\frac{dE}{dx}$ is the ionization energy loss in (MeV cm^2 g^{-1}), ρ is the hydrogen density and l is the distance between the entrance window of the target cell and the interaction vertex. The energy loss of the incident electron beam due to radiation (bremsstrahlung) causes a tail at the low energy side but does not shift the centroid of the incident electron energy. The ionizaton energy loss shifts the centroid by the amount E_{loss}. The radiative tail was cut away and only a very clean sample of events was used to measure the incident beam energy.

The angles θ and θ_p are functions of the central angles of the spectrometers (θ_0 and θ_{0p}), plus a contribution from where in the spectrometer acceptance the particles scattered to [33]:

$$\theta = \arccos\frac{\cos\theta_0 - \phi_{tgt}\sin\theta_0}{\sqrt{1+\theta_{tgt}^2+\phi_{tgt}^2}} \tag{3-4}$$

for the electron spectrometer, and:

$$\theta_p = \arccos\frac{\cos\theta_{0p} - \phi_{tgtp}\sin\theta_{0p}}{\sqrt{1+\theta_{tgtp}^2+\phi_{tgtp}^2}} \tag{3-5}$$

for the hadron spectrometer, where θ_{0p} is defined to be negative and θ_0 positive. $\theta_{tgt(p)}$ and $\phi_{tgt(p)}$ are the angles of the particle track with respect to the spectrometer central ray in the dispersive x and transverse y directions.

The error on the beam energy determined using this method is given by:

$$\Delta E = \sqrt{\left(\frac{\delta E}{\delta \theta}\right)^2 \Delta\theta^2 + \left(\frac{\delta E}{\delta \theta_p}\right)^2 \Delta\theta_p^2}\ , \tag{3-6}$$

where $\Delta\theta_0$ and $\Delta\theta_{0p}$ are the uncertainties in the surveyed positions of the spectrometer central angles. Taking the required partial derivatives of Equation 3-2 leads to:

$$\Delta E = \sqrt{\frac{M_p^2 \cot^2\theta_p}{4\sin^4\frac{\theta}{2}}\Delta\theta^2 + \frac{M_p^2 \cot^2\frac{\theta}{2}}{\sin^4\theta_p}\Delta\theta_p^2}\ . \tag{3-7}$$

The uncertainty in the central angles of both the electron and hadron spectrometers is 0.3 mrad from repeated surveys of their positions (Section 2.6). For the kinematics of this experiment and the 0.3 mrad angular uncertainties, the typical error on the beam energy determination was ∼0.2%.

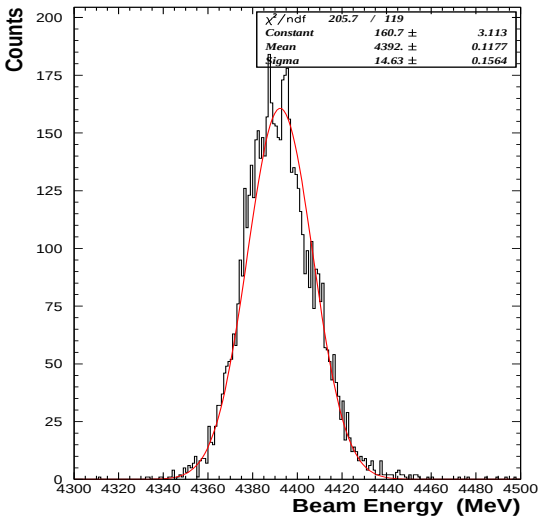

Fig. 3-3: Beam Energy as determined from $H(e,e'p)$ ($\theta_0 = 31.17^\circ$, $\theta_{0p} = 32.12^\circ$). The black curve is the data and the red curve is a Gaussian fit.

The reconstructed beam energy calculated using Equation 3-2, on an event by event basis, is shown in Figure 3-3. The width of the distribution is mostly due to multiple

scattering. The spectrometer horizontal angular resolution is ∼2 mrad (Section 2.6). Then, the energy resolution due to spectrometer angular resolution is ∼1%. For this kinematics, the nominal beam energy is 4424.0 MeV. The centroid of the distribution in Figure 3-3, representing the calculated beam energy before energy loss is taken into account, is 4392.1 MeV. The energy loss is calculated assuming that the incident electron interacts at the center of the cryotarget, after passing through 7.5 cm of liquid hydrogen. For this kinematics, the energy loss is 2.8 MeV, leading to a total energy extracted from the $H(e,e'p)$ analysis of 4394.9±4.7 MeV, where the error is calculated from Equation 3-7. This energy is 0.66% lower than the nominal beam energy of 4424.0 MeV.

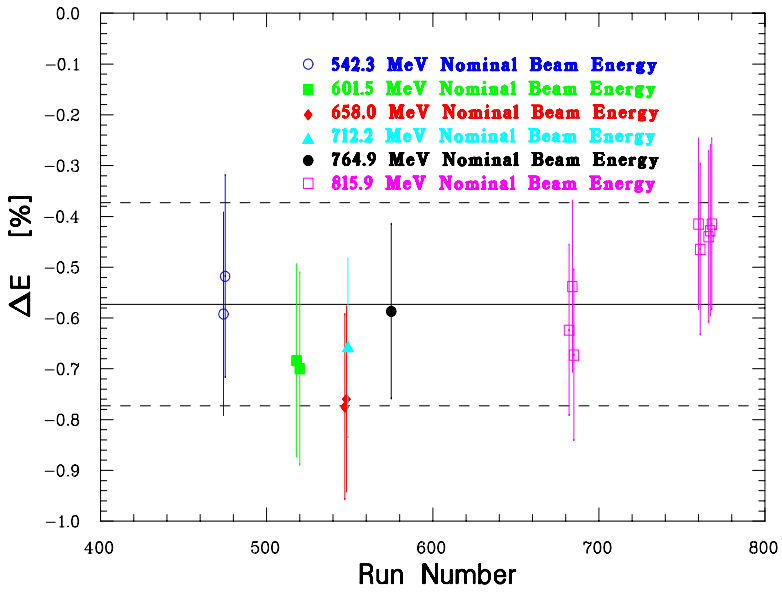

Fig. 3-4: Incident beam energy offset versus run number (time). The runs are all elastic $H(e,e'p)$ runs taken for the $B(Q^2)$ kinematics. The average energy difference is -0.57%. This value is indicated by the middle solid line, while the other two dashed lines indicate an error band of ±0.2%.

A total of seventeen $H(e,e'p)$ runs for the $B(Q^2)$ kinematics and eighteen runs for the $A(Q^2)$ kinematics were analyzed using this technique to extract the incident beam energy. They were all found to yield an energy below the nominal. A plot of the normalized energy

difference ((measured-nominal)/nominal) versus run number (time) is shown in Figures 3-4 and 3-5. Figure 3-4 shows the energy for the $B(Q^2)$ kinematical points, all taken at beam energies below 1.0 GeV, while Figure 3-5 shows the energy for the $A(Q^2)$ points, all taken at energies above 3.0 GeV. For the $B(Q^2)$ runs, the beam energy has been measured to be 0.57% lower, on average, than the nominal value reported by the accelerator. For the $A(Q^2)$ kinematics, the average energy difference is -0.58%.

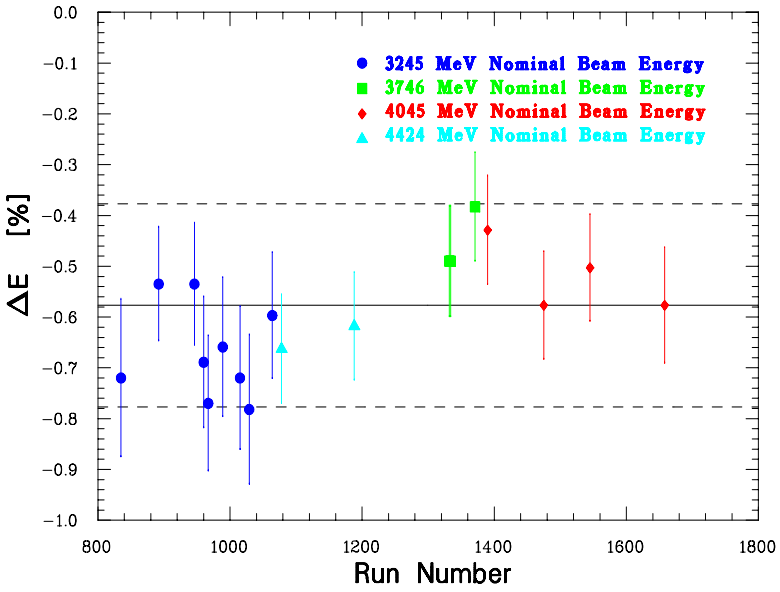

Fig. 3-5: Incident beam energy offset versus run number (time). The runs are all elastic $H(e, e'p)$ runs taken for the $A(Q^2)$ kinematics. The average energy difference is -0.58%. This value is indicated by the middle solid line, while the other two dashed lines indicate an error band of $\pm 0.2\%$.

3.5 Detector Calibrations

3.5.1 Vertical Drift Chamber Calibration

The vertical drift chambers of the Electron and Hadron spectrometers are filled with a gaseous mixture of argon and ethane. When a charged particle passes through the chambers, it ionizes the gas and the freed electrons drift along the electric field lines formed by the high voltage planes and signal wires (see Section 2.7.1 for a description of the VDC hardware).

In the vicinity of the signal wires, the electric field strength increases and the electrons gain enough energy between collisions to ionize additional gas molecules. Those electrons, in turn, can ionize more gas molecules, and so on, forming an avalanche of electrons incident on the wires. At the same time, the positive ions are drifting away from the signal wires, leading to an appreciable negative signal on the wires. A TDC, which is stopped by the event trigger, is used to infer the elapsed time between the initial ionization and a signal (above threshold) induced on a signal wire. This drift time, combined with the electron drift velocity, yields the drift distance (see Reference [34] for details). This drift distance can be converted into the perpendicular distance between the signal wire plane and the intercept of the particle with the chamber.

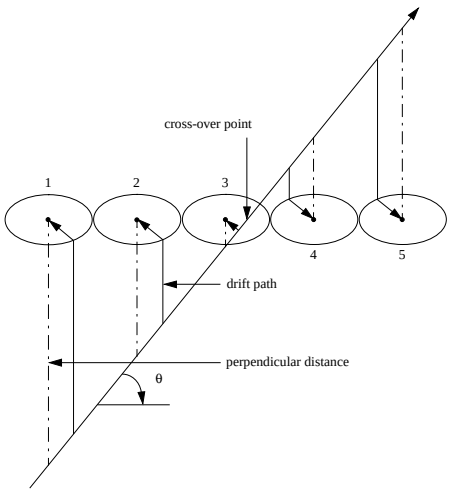

Fig. 3-6: A typical trajectory in one of the VDC wire planes. The drift paths are the paths of least time from the track to the wire. The perpendicular distances (dashed lines) to each hit wire are fit to reconstruct the particle's path (solid line) through the chambers. The circles indicate the boundary between the regions of linear electric field and the regions of radial electric field.

Typically, a charged particle induces a signal on five to six wires as it passes through the chamber. As illustrated in Figure 3-6, the particle's path through the VDC is reconstructed by fitting the perpendicular distances to each hit wire with a tracking algorithm. The

tracking algorithm chooses tracks by a goodness-of-fit test (χ^2), so the first track with a χ^2 within acceptable limits is chosen as the track of the particle which generated the trigger. Since there are four wire planes (2 VDCs per spectrometer, each with two wire planes), two positions and two angles can be obtained from the chambers, allowing determination of (x_{tra}, y_{tra}, θ_{tra}, ϕ_{tra}).

3.5.2 Scintillator Timing Corrections

The scintillator PMTs were gain-matched using cosmic rays. Timing calibration of the scintillators was done initially using cosmic data and then data taken during the experiment. Corrections have to be made for timing variations caused by signal pulse height variations, light propagation time in the scintillators, and over all timing offsets between the individual signals. Because the timing signal comes from a fixed threshold discriminator (LeCroy model 4413) the time between the start of the signal and the time that the threshold (60 mV) is exceeded depends on the height of the signal. Thus large signals will fire the discriminator earlier than small signals. These corrections are on the order of 1 ns and are parameterized as:

$$t_w \sim \frac{1}{\sqrt{(A-P)}} \ , \tag{3-8}$$

where t_w is the time walk correction, A is the ADC amplitude, and P is the pedestal of the ADC channel. This dependence is clearly seen by choosing hits in a small region of one of the scintillators (to minimize corrections due to light propagation in the scintillator) and comparing the time from that PMT hit with the pulse height. The velocity of light propagation along the scintillator can be measured by taking the difference in the times of PMTs on the opposite end of the scintillator. When plotted versus position along the scintillator, the velocity of propagation can be determined by the slope. Note that this velocity is not just the speed of light in the plastic scintillator, because most of the light

bounces off of the sides of the scintillator, rather than going directly towards the PMTs. The velocity correction therefore depends on both the index of refraction and the cross section of the scintillator. A velocity was measured for each plane, and all elements in that plane used this average correction. Finally, each tube has its own time offset due to variations in cable length or different response times of the PMTs. These are fit in the same way as the time walk corrections. The time-of-flight is calculated for a pair of scintillators, with velocity and pulse height walk corrections applied. The offsets are adjusted in order to make the time between the scintillator hits agree with the known velocity of the particle (β=-1 for cosmic rays, β=1 for electrons, and β as calculated from the momentum of the particle for hadrons).

Figure 3-7 shows the final β resolution for the HRSE scintillator planes. The best timing resolution at $\beta \simeq 1.0$ is 0.15 (FWHM). The reason for this is that one set of coefficients for the pulse height and velocity corrections were used per plane. A better resolution can be obtained by studying the individual paddles. The centroid of β is not exactly at 1.0 for the same reason.

Figure 3-8 shows the final resolution for the HRSH scintillator planes. The timing resolution for $\beta = 1$ hadrons is the same as for the HRSE. The resolution improves as β decreases because the uncertainty in the timing of the scintillator planes is the same, but the flight time is larger. Therefore, the relative uncertainty is proportional to the inverse of the time-of-flight, which is proportional to β. For low-Q^2 $D(e,e'd)$, where the accidentals $D(e,e'p)$ are noticeable, the resolution of the HRSH β was sufficient to separate protons from deuterons.

3.5.3 Čerenkov Calibration

The Čerenkov detector used in this experiment (see Section 2.7.3) was a threshold detector, where an electron with a momentum above 0.017 GeV/c or a pion with a momentum

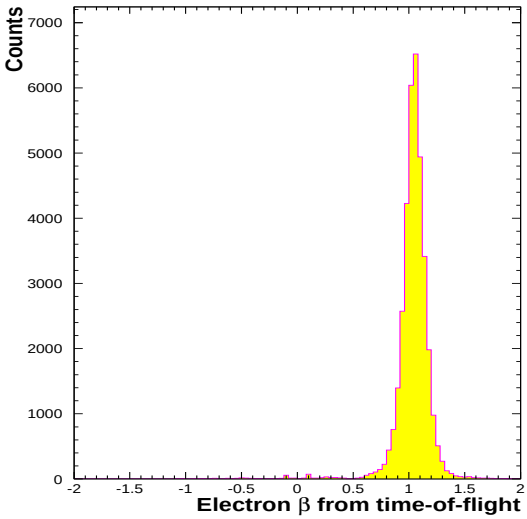

Fig. 3-7: Electron arm β for electrons from time-of-flight between the two scintillator planes.

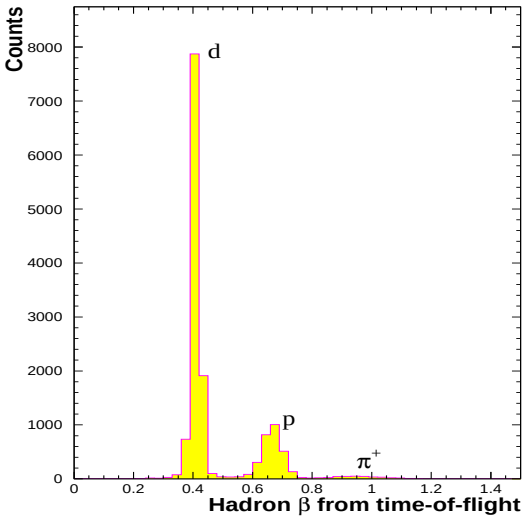

Fig. 3-8: Hadron arm β from time-of-flight between the two scintillator planes. The Hadron Spectrometer momentum setting was 0.842 GeV/c. d, p, and π^+ are clearly separated.

above 4.8 GeV/c could produce Čerenkov light. Since the threshold momentum for pions is above the maximum accepted momentum of the spectrometer, pions could only give a Čerenkov signal through the production of knock-on electrons.

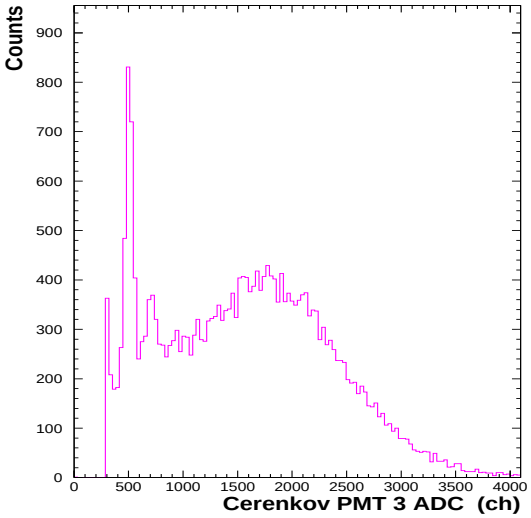

Fig. 3-9: ADC Spectrum of a typical PMT of the gas Čerenkov detector. The spike around channel 300 is the pedestal. The peak around channel 500 is the single photoelectron peak, while the peak around channel 700 is the two photoelectron peak.

The ADC spectrum for a single phototube on the Čerenkov detector is shown in Figure 3-9. The sharp pedestal peak, which is the offset voltage read out when there was no event corresponding to this phototube, is seen around channel 300. After the pedestal, the single and double photoelectron peaks (the PMT signals for one and two photoelectrons being liberated from the PMT photocathode by the incident light) can be seen. Next is a broad distribution that corresponds to the PMT signal for varying numbers of photoelectrons. Since the Čerenkov light emitted by the incident charged particle can strike more than one of the detector's mirrors, the sum of the ADC values (corrected for PMT gains) for all ten PMT's is used for particle identification. A histogram of this sum accumulated over the course of a run can be seen in Figure 3-10. To select a good electron event, a cut was placed

requiring particles to produce a Čerenkov ADC sum greater than a threshold value of ADC channel 500. The inefficiency of the Čerenkov cut is discussed in Section 3.8.2.

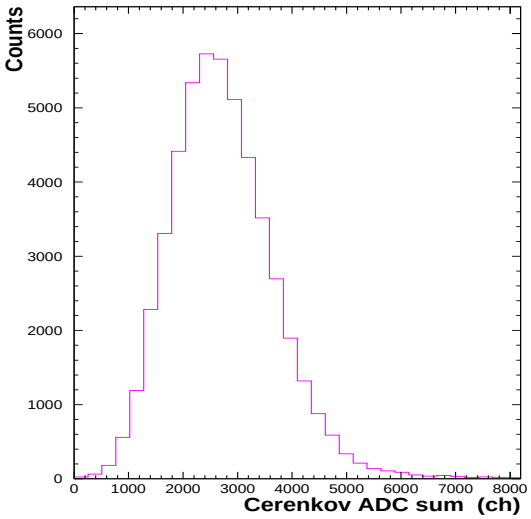

Fig. 3-10: Sum of the ADC spectra for all ten phototubes of the Čerenkov detector. A good electron event was required to have an ADC sum above channel 500.

The number of photoelectrons detected should have a Poisson distribution. For each mirror-PMT combination, the mean and the standard deviation of the ADC spectrum are determined, and the conversion from ADC channels to photoelectrons is determined by requiring that the mean value is equal to the square of the standard deviation. The average measured number of photoelectrons emitted from the Čerenkov phototubes was ∼11, as can be seen in Figure 3-11. The expected number of photoelectrons is ∼15 for a relativistic electron. The above analysis did not include Tube 7 which was coated with the wavelength shifter p-Terphenyl. The coating shifted some of the short wavelength Čerenkov light into the sensitive range of the PMT, resulting in ∼16 photoelectrons, on average, emitted per event. The 500 channel cut on the ADC sum corresponds to ∼2 photoelectrons.

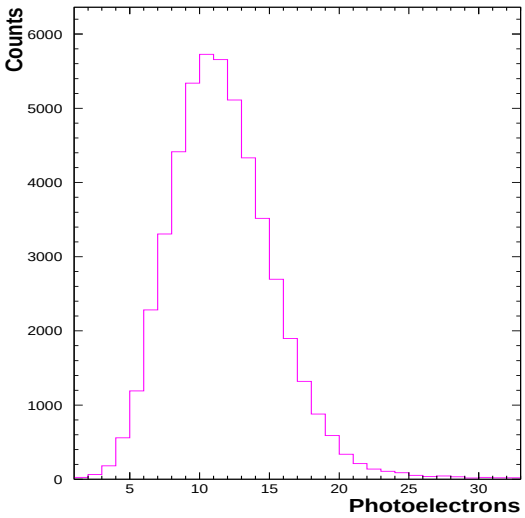

Fig. 3-11: Čerenkov photoelectrons for all ten phototubes of the Čerenkov detector. A good electron event was required to have at least 2 photoelectrons.

3.5.4 Lead-Glass Calorimeter Calibration

The goal of the calorimeter calibration (see Section 2.7.4 for the hardware description of the calorimeter) is to find for each block a coefficient that relates the actual energy deposited in the block to the raw signal from its PMT. The operating high voltages were set to match the gain of the individual PMTs using cosmic rays events. This procedure provides an initial calibration but it requires electron events to determine precisely the coefficients.

To determine the total energy deposited by an electron, the signals from both the preshower and shower detectors were summed. Calibration events were selected carefully by using information from the VDCs and the Čerenkov detector of the HRSE. A Čerenkov cut was especially required to guarantee an electron in the calorimeter. Calibration coefficients were fitted by minimizing the difference between the energy calculated using the calorimeter and the momentum calculated using the VDC track information and the spectrometer central momentum setting:

$$\chi^2 = \sum_{i=1}^{N} \left[E'^i - p'^i \right]^2 , \tag{3-9}$$

where E'^i is the total energy deposited by the i-th event in the calorimeter and is given by:

$$E'^i = \sum_{j \in M_{ps}^i} C_j \cdot (A_j^i - P_j) + \sum_{k \in M_{sh}^i} C_k \cdot (A_k^i - P_k) , \tag{3-10}$$

where i is a calibration event index, j and k are preshower and shower block indices, respectively, M_{ps}^i and M_{sh}^i represent the set of preshower and shower block indexes, A_j^i and A_k^i represent the ADC values, while, P_j and P_k represent the pedestal values, p'^i is the particle momentum measured by the spectrometer, and C_j, C_k are preshower and shower blocks calibration constants to be fitted. The total number of these constants is 144 (48 of them for preshower, and 96 for shower). A minimum of 9 events which deposited maximum energy in a block (or equivalently their center is in that block) are required for each block before its coefficient can be determined by the fit. In the software, to register a hit in a block, one must have $(A_j^i - P_j) > 5\,\sigma_j$ and $(A_k^i - P_k) > 1.5\,\sigma_k$, where σ is the standard deviation of the average pedestal of the j-th preshower ADC channel and of the k-th shower channel. The cut accounts for $\sim$15 channels for both detectors. More information about the calorimeter analysis software can be found in Reference [35].

A special "white spectrum" run (run number 1264) was taken in which the Electron arm momentum was reduced to $\sim$80% of its nominal elastic electron-proton scattering value. The new HRSE momentum setting was 1981.2 MeV/c. In this run electrons and pions covered the whole focal plane and good statistics was obtained in most of the calorimeter blocks. Thus, it was an ideal run to be used in calculating the preshower and shower coefficients. The coefficients were calculated using Equation 3-9. In Figure 3-12 the energy deposited in the preshower versus the energy deposited in the shower is shown for events (electrons

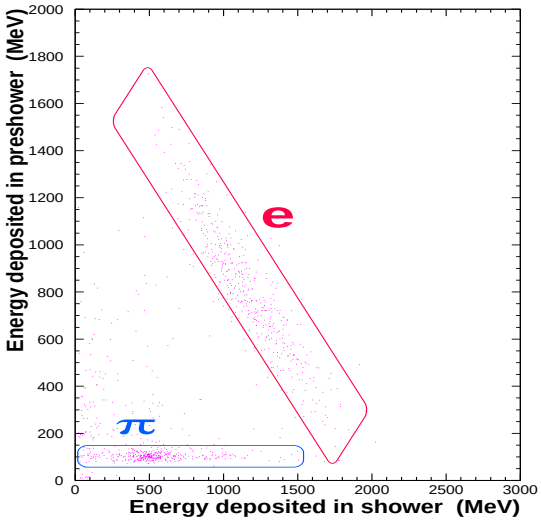

Fig. 3-12: Energy deposition in the preshower detector versus energy deposition in the shower detector for events from the special calibration run. Electrons and pions can be clearly separated.

and pions) from the special calibration run. For these ∼2000 MeV electrons, ∼800 MeV was deposited in the preshower and ∼1200 MeV was deposited in the shower. In the case of pions, most of them just pass straight through and loose energy only by ionization and direct Čerenkov light. On average they leave around ∼70 MeV in the preshower and ∼300 MeV in the shower. Pions can undergo nuclear interactions, too. In these cases, they deposit on average ∼600 MeV: ∼100 MeV in the preshower and ∼500 MeV in the shower (as seen Figure 3-12). It is clear from the above figures that the energy deposited by pions fluctuates a lot and can be very large.

The energy measured by the calorimeter divided by the particle momentum measured using the track determined from the VDCs is shown in Figure 3-13 for events from the special calibration run. For electrons this energy ratio should be one since electrons deposit all their energy in the calorimeter. Pions deposit mainly a small fraction of their energy and appear at an energy ratio of 0.3. The electrons can be also identified using the Čerenkov

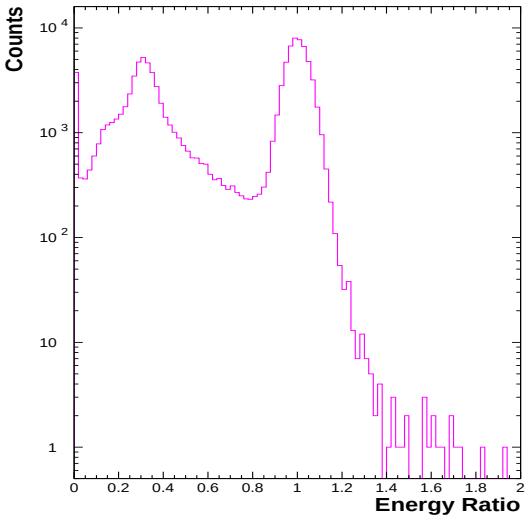

Fig. 3-13: Energy measured by the calorimeter divided by the particle momentum for events from the special calibration run. The peak at 0.3 is from pions while electrons give an energy ratio of one.

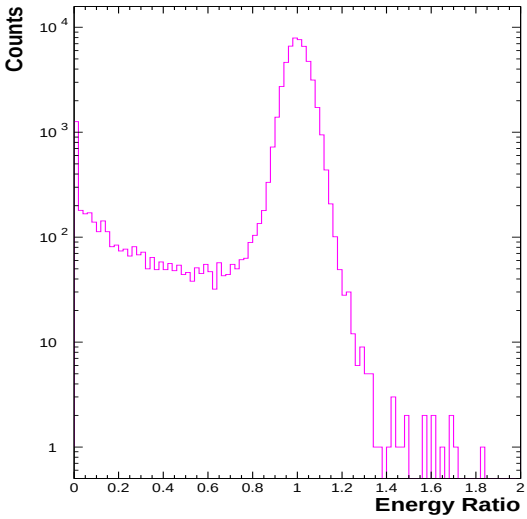

Fig. 3-14: Energy measured by the calorimeter divided by the particle momentum for events from the special calibration run. A cut on the Čerenkov detector was required to remove the pions (see text).

detector. Requiring the Čerenkov ADC sum to be greater than 500 channels, will remove the pions and only the electrons will be left as shown in Figure 3-14.

In Figure 3-15, the energy deposited in the preshower versus the energy deposited in the shower is shown for electrons which scattered elastically from protons with energy 337.6 MeV. These scattered electrons with 337.6 MeV have the lowest energy in the entire experiment. Here, most of the energy, ∼300 MeV, is deposited in the preshower and ∼40 MeV is deposited in the shower. The energy ratio for these electrons is shown in Figure 3-16. There was no pion contamination in the coincidence elastic data.

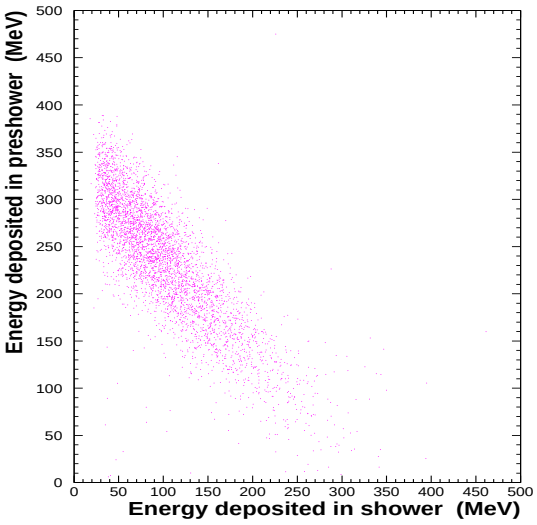

Fig. 3-15: Energy deposition in the preshower detector versus energy deposition in the shower detector from an *e-p* calibration run for $B(Q^2)$. The scattered electron energy was 337.6 MeV, the lowest in the entire experiment.

The centroids of the energy ratio for all $H(e,e')p$ runs are shown in Figure 3-17. The calorimeter can determine the energy of the electrons to ∼2% in the range of ∼300 MeV to ∼3000 MeV. Since a cut on the energy ratio is needed in the analysis of this experiment, the fluctuations seen in the centroid of the energy ratio indicate a small variation in the calorimeter efficiency correction (see Section 3.8.2). The energy resolution of the calorimeter

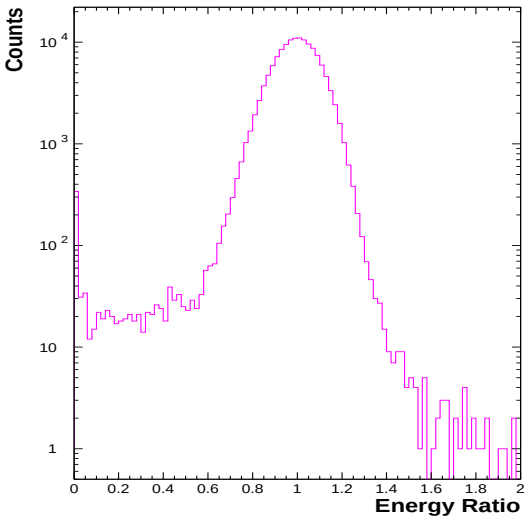

Fig. 3-16: Energy measured by the calorimeter divided by the particle momentum from an e-p calibration run for $B(Q^2)$. The scattered electron energy was 337.6 MeV, the lowest in the entire experiment.

is $\sigma = 2.9\% \oplus 5.4\%/\sqrt{E'}$, where E' is in GeV and $\oplus$ means that both contributions have to be added in quadrature. The first term is the systematic uncertainty that occurs because of noise, pedestal fluctuations, non-uniformities, and calibration uncertainties. The second term is due to statistical fluctuations in the electromagnetic shower development. The number of Čerenkov photons produced in the electromagnetic shower is proportional to the total charge track length which, in turn, is proportional to the initial particle energy. Thus, the total number of photoelectrons (pe) is $N_{pe} \sim E'$, and the statistical uncertainty is proportional to $1/\sqrt{N_{pe}}$ or to $1/\sqrt{E'}$. For a 1 GeV electron, the statistical uncertainty in the energy resolution of the calorimeter is 5.4% which corresponds to the production of ∼343 photoelectrons.

During the analysis, new calorimeter coefficients were calculated for each run. These sets of coefficients were used to check for energy dependence and time stability of the coefficients. The dependence of the coefficients on the scattered electron energy is shown in Figures 3-19

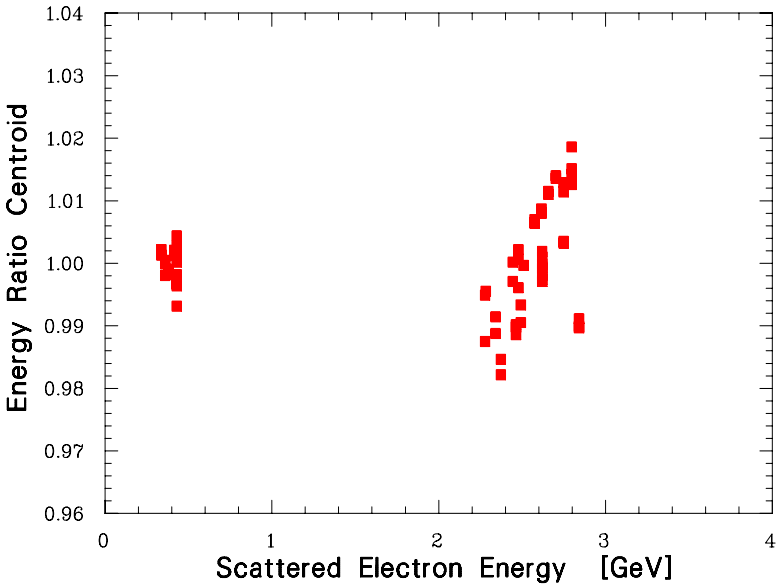

Fig. 3-17: The centroid of the Electron arm calorimeter energy ratio for all *e-p* calibration runs versus scattered electron energy.

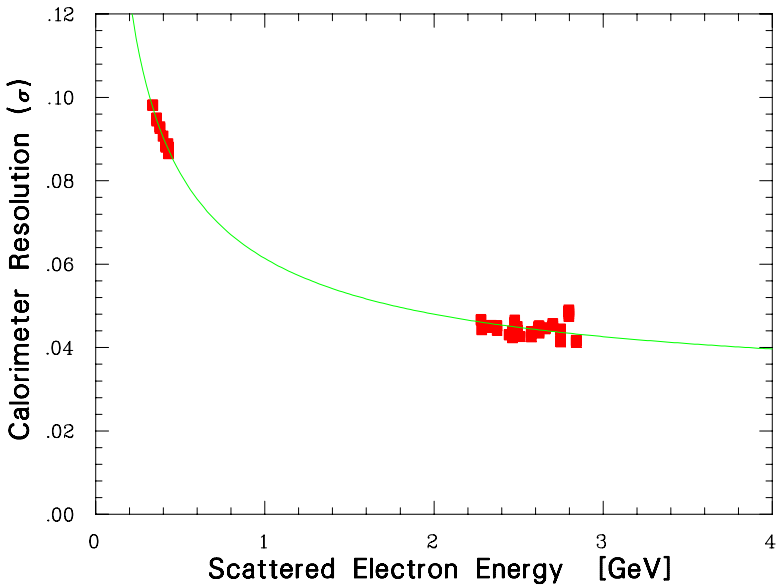

Fig. 3-18: Electron arm calorimeter resolution versus scattered electron energy. Data are from all *e-p* calibration runs. The best fit is $\sigma = 2.9\% \oplus 5.4\%/\sqrt{E'}$, where E' is in GeV.

and 3-20. The time dependence of the coefficients is shown in Figures 3-21 and 3-22 over the period of two months. The coefficients were quite stable throughout the experiment; therefore, only two sets of coefficients were used in the analysis. For $B(Q^2)$, we used the average of the coefficients obtained from the e-p backward runs while for $A(Q^2)$, we used the average of the coefficients obtained from the e-p forward runs. These two sets of coefficients are plotted in Figure 3-23 along with the set of coefficients which was obtained from the special run (run 1264). Only the coefficients of blocks which actually fired are shown. Most of the events were in the middle of the calorimeter and many blocks on the edge had no hits.

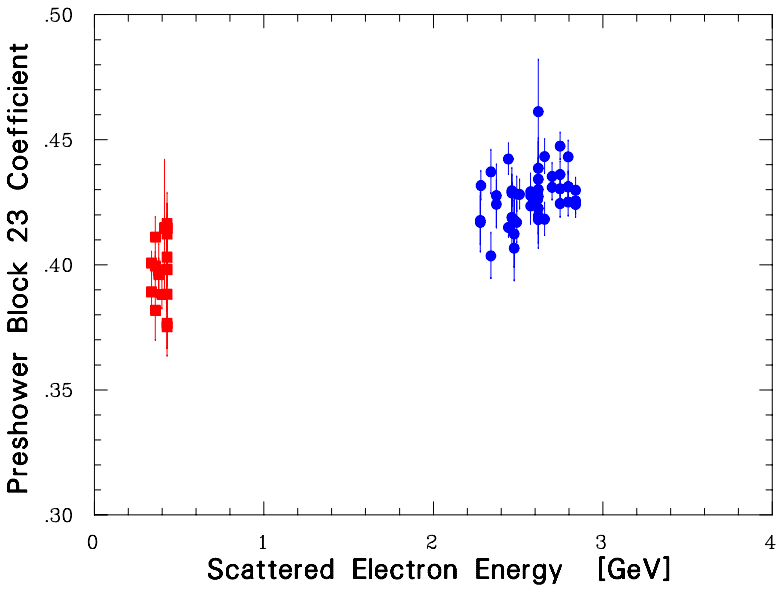

Fig. 3-19: Preshower block 23 coefficient versus scattered electron energy.

The reactions we studied during our experiment, $H(e,e')p$ and $D(e,e')d$, resulted in no pion contamination. The preshower and shower detectors were used mainly to identify electrons when the signal rate for the high-Q^2 e-d elastic scattering was as small as $\sim$1 event per day.

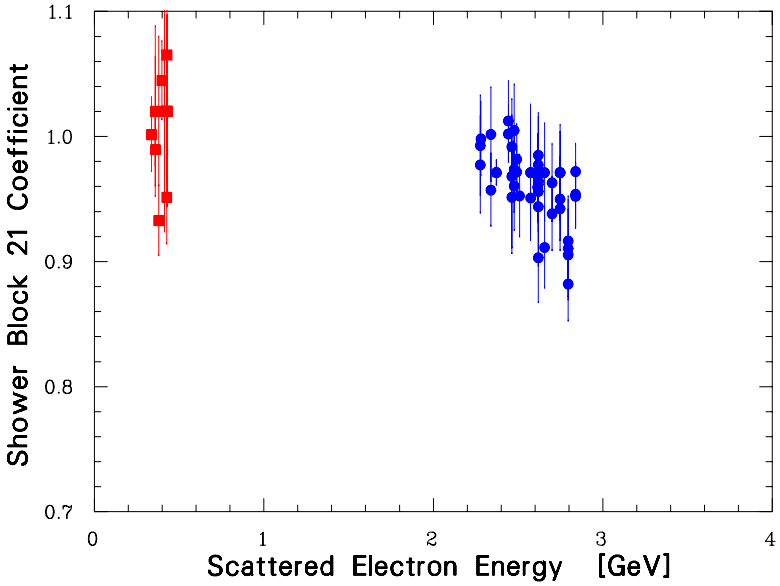

Fig. 3-20: Shower block 21 coefficient versus scattered electron energy.

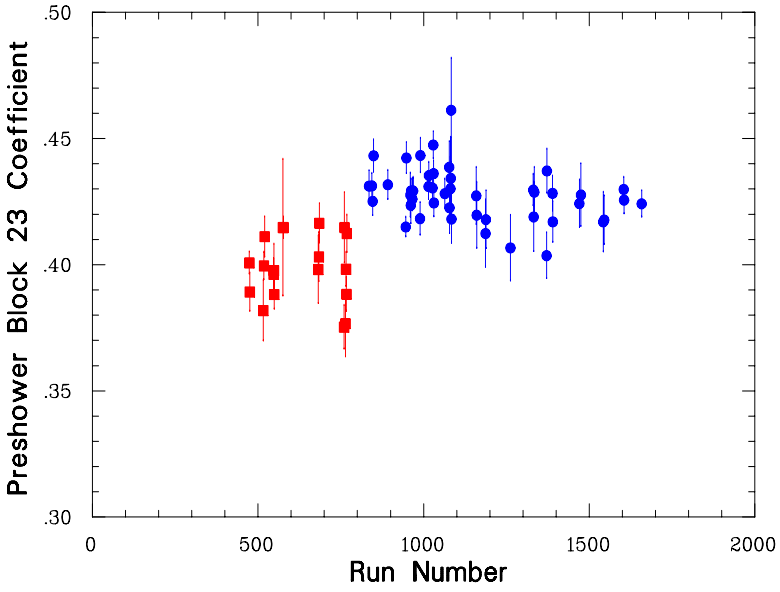

Fig. 3-21: Preshower block 23 coefficient versus run number (time).

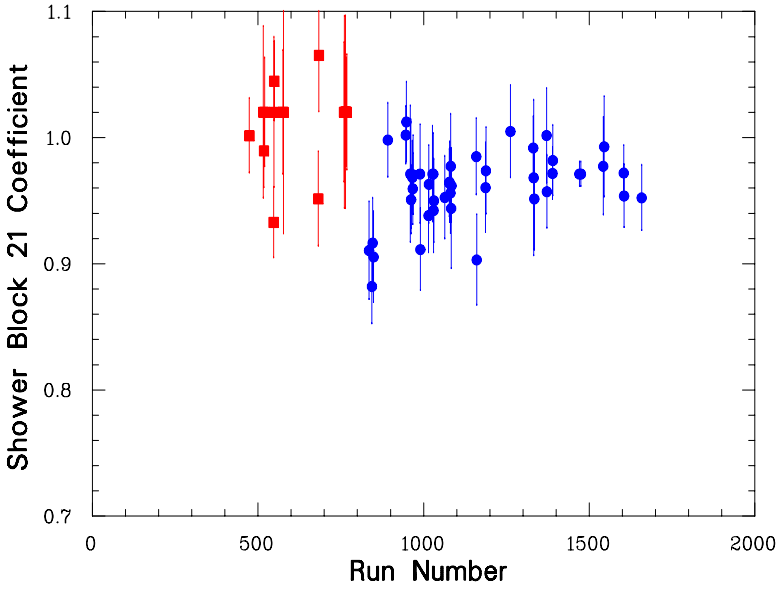

Fig. 3-22: Shower block 21 coefficient versus run number (time).

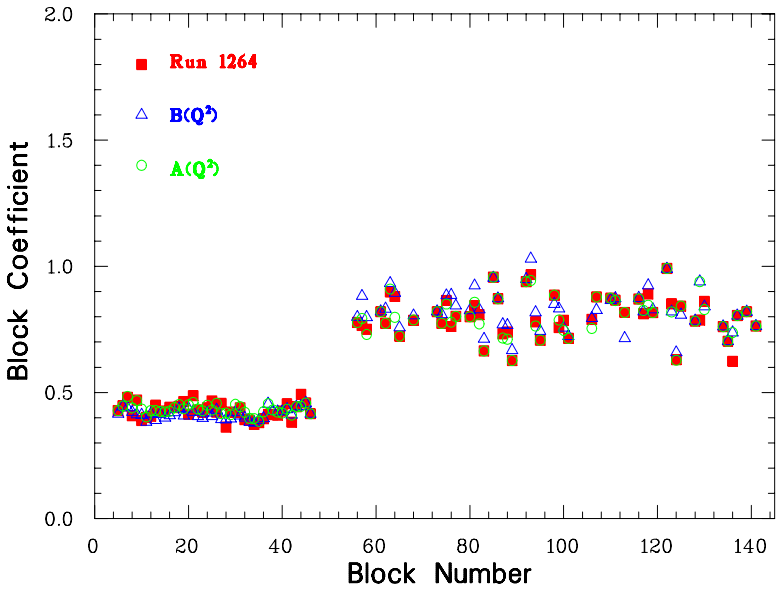

Fig. 3-23: The coefficients of preshower and shower blocks used in the analysis.

3.6 Coincidence Time-of-Flight

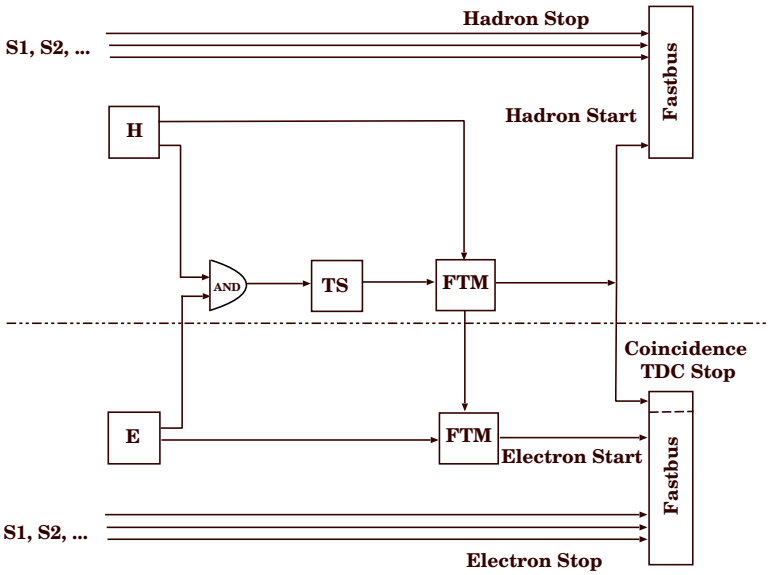

Fig. 3-24: A simplified schematic of the coincidence trigger setup.

The coincidence time-of-flight was used to identify *e-p* and *e-d* elastic events. The peak of the raw coincidence time-of-flight is very wide (∼20 ns). Corrections can be applied to reduce the width of the peak. The corrected coincidence time-of-flight has a higher true to accidental ratio which makes it easier to separate the real coincidence events from the random background.

The coincidence time-of-flight was measured using the TDCs of both arms. The Hadron arm TDC is a LeCroy 1877 model with common stop, 0.5 ns resolution, and allows up to 6 hits. Though not as accurate as the electron TDC, it has the advantage of handling random hits at very high rates. Since the Hadron arm TDC is a multihit TDC, the true hit is registered most of the time. Its start comes from the HRSE trigger and its stop from the HRSH trigger. The Electron arm TDC is a LeCroy 1875A model with common start and 0.1 ns resolution The electron coincidence time-of-flight TDC starts with the trigger of the HRSE and stops with the trigger of the HRSH, as shown in the simplified schematic

diagram of the coincidence trigger (Figure 3-24). The coincidence window was ~114 ns. The Electron arm measurement of the coincidence time-of-flight, ΔT_{COINC}, was used in the analysis because of the better time resolution than the Hadron arm measurement.

Corrections to the coincidence time-of-flight were done in the analysis software. These corrections are summarized in the following discussion. Actual TDC values are denoted by ΔT; these are the only quantities which are actually measured. The TC_{RAW} is then:

$$TC_{RAW} \equiv \Delta T_{COINC} = r_H - r_E \ , \tag{3-11}$$

where r_H is the stop of the coincidence TDC (this signal is the common start of the HRSH trigger) and r_E is the start of the coincidence TDC (this signal is the common start of the HRSE trigger, see Figure 3-24).

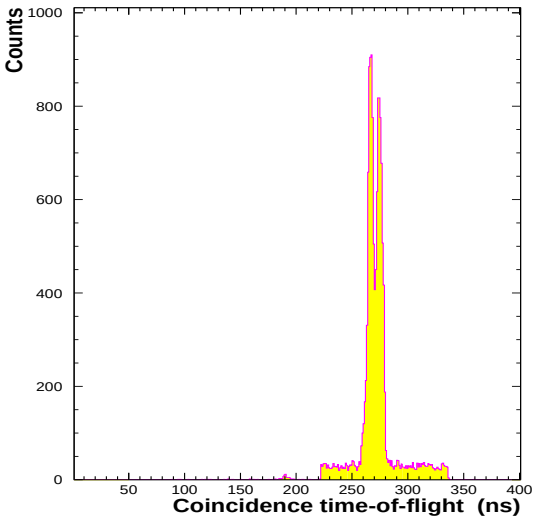

Fig. 3-25: Raw coincidence time-of-flight. The two peaks are caused by uncorrected offsets between the PMTs. The data are from an *e-d* check-out run taken with 100 μA at Q^2 = 0.685 (GeV/c)^2. The actual production data for this Q^2 were taken with 5 μA to reduce the accidental background.

The raw coincidence time, TC_{RAW}, shown in Figure 3-25, is very wide and there are

many corrections to be applied. Since the start signals, r_E and r_H, go through electronic modules, they have jitter. It is better to use the stop signals, s_E and s_H, since they just go through cables. Then:

$$\begin{aligned} TC_{COR} &= \Delta T_{COINC} - \Delta T(E) + \Delta T(H) \\ &= (r_H - r_E) - (s_E - r_E) + (s_H - r_H) \\ &= s_H - s_E \ . \end{aligned} \tag{3-12}$$

As in the case of β from time-of-flight, there are corrections to the individual PMTs timing. The mean time of both ends of the scintillator is used, which is the average of the times measured by the PMTs on each end. Use of the mean time eliminates the dependence on position along the scintillator, and removes the light propagation correction. The offsets, t_0, and the time walk, t_w, corrections are then applied. Figure 3-26 shows clearly the effect of neglecting the offsets on the coincidence time-of-flight (peak becomes very wide). Figure 3-27 shows the improvement when offset corrections are applied.

The corrected coincidence time-of-flight with all the corrections included is then:

$$\begin{aligned} TC_{COR} &= \Delta T_{COINC} \\ &- \frac{1}{2}\left[\Delta T(ES1L) + \Delta T(ES1R)\right] \\ &+ \frac{1}{2}\left[t_0(ES1L) + t_0(ES1R) + t_w(ES1L) + t_w(ES1R)\right] \\ &- t_{12}(E) + t_f(E) \\ &+ \frac{1}{2}\left[\Delta T(HS1L) + \Delta T(HS1R)\right] \\ &- \frac{1}{2}\left[t_0(HS1L) + t_0(HS1R) + t_w(HS1L) + t_w(HS1R)\right] \end{aligned}$$

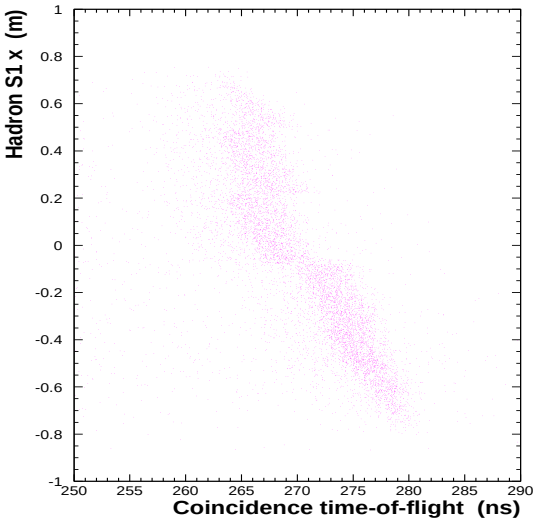

Fig. 3-26: The x coordinate along the Hadron arm scintillator plane S1 versus raw coincidence time-of-flight. The effect of different PMT offsets is evident. These offsets produce two peaks in the raw coincidence time-of-flight (see Figure 3-25).

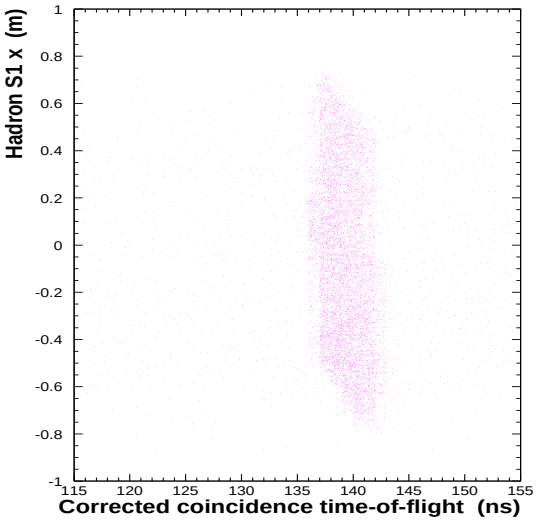

Fig. 3-27: The x coordinate along the Hadron arm scintillator plane S1 versus corrected coincidence time-of-flight. All corrections are included except the path difference correction.

$$+ \quad t_{12}(H) - t_f(H) \ , \tag{3-13}$$

where the TDC offsets, t_0, and the time walk, t_w, corrections are calculated by studying β from the time-of-flight between the two scintillator planes in each arm (see Section 3.5.2). t_{12} is the correction for the time-of-flight from scintillator plane S1 to S2, l_{12}/v, where l_{12} is the flight path between the two scintillators measured for each event using the VDC information. v is the speed of the particle in the spectrometer and it is $v = c$ for electrons and $v = P/E$ for hadrons, where P is the hadron momentum and $E = \sqrt{P^2 + M^2}$ is the hadron energy with M being the hadron mass.

The path length correction, t_f, accounts for the flight time through the spectrometer. The time it takes a particle to reach scintillator plane S1 from the target is:

$$t_f = \frac{L}{v} = \frac{L_o}{v} + \frac{\Delta L}{v} \ . \tag{3-14}$$

where L_o is the distance from the target to S1 and is equal to 24.807 m for the HRSE and to 24.713 m for the HRSH. The distance from the target to the first VDC for the central trajectory is 23.426 m for both arms. From the first VDC to S1 is 1.381 m for the HRSE and 1.287 m for the HRSH. The path difference, ΔL, accounts for the difference between the central ray through the spectrometer and a given ray. $\Delta L(E)$ for the electrons and $\Delta L(H)$ for the hadrons are calculated by parameterizing them in terms of the focal plane coordinates, x_{tra} and θ_{tra}:

$$\begin{aligned} \Delta L(E) &= m_1(E) \ . \ x_{tra(E)} + m_2(E) \ . \ \theta_{tra}(E) \ , \\ \Delta L(H) &= m_1(H) \ . \ x_{tra}(H) + m_2(H) \ . \ \theta_{tra}(H) \ . \end{aligned} \tag{3-15}$$

The path difference coefficients, m_1 and m_2, are calculated by minimizing the width of the corrected coincidence time. These coefficients are listed in Table 3-1 along with the predicted values from a SNAKE simulation [24]. The SNAKE fit is good to the 1 cm level.

	Electron Arm	Hadron Arm	SNAKE Simulation
L_0 (m)	24.807	24.713	24.726
m_1 (m)	1.2579	1.3104	2.0210
Maximum ΔL (m)	1.2579	1.3104	
Maximum Δt (ns)	4.1930	4.3680	
m_2 (m)	-6.7026	-8.3651	-14.6283
Maximum ΔL (m)	1.3405	1.6730	
Maximum Δt (ns)	4.4683	5.5767	

Table 3-1: Path difference correction coefficients.

Figure 3-28 shows the corrected coincidence time before adding the path difference correction plotted versus the electron θ_{tra}. The dependence is removed when correcting for path difference as seen in Figure 3-29. The final corrected coincidence time-of-flight is shown in Figure 3-30. The path difference correction reduces σ by a factor of 2. The resulting corrected coincidence time-of-flight has $\sigma \sim$ 0.5-0.7 ns for all the data.

A check-out deuteron run was taken at $Q^2 = 0.7$ (GeV/c)^2 during the forward running with 100 μA. In Figure 3-31, the corrected coincidence time is shown. Real deuteron and random proton peaks can be seen (the mass used to evaluate the path length correction in this case is the mass of the proton). As shown in the previous chapter, the CEBAF accelerator provided very narrow current pulses ($\sim$2 ps) roughly 2 ns apart, corresponding to a third of the nominal accelerator frequency of 1497 MHz (each hall received 499 MHz current frequency). The 2 ns, uniformly distributed ripples in the proton accidentals are due to the beam current microstructure.

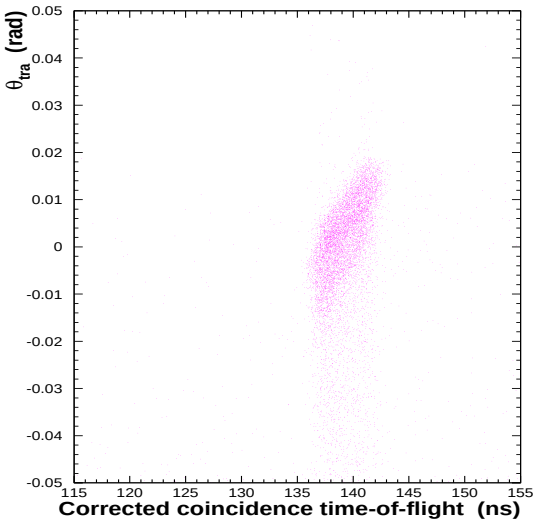

Fig. 3-28: The Electron arm θ_{tra} versus corrected coincidence time-of-flight. All the corrections are included except the path difference correction.

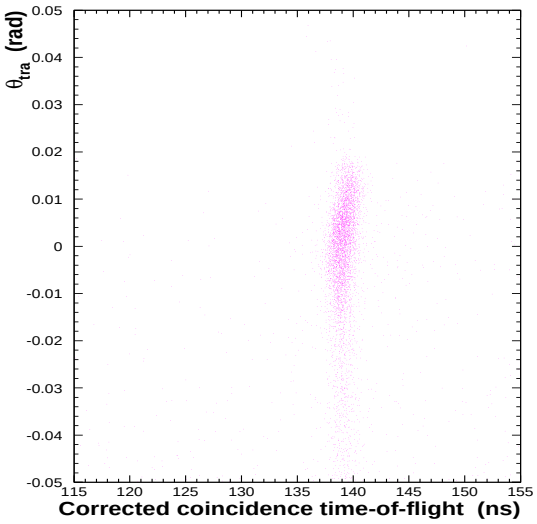

Fig. 3-29: The Electron arm θ_{tra} versus corrected coincidence time-of-flight. All the corrections are included here.

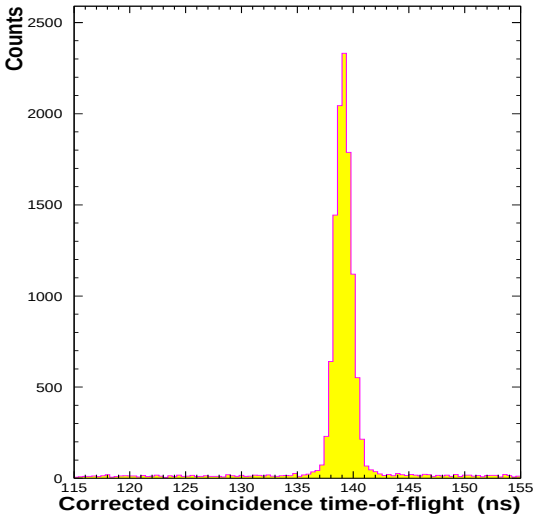

Fig. 3-30: The final corrected coincidence time-of-flight. The raw one is shown in Figure 3-25.

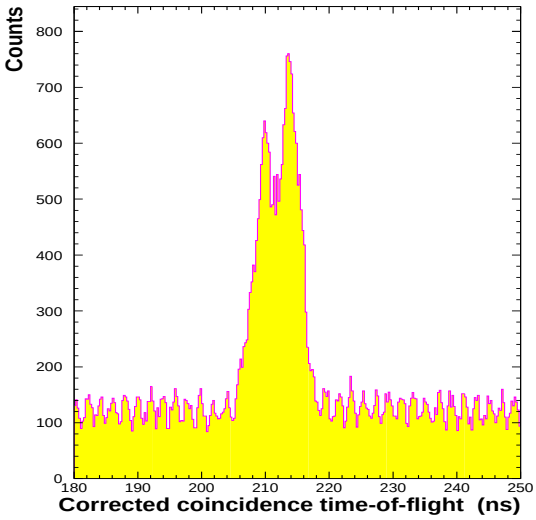

Fig. 3-31: Corrected coincidence time-of-flight. The mass used to evaluate the path length correction in this case is the mass of the proton. The 2 ns, uniformly distributed ripples in the proton accidentals are due to the beam current microstructure.

3.7 Particle Identification

The HRSE Čerenkov and calorimeter detectors were used to distinguish between electrons and negatively charged pions or other background. Deuterons from elastic electron-deuteron scattering events were separated from other particles in the hadron spectrometer by means of a time-of-flight cut. The time-of-flight allows for the discrimination between a real coincidence event and an accidental coincidence event. A real coincidence event involves two particles emerging from the target at the same instant, and thus a narrow peak is expected in the time-of-flight spectrum. An accidental coincidence event is caused by two uncorrelated single arm events which fall within the coincidence timing window, and therefore, it will contribute to the continuous flat background in the time-of-flight spectrum.

The low-Q^2 deuteron data contain a small amount of background in the corrected coincidence time-of-flight spectrum. These events are mainly protons and were removed by using β from the hadron time-of-flight between the two scintillator planes, as shown in Figure 3-8.

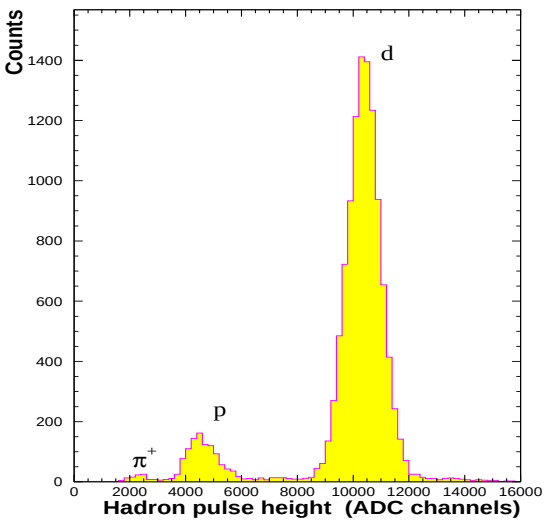

Fig. 3-32: Hadron arm scintillator pulse height. The Hadron arm momentum setting was 0.842 GeV/c. d, p, and π^+ particles are clearly separated.

Another way to distinguish protons from deuterons in the Hadron arm is to use the dependence of ionization energy loss in the scintillators on the particle β. Shown in Figure 3-32, is the pulse height (PH) in the Hadron arm scintillators defined as the sum of the signals, ph, from the left (L) and the right (R) PMTs of the two scintillator planes, S1 and S2:

$$PH = ph(HS1L) + ph(HS1R) + ph(HS2L) + ph(HS2R) \ , \tag{3-16}$$

where ph is calculated from

$$ph = (A - P) \times g \ . \tag{3-17}$$

Here, g is the gain matching factor, A is the ADC amplitude of the PMT, and P is pedestal of the corresponding channel.

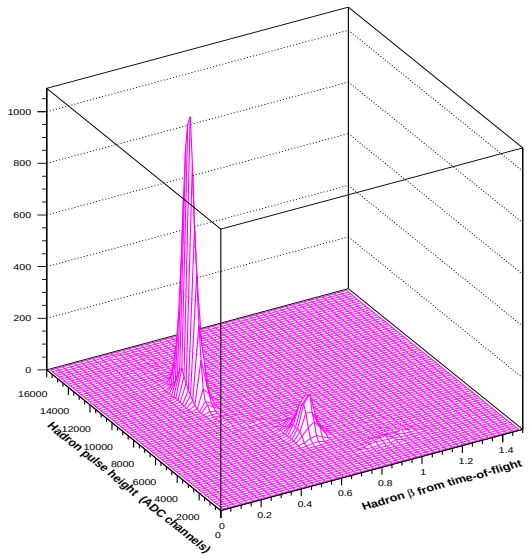

Fig. 3-33: Hadron arm scintillator pulse height versus Hadron arm β. The Hadron arm momentum setting was 0.842 GeV/c. d, p, and π^+ particles are clearly separated.

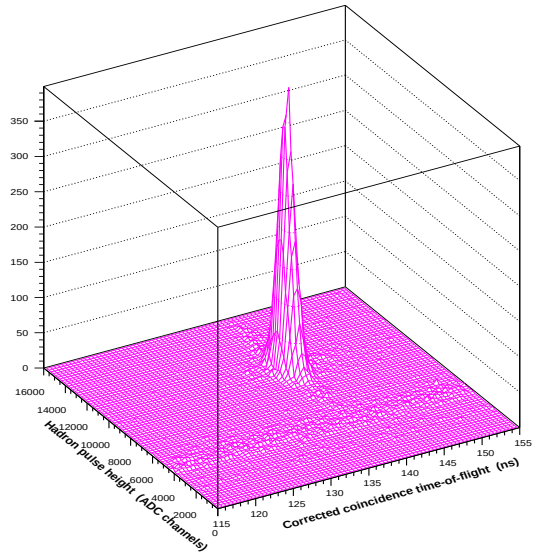

Fig. 3-34: Coincidence time-of-flight versus Hadron arm scintillator pulse height.

Figure 3-33 shows the Hadron arm β versus the pulse height. d, p, and π^+ particles are clearly separated. Figure 3-34 shows the corrected coincidence time-of-flight versus the pulse height in the Hadron arm scintillators.

3.8 Corrections to the Experimental Data

There are several effects that would reduce the extracted number of coincidence events and yield an artificially low cross section. The first is that of detector and trigger inefficiencies. Another effect that could decrease the number of coincidence events is re-scattering or absorption of the recoiling proton or deuteron on its way out of the cryotarget, through the scattering chamber exit window or in the windows of the spectrometer. A "boiling" correction is also applied to the data, since the density of the target varies as a function of the incident beam current. These corrections are discussed in detail in the sections that follow.

Class	Electron Arm		Hadron Arm	
	e-p Backward (%)	*e-p* Forward (%)	*e-p* Backward (%)	*e-p* Forward (%)
1 ($S1 = 0$ $S2 = 0$)	0	0	0	0
2 ($S1 = 0$ $S2 = 1$)	5	5	5	10
3 ($S1 = 1$ $S2 = 0$)	30	10	70	45
4 ($S1 = 0$ $S2 > 1$)	0	0	0	0
5 ($S1 > 1$ $S2 = 0$)	0	0	10	10
6 ($S1 = 1$ $S2 = 1$)	0	0	5	5
7 ($S1 = 1$ $S2 > 1$)	30	40	5	20
8 ($S1 > 1$ $S2 = 1$)	30	30	5	10
9 ($S1 > 1$ $S2 > 1$)	5	15	0	0

Table 3-2: Classification of the inefficient events in each arm.

3.8.1 Trigger Inefficiencies

Elastic *e-p* calibration data were used to study the trigger and scintillators inefficiencies. The trigger inefficiency of each arm is determined by taking the ratio of apparently good coincidence events that resulted in a trigger in only one arm to the events that gave a trigger in both arms. These events were primarily determined by looking for single arm events that passed a cut on the TC_{RAW} histogram. The data acquisition is setup such that all the Read Out Controllers are read for every type of trigger. So, for trigger 1, the Hadron arm detectors are also read. The same is true for all other trigger types. When a true *e-p* event produces a S1 trigger in the Electron arm but not a S3 trigger in the Hadron arm (see the discussion below explaining the different reasons for this), it will be registered in the CODA file as trigger type 1. Although the proton fails to produce S3, it can still give a correct signal in the TC_{RAW} histogram. The TC_{RAW} histogram was used to check for trigger inefficiencies instead of TC_{COR} because there may not be enough information to correct the raw coincidence time-of-flight.

There are several effects that cause true *e-p* events to fail to produce S1 trigger in the electron arm or S3 trigger in the hadron arm resulting in an inefficiency. Section 2.8

describes how these triggers are formed and under what conditions. The inefficient events in each arm are classified in Table 3-2. The events are classified according to the number of hits in the scintillator plane 1 and in the scintillator plane 2. 0 means that there was no hit in any of the scintillator paddles. Class 2 and class 4 are due to scintillator plane 1 inefficiency. Class 3 and class 5 are due to scintillator plane 2 inefficiency. In the hadron arm, this is mainly due to proton losses through nuclear interactions in scintillator plane 1 and only a small fraction of it is an actual inefficiency of the scintillator plane itself. Class 6 is due to large-angle VDC events. Class 7 and class 8 are due to multiple hits in the same plane which are far from each other. During the forward data taking, the MLU programming was changed in order to reduce the inefficiency due to class 7 and class 8. The effect of this change should be visible in the electron arm where the inefficiency from these two classes is large. However, no definite reduction in the trigger inefficiency was observed (see Figure 3-35).

The electron arm trigger inefficiency is plotted in Figure 3-35 versus run number, and in Figure 3-36 versus electron arm rate. The electron arm trigger was on average 1.5% inefficient for *e-p* calibration data for $B(Q^2)$ and 1.0% inefficient for *e-p* calibration data for $A(Q^2)$. The hadron arm trigger inefficiency is plotted in Figure 3-37 versus run number and in Figure 3-38 versus hadron arm rate. The hadron arm trigger inefficiency was on average 1.0% for *e-p* calibration data for $B(Q^2)$ and 1.8% for *e-p* calibration data for $A(Q^2)$.

The total trigger inefficiency is the sum of the electron arm and the hadron arm inefficiencies. A 2.5% total trigger inefficiency correction was applied to the *e-p* calibration data for $B(Q^2)$. Similarly, a 2.8% total trigger inefficiency correction was applied to the *e-p* calibration data for $A(Q^2)$. A systematic uncertainty of 0.5% was assigned to both corrections. The systematic uncertainty is taken to be the spread of the values of the trigger inefficiency. For the deuteron data, the electron arm inefficiency is taken to be the same as for the proton data. The hadron arm inefficiency classified as class 3 and class 5 should double for the

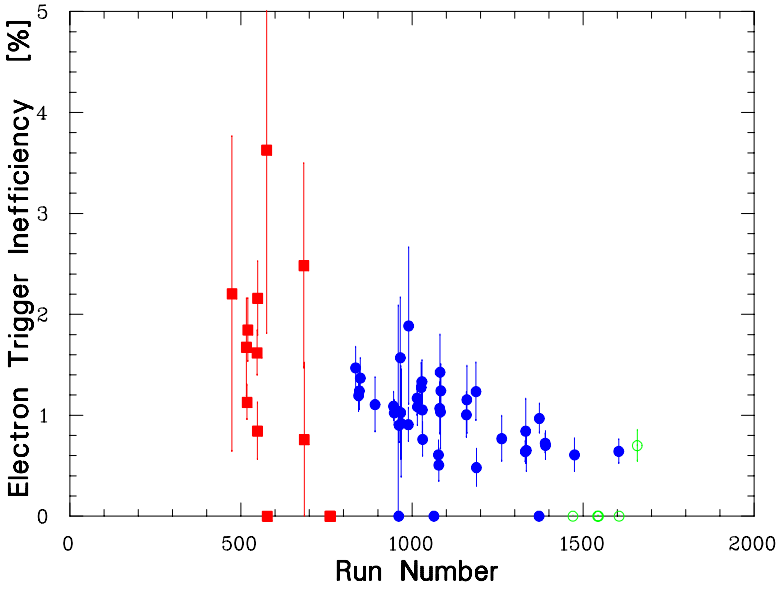

Fig. 3-35: Electron arm trigger inefficiency versus run number for *e-p* calibration data. The filled squares are the trigger inefficiency for the backward running. The filled circles are the trigger inefficiency for the forward running with the "old" MLU file. The hollow circles are the trigger inefficiency for the forward running with the "new" MLU file.

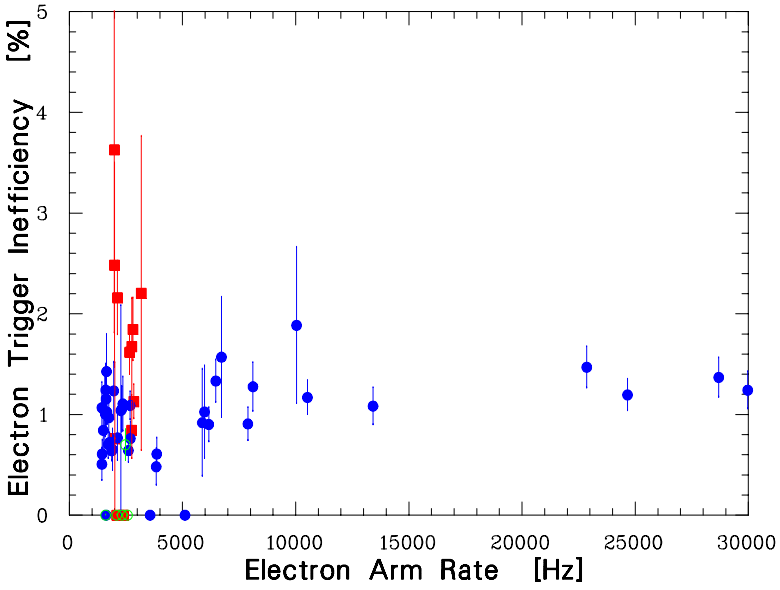

Fig. 3-36: Electron arm trigger inefficiency versus electron arm rate for *e-p* calibration data. Data points have the same meaning as those in Figure 3-35.

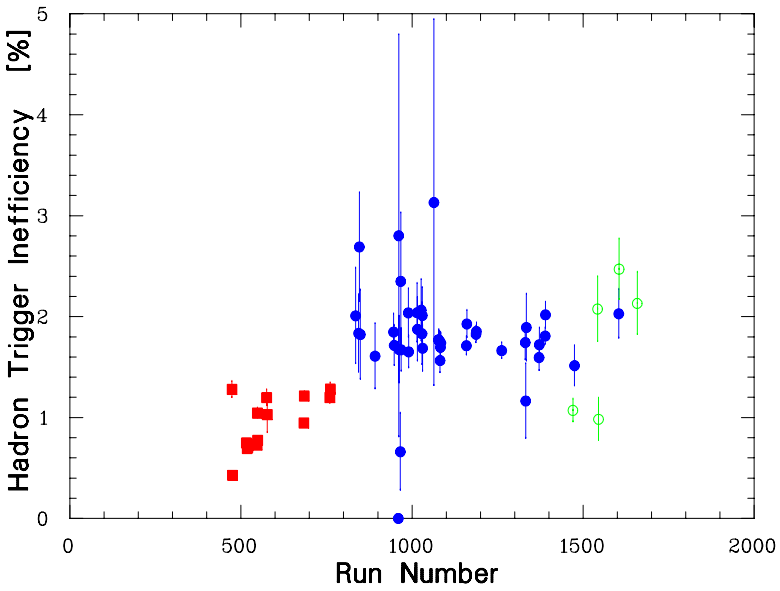

Fig. 3-37: Hadron arm trigger inefficiency versus run number for *e-p* calibration data. Data points have the same meaning as those in Figure 3-35.

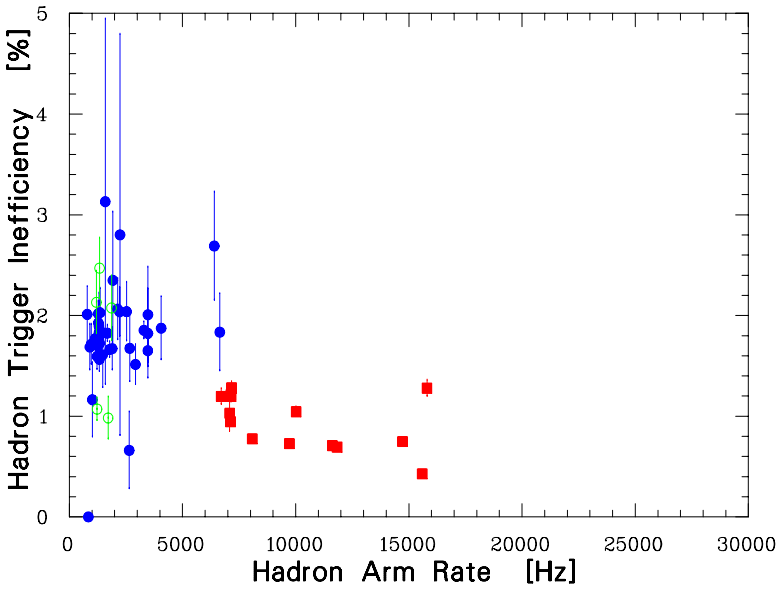

Fig. 3-38: Hadron arm trigger inefficiency versus hadron arm rate for *e-p* calibration data. Data points have the same meaning as those in Figure 3-35.

	Electron Arm Inefficiency %	Hadron Arm Inefficiency %	Total Inefficiency %
Proton			
Backward calibration data	1.5	1.0	2.5±0.5
Forward calibration data	1.0	1.8	2.8±0.5
Deuteron			
$B(Q^2)$	1.5	1.7	3.2±0.8
$A(Q^2)$	1.0	2.5	3.5±0.8

Table 3-3: Trigger inefficiency corrections (C_{rni}).

deuterons assuming it results from nuclear interaction losses. The hadron arm inefficiency for deuteron events was taken to be 70% higher than the proton for backward data and 40% higher for forward data. A 3.2% total trigger inefficiency correction was applied for $B(Q^2)$. Similarly, a 3.5% total trigger inefficiency correction was applied for $A(Q^2)$. A systematic uncertainty of 0.8% was assigned to both corrections. Table 3-3 summarizes the trigger inefficiency corrections (denoted as C_{trig}).

The above analysis shows that the fraction of protons which gave a signal in the scintillator plane S1 but did not fire the scintillator plane S2 is 0.7%. This is expected, since the fraction of nuclear interacting protons in scintillator plane S1 is given by $P_{int} = 1-e^{-0.5/80} \simeq 0.006$ (see Section 3.8.3). Here, 0.5 cm is the thickness of scintillator plane S1 and 80 cm is the nuclear collision length, λ, of protons in the plastic. This percentage should double for deuterons.

Several *e-p* calibration runs have had the coincidence trigger prescaled by a prescale factor greater than 1. This meant good events were prescaled and registered as event types 1 or 3. When calculating the trigger inefficiency, coincidence events that were prescaled produced a very large false trigger inefficiency and special care had to be taken in the

analysis to account for this. In the software, event types 1 and 3 were checked to see whether they had originated from prescaled coincidence events. If they did, these events were not included in calculating the trigger inefficiency.

The efficiency of each scintillator plane in each arm was determined by taking the ratio of the events that did not fire that plane to the events that fired the plane. The other plane in that arm was required to have only one hit. The other arm was required to have an event passing a cut on the TC_{RAW} histogram.

The scintillator inefficiencies are plotted in Figures 3-39, 3-40, 3-41, and 3-42 versus run number. The scintillators were, on average, $\lesssim$0.3% inefficient. The hadron arm scintillator S2 plane shows inefficiency of an order 1.0%. The extra 0.7% is due to proton loses in the S1 plane. For the deuterons this number is expected to double. The hadron arm scintillator S2 plane is expected to be 1.7% inefficient for deuterons. The hadron arm scintillator S2 plane inefficiency is plotted in Figure 3-43 versus the recoil proton momentum.

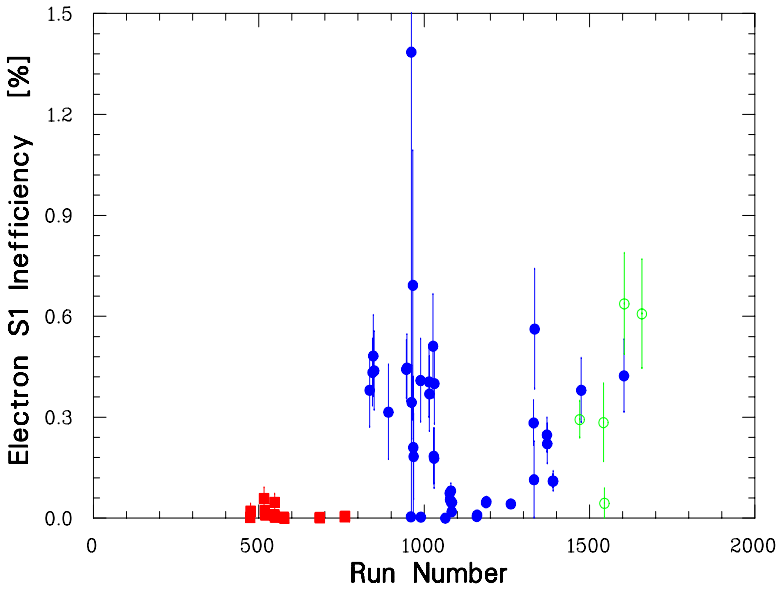

Fig. 3-39: Electron arm S1 inefficiency versus run number measured using *e-p* calibration data. Data points have the same meaning as those in Figure 3-35.

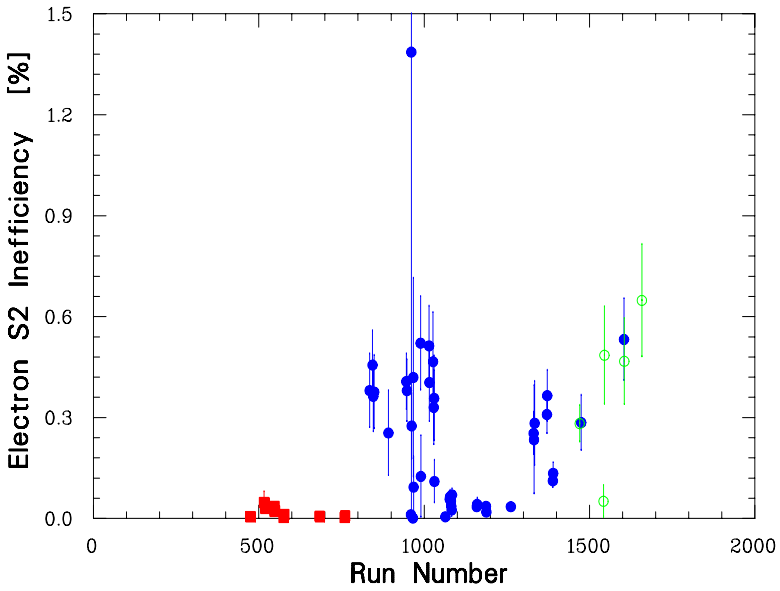

Fig. 3-40: Electron arm S2 inefficiency versus run number measured using *e-p* calibration data. Data points have the same meaning as those in Figure 3-35.

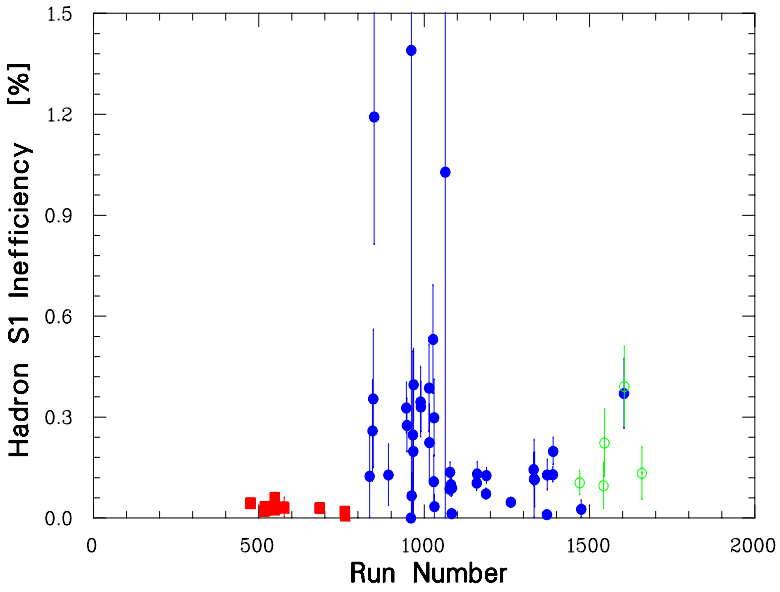

Fig. 3-41: Hadron arm S1 inefficiency versus run number measured using *e-p* calibration data. Data points have the same meaning as those in Figure 3-35.

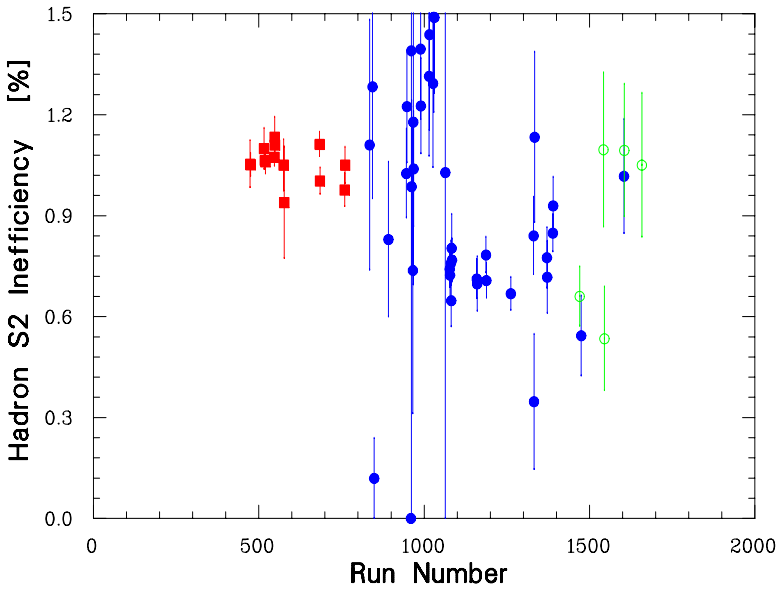

Fig. 3-42: Hadron arm S2 inefficiency versus run number measured using *e-p* calibration data. Data points have the same meaning as those in Figure 3-35.

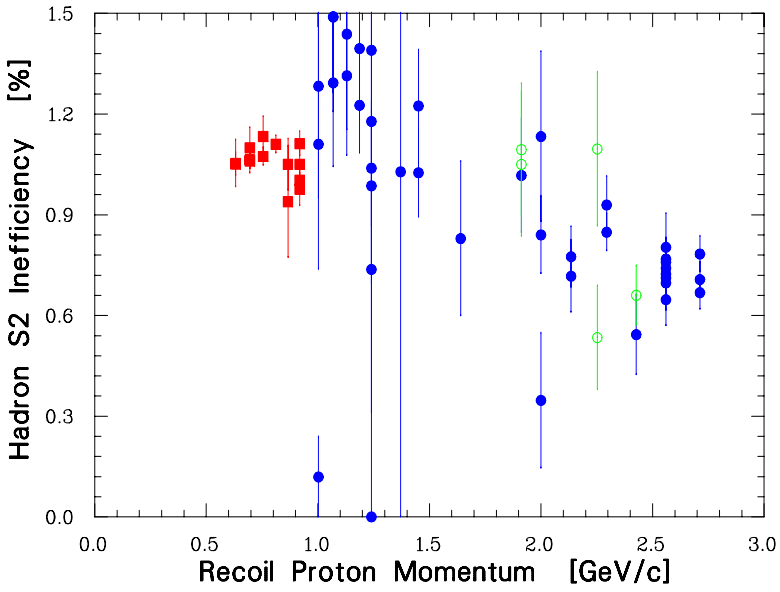

Fig. 3-43: Hadron arm S2 inefficiency versus recoil proton momentum measured using *e-p* calibration data. Data points have the same meaning as those in Figure 3-35.

3.8.2 Detector Inefficiencies

The tracking efficiency is defined as the number of events for which at least one track is found, divided by the number of good events (for which we expect to have a real track). These events are required to be coincidence events passing cuts imposed on the TC_{RAW} histogram and the Čerenkov and calorimeter detectors.

The tracking efficiency of the Electron arm VDCs is plotted versus the scattered electron energy in Figure 3-44. The tracking efficiency of the Hadron arm VDCs is plotted versus the recoil proton momentum in Figure 3-45. The VDCs were almost 100.0% efficient. No VDCs inefficiency correction was applied to the cross section.

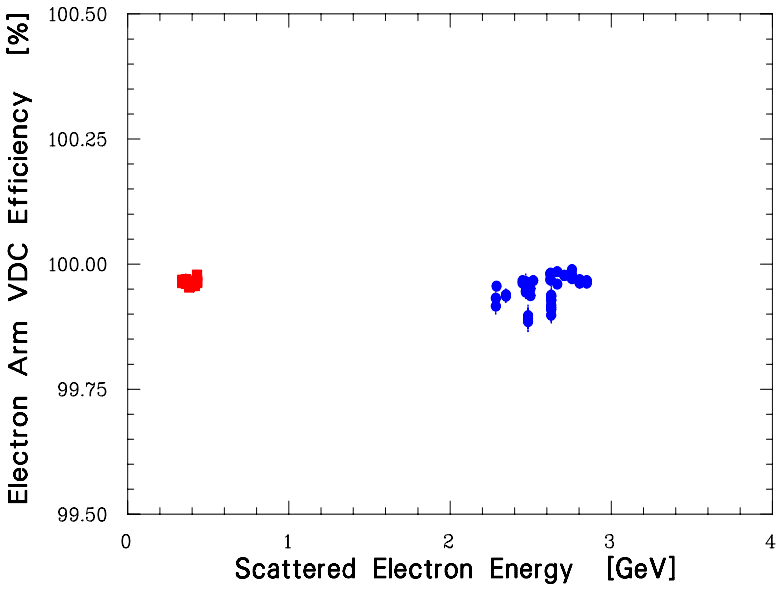

Fig. 3-44: Electron arm VDCs efficiency versus scattered electron energy.

About 2% of the events have misreconstructed angles, θ_{tra} and ϕ_{tra}, and position, x_{tra} and y_{tra}, in the VDCs (∼1% in each arm) (see Figure 3-46 and Figure 3-47). The misreconstructed events were examined, and it was found that about half of them had more than 15 hits in at least one of the VDC's four planes. For comparison, a typical "clean" event has on average ∼5 hits per plane. The large number of extra hits causes the VDC software

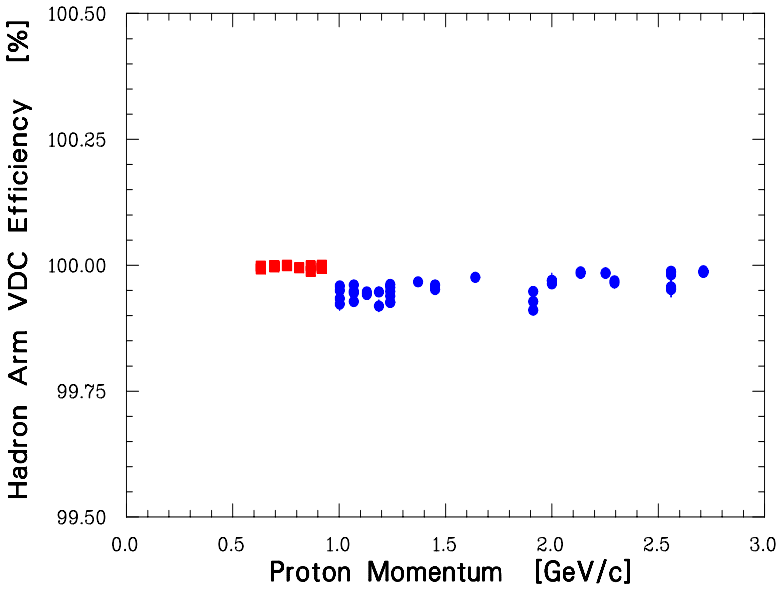

Fig. 3-45: Hadron arm VDCs efficiency versus recoil proton momentum.

to misreconstruct the events. These events are good events which pass coincidence and detector cuts and have only one track in each arm. Most likely the extra hits were produced by δ-ray electrons which were produced by electrons or recoil nuclei passing through the VDCs. Another source of extra hits is photons produced in the avalanche in the VDC gas which causes nearby avalanches in the same plane. For the analysis of this experiment, no cuts on reconstructed angle or position quantities at the focal plane or at the target are needed. Consequently, the only effect this misreconstruction will have is the widening of the corrected coincidence time-of-flight and the energy ratio.

The Čerenkov inefficiency is defined as the number of events for which the sum of the gas Čerenkov ADC signals is less than 500 channels or greater than 8000 channels, divided by the number of coincidence events passing cuts imposed on the TC_{COR} histogram and calorimeter detector. The upper cut (8000 channels) is needed because variables are initialized to a big number in the software.

The inefficiency of the gas Čerenkov in the electron arm is plotted versus the scattered

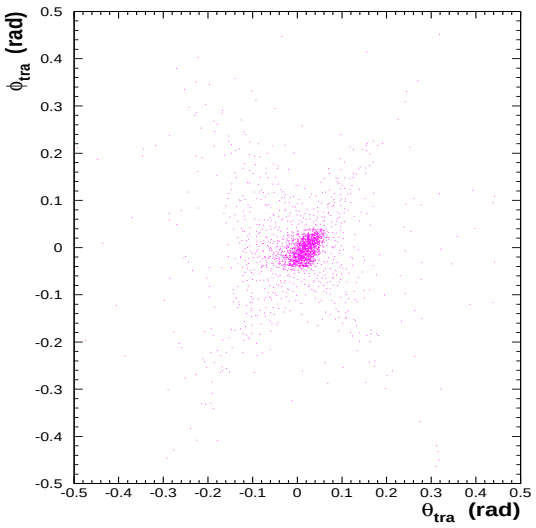

Fig. 3-46: Electron arm ϕ_{tra} versus θ_{tra}. The events outside the high density of points are caused by misreconstruction in the VDC caused by many wires firing in the VDCs.

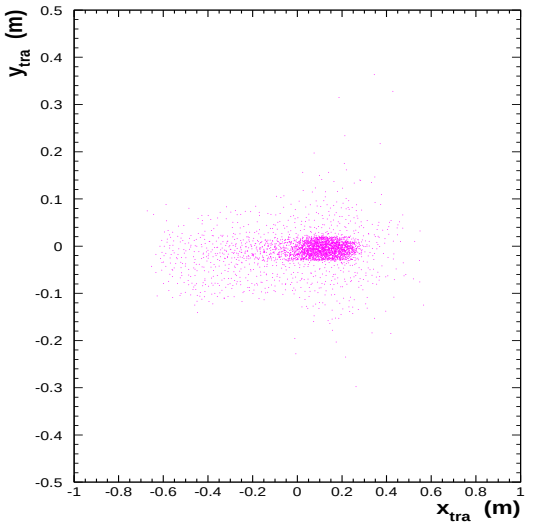

Fig. 3-47: Electron arm y_{tra} versus x_{tra}. The events outside the high density of points are caused by misreconstruction in the VDC caused by many wires firing in the VDCs.

electron energy in Figure 3-48. Most of the inefficient events gave a sum of ADC signals less than 500 channels. A 0.4% gas Čerenkov inefficiency correction was applied to the cross sections, and a systematic uncertainty of 0.1% was assigned to this correction.

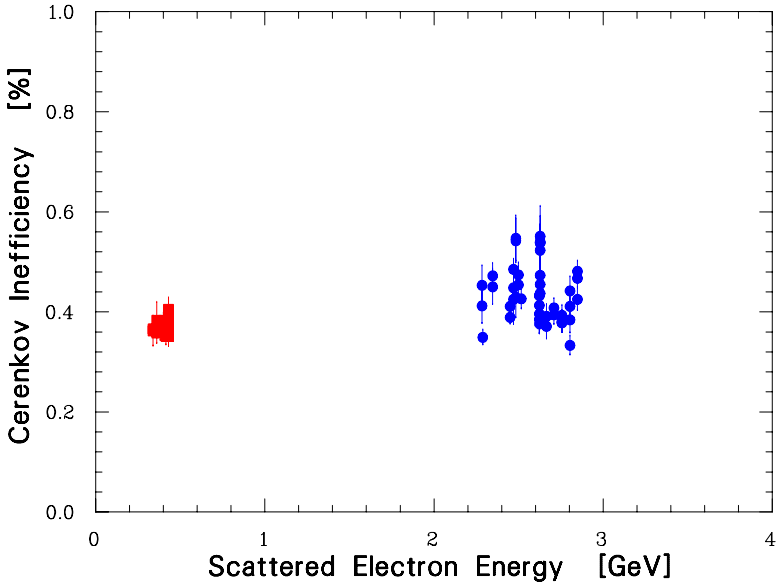

Fig. 3-48: Electron arm Čerenkov inefficiency versus scattered electron energy.

The calorimeter inefficiency is defined as the number of events for which the energy ratio is less than 0.50 for the backward running (0.65 for the forward running), divided by the number of coincidence events with cuts on the TC_{COR} histogram and the Čerenkov detector.

The inefficiency of the Electron arm calorimeter is plotted versus the scattered electron energy in Figure 3-49. A 0.6% calorimeter inefficiency correction was applied to the backward cross sections, and a systematic uncertainty of 0.2% was assigned to this correction. A 1.0% calorimeter inefficiency correction was applied to the forward cross sections, and a systematic uncertainty of 0.2% was assigned to this correction. Fluctuation in the inefficiency is due to the fluctuation in the position of the energy ratio peak. When the peak is at less than 1 the inefficiency is higher. Table 3-4 summarizes the detectors inefficiency

	Backward Runs Inefficiency %	Forward Runs Inefficiency %
VDCs	0.0	0.0
Gas Čerenkov	0.4±0.1	0.4±0.1
Calorimeter	0.6±0.2	1.0±0.2
Total	1.0±0.3	1.4±0.3

Table 3-4: Detector inefficiency corrections (C_{det}).

corrections (denoted as C_{det}).

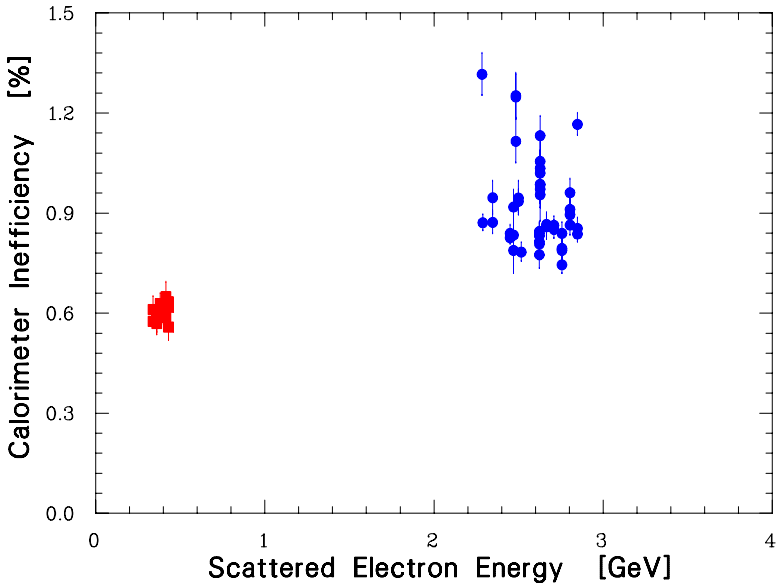

Fig. 3-49: Electron arm calorimeter inefficiency versus scattered electron energy.

3.8.3 Recoil Nuclear Interactions

A portion of the nuclei recoiling from elastic electron scattering interactions undergo further interaction along their way out of the target (both within the target fluid and within the aluminum walls of the target cell) or on their way through the scattering chamber and

spectrometer windows. These interactions can cause the recoil nuclei to be absorbed or to deviate from their original path and to fail to reach the recoil detectors. To account for these losses, a correction (denoted as C_{rni}) is applied to the measured cross sections. Note that this correction only takes into account recoil interactions in the target or spectrometer and scattering chamber windows. Recoil interactions within the scintillators are taken into account in the trigger inefficiency correction (Section 3.8.1). Recoil losses within the VDCs were very small ($\ll 0.1\%$). It was assumed, that once a proton or a deuteron interacted in any way in the target or windows, it was lost.

For hydrogen, the C_{rni} correction is a combination of two corrections: one that takes into account proton-proton interactions within the target fluid and one that takes into account proton-aluminum interactions within the target cell walls, the scattering chamber exit window and the spectrometer entrance window. The percentage of protons lost in each material was calculated using the nuclear collision length, λ, of nucleons in matter:

$$\lambda = \frac{A}{N_{av}\rho\sigma} \ , \tag{3-18}$$

where A and ρ are, respectively, the atomic mass and density of the material, N_{av} is Avogadro's number and σ is the cross section of the reaction in question. The proton-proton total cross sections, σ_{pp}, are from [36], while the proton-aluminum total cross section is approximated by:

$$\sigma_{pAl} = A_{Al}^{2/3}\ \sigma_{pp} \ , \tag{3-19}$$

where $A^{2/3}$ is the cross sectional area of the nucleus. The fraction of interacting particles is given by $P_{int} = 1 - e^{-x/\lambda}$, where x is the distance traveled by the proton in the material.

For deuterium, the C_{rni} correction takes into account deuteron-deuteron interactions within the target fluid and deuteron-aluminum interactions within the target cell walls, the

scattering chamber exit window and the spectrometer window. The correction is done as above for hydrogen, using the nuclear collision length. The deuteron-deuteron total cross section is approximated by $\sigma_{dd} \simeq 2(\sigma_{pp} + \sigma_{pn})$, while the deuteron-aluminum total cross section is approximated by:

$$\sigma_{dAl} = A_{Al}^{2/3} \, (\sigma_{pp} + \sigma_{pn}) \ , \tag{3-20}$$

where σ_{pp} and σ_{pn} are the proton-proton and neutron-proton total cross sections calculated at half the deuteron momentum.

Material	Thickness cm	C_{rni}
Target Fluid		
Hydrogen (Backward)	6.14-6.74	1.0065-1.0072
Hydrogen (Forward)	3.91-6.07	1.0046-1.0123
Deuterium (Backward)	7.23-7.32	1.0795-1.0511
Deuterium (Forward)	3.51-5.11	1.0241-1.0450
Aluminum		
Target cell sidewall (0.007 inch)		
Scattering chamber exit window (0.016 inch)		
Spectrometer entrance window (0.007 inch kapton)		
Total Al	0.075	
Hydrogen (Backward)	0.075	1.0010-1.0010
Hydrogen (Forward)	0.075	1.0011-1.0019
Deuterium (Backward)	0.075	1.0029-1.0042
Deuterium (Forward)	0.075	1.0023-1.0042

Table 3-5: Summary of the recoil nuclear interactions corrections. The thickness of the target fluid varies with the central angle of the HRSH. The 0.007 inch kapton at the HRS entrance is treated as aluminum because its effect is very small anyway. A systematic uncertainty of 25% of C_{rni} is assigned to this correction.

Table 3-5 summarizes the recoil nuclear interactions corrections for both hydrogen and

deuterium. A systematic uncertainty of 25% of the value of C_{rni} is assigned to this correction. The proton-proton and neutron-proton total cross sections, σ_{pp} and σ_{pn}, are calculated from a fit to the world data [36] shown in Figure 3-50. σ_{pp} and σ_{pn} are given by:

$$\begin{aligned}
\sigma_{pp} &= (6.3467 \times 10^2 - 4.4204 \times 10^3\ P_r + 1.2947 \times 10^4\ P_r^2 \\
&\quad -1.9559 \times 10^4\ P_r^3 + 1.6017 \times 10^4\ P_r^4 - 6.7262 \times 10^3\ P_r^5 \\
&\quad +1.1339 \times 10^3\ P_r^6) \quad \text{mb} \quad , P_r < 1.5 \quad \text{GeV/c} \quad ; \\
&= (52.56 - 2.64\ Pr) \quad \text{mb} \quad , P_r \geq 1.5 \quad \text{GeV/c} \quad , \qquad \text{(3-21)}
\end{aligned}$$

$$\begin{aligned}
\sigma_{pn} &= (2.9376 \times 10^2 - 7.2337 \times 10^2\ P_r + 2.4383 \times 10^2\ P_r^2 \\
&\quad +1.1494 \times 10^3\ P_r^3 - 1.6664 \times 10^3\ P_r^4 + 9.8066 \times 10^2\ P_r^5 \\
&\quad -2.7380 \times 10^2\ P_r^6 + 2.9913 \times 10^1\ P_r^7) \quad \text{mb} \quad , \qquad \text{(3-22)}
\end{aligned}$$

where P_r is the momentum of the recoil proton or half the momentum of the recoil deuteron.

3.8.4 Target Density Correction

With beam on, there is an additional current-dependent uncertainty in the target density due to local boiling. Several efforts were made to study the target density variation as a function of beam current [19]. For all of these tests, the beam spot size (raster size) was maintained at ± 1.7 mm by ± 1.4 mm (x and y dimensions, respectively). Figure 3-51 shows the results of the two boiling tests conducted on liquid hydrogen. Plotted is the analyzed yield (number of events, normalized to charge and corrected for dead time) versus the incident beam current. Both data sets have been normalized to their lowest current point. Both data sets agree within error bars (statistical) in the region of overlap. Hydrogen shows a significant boiling effect above $\sim$40 μA. This does not affect appreciably our $H(e, e'p)$

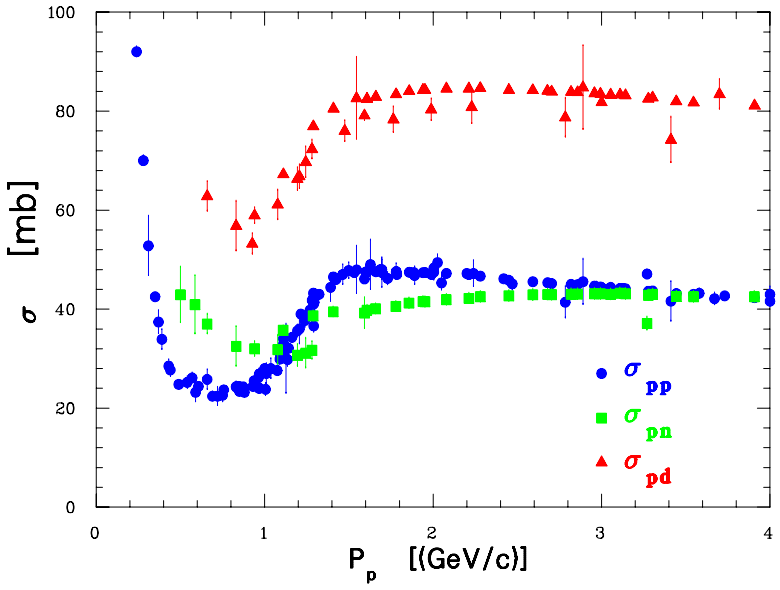

Fig. 3-50: Proton-proton, proton-neutron, and proton-deuteron total cross sections versus the proton momentum. The data are from Reference [36].

calibration data because they were all taken at a beam current of 10 μA, where boiling effects are very small. Figure 3-52 shows the results of the two boiling tests conducted on liquid deuterium. The results of the deuterium boiling studies at high current are of importance because the majority of the data for the structure function measurements were taken at beam currents greater than 50 μA. Based on these boiling studies, a current-dependent density correction was applied for both hydrogen and deuterium data runs.

The target density change as a function of beam current was studied for both hydrogen and deuterium by monitoring the event rate as a function of current, from 10–120 μA. Hydrogen (deuterium) was found to exhibit a 5.0% (2.5%) density decrease at an incident beam current of 120 μA compared to its density at 10 μA. The density decrease was linear as a function of current. In the cross section calculations, a corrected density was used in place of the nominal target liquid density, ρ_0, parameterized as:

$$\rho_p = \rho_{0p}(1 - 0.00042 \times I_{ave}) \ , \tag{3-23}$$

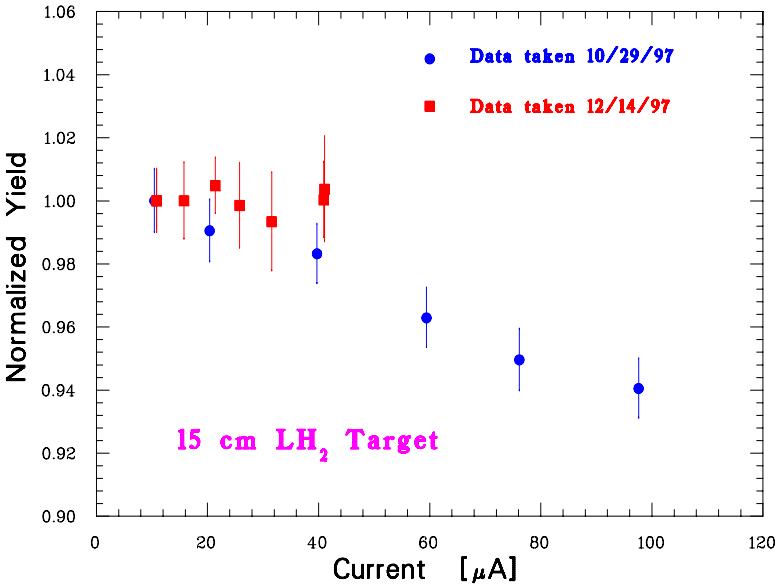

Fig. 3-51: Normalized yield versus current for the 15 cm LH_2 target. Shown are data taken on 10/29/97 and 12/14/97.

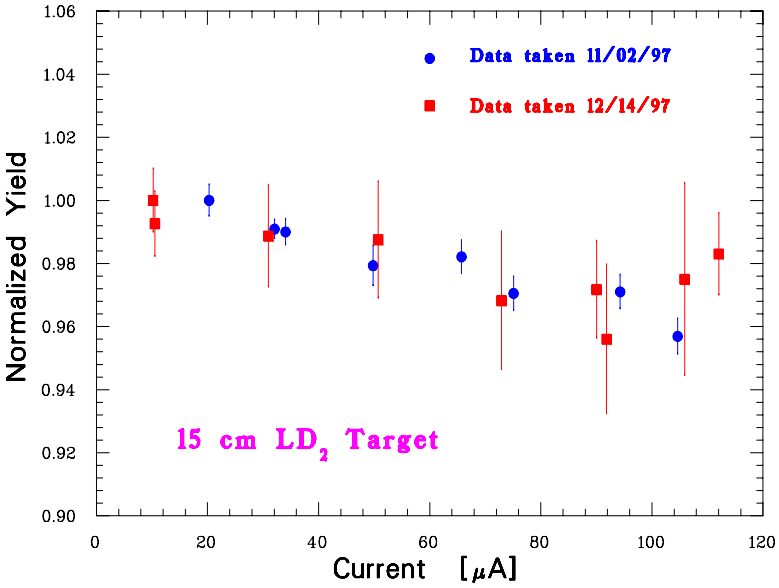

Fig. 3-52: Normalized yield versus current for the 15 cm LD_2 target. Shown are data taken on 11/02/97 and 12/14/97.

for hydrogen, and:

$$\rho_d = \rho_{0d}(1 - 0.00021 \times I_{ave}) \ , \tag{3-24}$$

for deuterium, where I_{ave} is the average beam current in μA.

An overall 1.0% total systematic uncertainty was assigned to the effective target length due to uncertainties in target density resulting from uncertainties in equations of state, localized boiling, amounts of para H_2, target gas purity, and uncertainties in the target length due to uncertainties in thermal contraction and the position of the beam on the target (the target entrance and exit windows are concave).

3.9 Monte Carlo Simulation

To extract the deuteron elastic structure functions, we measured elastic electron-deuteron cross sections. To check our normalization, we also measured elastic electron-proton cross sections. The cross sections were measured by detecting the recoil nucleus (deuteron or proton) in coincidence with the electron. In a cross section determination, two quantities among others need special attention: the solid angle and radiative corrections. In a coincidence experiment, these two quantities are convoluted together. The solid angle depends on the individual acceptance of each spectrometer and on the particular kinematics of the measurement. The standard way to determine the convolution of these two quantities is using Monte Carlo techniques.

A Monte Carlo program [37] was used to model the double-arm solid angle and the focal plane event distributions for each of the elastic e-p and e-d kinematics of the experiment. The sequence of operations begins with the generation of an elastic electron-nucleus scattering event in the target. The z position of the event is generated using random numbers uniformly distributed over the target length L. The x and y coordinates of the interaction vertex are generated taking into account the dimensions of the beam rastering. The electron

scattering angles, θ and ϕ, are generated using random numbers uniformly distributed between predefined θ and ϕ limits, which are chosen to be larger than the angular acceptance of the electron spectrometer. The incident electron's energy is modeled using a Gaussian distribution of random numbers around the central energy of the beam, with an energy spread of 10^{-4}. The value of E is corrected for ionization energy loss and radiation loss for passage through a length z of target material. To end the event generation sequence, the scattered electron energy, the recoil particle momentum, and the recoil angles are calculated from elastic kinematics. All angles are corrected for multiple scattering in the target material.

The Monte Carlo simulation contains a realistic model of the two Hall A magnetic spectrometers. The particles can be transported through the spectrometers to the detectors in two ways. The first is by tracing each particle (ray) through a model of the spectrometer system. The second is by using TRANSPORT [21] matrix elements directly. TRANSPORT matrix elements are obtained by first ray-tracing a group of particles through the spectrometer. Then the matrix elements are obtained by a least squares fit to the initial and final coordinates of the particles. The matrix method uses less computer time than the ray-tracing method, but it requires an extensive study of the apertures of the system before it can be used.

For the ray-tracing method, information about each spectrometer element needs to be supplied. An element can be a magnetic element, such as a quadrupole or dipole, a drift length or an aperture. The information supplied for each magnet is its magnetic field and effective length. For the drifts, the drift distances are supplied, and for the apertures, their dimensions. Particles were traced through the three quadrupoles of the HRSE and HRSH using the ray-tracing method. Particles were stepped through the quadrupoles in 40 steps. At the end of each step, the coordinates of the particles with respect to the central ray were calculated using the Lorentz force equation. For the HRSE and HRSH dipoles, a

combination of the ray-tracing and the TRANSPORT matrix method was used to trace the particles. Particles were ray-traced through the magnetic field of the dipole in ten steps, using matrix elements to transfer the particles from one step to another. At the end of each step in every routine, particles were checked to see if they hit any apertures, which were assumed to be perfectly absorbing. This allowed for a clear picture of the acceptance-defining apertures, like the magnet pole faces or parts of the vacuum system, inside the spectrometers. Electron and recoil distributions were plotted for events which successfully made it to the detectors. Figure 3-53 shows a comparison between data and Monte Carlo predictions for the HRSE focal plane distributions. Figure 3-54 shows a comparison between data and Monte Carlo predictions for the HRSH focal plane distributions. The data are from a $H(e,e'p)$ calibration run for e-d at $Q^2 = 5.90$ (GeV/c)^2, using the 15 cm hydrogen target, with an incident electron beam energy of 4.397 GeV. Both the electron and hadron distributions are described very well by the Monte Carlo, giving us confidence that the spectrometer and its apertures are well modeled.

3.9.0.1 Solid Angle

In this experiment, the scattered electron and recoil nucleus are detected in coincidence, so the double-arm solid angle is a convolution of the acceptances of the two spectrometers coupled together by elastic kinematics and radiative effects. This double-arm solid angle is used in the cross section determination ($\Delta\Omega_{MC}$ in Equation 3-32) and is determined from the Monte Carlo simulation used to model this experiment. It includes the effective elastic solid angle as well as the energy dependent portions of the radiative corrections. It is averaged over the target length L, the incident electron energy E and the phase space of the incident beam. The computation of $\Delta\Omega_{MC}$ is described in detail in Reference [37] and summarized below.

For a given incident beam energy E and scattering angle θ, the double-arm solid angle

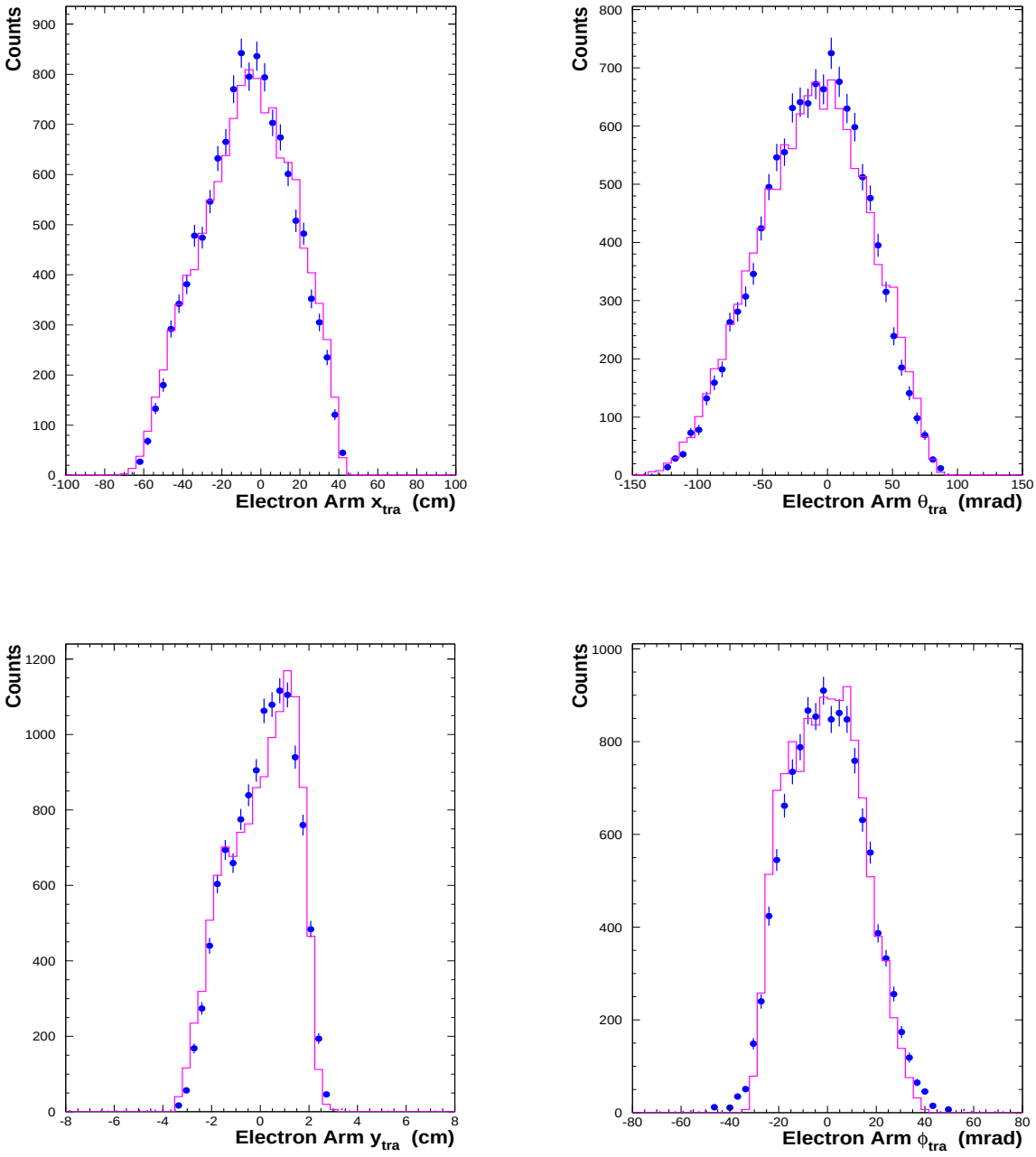

Fig. 3-53: Data versus Monte Carlo comparison. The solid line is the Monte Carlo prediction and the circles are HRSE data from a $H(e,e'p)$ calibration run for e-d at $Q^2 = 5.90$ (GeV/c)^2, using the 15 cm hydrogen target, with an incident electron beam energy of 4.397 GeV.

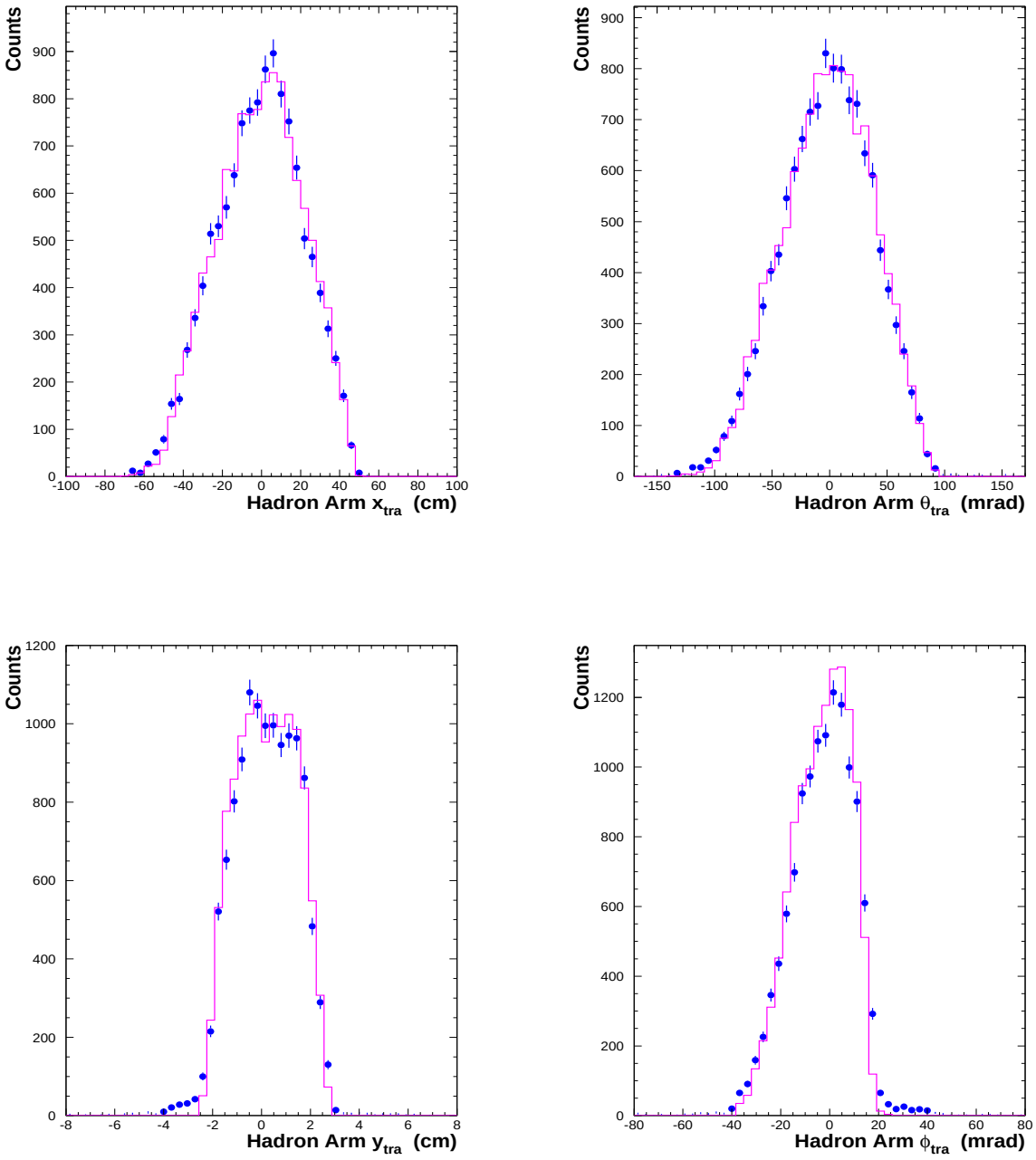

Fig. 3-54: Data versus Monte Carlo comparison. The solid line is the Monte Carlo prediction and the circles are HRSH data from a $H(e,e'p)$ calibration run for e-d at $Q^2 = 5.90$ (GeV/c)^2, using the 15 cm hydrogen target, with an incident electron beam energy of 4.397 GeV.

is given by the two dimensional integral:

$$\Delta\Omega_{MC} = \int\int C_{MC}\ \ g(E,\theta)\ \ f_{RC}(\Delta E', \Delta P_r)\ d\theta d\phi\ , \tag{3-25}$$

where $f_{RC}(\Delta E', \Delta P_r)$ represents the portion of the radiative corrections that depend upon the momentum acceptances $\Delta E'$ and ΔP_r of the electron and recoil spectrometers respectively. The integral is weighted by:

$$g(E,\theta) = \frac{\sigma(E,\theta)}{\sigma(E_0,\theta_0)}\ , \tag{3-26}$$

where $g(E,\theta)$ represents the shape of the unradiated elastic cross section $\sigma(E,\theta)$ normalized to unity at the central beam energy E_0 and central spectrometer angle θ_0. C_{MC} represents the corrections due to ionization loss and multiple scattering [37]. The two dimensional integral of Equation (3-25) is performed using standard Monte Carlo techniques: for N_T trial points randomly and uniformly distributed over the target length, between $\theta_1 \leq \theta \leq \theta_2$ and $\phi_1 \leq \phi \leq \phi_2$, the integral is approximated by:

$$\int_{\theta_1}^{\theta_2}\int_{\phi_1}^{\phi_2} f(\theta,\phi)d\theta d\phi \simeq (\theta_2-\theta_1)(\phi_2-\phi_1)\frac{1}{N_T}\sum_{i=1}^{N_T} f(\theta_i,\phi_i)\ , \tag{3-27}$$

where $f(\theta,\phi) \equiv C_{MC}\ g(E,\theta)\ f_{RC}(\Delta E', \Delta P_r)$.

In the Monte Carlo loop, the energy loss due to ionization, multiple scattering and electron radiation loss are applied to each trial event. In the case of a good event, where both the scattered electron and recoiling nucleus pass all the way through the modeled spectrometers to the detectors, $f(\theta,\phi) = g(E,\theta)$, otherwise $f(\theta,\phi) = 0$. A systematic uncertainty of 3.0% was assigned to the simulated double-arm solid angle.

3.10 Radiative Corrections

Radiation effects necessitate important corrections in the analysis of electron scattering experiments. Radiative processes may be grouped into two categories: internal radiation

and external radiation. Internal radiation occurs when the electron radiates real and virtual photons in the presence of the target nucleus involved in the elastic reaction (referred to as internal bremsstrahlung and vertex corrections, respectively). In external radiation, the electron radiates real and virtual photons in the presence of the Coulomb fields of nuclei other than the target nucleus (external bremsstrahlung).

The radiative corrections for this experiment are calculated within the Monte Carlo (Section 3.9) using the formalism of Reference [38]. The radiative corrections are accounted for by two factors. The first, $\Delta\Omega_{MC}$, was discussed in Section 3.9. The second, $F(Q^2,T)$ accounts for the change in the interaction vertex due to radiative effects. It is given by:

$$\begin{aligned} F(Q^2,T) = 1 + 0.5772\, b\, T \quad &+ \quad \frac{2\alpha}{\pi}\left[\frac{-14}{9} + \frac{13}{12}\ln\frac{Q^2}{m_e^2}\right] \\ &- \quad \frac{\alpha}{2\pi}\ln\frac{E}{E'} \\ &+ \quad \frac{\alpha}{\pi}\left[\frac{1}{6}\pi^2 - \Phi(\cos^2\frac{\theta}{2})\right] \ , \end{aligned} \tag{3-28}$$

where Φ is the Spence function defined as:

$$\Phi(x) = \int_0^x \frac{-ln\,|1-y|}{y} dy \ , \tag{3-29}$$

and T is the total path length (in radiation lengths) that the electron traverses in the target before and after scattering. The factor b is given by:

$$b = \frac{4}{3}\left[1 + \frac{1}{9}\left[\frac{Z+1}{Z+\xi}\right](\ln 183 Z^{-1/3})^{-1}\right] \ , \tag{3-30}$$

where Z is the atomic number of the target material and ξ is given by:

$$\xi = \frac{\ln 1440 Z^{-2/3}}{\ln 183 Z^{-1/3}} \ . \tag{3-31}$$

The $F(Q^2, T)$ values used in the cross section calculations (see Equation 3-32) are given in Appendix C. A systematic uncertainty of 1.5% was assigned to the radiative corrections.

3.11 Empty-Cell Subtraction

To estimate the contribution of the entrance and exit windows of the target cell to the measured cross sections, data were taken using the aluminum dummy targets. The *e-p* calibration data for $B(Q^2)$ were taken at an electron scattering angle of 90.0° using the 15 cm hydrogen cell. Under these conditions the target windows were outside the electron arm acceptance (y_{tgt} acceptance is ±5 cm), so no contribution was expected. To check this, a run was taken using the 15 cm dummy and no coincidence events were detected. The *e-d* production data for $B(Q^2)$ were taken using the 15 cm deuterium target with the attached collimator that covers the entrance and exit windows of the target cell, so there was no contribution from the windows.

The *e-p* calibration data for $A(Q^2)$ were taken at forward electron scattering angles using the 15 cm hydrogen cell. Dummy target data were taken at each kinematical point with 25 μA beam current and the contribution was measured to be always <0.06%. Dummy target data were also taken at each *e-d* $A(Q^2)$ kinematical point with 25 μA beam current. No coincidence events were ever detected.

3.12 Electron-Proton Elastic Cross Section Calibration

For each $A(Q^2)$ and $B(Q^2)$ kinematical point, a coincidence *e-p* elastic cross section measurement was also made. The *e-p* measurements calibrated our method of cross section determination, by comparing the measured *e-p* elastic cross section to the existing world data [39]. The kinematics of the *e-p* measurements were chosen so that the solid angle Jacobian matched that of the corresponding *e-d* measurement for $A(Q^2)$. For $B(Q^2)$, to match exactly the Jacobians of *e-p* and *e-d* scattering, the electron arm should be at ∼110°-120°. Since the hydrogen target was not equipped with a collimator to block scattered

electrons which pass through the cell block of the hydrogen cell, the *e-p* calibration data for $B(Q^2)$ were all taken at an electron scattering angle of 90.0°. A complete list of the kinematics of this experiment is given in Appendix B. Elastic *e-p* data were taken both with and without the acceptance-defining collimators in front of the spectrometers for each $A(Q^2)$ point. For the $B(Q^2)$ points, the *e-p* data were taken with the acceptance-defining collimators in front of the spectrometers.

The elastic electron-proton cross sections were calculated using:

$$\frac{d\sigma}{d\Omega} = \frac{N_{ep} C_{eff}}{N_i N_t (\Delta\Omega)_{MC} F(Q^2, T)} \ , \tag{3-32}$$

where:

- N_{ep} is the number of double-arm elastic *e-p* events extracted from the analysis.
- N_i is the number of incident electrons.
- N_t is the number of target nuclei (in units of nuclei/cm^2) corrected for target boiling (Section 3.8.4).
- $(\Delta\Omega)_{MC}$ is the effective double-arm solid angle from the Monte Carlo simulation (Section 3.9).
- $F(Q^2, T)$ is the portion of radiative corrections that depend only on Q^2 and T. This factor is calculated by the Monte Carlo simulation. The radiative corrections that depend on the momentum acceptances of the spectrometers are included in the double-arm solid angle calculation (Section 3.10).
- $C_{eff} = C_{det} C_{trig} C_{cdt} C_{rni}$ represents the corrections for detector (Čerenkov and calorimeter) inefficiency (C_{det}), trigger inefficiency (C_{trig}), computer dead time (C_{cdt}) and

losses of recoil nuclei due to nuclear interactions (C_{rni}). These corrections were discussed in detail in Section 3.8. The computer dead time correction was discussed in Section 2.8.4.

E	$\overline{Q^2}$	$\overline{\theta}$	$\frac{d\sigma}{d\Omega}$	Total Error	Ratio to Model
GeV	$(\mathrm{GeV/c})^2$	deg.	$\mathrm{cm}^2/\mathrm{sr}$	%	
0.5392	0.366	90.02	1.404×10^{-32}	3.8	0.990
0.5980	0.433	90.01	9.975×10^{-33}	3.8	1.020
0.6542	0.500	89.99	6.927×10^{-33}	3.8	0.995
0.7081	0.567	90.01	5.238×10^{-33}	3.9	1.032
0.7605	0.634	90.01	4.011×10^{-33}	3.9	1.061
0.8112	0.701	90.01	2.949×10^{-33}	3.9	1.029

Table 3-6: Measured elastic *e-p* cross sections for $B(Q^2)$ kinematics. E is the corrected accelerator beam energy. $\overline{Q^2}$ and $\overline{\theta}$ are from the Monte Carlo simulation where the variation of the cross section over the acceptance is taken into account. The model uses the dipole formula and assumes form factor scaling.

A complete list of the quantities used to calculate the *e-p* cross sections is given in Appendix C. The cross sections are reported at the average Q^2 and θ values, $\overline{Q^2}$ and $\overline{\theta}$, as determined by the Monte Carlo simulation. These values are weighted by an *e-p* elastic cross section model. The double-arm solid angle includes a multiplicative factor to account for the difference between the weighted average cross section and the cross section at the $\overline{Q^2}$ and $\overline{\theta}$ values. This factor is 1.001 (1.015), on average, for the 90° backward (forward) *e-p* kinematics. Tables 3-6 and 3-7 and Figures 3-55 and 3-56 show our measured *e-p* elastic cross sections (for the kinematics of the $B(Q^2)$ and $A(Q^2)$ measurements) divided by the Rosenbluth formula prediction using the dipole formula for the proton electric form factor

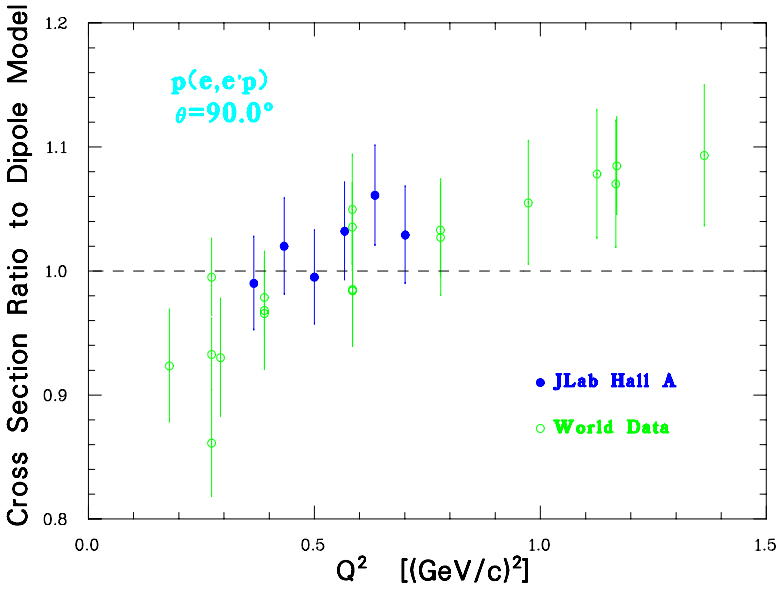

Fig. 3-55: Measured elastic e-p cross sections for the $B(Q^2)$ kinematics divided by the Rosenbluth formula prediction using the dipole formula and assuming form factor scaling. Also shown are the world data [39].

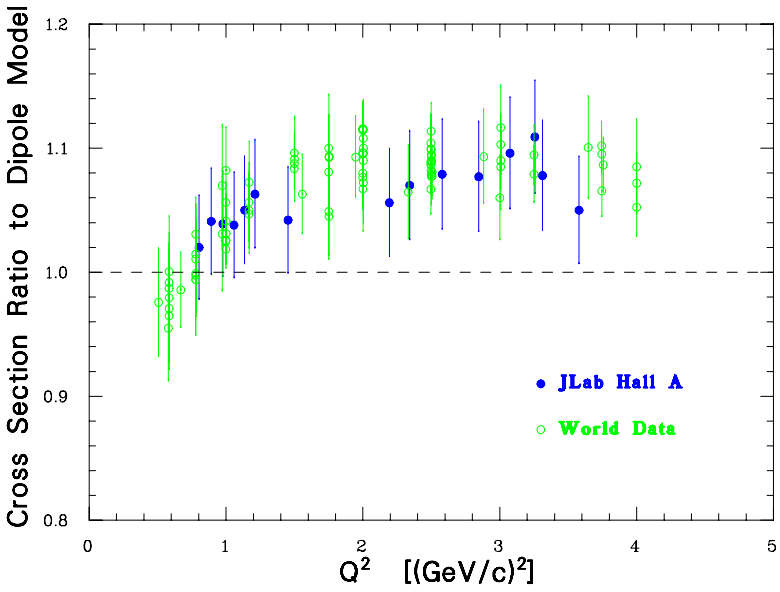

Fig. 3-56: Measured elastic e-p cross sections for the $A(Q^2)$ kinematics divided by the Rosenbluth formula prediction using the dipole formula and assuming form factor scaling. Also shown are the world data [39]. Cross sections shown are for the "oo" collimator configuration.

E GeV	Collimator Configuration	$\overline{Q^2}$ $(\mathrm{GeV/c})^2$	$\overline{\theta}$ deg.	$\frac{d\sigma}{d\Omega}$ $\mathrm{cm}^2/\mathrm{sr}$	Total Error %	Ratio to Model
3.227	ii	0.803	17.20	9.296×10^{-32}	4.1	0.964
3.227	oo	0.803	17.19	9.850×10^{-32}	4.1	1.020
3.227	ii	0.894	18.31	6.114×10^{-32}	4.1	0.991
3.227	oo	0.892	18.29	6.485×10^{-32}	4.1	1.041
3.227	ii	0.979	19.34	4.110×10^{-32}	4.1	0.987
3.227	oo	0.977	19.31	4.369×10^{-32}	4.1	1.039
3.227	ii	1.061	20.31	2.898×10^{-32}	4.1	0.994
3.227	oo	1.058	20.27	3.064×10^{-32}	4.1	1.038
3.227	ii	1.139	21.22	2.117×10^{-32}	4.1	1.004
3.227	oo	1.136	21.18	2.241×10^{-32}	4.1	1.050
3.227	ii	1.216	22.11	1.565×10^{-32}	4.1	1.008
3.227	oo	1.211	22.04	1.685×10^{-32}	4.1	1.063
3.227	ii	1.338	23.51	1.012×10^{-32}	4.1	1.033
3.227	ii	1.463	24.93	6.521×10^{-33}	4.1	1.037
3.227	oo	1.453	24.81	6.787×10^{-33}	4.1	1.042
3.227	ii	1.764	28.39	2.503×10^{-33}	4.1	1.063
4.022	ii	2.203	25.41	1.383×10^{-33}	4.2	1.028
4.022	oo	2.193	25.31	1.459×10^{-33}	4.2	1.056
3.725	ii	2.352	29.38	7.516×10^{-34}	4.1	1.040
3.725	oo	2.342	29.27	7.941×10^{-34}	4.1	1.070
3.729	ii	2.593	31.70	4.241×10^{-34}	4.1	1.054
3.729	oo	2.579	31.55	4.492×10^{-34}	4.1	1.079
4.022	ii	2.860	31.05	3.029×10^{-34}	4.1	1.066
4.022	oo	2.846	30.92	3.156×10^{-34}	4.1	1.077
4.022	ii	3.080	33.06	1.792×10^{-34}	4.1	1.014
4.022	oo	3.074	33.00	1.962×10^{-34}	4.1	1.096

E	Collimator Configuration	$\overline{Q^2}$	$\overline{\theta}$	$\frac{d\sigma}{d\Omega}$	Total Error	Ratio to Model
GeV		$(\mathrm{GeV/c})^2$	deg.	$\mathrm{cm}^2/\mathrm{sr}$	%	
4.399	ii	3.327	31.24	1.558×10^{-34}	4.1	1.055
4.399	oo	3.312	31.11	1.642×10^{-34}	4.1	1.078
4.022	ii	3.257	34.75	1.278×10^{-34}	4.1	1.048
4.022	oo	3.256	34.73	1.357×10^{-34}	4.1	1.109
4.397	ii	3.594	33.46	9.081×10^{-35}	4.1	1.030
4.397	oo	3.579	33.35	9.510×10^{-35}	4.1	1.050

Table 3-7: Measured elastic *e-p* cross sections for $A(Q^2)$ kinematics. E is the corrected accelerator beam energy. "ii" indicates that data were taken with the acceptance-defining collimators in front of the spectrometers. "oo" indicates that data were taken without the acceptance-defining collimators in front of the spectrometers. $\overline{Q^2}$ and $\overline{\theta}$ are from the Monte Carlo simulation where the variation of the cross section over the acceptance is taken into account.

$G_E^p(Q^2)$:

$$G_E^p(Q^2) = \frac{1}{(1+Q^2/0.71)^2} \ , \tag{3-33}$$

(with Q^2 in units of $(\mathrm{GeV/c})^2$) and assuming form factor scaling for the proton magnetic form factor $G_M^p(Q^2)$:

$$G_M^p(Q^2) = \mu_p \ G_E^p(Q^2) \ , \tag{3-34}$$

where μ_p is the magnetic moment of the proton. The cross section for elastic electron-proton scattering is given in term of the proton form factors by:

$$\frac{d\sigma}{d\Omega} = \sigma_M \left[\frac{G_E^2(Q^2) + \tau G_M^2(Q^2)}{1+\tau} + 2\tau G_M^2(Q^2) \tan^2(\theta/2) \right] \ , \tag{3-35}$$

where $\tau = \frac{Q^2}{4M_p^2}$. For the $B(Q^2)$ kinematics, the *e-p* calibration data were found to agree with the world data [39]. For the $A(Q^2)$ kinematics, the *e-p* calibration data taken without

the acceptance-defining collimators were found to agree with the world data [39]. The *e-p* calibration data taken with the acceptance-defining collimators were found to be 3.8% lower, on average, than the ones taken without the acceptance-defining collimators. Therefore, all elastic electron-deuteron cross section data (for the $A(Q^2)$ measurements) taken with the acceptance-defining collimators have been increased by 3.8%. The statistical error of all *e-p* elastic cross sections is much less than 1%. Table 3-8 summarizes the systematic uncertainties for the elastic *e-p* cross sections as determined in the sections given in the table.

Source	Magnitude	Section
Beam charge	1.2%	3.3
Scattering angle	0.1-0.7%	2.6
Beam energy	0.7-1.7%	3.4
Target effective length	1.0%	3.8.4
Double-arm solid angle	3.0%	3.9
Radiative corrections	1.5%	3.10
Trigger inefficiency (C_{trig})	0.5%	3.8.1
Detector inefficiencies (C_{det})	0.3%	3.8.2
Recoil nuclear interactions (C_{rni})	0.1-0.4%	3.8.3
Total	3.8-4.1%	

Table 3-8: Systematic uncertainties of the measured *e-p* elastic cross sections.

Chapter 4

Results

4.1 Electron-Deuteron Elastic Cross Sections

The cross section for elastic electron-deuteron scattering was calculated using:

$$\frac{d\sigma}{d\Omega} = \frac{N_{ed} C_{eff}}{N_i N_t (\Delta\Omega)_{MC} F(Q^2, T)} \ , \tag{4-1}$$

where N_{ed} is the number of double-arm elastic *e-d* events extracted from the analysis and all other quantities are as in Equation 3-32. A complete list of the quantities used in calculating the *e-d* cross sections is given in Appendix C. The cross sections are reported at the average Q^2 and θ values, $\overline{Q^2}$ and $\overline{\theta}$, as determined by the Monte Carlo simulation. These values are weighted by an *e-d* elastic cross section model. The double-arm solid angle includes a multiplicative factor to account for the difference between the weighted average cross section and the cross section at the $\overline{Q^2}$ and $\overline{\theta}$ values. This factor is 1.005 (1.035), on average, for the 144.5° backward (forward) *e-d* kinematics. Figures 4-1 and 4-2 show the corrected coincidence time-of-flight for a few representative kinematical points. The number of double-arm elastic *e-d* events was determined from the time-of-flight peaks. The 12 events detected at $Q^2 = 5.90$ (GeV/c)^2 with beam energy of 4.397 GeV are shown in the correlation histogram of the Hadron and Electron arm relative momenta (Figure 4-3). It took a week of beam time with a total charge of 19.2 C to collect these 12 events.

The measured *e-d* cross sections for each of our kinematics is shown in Tables 4-1 and 4-2, along with their statistical and systematic errors. As discussed in section 3.12, the elastic electron-deuteron cross section data (for the $A(Q^2)$ measurements) taken with the acceptance-defining collimators have been increased by 3.8%. A breakdown of the

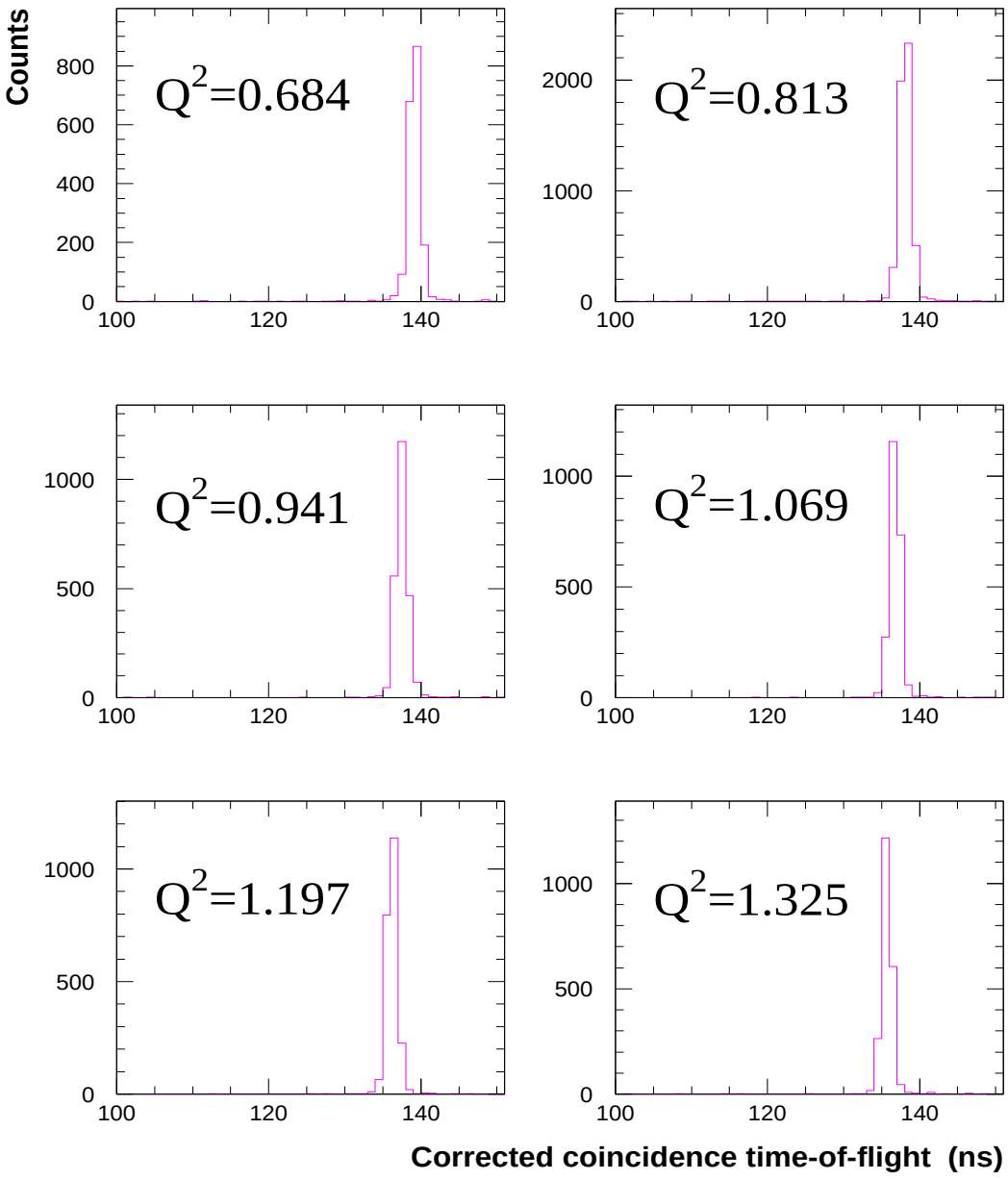

Fig. 4-1: The corrected e-d coincidence time-of-flight spectra for all $B(Q^2)$ kinematics. The calorimeter and Čerenkov cuts have been applied.

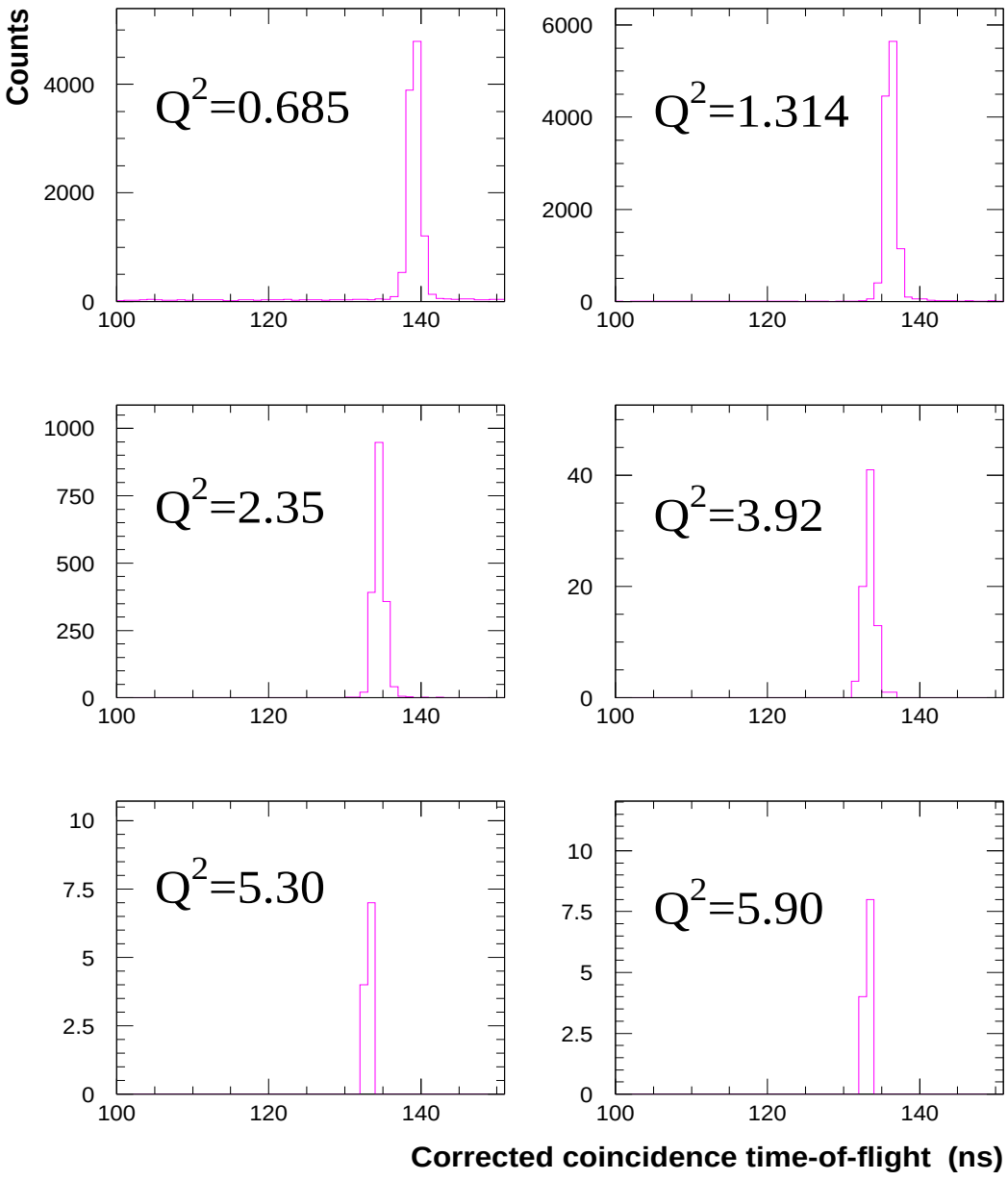

Fig. 4-2: The corrected e-d coincidence time-of-flight spectra for selected $A(Q^2)$ kinematics. The calorimeter and Čerenkov cuts have been applied.

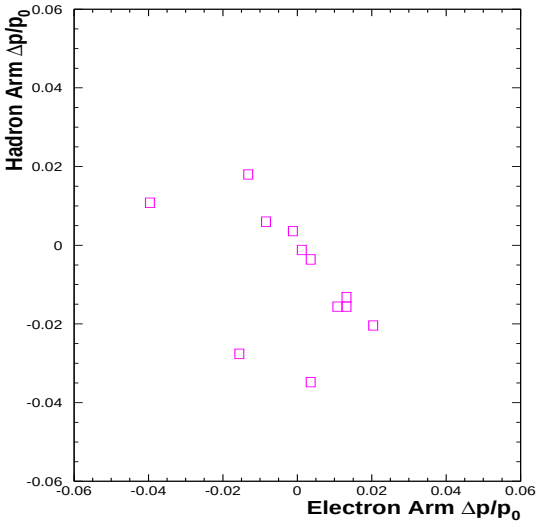

Fig. 4-3: The 12 events detected at $Q^2 = 5.90$ (GeV/c)^2 with beam energy of 4.397 GeV are shown in the correlation histogram of the Hadron and Electron arm relative momenta. It took a week of beam time with a total charge of 19.2 C to collect these 12 events.

systematic errors is shown in Table 4-3. The total systematic error has been estimated to be 4.5-5.5% and is dominated by the 3.0% uncertainty in the double-arm solid angle.

4.2 Rosenbluth Separation of $A(Q^2)$ and $B(Q^2)$ at Low Q^2

At low Q^2, $A(Q^2)$ and $B(Q^2)$ were extracted from the data using the Rosenbluth separation technique. This technique involves a measurement of the elastic *e*-*d* cross section at two different angles (one forward, one backward) while keeping the momentum transfer fixed. At forward angles, the contribution from the electric structure function to the cross section dominates, while at backward angles, the contribution from the magnetic structure function to the cross section is enhanced because of the $\tan^2(\theta/2)$ factor in the Rosenbluth formula.

To do the Rosenbluth separation, the two cross sections measured at the same momentum transfer were combined to yield, in effect, two equations with two unknowns:

E	$\overline{Q^2}$	$\overline{\theta}$	$\frac{d\sigma}{d\Omega}$	Statistical Error	Systematic Error	Total Error
GeV	$(\mathrm{GeV/c})^2$	deg.	$\mathrm{cm}^2/\mathrm{sr}$	%	%	%
0.5392	0.684	144.55	8.00×10^{-37}	2.3	4.7	5.2
0.5980	0.813	144.55	3.20×10^{-37}	1.4	4.6	4.8
0.6542	0.941	144.53	1.48×10^{-37}	2.1	4.5	5.0
0.7081	1.069	144.52	6.33×10^{-38}	2.1	4.5	5.0
0.7605	1.197	144.52	3.45×10^{-38}	2.1	4.5	5.0
0.8112	1.325	144.51	1.84×10^{-38}	2.1	4.6	5.1

Table 4-1: Measured elastic *e-d* cross sections for the 6 kinematical points for the $B(Q^2)$ extraction. E is the corrected accelerator beam energy. $\overline{Q^2}$ and $\overline{\theta}$ are from the Monte Carlo simulation where the variation of the cross section over the acceptance is taken into account.

$$\sigma_F = A(Q^2) + B(Q^2)\tan^2(\theta_F/2) \ , \tag{4-2}$$

and

$$\sigma_B = A(Q^2) + B(Q^2)\tan^2(\theta_B/2) \ , \tag{4-3}$$

where σ_F and σ_B are the forward and backward angle cross section measurements, taken at the same Q^2, normalized to their respective Mott cross section values. Since the forward cross sections were taken at slightly different Q^2 values, they were adjusted to the Q^2 values of the backward cross sections.

Equations 4-2 and 4-3 were solved simultaneously at six different values of Q^2 to extract $A(Q^2)$ and $B(Q^2)$. The resulting $A(Q^2)$ error is the statistical and systematic error from Table 4-2 added in quadrature. The statistical error on $B(Q^2)$ is calculated from Equations 4-2 and 4-3 taking into account the statistical errors of σ_F and σ_B. The relative systematic error between the forward and backward cross sections is estimated to be 3.0%.

E GeV	Collimator Configuration	$\overline{Q^2}$ $(\mathrm{GeV/c})^2$	$\overline{\theta}$ deg.	$\frac{d\sigma}{d\Omega}$ $\mathrm{cm}^2/\mathrm{sr}$	Statistical Error %	Systematic Error %	Total Error %
3.227	oo	0.685	15.22	3.99×10^{-34}	0.8	4.5	4.6
3.227	oo	0.811	16.66	1.62×10^{-34}	0.7	4.6	4.7
3.227	oo	0.938	18.02	7.43×10^{-35}	1.0	4.6	4.7
3.227	oo	1.063	19.31	3.67×10^{-35}	0.8	4.7	4.8
3.227	oo	1.188	20.55	1.98×10^{-35}	0.9	4.7	4.8
3.227	oo	1.314	21.75	1.01×10^{-35}	0.8	4.8	4.9
3.227	ii	1.53	23.76	3.65×10^{-36}	1.5	4.9	5.1
3.227	ii	1.76	25.79	1.40×10^{-36}	1.3	5.0	5.2
3.227	ii	2.35	30.82	1.34×10^{-37}	2.4	5.1	5.6
4.022	oo	3.01	27.96	2.38×10^{-38}	5.1	5.5	7.5
3.725	oo	3.41	33.25	5.32×10^{-39}	6.3	5.4	8.3
3.729	oo	3.92	36.61	1.37×10^{-39}	9.6	5.4	11.0
4.022	oo	4.40	36.24	5.00×10^{-40}	14.1	5.3	15.1
4.022	oo	4.91	39.32	1.25×10^{-40}	16.9	5.2	17.7
4.399	oo	5.30	37.18	4.51×10^{-41}	30.2	5.1	30.6
4.022	oo	5.30	41.82	4.57×10^{-41}	28.9	5.1	29.3
4.397	oo	5.90	40.47	3.55×10^{-41}	28.9	4.9	29.3
4.022	oo	5.90	45.74	8.13×10^{-42}	100.0	4.8	100.0

Table 4-2: Measured elastic e-d cross sections for the 18 kinematical points for the $A(Q^2)$ extraction. E is the corrected accelerator beam energy. "ii" indicates that data were taken with the acceptance-defining collimators in front of the spectrometers. "oo" indicates that data were taken without the acceptance-defining collimators in front of the spectrometers. $\overline{Q^2}$ and $\overline{\theta}$ are from the Monte Carlo simulation where the variation of the cross section over the acceptance is taken into account.

Source	Magnitude	Section
Beam charge	1.2%	3.3
Scattering angle	0.1-0.9%	2.6
Beam energy	1.7-3.8%	3.4
Target effective length	1.0%	3.8.4
Double-arm solid angle	3.0%	3.9
Radiative corrections	1.5%	3.10
Trigger inefficiency (C_{trig})	0.8%	3.8.1
Detector inefficiencies (C_{det})	0.3%	3.8.2
Recoil nuclear interactions (C_{rni})	0.7-2.1%	3.8.3
Total	4.5-5.5%	

Table 4-3: Systematic uncertainties of the measured *e-d* elastic cross sections.

Source	Magnitude
Beam charge	1.0%
Scattering angle	0.5%
Beam energy	2.0%
Target effective length	0.5%
Double-arm solid angle	1.5%
Radiative corrections	0.5%
Trigger inefficiency	0.2%
Detector inefficiencies	0.1%
Recoil nuclear interactions	1.0%
Total	3.0%

Table 4-4: Breakdown of relative systematic errors between the backward and forward elastic *e-d* cross section measurements.

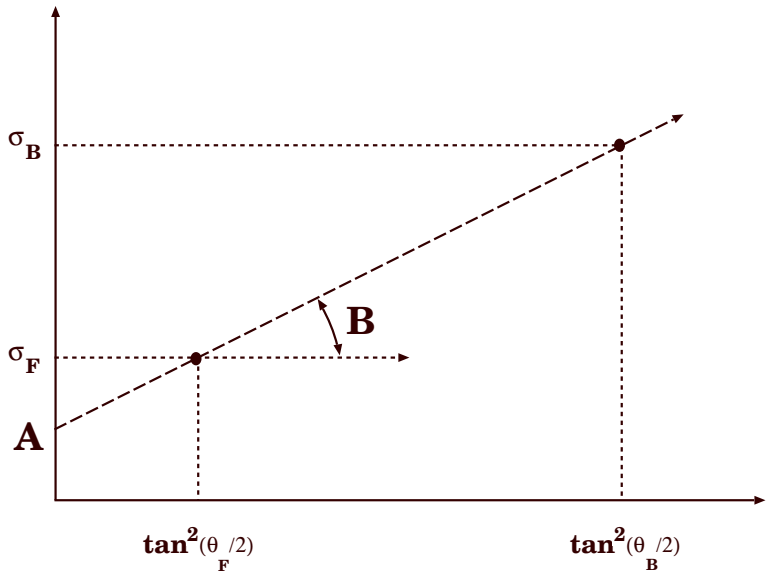

Fig. 4-4: Schematic of the Rosenbluth separation of $A(Q^2)$ and $B(Q^2)$.

A breakdown of the relative systematic error is given in Table 4-4. An overall systematic error shared by both cross sections does not contribute to $B(Q^2)$ since $B(Q^2)$ is the slope in the Rosenbluth separation (see Figure 4-4). The systematic error on $B(Q^2)$ is then the relative systematic error multiplied by $A(Q^2)/(B(Q^2)\tan^2(144.5^\circ/2))$. Table 4-5 lists the extracted values of $A(Q^2)$ and $B(Q^2)$, along with their statistical and systematic errors added in quadrature.

Figure 4-5 shows the $A(Q^2)$ results (solid circles), along with the previous data from SLAC [1], Saclay [5], Bonn [7] and CEA [6]. Also shown, are the recent $A(Q^2)$ data, in the Q^2 range from 0.7 to 1.8 $(\mathrm{GeV/c})^2$, from JLab Hall C [40]. As seen in the figure, our results agree with the previous SLAC [1] and Saclay [5] measurements and are significantly higher than the Bonn [7] and CEA [6] data in the region of overlap, resolving the discrepancy that existed among the low-Q^2 data sets. The $B(Q^2)$ results are shown in Figure 4-6 (solid circles) along with the existing data from SLAC [2], Saclay [8] and Bonn [7]. It is evident that our, much improved, magnetic structure function results are in good agreement with

$\overline{Q^2}$ $(\mathrm{GeV/c})^2$	$A(Q^2)$	Total Error %	$B(Q^2)$	Statistical Error %	Systematic Error %	Total Error %
0.684	2.64×10^{-4}	4.6	3.37×10^{-5}	4.2	2.4	4.8
0.813	1.55×10^{-4}	4.7	1.53×10^{-5}	2.9	3.1	4.3
0.941	9.84×10^{-5}	4.7	7.70×10^{-6}	4.9	3.9	6.3
1.069	6.46×10^{-5}	4.8	2.60×10^{-6}	7.7	7.7	10.9
1.197	4.50×10^{-5}	4.8	1.35×10^{-6}	9.7	10.3	14.1
1.325	2.92×10^{-5}	4.9	7.28×10^{-7}	11.5	12.3	16.8

Table 4-5: Table of the extracted $A(Q^2)$ and $B(Q^2)$ values from the Rosenbluth separation.

the previous data in the region of overlap.

4.3 $A(Q^2)$ at Large Q^2

At large Q^2, $A(Q^2)$ was extracted from the measured cross sections shown in Table 4-2 using the Rosenbluth formula:

$$\frac{d\sigma}{d\Omega} = \sigma_M[A(Q^2) + B(Q^2)\tan^2(\theta/2)] \ , \tag{4-4}$$

and assuming that $B(Q^2)$ does not contribute. This assumption is supported by the existing $B(Q^2)$ data ([2], [8], [7]) which are shown in Figure 1-6 together with the existing $A(Q^2)$ data ([1], [5], [7], [6]). As seen in the figure, $B(Q^2)$ is always at least a factor of 10 lower than $A(Q^2)$. The contribution of $B(Q^2)$ to the measured cross section is further reduced by the $\tan^2(\theta/2)$ factor of the Rosenbluth formula.

The extracted values of $A(Q^2)$ are shown in Table 4-6. For each of the last two Q^2 points, data were taken with two different beam energies. For each point, the $A(Q^2)$ value reported is the weighted average of the two measurements. The weighting factor is the product of the Mott cross section for each beam energy times the accumulated total charge.

Figure 4-7 shows all the $A(Q^2)$ results from this experiment (solid circles), along with

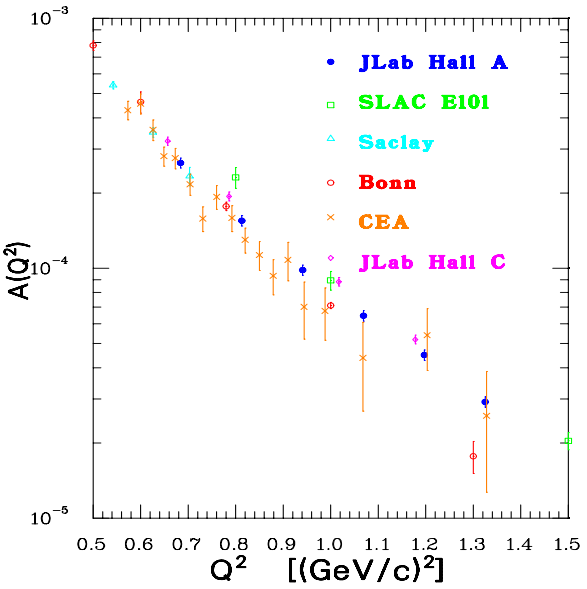

Fig. 4-5: JLab Hall A $A(Q^2)$ measurements up to $Q^2 = 1.5$ (GeV/c)^2 along with previous measurements from SLAC [1], Saclay [5], Bonn [7], CEA [6] and JLab Hall C [40].

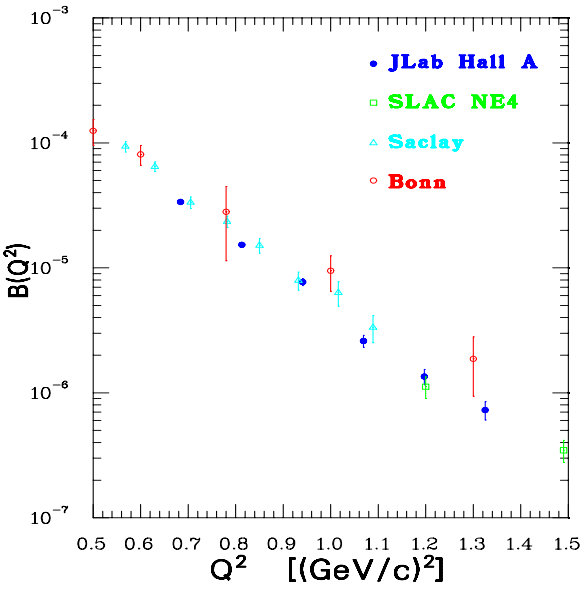

Fig. 4-6: JLab Hall A $B(Q^2)$ measurements up to $Q^2 = 1.5$ (GeV/c)^2 along with previous measurements from SLAC [2], Saclay [8] and Bonn [7].

$\overline{Q^2}$ (GeV/c)^2	$A(Q^2)$	Total Error %
1.53	1.57×10^{-5}	5.1
1.76	8.52×10^{-6}	5.2
2.35	1.78×10^{-6}	5.6
3.01	3.34×10^{-7}	7.5
3.41	1.37×10^{-7}	8.3
3.92	5.49×10^{-8}	11.0
4.40	2.27×10^{-8}	15.1
4.91	8.30×10^{-9}	17.7
5.30	3.37×10^{-9}	21.5
5.90	2.86×10^{-9}	28.2

Table 4-6: Table of extracted $A(Q^2)$ values at large Q^2. The total error represents the statistical and systematic uncertainties added in quadrature.

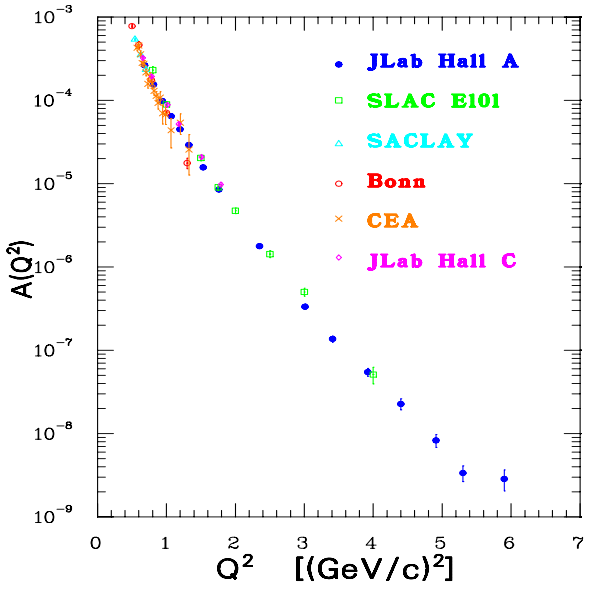

Fig. 4-7: JLab Hall A $A(Q^2)$ measurements up to $Q^2 = 6$ (GeV/c)^2 along with previous measurements from SLAC [1], Saclay [5], Bonn [7], CEA [6] and JLab Hall C [40].

the previous data from SLAC [1], Saclay [5], Bonn [7] and CEA [6]. Also shown, are the recent $A(Q^2)$ data, in the Q^2 range from 0.7 to 1.8 $(\mathrm{GeV/c})^2$, from JLab Hall C [40]. Our data agree with the previous SLAC data [1] and continue the fall off smoothly with Q^2, showing no evidence of any diffractive structure.

Chapter 5

Theoretical Overview

5.1 Introduction

In this chapter, a comprehensive survey of the theoretical approaches used to describe the deuteron elastic structure functions will be presented. These approaches can be categorized in two main approaches: the "conventional" meson-nucleon approach and the quark-gluon approach.

The deuteron elastic structure functions, $A(Q^2)$ and $B(Q^2)$, can be calculated in terms of the non-relativistic (NRIA) and relativistic impulse approximations (RIA), both with and without the inclusion of meson-exchange currents (MEC). This approach views the deuteron as a collection of interacting nucleons and mesons. At large momentum transfers, explicit quark and gluon degrees of freedom are expected to play an important role. At sufficiently large momentum transfer, the Q^2 evolution of the elastic structure functions can be calculated in both the quark dimensional scaling model and in perturbative quantum chromodynamics (pQCD). In the following sections, a summary of the theoretical descriptions of the deuteron elastic structure functions, as well as a comparison to the present and previous experimental data will be presented.

5.2 Non-Relativistic Impulse Approximation

The non-relativistic impulse approximation, in which the virtual photon interacts with one of the nucleons and leaves the other as spectator as shown in Figure 5-1(a), is the traditional approach for the calculation of the deuteron form factors as the sum of scattering off the moving proton and neutron. In the NRIA the standard parameterization of the

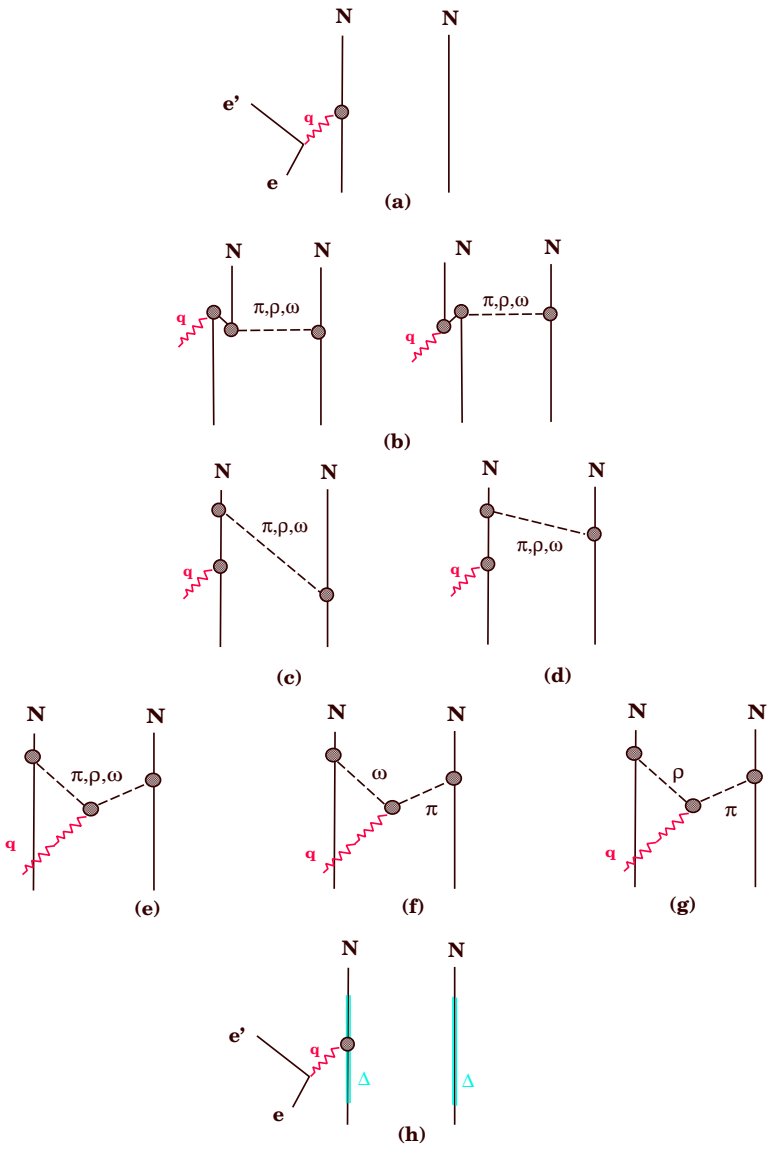

Fig. 5-1: (a): The ordinary impulse approximation for elastic e-d scattering. Meson-exchange current corrections with the photon insertion on a nucleon line: (b) the pair graph, (c) the recoil graph, (d) the re-normalization graph. Graphs of type (c) and (d) are collectively called retardation graphs. Meson-exchange current correction with photon insertion on meson(s): (e) has the same meson on both sides of the insertion, (f) and (g) have different mesons. Only (g) can contribute to e-d elastic scattering because of G-parity conservation. (h) Isobar contributions.

electromagnetic form factors of the deuteron in terms of the electromagnetic form factors of the nucleons and the deuteron wave function has the form [41]:

$$\begin{aligned} F_C &= G_E^S C_E \ , \\ F_Q &= G_E^S C_Q \ , \\ F_M &= \frac{M_d}{M_p}(G_M^S C_S + \frac{1}{2} G_E^S C_L) \ , \end{aligned} \tag{5-1}$$

where G_E^S and G_M^S are the isoscalar electric and magnetic form factors of the nucleon:

$$\begin{aligned} G_E^S &= G_E^p + G_E^n \ , \\ G_M^S &= G_M^p + G_M^n \ , \end{aligned} \tag{5-2}$$

which take into account the fact that the proton and the neutron are not point currents but have their own electromagnetic form factors $G_{E,M}^p$ and $G_{E,M}^n$. The structure functions C_E, C_Q, C_S and C_L of elastic electron-deuteron scattering give the distribution of the neutron and proton point currents as determined by the deuteron S- and D-states $u(r)$ and $w(r)$, respectively, with r being the separation of the two nucleons in the deuteron. They are given by the quadrature formulae:

$$\begin{aligned} C_E &= \int_0^\infty [u^2(r) + w^2(r)] j_0(\frac{Qr}{2}) dr \ , \\ C_Q &= \frac{3}{\sqrt{2}\eta} \int_0^\infty w(r) \Big[u(r) - \frac{w(r)}{2\sqrt{2}} \Big] j_2(\frac{Qr}{2}) dr \ , \\ C_S &= \int_0^\infty \Bigg\{ \Big[u^2(r) - \frac{1}{2} w^2(r) \Big] j_0(\frac{Qr}{2}) \\ &\quad + \frac{1}{2} \Big[\sqrt{2} u^2(r) + w^2(r) \Big] j_2(\frac{Qr}{2}) \Bigg\} dr \ , \end{aligned} \tag{5-3}$$

$$C_L = \frac{3}{2} \int_0^\infty w^2(r) \Big[j_0(\frac{Qr}{2}) + j_2(\frac{Qr}{2}) \Big] dr \ , \tag{5-4}$$

with the normalization condition:

$$\int_o^\infty [u^2(r) + w^2(r)]dr = 1 \ , \tag{5-5}$$

where j_0 and j_2 are spherical Bessel Functions. The magnetic dipole and the charge quadrupole static moments of the deuteron are given by:

$$\begin{aligned} Q_d^{NRIA} &= \frac{1}{20}\int_0^\infty \Big[\sqrt{8}u(r)w(r) - w^2(r)\Big]r^2dr \ , \\ \mu_d^{NRIA} &= \mu_p + \mu_n - \frac{3}{2}\Big(\mu_p + \mu_n - \frac{1}{2}\Big)P_D \ , \end{aligned} \tag{5-6}$$

where

$$P_D = \int_o^\infty w^2(r)dr \tag{5-7}$$

is the probability of the deuteron D-state.

NRIA models with various assumptions for nucleon form factors and deuteron wave functions derived from different nucleon-nucleon potential models give a wide range of predictions for the deuteron elastic structure functions [41, 42]. Here we will discuss in detail the predictions using the deuteron wave functions of the newly constructed high-quality nucleon-nucleon potential by Wiringa *et al.* [43], designated as Argonne v_{18}. The model has a charge-independent part with 14 operator components that is an updated version of the Argonne v_{14} potential. Three additional charge-dependent and one charge-asymmetric operators are added, along with a complete electromagnetic interaction. The potential has been fit to the Nijmegen *pp* and *np* scattering data, low-energy NN scattering parameters, and the deuteron binding energy.

The static deuteron properties predicted by Argonne v_{18} are shown in Table 5-1 and compared to experimental values. The binding energy, E_d, is fit exactly by definition. The asymptotic S-state normalization, A_S, the A_D/A_S-ratio, η, and the deuteron charge radius, r_d, all come out close to the experimental values. The magnetic moment, μ_d, and the

	Experiment	Argonne v_{18}	+ RC + MEC	Units
E_d	2.224575(9)	2.224575		MeV
A_S	0.8846(8)	0.8850		$\text{fm}^{-1/2}$
η	0.0256(4)	0.0250		
r_d	1.9660(68)	1.967		fm
μ_d	0.857406(1)	0.847	0.871	μ_N
Q_d	0.2859(3)	0.270	0.275	fm^2
P_D		5.76		%

Table 5-1: Static properties of the deuteron.

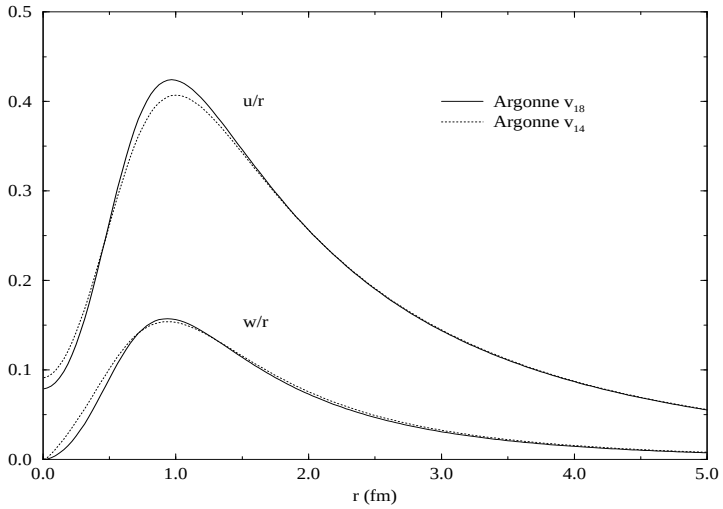

Fig. 5-2: Deuteron S- and D-state wave function components divided by r calculated with the Argonne v_{18} and v_{14} potentials.

quadrupole moment, Q_d, are both under-predicted in the non-relativistic impulse approximation; both have significant relativistic (RC) and meson-exchange corrections (discussed below). The S- and D-state components of the deuteron wave function are shown, for the Argonne v_{18} and v_{14} potentials, in Figure 5-2.

The electromagnetic current operator [44, 45] consists of one- and two-body parts. The one-body part has the standard NRIA form, with inclusion, in the charge component, of the Darwin-Foldy and spin-orbit relativistic corrections [46]. The two-body charge operators contain contributions that correspond, in an One-Boson-Exchange (OBE) picture, to those obtained from pion- and vector-meson (ρ and ω) exchanges (see Figure 5-1-b, -c, and -d). The two-body current operators are constructed from the spin-orbit and quadratic momentum-dependent components of the interaction with the methods developed in References [44, 47]. The two-body contribution associated with the $\rho\pi\gamma$ meson-exchange current was also included. In the $\rho\pi\gamma$ vertex a coupling constant of 0.56 was used with a monopole form factor, $(1+Q^2/m_\omega^2)^{-2}$, where m_ω is the mass of ω meson. The Höhler parameterization [48] was used for the nucleon electromagnetic form factors.

The calculated $A(Q^2)$ structure function is shown in Figure 5-3. The impulse approximation alone using the v_{18} potential is found to under-predict the experimental data. The relativistic and meson-exchange current corrections bring the theoretical calculation in excellent agreement with the experimental data over the shown range of Q^2. The calculated $B(Q^2)$ structure function is shown in Figure 5-4. The impulse approximation alone using the v_{18} potential is found to under-predict the experimental data in the momentum transfer range 0.4–1.6 $(\mathrm{GeV/c})^2$, and has a zero around 1.7 $(\mathrm{GeV/c})^2$. The calculated $B(Q^2)$ structure function with relativistic and meson-exchange current corrections is found to over-predict the experimental data in the momentum transfer range 0.4–1.8 $(\mathrm{GeV/c})^2$, and has a zero around 2.4 $(\mathrm{GeV/c})^2$. The leading two-body contributions are those due to the spin-orbit and quadratic spin-orbit components of the interaction. They are of opposite sign.

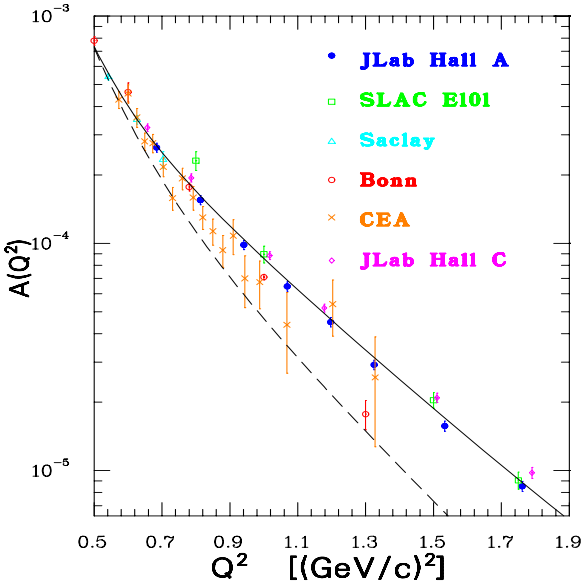

Fig. 5-3: The electric structure function $A(Q^2)$ in the non-relativistic impulse approximation using the Argonne v_{18} potential (dashed line) and with relativistic and MEC corrections (solid line) [43].

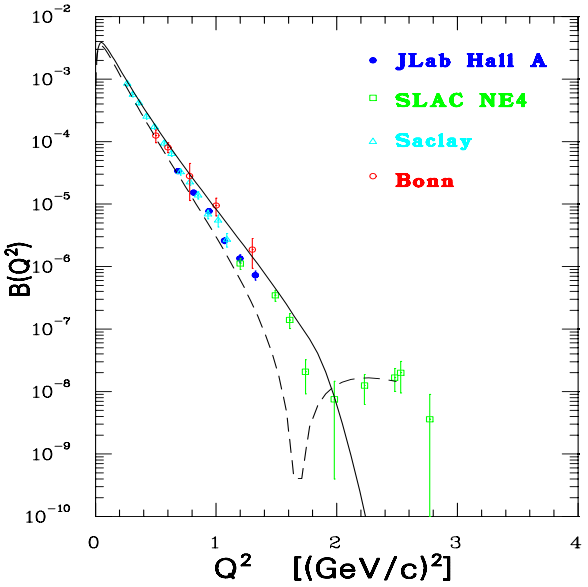

Fig. 5-4: The magnetic structure function $B(Q^2)$ in the non-relativistic impulse approximation using the Argonne v_{18} potential (dashed line) and with relativistic and MEC corrections (solid line) [43].

However, the overestimation of the data indicates that the degree of cancellation between them is not quite enough. The $\rho\pi\gamma$ part of the meson-exchange current contributions to $B(Q^2)$ is found to be rather small.

5.2.1 Isobar Configurations

In addition to meson-exchange current corrections to the non-relativistic impulse approximation, isobar configurations (IC) in the deuteron could contribute to its electromagnetic form factors. Blunden, Greenber, Lomon, and Sitarki [49, 50] compared elastic deuteron form factor data with predictions of models coupling NN and $\Delta\Delta$ channels by realistic meson-exchange potentials, at long range, and a homogeneous boundary condition, at a radius r_0 of quantum chromodynamics asymptotic freedom. The models, which couple the $NN(^3S_1, ^3D_1)$ states to the $\Delta\Delta(^3S_1, ^3D_1, ^7D_1)$ channels, are fitted to the NN scattering data for $T_{lab} < 1$ GeV. There are two successful models, differing in r_0, called C' and D'. The static deuteron properties for these two models are listed in Table 5-2. Model C' corresponds to the minimum radius of asymptotic freedom of Feshbach-Lomon [51] $r_0 = 0.74$ fm and model D' to the radius required by the Cloudy Bag Model [52] $r_0 = 1.05$ fm. π, ρ, and ω pair terms (Figure 5-1-b) and $\rho\pi\gamma$ (Figure 5-1-g) MEC contributions were included. The $\rho\pi\gamma$ MEC was calculated with $g_{\rho\pi\gamma} = 0.56$ and a dipole form factor for the $\rho\pi\gamma$ vertex,

$$f_{\rho\pi\gamma}(Q^2) = \frac{1}{(1 + Q^2/\Lambda_G^2)^2} \ , \tag{5-8}$$

with $\Lambda_G = 0.885$ GeV/c.

Model	P_D %	$P_{\Delta S}$ %	$P_{\Delta 3}$ %	$P_{\Delta 7}$ %	r_0 fm	η	Q_d fm^2	μ_d μ_N
C'	5.69	0.00	1.12	0.64	0.74	0.0254	0.285	0.869
D'	5.34	0.00	5.13	2.07	1.05	0.0258	0.285	0.869

Table 5-2: Deuteron properties of the models C' and D' of Blunden *et al.* [49, 50].

In the deuteron only $\Delta\Delta$ states are allowed and these are ${}^3S_1^{\Delta\Delta}$, ${}^3D_1^{\Delta\Delta}$, ${}^7D_1^{\Delta\Delta}$ and ${}^7G_1^{\Delta\Delta}$. $N\Delta$ states are not allowed because the deuteron isospin is $I_d = 0$, while $N\Delta$ states have $I_{N\Delta} = 1$. The deuteron wave function can be decomposed as:

$$\mid \Psi_d\rangle = c_1 \mid {}^3S_1^{NN}\rangle + c_2 \mid {}^3D_1^{NN}\rangle + c_3 \mid {}^3S_1^{\Delta\Delta}\rangle + c_4 \mid {}^3D_1^{\Delta\Delta}\rangle + c_5 \mid {}^7D_1^{\Delta\Delta}\rangle + c_6 \mid {}^7G_1^{\Delta\Delta}\rangle \ . \quad (5\text{-}9)$$

The $\Delta\Delta$ state probability in the deuteron, $P^{\Delta\Delta}$, for the C' model is 1.78% and for the D' model is 7.2%. The obvious question is whether such a large probability of $\Delta\Delta$ state in the deuteron and generally in the NN system is reasonable. Recent experimental estimates [53] put an upper $P^{\Delta\Delta}$ limit at 0.4 %. That is:

$$P^{\Delta\Delta} = c_3^2 + c_4^2 + c_5^2 + c_6^2 \simeq 0.4\% \ . \quad (5\text{-}10)$$

Figure 5-5 shows the results of models C' and D' for $B(Q^2)$, using both Höhler [48] and Gari and Krümpelmann [54] (GK) parameterizations of the nucleon electromagnetic form factors. Note that the GK nucleon form factors lead to good agreement with the data over the entire range of Q^2 with both C' and D' models.

Figure 5-6 shows the results of models C' and D' for $A(Q^2)$. The $A(Q^2)$ data require that the Höhler nucleon form factors be used with model C' and that the GK nucleon form factors be used with model D'. At high Q^2, where more uncertainties due to relativistic and MEC contributions arise, the $A(Q^2)$ data favor the Höhler electric while the $B(Q^2)$ data favor the GK magnetic nucleon form factor.

Dymarz and Khanna [55] showed that the strongest Δ-isobar states in the deuteron, ${}^3S_1^{\Delta\Delta}$ and ${}^7D_1^{\Delta\Delta}$, contribute differently to the deuteron static moments and form factors. The experimental limitation of the total $\Delta\Delta$ probability to be less than 0.4% is in good agreement with their model. They have also shown that the probability of the ${}^7D_1^{\Delta\Delta}$ state depends almost entirely on the $NN \rightarrow \Delta\Delta$ transition potential and is not sensitive to the

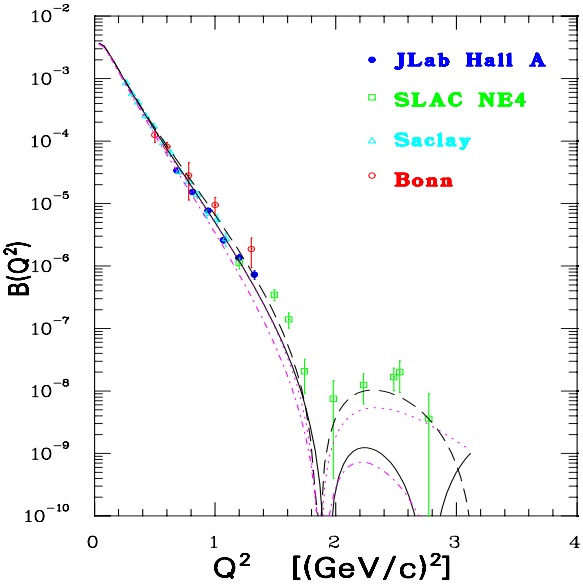

Fig. 5-5: The magnetic structure function $B(Q^2)$ for the model C' of References [49, 50] with Höhler (solid curve) and GK (dashed curve) nucleon form factors, and for model D' with Höhler (dash-dotted curve) and GK (dotted curve) nucleon form factors.

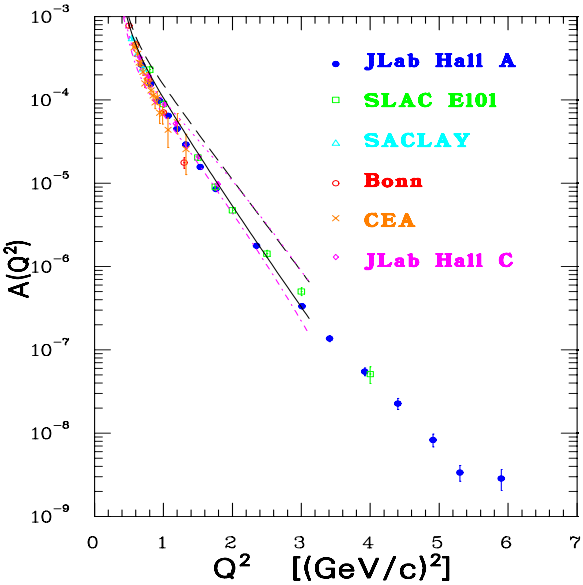

Fig. 5-6: The electric structure function $A(Q^2)$ for the model C' of References [49, 50] with Höhler (solid curve) and GK (dashed curve) nucleon form factors, and for model D' with Höhler (dash-dotted curve) and GK (dotted curve) nucleon form factors.

details of the calculations. Contrary to this, the probability of the ${}^3S_1^{\Delta\Delta}$ state depends on the details of the model. It is possible from the contributions of these states to μ_d and $B(Q^2)$ to put severe constraints on the probability of the $\Delta\Delta$ components in the deuteron wave function: on the ${}^3S_1^{\Delta\Delta}$ state mainly from $B(Q^2)$ at large Q^2 and on the ${}^7D_1^{\Delta\Delta}$ state from μ_d. $A(Q^2)$ offers little additional information on the distribution of the strength among $\Delta\Delta$ components of the deuteron wave function due to the weak dependence on these components.

Dymarz and Khanna [55, 56, 57, 58] calculated the deuteron elastic structure functions in the non-relativistic impulse approximation including isobar configurations and meson-exchange currents. They used the GK parameterization of the nucleon form factors. In the $\rho\pi\gamma$ vertex a coupling constant of 0.56 was used with a dipole form factor, $(1+Q^2/m_\omega^2)^{-2}$, where m_ω is the mass of ω meson. From the different models that have been developed only the results of $W1$ model will be presented.

The $W1$ model yields a D-state probability of $P({}^3D_1^{NN}) = 4.21\%$ and four $\Delta\Delta$ components with an overall probability of 0.36%. This strength is located mainly in the ${}^3S_1^{\Delta\Delta}$ (0.22%) and in the ${}^7D_1^{\Delta\Delta}$ (0.12%) states. The predictions of the $W1$ model are shown in Figures 5-7 and 5-8. For $A(Q^2)$, the NRIA is in good agreement with the experimental data while MEC contributions destroy this agreement at intermediate and large Q^2. For $B(Q^2)$, the NRIA with IC and π-pair currents (shown in Figure 5-1-b) is in reasonable agreement with the data. Adding the $\rho\pi\gamma$-current washes out the minimum at $Q^2 = 2$ (GeV/c)^2 and overestimates the experimental data for $Q^2 > 1.5$ (GeV/c)^2.

5.3 Relativistic Impulse Approximation

When the momentum transfered to the target nucleus is larger than the nucleon mass, the usual non-relativistic assumption that all momenta are small compared to the constituent masses is no longer valid and the traditional non-relativistic techniques to describe

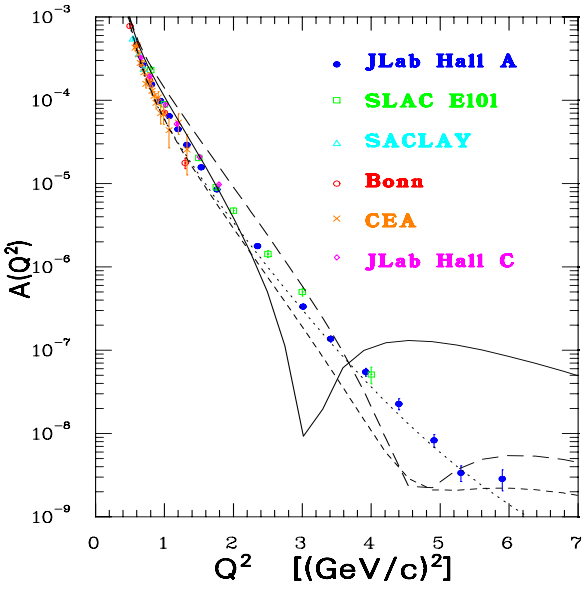

Fig. 5-7: The electric structure function $A(Q^2)$ for the deuteron wave function of model $W1$ of Reference [55] with Δ-isobars. The four curves represent calculations with NRIA (dotted line); NRIA+IC (short dashed line); NRIA+IC+MEC (π-pair) (long dashed line), NRIA+IC+MEC (π-pair and $\rho\pi\gamma$) (solid line).

these reactions may be unreliable. For this reason, it is necessary to develop relativistically covariant models of nuclear few-body systems.

In the one-photon-exchange approximation, the invariant amplitude for elastic electron-deuteron scattering is just the contraction of the electron and deuteron currents, multiplied by the photon propagator:

$$\mathcal{M} = \langle k', m' \mid J^e_\mu \mid k, m \rangle \frac{1}{q^2} \langle p', h' \mid J^\mu_d \mid p, h \rangle \ , \tag{5-11}$$

where $\langle k'm' \mid J^e_\mu \mid km \rangle = ie\overline{u}_{m'}(k')\gamma_\mu u_m(k)$ is the electron electromagnetic current matrix element, k and k' are the initial and final electron momenta, and m and m' are the corresponding helicities. Lorentz covariance and time-reversal allow the deuteron current to be written as a decomposition of the electromagnetic vertex; the deuteron EMFF are defined by this decomposition:

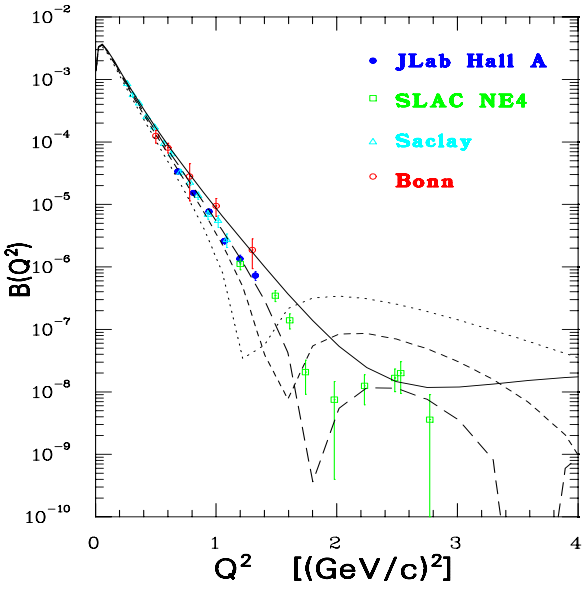

Fig. 5-8: The magnetic structure function $B(Q^2)$ for the deuteron wave function of model $W1$ of Reference [55] with Δ-isobars. The four curves represent calculations with NRIA (dotted line); NRIA+IC (short dashed line); NRIA+IC+MEC(π-pair) (long dashed line), NRIA+IC+MEC (π-pair and $\rho\pi\gamma$) (solid line).

$$\begin{aligned}\langle p',h'|J_\rho|p,h\rangle &= e_\mu^{*h'}(p')\left\{P_\rho\left[\mathcal{F}_1(Q^2)g^{\mu\nu}+\mathcal{F}_2(Q^2)\frac{q^\mu q^\nu}{2M_d^2}\right]+\mathcal{G}_1(Q^2)(g_\rho^\mu q^\nu-g_\rho^\nu q^\mu)\right\}e_\nu^h(p)\\ &\equiv e_\mu^{*h'}(p')T_\rho^{\mu\nu}e_\nu^h(p). \qquad (5\text{-}12)\end{aligned}$$

Here $e_\mu^h(p)$ is the deuteron polarization vector, p and p' are the initial and final deuteron momenta, h and h' are the corresponding helicities, $P=p+p'$ and $q=p'-p$. The deuteron polarization four-vectors of the initial and final states satisfy the relations:

$$\begin{aligned}e_\mu^*(p,h)e^\mu(p,h') &= -\delta_{hh'}\ ,\\ \sum_h e_\mu^*(p,h)e_\nu(p,h) &= -g_{\mu\nu}+\frac{p_\mu p_\nu}{M_d^2}\ ,\\ p_\mu e^\mu(p,h) &= 0\ . \qquad (5\text{-}13)\end{aligned}$$

The charge monopole, the magnetic dipole, and the charge quadrupole form factors of the deuteron are expressed through $\mathcal{F}_1$, $\mathcal{F}_2$ and $\mathcal{G}_1$ as follows:

$$
\begin{aligned}
F_C &= -\mathcal{F}_1 + \frac{2\eta}{3}[-\mathcal{F}_1 - \mathcal{G}_1 + (1+\eta)\mathcal{F}_2] \ , \\
F_M &= \mathcal{G}_1 \ , \\
F_Q &= -\mathcal{F}_1 - \mathcal{G}_1 + (1+\eta)\mathcal{F}_2 \ . \qquad \text{(5-14)}
\end{aligned}
$$

For any further theoretical calculations of the deuteron form factors, one must first calculate the deuteron current matrix elements through a covariant relativistic description of the deuteron. To do this one needs first to calculate the deuteron electromagnetic current and the deuteron wave function.

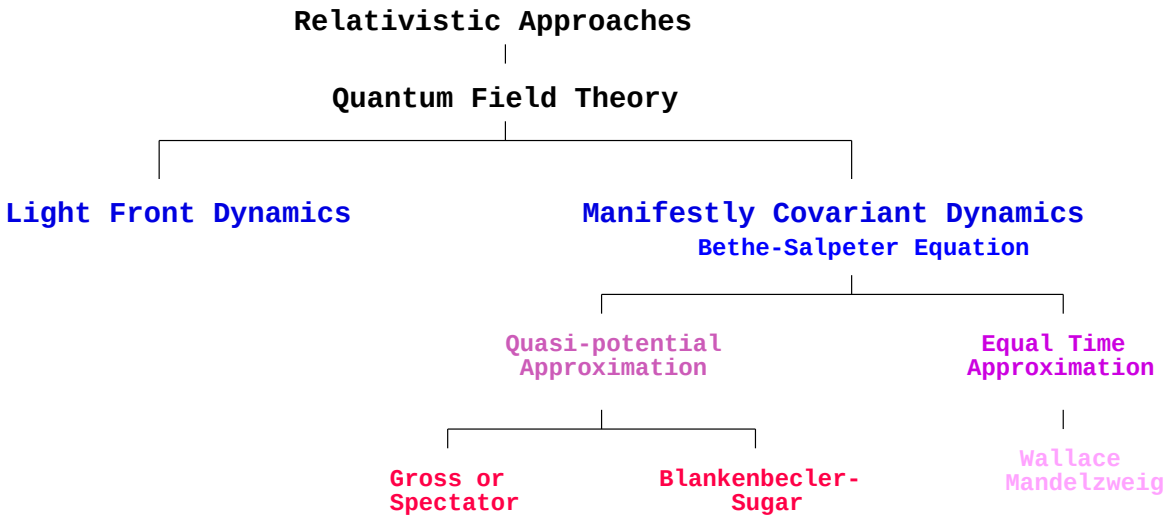

Fig. 5-9: The approaches that can be used for a relativistic description of the deuteron.

There are two approaches in the construction of covariant models that can be used for a relativistic description of the deuteron: Light-Front (LFD) or Light-Cone Dynamics [59, 60, 61, 62, 63] and Manifestly Covariant Dynamics. Light Front Dynamics is based on the evaluation of field theories quantized on the light-cone. It uses conventional quantum mechanics, in which the theoretical framework is well known and understood. The negative

energy states are excluded. Its only disadvantage is that some of the Lorentz transformations include the interaction, and therefore can not be evaluated without doing additional dynamical calculations.

The Manifestly Covariant Dynamics approach uses the Bethe-Salpeter formalism [64] and related quasi-potential Equations [65, 66, 3, 67], based on Feynman perturbation theory and, as such, maintains manifest Lorentz invariance. Here, all Lorentz transformations are kinematic but the disadvantage comes from the inclusion of negative energy states in the dynamics. There are different choices for each approach, as Figure 5-9 illustrates.

5.3.1 Light-Front Dynamics

The electromagnetic properties of the deuteron are exhaustively described by three electromagnetic form factors. This means, that although h' and h run over three values $0, \pm 1$ and the index ρ runs over four values, there are only three independent elements in the set of four $(3 \times 3\ )$-matrices $\langle p', h' \mid J_\rho \mid p, h \rangle$. In principle, in order to find the form factors, it is enough to calculate any three independent matrix elements and to express the form factors through them. This procedure, based on the matrix elements of the "plus" component $J^+ = J^0 + J^z$ of the electromagnetic current, is realized in light-front dynamics. In this approach the wave functions are defined on the light-front plane $t + z = 0$. However, it was found that, in this approach, different triplets of the matrix elements of the one-body current give different sets of form factors as will be discussed next.

The current J_ρ is a rather complicated operator because is for interacting particles and thus contains the interaction. As a result, the transformation properties of the current J_ρ and the state vector $\mid p, h \rangle$ are consistent with each other, which leads to the covariance (*i.e.* to the correct transformation properties) of the matrix elements $\langle p', h' \mid J_\rho \mid p, h \rangle$.

In practice, the current operator, J_ρ, is replaced by the one for free particles, $\tilde{J}_\rho$. That is, instead of $\langle p', h' \mid J_\rho \mid p, h \rangle$ the following matrix elements are calculated:

$$\tilde{J}^{\rho}_{hh'} \equiv \langle p', h' \mid \tilde{J}_{\rho} \mid p, h \rangle \ . \tag{5-15}$$

The decomposition of Equation 5-12 in the light-front dynamics is assumed to be valid not only for the current J_ρ but also for the free one $\tilde{J}_\rho$. Then in order to find the form factors it would be enough, in principle, to calculate any three independent matrix elements, for example the $\tilde{J}^+_{11}$, $\tilde{J}^+_{1-1}$, $\tilde{J}^+_{10}$ ones used in References [68, 69, 71].

In order to investigate the sensitivity of the results to the choice of the matrix elements, Grach and Kondratyuk [69] (see also Karmanov [70]) obtained two solutions for the deuteron form factors, which differ from each other by the set of the matrix elements used in the calculations (so-called solutions A and B):

A: $\tilde{J}^+_{11}$, $\tilde{J}^+_{1-1}$, $\tilde{J}^+_{00}$;

B: $\tilde{J}^+_{11}$, $\tilde{J}^+_{1-1}$, $\tilde{J}^+_{10}$.

They found that solution A differs noticeably from solution B especially for the magnetic form factor. This ambiguity proceeds from the incorrectness of the decomposition of Equation 5-12 for the matrix elements of the free current operator $\langle p', h' \mid \tilde{J}_\rho \mid p, h \rangle$ calculated by using the light-front wave functions for an interacting bound system. The transformation properties of the free current and of the bound system wave function are incompatible with each other, which destroys the covariance. Therefore, the decomposition of Equation 5-12, essentially based on the covariance of $\langle p', h' \mid J_\rho \mid p, h \rangle$, is invalid for the matrix element $\langle p', h' \mid \tilde{J}_\rho \mid p, h \rangle$. Equation 5-12 becomes invalid in approximate practical calculations when the current operator of interacting particles is replaced by the free one. The lack of covariance means that the matrix element $\langle p', h' \mid \tilde{J}_\rho \mid p, h \rangle$ depends on the system of reference owing to the fact that the state vector defined on the light front surface $t + z = 0$ depends on this surface.

Karmanov and Smirnov [72, 73] have shown that the previous calculations [68, 69, 59, 71] of the deuteron electromagnetic form factors in the light-front dynamics contain non-physical contributions. They defined the light front surface by the invariant equation $(\omega \cdot x) = 0$, where ω is a four-vector: $\omega = (\omega_0, \vec{\omega})$, $\omega^2 = 0$. The matrix element $\langle p', h' \mid \tilde{J}_\rho \mid p, h\rangle$ is now explicitly covariant, but, as in the case of $t + z = 0$, it depends on the position of this light-front surface, *i.e.* on the four-vector ω which participates in the decomposition of the matrix element $\langle p', h' \mid \tilde{J}_\rho \mid p, h\rangle$ in invariant amplitudes. This decomposition has the form:

$$\tilde{J}^\rho_{hh'} = \langle p', h'|\tilde{J}_\rho|p, h\rangle = \frac{1}{2\omega \cdot p} e^{*h'}_\mu(p')\tilde{J}^{\mu\nu}_\rho e^h_\nu(p), \quad \text{where} \quad \tilde{J}^{\mu\nu}_\rho = T^{\mu\nu}_\rho + B^{\mu\nu}_\rho(\omega)\ , \qquad (5\text{-}16)$$

where $T^\rho_{\mu\nu}$ is given by Equation 5-12 and $B^\rho_{\mu\nu}$ contain eight new tensor structures depending on ω:

$$\begin{aligned} B^{\mu\nu}_\rho &= \frac{M_d^2}{2(\omega \cdot p)}\,\omega_\rho \left[B_1 g^{\mu\nu} + B_2 \frac{q^\mu q^\nu}{M_d^2} + B_3 M^2 \frac{\omega^\mu \omega^\nu}{(\omega \cdot p)^2} + B_4 \frac{q^\mu \omega^\nu - q^\nu \omega^\mu}{2\omega \cdot p}\right] \\ &+ B_5 P_\rho M_d^2 \frac{\omega^\mu \omega^\nu}{(\omega \cdot p)^2} + B_6 P_\rho \frac{q^\mu \omega^\nu - q^\nu \omega^\mu}{2\omega \cdot p} + B_7 M_d^2 \frac{g^\mu_\rho \omega^\nu + g^\nu_\rho \omega^\mu}{\omega \cdot p} \\ &+ B_8 q_\rho \frac{q^\mu \omega^\nu + q^\nu \omega^\mu}{2\omega \cdot p}\ , \end{aligned} \qquad (5\text{-}17)$$

where $B_{1-8}(Q^2)$ are invariant functions and $P = p + p'$. Increasing the number of the invariant functions in Equation 5-17, in comparison with Equation 5-12, from three to eleven means that the number of independent matrix elements $\langle p', h' \mid \tilde{J}_\rho \mid p, h\rangle$ (at arbitrary values of the indices h, h', ρ) is equal to eleven. For the particular choice $\omega = (1, 0, 0, -1)$ one returns to the case $t + z = 0$ and has $\omega^+ = 0$. Thus, it follows from the condition $\omega \cdot q = 0$ that $q^+ = 0$. In this case, the physical and non-physical terms turn out to be unseparated from each other because of the non-covariance of the approach, but the number of independent matrix elements remains equal to eleven.

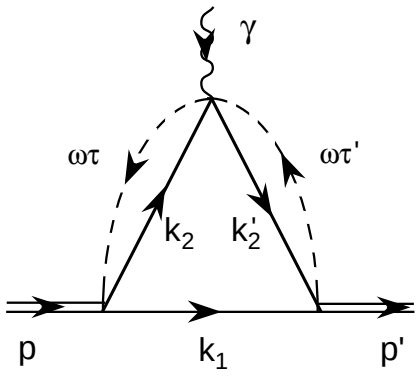

Fig. 5-10: Electromagnetic vertex of the deuteron in light-front dynamics (see text).

The decomposition of Equation 5-12 is valid for the full electromagnetic current operator. The one-body current $\tilde{J}_\rho$ (see Figure 5-10) is given by the following analytical expression:

$$\begin{aligned}
\langle h'|\tilde{J}_\rho|h\rangle &= e^{*h'}_\mu(p')\tilde{J}^{\mu\nu}_\rho e^h_\nu(p)\ , \quad \text{where} \\
\tilde{J}^{\mu\nu}_\rho &= \frac{M_N}{(2\pi)^3}\int Tr[\phi'^\mu(\hat{k}'_2+M_N)\Gamma_\rho(\hat{k}_2+M_N)\phi^\nu(\hat{k}_1-M_N)] \\
&\quad \times\frac{\theta(\omega\cdot k_1)\theta(\omega\cdot k_2)\theta(\omega\cdot k'_2)}{(1-\omega\cdot k_1/\omega\cdot p)^2}\frac{d^3k_1}{2\varepsilon_{k_1}}\ ,
\end{aligned} \tag{5-18}$$

where $\hat{k} = k_\mu\gamma^\mu$. The matrix ϕ^μ is given by Equation 5-31, while the matrix ϕ'^ν is obtained from ϕ_ν by the replacement $k_2 \to k'_2$. Γ_ρ is the electromagnetic vertex of the nucleon given by:

$$\Gamma^\rho = F_1\gamma^\rho + \frac{iF_2}{2M_N}\sigma^{\rho\alpha}q_\alpha\ , \tag{5-19}$$

with F_1 and F_2 being the nucleon Dirac and Pauli elecromagnetic form factors.

The explicit expressions for the form factors are obtained by solving Equation 5-16 relative to $\mathcal{F}_1$, $\mathcal{F}_2$ and $\mathcal{G}_1$. The result is:

$$\mathcal{F}_1 = \tilde{J}^{\mu\nu}_{\rho}\frac{\omega^{\rho}}{2\omega\cdot p}\left[g_{\mu\nu}-\frac{q_\mu q_\nu}{q^2}-\frac{P_\mu\omega_\nu+P_\nu\omega_\mu}{2\omega\cdot p}+P^2\frac{\omega_\mu\omega_\nu}{4(\omega\cdot p)^2}\right] , \tag{5-20}$$

$$\begin{aligned}\frac{\mathcal{F}_2}{2M_d^2} &= -\tilde{J}^{\mu\nu}_{\rho}\frac{\omega^{\rho}}{2(\omega\cdot p)q^2}\left[g_{\mu\nu}-2\frac{q_\mu q_\nu}{q^2}-\frac{P_\mu\omega_\nu+P_\nu\omega_\mu}{2\omega\cdot p}\right.\\ &\left.+M_d^2\frac{\omega_\mu\omega_\nu}{(\omega\cdot p)^2}-\frac{q_\mu\omega_\nu-q_\nu\omega_\mu}{2\omega\cdot p}\right] ,\end{aligned} \tag{5-21}$$

$$\begin{aligned}\mathcal{G}_1 &= \frac{1}{4}\tilde{J}^{\mu\nu}_{\rho}\left\{2\frac{g^{\rho}_{\mu}q_\nu-g^{\rho}_{\nu}q_\mu}{q^2}+\frac{g^{\rho}_{\mu}\omega_\nu+g^{\rho}_{\nu}\omega_\mu}{\omega\cdot p}\right.\\ &+\frac{\omega^{\rho}}{\omega\cdot p}\left[-P^2\frac{q_\mu\omega_\nu-q_\nu\omega_\mu}{2(\omega\cdot p)q^2}+\frac{q_\mu P_\nu-q_\nu P_\mu}{q^2}+P^2\frac{\omega_\mu\omega_\nu}{2(\omega\cdot p)^2}-\frac{P_\mu\omega_\nu+P_\nu\omega_\mu}{2(\omega\cdot p)}\right]\\ &\left.+P^{\rho}\left[\frac{q_\mu\omega_\nu-q_\nu\omega_\mu}{(\omega\cdot p)q^2}-\frac{\omega_\mu\omega_\nu}{(\omega\cdot p)^2}\right]-q^{\rho}\frac{q_\mu\omega_\nu+q_\nu\omega_\mu}{(\omega\cdot p)q^2}\right\} .\end{aligned} \tag{5-22}$$

These expressions determine the deuteron electromagnetic form factors. In spite of the fact that ω enters the right hand side of Equations 5-20–5-22, these expressions do not depend on ω. Using the exact decomposition of Equation 5-12, one can express the matrix elements $< h'|J^+|h > \equiv J^+_{h'h}$ in terms of the form factors:

$$J^+_{11} = -\mathcal{F}_1+\eta\mathcal{F}_2 , \tag{5-23}$$

$$J^+_{1-1} = -\eta\mathcal{F}_2 , \tag{5-24}$$

$$J^+_{10} = -\sqrt{2\eta}(\mathcal{F}_1-\eta\mathcal{F}_2+\mathcal{G}_1/2) , \tag{5-25}$$

$$J^+_{00} = -(1-2\eta)\mathcal{F}_1-2\eta^2\mathcal{F}_2+2\eta\mathcal{G}_1 . \tag{5-26}$$

The four matrix elements in Equations 5-23–5-26 can be expressed through three form factors and, hence, are not independent from each other. They satisfy the relation:

$$(1+2\eta)J^+_{11}+J^+_{1-1}-2\sqrt{2\eta}J^+_{10}-J^+_{00}=0 , \tag{5-27}$$

which can be checked by direct substitution. This condition is called the "angular condition".

In principle, with the exact matrix elements $J^+_{h'h}$ one can calculate any triplet of matrix elements and find the form factors. This is not possible however for the approximate ones $\tilde{J}^+_{h'h}$. These matrices are not given by the decomposition 5-12, but should be calculated according to Equation 5-16. The matrix elements of 5-16 have the form:

$$\begin{aligned}
\tilde{J}^+_{1,1} &= -\mathcal{F}_1 + \eta\mathcal{F}_2 \ , \\
\tilde{J}^+_{1,-1} &= -\eta\mathcal{F}_2 \ , \\
\tilde{J}^+_{1,0} &= -\sqrt{2\eta}(\mathcal{F}_1 - \eta\mathcal{F}_2 + \mathcal{G}_1/2) + \sqrt{\eta/2}B_6 \ , \\
\tilde{J}^+_{0,0} &= -(1-2\eta)\mathcal{F}_1 - 2\eta^2\mathcal{F}_2 + 2\eta\mathcal{G}_1 - 2\eta B_6 + B_5 + B_7 \ . \qquad (5\text{-}28)
\end{aligned}$$

The matrix elements $\tilde{J}^+_{11}, \tilde{J}^+_{1-1}$ have the same form as J^+_{11}, J^+_{1-1}, whereas $\tilde{J}_{10}, \tilde{J}^+_{00}$ differ from J^+_{10}, J^+_{00} by the items containing the non-physical form factors B_5, B_6, B_7. The non-physical form factors B_{1-4} and B_8 do not contribute to these matrix elements.

The matrix elements $\tilde{J}^+_{h'h}$ do not satisfy the condition (5-27). Substituting $\tilde{J}^+_{h'h}$ in Equation 5-27 instead of $J^+_{h'h}$, we obtain:

$$\Delta \equiv (1+2\eta)\tilde{J}^+_{11} + \tilde{J}^+_{1-1} - 2\sqrt{2\eta}\tilde{J}^+_{10} - \tilde{J}^+_{00} = -(B_5 + B_7) \ . \qquad (5\text{-}29)$$

The relativistic light-front deuteron wave function is determined by six invariant spin components, in contrast to two components (S- and D-states) in the non-relativistic case. The decomposition of the wave function $\Phi^h_{\sigma_2\sigma_1}$ in independent spin structures has the general form [74]:

$$\Phi^h_{\sigma_2\sigma_1} = \sqrt{M_N}e^h_\mu(p)\bar{u}^{\sigma_2}(k_2)\phi_\mu U_c\bar{u}^{\sigma_1}(k_1) \ , \qquad (5\text{-}30)$$

with:

$$\phi_\mu = \varphi_1 \frac{(k_1-k_2)_\mu}{2M_N^2} + \varphi_2 \frac{1}{M_N}\gamma_\mu + \varphi_3 \frac{\omega_\mu}{\omega\cdot p} + \varphi_4 \frac{(k_1-k_2)_\mu \hat{\omega}}{2M_N \omega\cdot p}$$
$$+\varphi_5 \frac{i}{2M_N^2 \omega\cdot p}\gamma_5 \epsilon_{\mu\nu\rho\gamma}(k_1+k_2)_\nu (k_1-k_2)_\rho \omega_\gamma + \varphi_6 \frac{M_N \omega_\mu \hat{\omega}}{(\omega\cdot p)^2} \ , \qquad (5\text{-}31)$$

where M_N is the nucleon mass, $\hat{\omega} = \omega_\mu \gamma^\mu$, p and $k_{1,2}$ are the on-mass-shell deuteron and nucleon momenta, $e^h_\nu(p)$ is the deuteron polarization vector, $\bar{u}^\sigma(k)$ is the nucleon spinor, $U_c = \gamma_2\gamma_0$ is the charge conjugation matrix. We notice that the wave function defined on the light-front plane depends on the orientation of this plane through the argument ω.

The light-front deuteron wave function is determined by six invariant functions φ_{1-6}, depending on two scalar variables, *e.g.*, $s = (k_1+k_2)^2$ and $t = (p-k_1)^2$. The extra spin structures in front of φ_{3-6} are constructed by means of the four-vector ω. Other possible structures (like $e^h_\mu \overline{u}_2 \hat{\omega}\gamma_\mu U_c \overline{u}_1$) are expressed through the six structures given by Equation 5-31.

In the reference system where $\vec{k}_1 + \vec{k}_2 = 0$, decomposition of the wave function of Equation 5-31 takes the form [75]:

$$\Psi^h_{\sigma_2\sigma_1}(\vec{k},\vec{n}) = \sqrt{M_N} w^\dagger_{\sigma_2} \psi^h(\vec{k},\vec{n}) \sigma_y w^\dagger_{\sigma_1} \ , \qquad (5\text{-}32)$$

with:

$$\begin{aligned}
\vec{\psi}(\vec{k},\vec{n}) &= f_1 \frac{1}{\sqrt{2}}\vec{\sigma} + f_2 \frac{1}{2}\left(\frac{3\vec{k}(\vec{k}\cdot\vec{\sigma})}{\vec{k}^2} - \vec{\sigma}\right) + f_3 \frac{1}{2}(3\vec{n}(\vec{n}\cdot\vec{\sigma}) - \vec{\sigma}) \\
&+ f_4 \frac{1}{2k}(3\vec{k}(\vec{n}\cdot\vec{\sigma}) + 3\vec{n}(\vec{k}\cdot\vec{\sigma}) - 2(\vec{k}\cdot\vec{n})\vec{\sigma}) \\
&+ f_5 \sqrt{\frac{3}{2}}\frac{i}{k}[\vec{k}\times\vec{n}] + f_6 \frac{\sqrt{3}}{2k}[[\vec{k}\times\vec{n}]\times\vec{\sigma}] \ , \qquad (5\text{-}33)
\end{aligned}$$

where $\vec{k}$ is the value of $\vec{k}_1$ in this system of reference, $\vec{n}$ is the direction of $\vec{\omega}$ in this system, w_σ is the two-component nucleon spinor. The relation between ψ^h and $\vec{\psi}$ is the same as the

relation between the spherical function $Y_1^h(\vec{n})$ and $\vec{n}$. The scalar functions f_{1-6} depend on the scalars $\vec{k}^{\,2}$ and $\vec{n}\cdot\vec{k}$ or $k \equiv |\vec{k}|$ and $z = \cos(\widehat{\vec{n}\vec{k}})$. The components φ_i in Equation 5-31 and f_i in Equation 5-33 are linearly related with each other [63, 74]. The equation for the wave function $\Phi^h_{\sigma_1\sigma_2}$ has the form:

$$\begin{aligned}\left[4(\vec{k}^{\,2}+M_N^2)-M_d^2\right]\vec{\psi}_{\sigma_1\sigma_2} &= -\frac{M_N^2}{2\pi^3} \\ &\times \sum\int\left[\vec{\psi}'(\vec{k}\,',\vec{n})\sigma_y\right]_{\sigma_1'\sigma_2'} V^{\sigma_1'\sigma_2'}_{\sigma_1\sigma_2''}(\vec{k}\,',\vec{k},\vec{n},M)(\sigma_y)_{\sigma_1''\sigma_1}\frac{d^3k'}{\varepsilon_{k'}}\ .\end{aligned} \tag{5-34}$$

In the region $k \ll M_N$, the functions f_{3-6} which are of relativistic origin become negligible, $f_{1,2}$ do not depend anymore on z and turn into the S- and D-state wave functions: $f_1 \simeq u_S$, $f_2 \simeq -u_D$. From the general decomposition of Equation 5-33, one recovers the usual non-relativistic wave function:

$$\vec{\psi}_{NR}(\vec{k}\,) = u_S(k)\frac{1}{\sqrt{2}}\vec{\sigma} - u_D(k)\frac{1}{2}\left[\frac{3\vec{k}(\vec{k}\cdot\vec{\sigma})}{\vec{k}^{\,2}} - \vec{\sigma}\right]\ . \tag{5-35}$$

A peculiarity of LFD is the existence, in addition to the impulse approximation (Figure 5-10), of the so called instantaneous (or contact) interaction in the $NNB\gamma$ vertex, where B is any of the mesons building the NN potential. There are four diagrams corresponding to the contact terms as shown in Figure 5-11.

Substituting the tensor $\tilde{J}^{\rho}_{\mu\nu}$ defined by Equation 5-18 into Equations 5-20–5-22 for $\mathcal{F}_1$, $\mathcal{F}_2$ and $\mathcal{G}_1$, and calculating the contractions and traces, one finds the expression for the form factors. Carbonell and Karmanov [77] calculated the deuteron form factors in the framework of the relativistic nucleon-meson dynamics, by means of the explicitly covariant light-front approach. Their perturbative method to calculate the wave function is restricted to relative nucleon momenta k smaller than the nucleon mass M_N. Then one should expect a reasonable description of the experimental data in the momentum transfer region

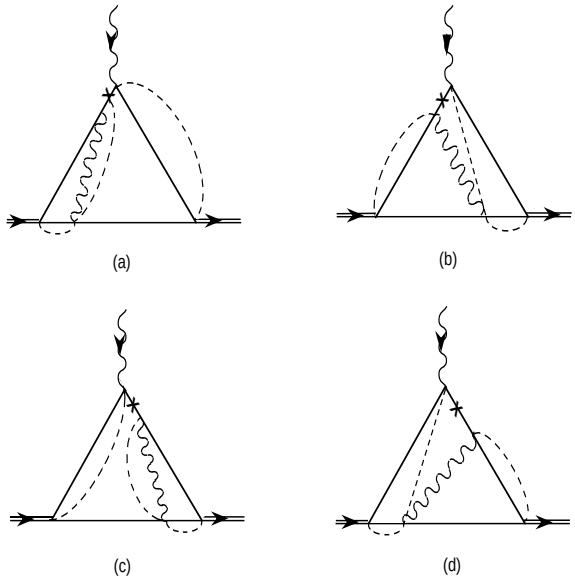

Fig. 5-11: Contact term contribution to the electromagnetic interaction with the deuteron (see text).

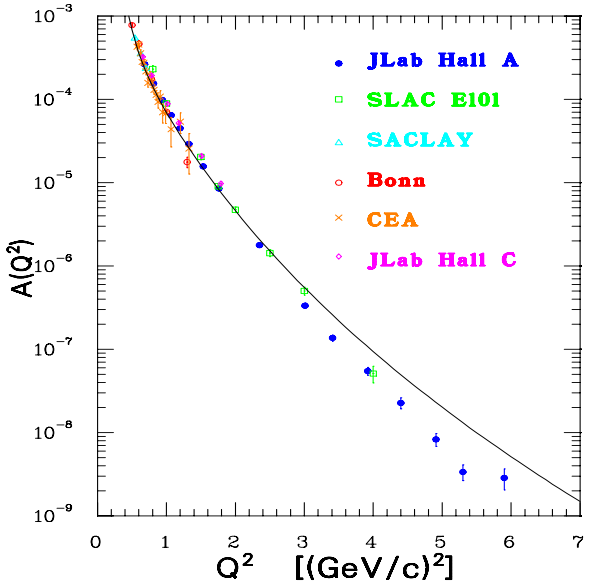

Fig. 5-12: $A(Q^2)$ data compared to the model of Carnobell and Karmanov [77]. The solid line is the relativistic impulse approximation with relativistic deuteron components f_1 and f_2 with the inclusion of the f_5 component (only to first order) and the contact term. The nucleon form factors were taken from Mergell *et al.* [76].

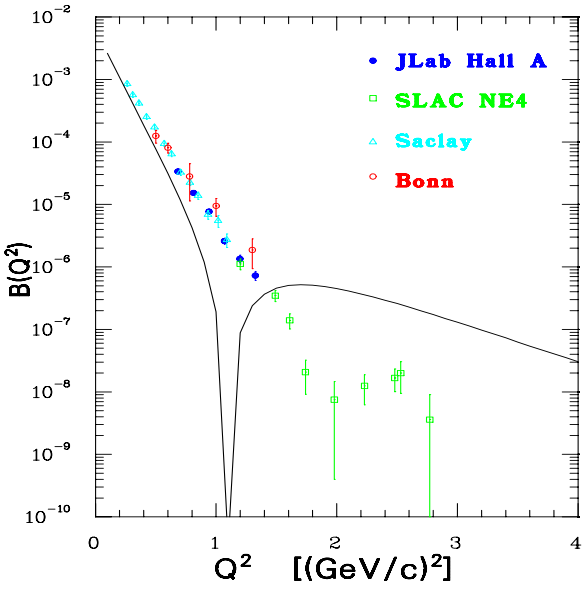

Fig. 5-13: $B(Q^2)$ data compared to the model of Carnobell and Karmonov [77]. The solid line is the relativistic impulse approximation with relativistic deuteron components f_1 and f_2 with the inclusion of the f_5 component (only to first order) and the contact term. The nucleon form factors were taken from Mergell *et al.* [76].

$Q^2 \leq (2M_N)^2 \sim 3.5$ (GeV/c)^2. They used a parameterization of the nucleon electromagnetic form factors obtained by Mergell *et al.* [76]. Their results are shown in Figures 5-12 and 5-13. Only the first order contribution from f_5 was kept and terms like f_5^2 were removed from the calculation of the form factor. There is good agreement in describing $A(Q^2)$ up to $Q^2 = 2.5$ (GeV/c)^2, a momentum region where the departure from a non-relativistic description reaches one order of magnitude. Their calculations do not describe $B(Q^2)$, especially in the region of the minimum. The minimum disappears when using only f_1 and f_2 and appears again when f_5, which is of relativistic origin, is included. This minimum is thus a consequence of delicate cancellation between the f_5 contribution and the contributions of f_1 and f_2. None of the f_1, f_2, f_5 components have been calculated with enough accuracy in their perturbative approach. The contribution of the contact terms to $A(Q^2)$ and low-Q^2 $B(Q^2)$ is found to be small. Note that meson-exchange currents and isobar configurations

were not taken into account in the above LFD calculations. However, to leading order in $1/M_N$, the extra component f_5 accounts for the so called pair terms in deuteron electro-disintegration amplitude [78]. Furthermore, starting from $k \simeq 0.5$ GeV/c, component f_5 dominates over all other components, including f_1 and f_2.

5.3.2 Manifestly Covariant Dynamics

Manifestly Covariant Dynamics can be said to have started with the introduction of the Bethe-Salpeter (BS) Equation in 1951. Some authors refer to any equation for the scattering amplitude T which is of the linear form:

$$T = K - KG_{BS}T \ , \tag{5-36}$$

where K is the Bethe-Salpeter interaction kernel and G_{BS} is the Bethe-Salpeter free two-body propagator, as a BS equation. The interacting two-body propagator is then:

$$G = G_{BS} - G_{BS}TG_{BS} \ . \tag{5-37}$$

5.3.2.1 Quasi-Potential Approximation

The Bethe-Salpeter equation is a four-dimensional equation which makes it very difficult to solve. This leads to consideration of a class of two-body equations called quasi-potential equations. These equations are an approximation to the Bethe-Salpeter equation involving replacing the free propagator G_{BS} by a new propagator g. The scattering matrix equation can now be rewritten as:

$$T = U - UgT \ , \tag{5-38}$$

where U is the quasi-potential defined as:

$$U = K - K(G_{BS} - g)U \ . \tag{5-39}$$

The new propagator g is usually chosen to include a one-dimensional delta function constraining the relative energy of the freely propagating pair. Then Equation 5-38 becomes a three-dimensional equation for the amplitude T. In principle U should be determined by solving the four-dimensional Equation 5-39. However, given the difficulty of solving such equations, and the lack of knowledge about the best form of U for hadronic physics, usually U is chosen to be a one-boson-exchange interaction:

$$U = V_{OBE} \ , \tag{5-40}$$

with coupling constants selected to provide a realistic description of the NN scattering data and deuteron static properties.

Van Orden *et al.* [66] calculated the elastic electromagnetic form factors for the deuteron in the context of a one-boson-exchange model using the Gross or Spectator Equation [79]. The Gross equation is an example of a quasi-potential equation. This equation is obtained by imposing a constraint on the propagation of particles in intermediate states, in which the relative energy is constrained by restricting the spectator nucleon to its mass shell.

Different models for the NN interaction were presented in Reference [80]. Each model was fitted to the NN phase shift data [82] and constrained so that the deuteron binding energy is correct. These models use a one-boson-exchange kernel containing six mesons: π, η, σ, δ, ω and ρ, where the δ meson is a scalar-isovector companion to the σ with a mass comparable to the σ mass. The properties of these mesons are listed in Table 5-3. The interaction model used in the calculations shown here is a variation of model IIB, in which the parameters of the model have been adjusted to fit the Nijmegen energy dependent np phase shifts [83].

	π	ρ	ω	σ	η
mass (MeV)	138.8	763.6	782.8	$\sim$500	548.8
Spin-party, J^π	0^-	1^-	1^-	0^+	0^-
Isospin, I	1	1	0	0	0

Table 5-3: Properties of mesons used in one-boson-exchange models of the NN potential.

The deuteron wave functions for model W16 of Reference [80], similar to the IIB model, are shown in Figure 5-14 along with the IIB model wave functions. There are four wave functions, the usual S- and D-state wave functions that appear in the non-relativistic treatment of the deuteron and singlet and triplet P-states of relativistic origin. These new components of the full wave function are associated with the extra degrees of freedom present when the interacting nucleon is a virtual Dirac particle, and each has the character of a P-state. They are small numerically if measured by their contribution to the overall normalization of the wave function, but in momentum space they and the S- and D-state functions have comparable magnitude at high momenta. Note that although the orbital angular momentum of these small components is $l = 1$, they do not represent parity violating effects because, in common with the small components in the Dirac equation, the overall parity of a small component is opposite to its spatial parity. The normalization condition satisfied by these wave functions is:

$$\int_o^\infty dr\Big\{u^2 + w^2 + v_t^2 + v_s^2\Big\} + \langle\frac{\partial V_{OBE}}{\partial M_d}\rangle = 1 \ , \tag{5-41}$$

where the contributions to the normalization of the wave function from these components are: 92.979% for the S-state, 5.015% for the D-state, 0.049% for the triplet P-state and 0.009% for the singlet P-state. The remaining 2% is associated with the derivative term arising from the energy dependence of the kernel V_{OBE} [80].

The application of the Gross equation to the calculation of nucleon-nucleon scattering

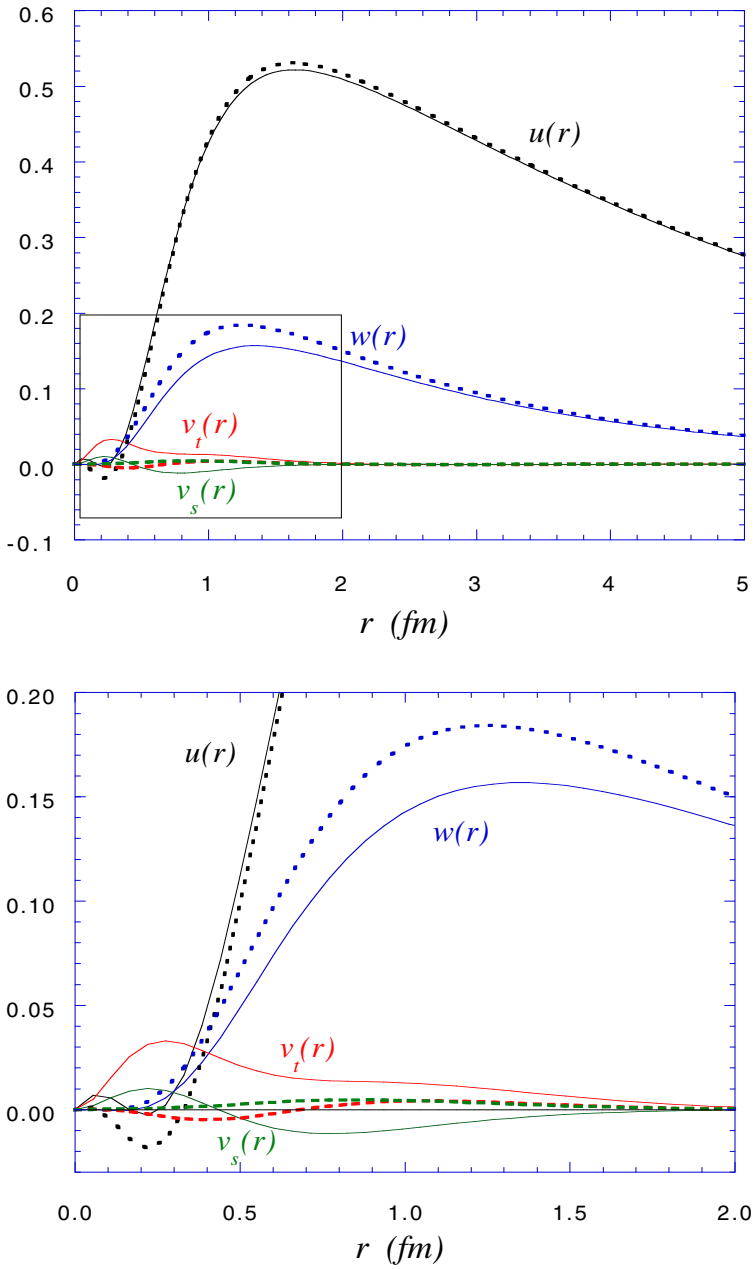

Fig. 5-14: The four relativistic wave functions for Models IIB (solid lines) and W16 (dotted lines) of Reference [80]. The boxed region in the upper panel is shown in the lower panel.

and the deuteron bound state is described in considerable detail in Reference [80], which uses a one-boson-exchange interaction kernel, explicitly antisymmetrized in order to insure that the Pauli principle is exactly satisfied. There is an important feature that characterizes the OBE kernels: the meson-nucleon couplings include off-shell couplings and form factors which depend upon the invariant masses of the three virtual particles connected to the interaction vertex. The vertex form factors can be written in a factorizable form [80, 81]

$$F_i(p'^2, p^2, \ell^2) \equiv h(p'^2)h(p^2)f_i(\ell^2) \ , \tag{5-42}$$

where p and p' are the initial and final nucleon four-momenta, $\ell = p - p'$ is the meson four-momentum, and $f(\ell^2)$ and $h(p^2)$ are meson and nucleon form factors, respectively. These form factors are given by:

$$h(p^2) \equiv \frac{2(\Lambda_N^2 - m^2)^2}{(\Lambda_N^2 - p^2)^2 + (\Lambda_N^2 - m^2)^2} \tag{5-43}$$

and:

$$f_i(\ell^2) \equiv \frac{(\Lambda_m^2 - m_i^2)^2 + \Lambda_m^4}{(\Lambda_m^2 - \ell^2)^2 + \Lambda_m^4} \ , \tag{5-44}$$

where the mass of the i-th meson is denoted by m_i and the nucleon and meson form factor masses (equal for all mesons) are denoted by Λ_N and Λ_m. These form factors are essential for the convergence of the equations.

The construction of appropriate current matrix elements for the Gross equation that maintain gauge invariance is discussed in Reference [81]. For the electromagnetic interactions to conserve current, the electromagnetic currents for the off-shell nucleons and mesons must satisfy the Ward-Takahashi (WT) identities [84]. In order to satisfy the WT identities in the presence of the form factors (Equation 5-42), an off-shell single-nucleon current operator must be introduced. A minimal form of the operator is given by [85]:

$$
\begin{aligned}
J^{(i)\mu}(p',p) &= F_1(Q^2) f_0(p'^2,p^2)\,\gamma^\mu \\
&\quad + \frac{F_2(Q^2)}{2M_N} h_0(p'^2,p^2)\, i\sigma^{\mu\nu} q_\nu \\
&\quad + F_3(Q^2) g_0(p'^2,p^2)\, \frac{\not{p}' - M_N}{2M_N}\,\gamma^\mu\,\frac{\not{p} - M_N}{2M_N}\ ,
\end{aligned}
\tag{5-45}
$$

where:

$$
f_0(p'^2,p^2) \equiv \frac{h(p^2)}{h(p'^2)}\,\frac{M_N^2 - p'^2}{p^2 - p'^2} + \frac{h(p'^2)}{h(p^2)}\,\frac{M_N^2 - p^2}{p'^2 - p^2}\ , \tag{5-46}
$$

$$
g_0(p'^2,p^2) \equiv \left(\frac{h(p^2)}{h(p'^2)} - \frac{h(p'^2)}{h(p^2)}\right)\frac{4M_N^2}{p'^2 - p^2}\ , \tag{5-47}
$$

and $F_3(Q^2)$ and $h_0(p'^2,p^2)$ are arbitrary functions subject only to the constraints that $F_3(0) = 1$ and $h_0(M_N^2, M_N^2) = 1$. In the calculations presented here, $h_0(p'^2,p^2) = f_0(p'^2,p^2)$ and $F_3(Q^2) = G_E^p(Q^2)$, for simplicity.

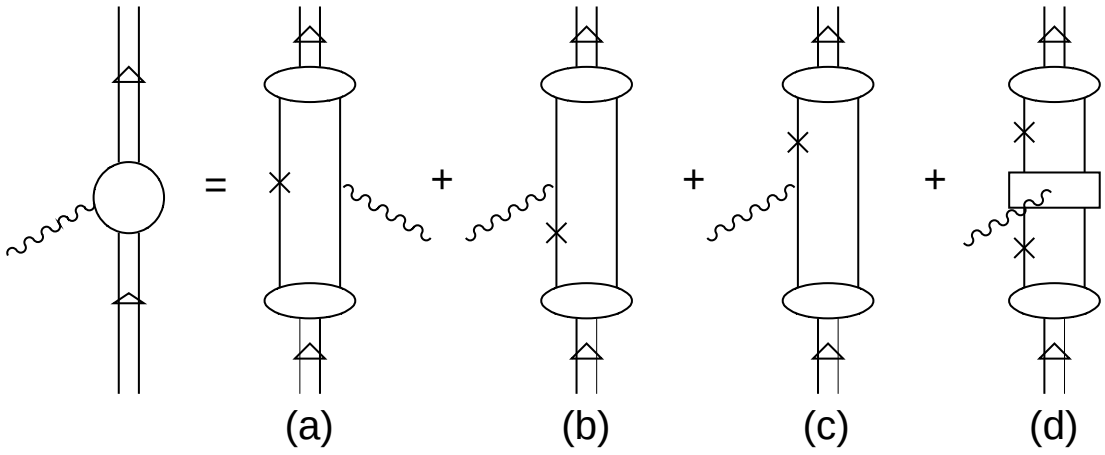

Fig. 5-15: Feynman diagrams representing the Gross current matrix element in electron-deuteron elastic scattering (see text).

In constructing the current matrix element it is necessary that the on-shell constraint

used in the Gross equation be consistently applied to the calculation of the current matrix element. In the case of the Gross equation, the correct expression for the current matrix element can be obtained by keeping only the positive energy nucleon poles for particle 1 in the evaluation of the energy loop integrals of the Bethe-Salpeter current matrix element. For the elastic matrix elements this leads to the Feynman diagrams displayed in Figure 5-15. Here the ovals represent the deuteron vertex functions, single lines represent nucleon propagators, lines with crosses denote on-shell nucleons, and the wavy lines represent virtual photons.

The Blankenbecler-Sugar-Logunov-Tavkheidze (BSLT) [86, 87] equation is another example of quasipotential reduction of the Bethe-Salpeter Equation. Here both particles are treated in a symmetrical way by keeping both particles equally off-shell. The three-dimensional reduction is obtained by setting relative energies to zero. Hummel and Tjon [3] calculated the elastic electromagnetic form factors for the deuteron in the context of a one-boson-exchange model using the BSLT equation. The BSLT current matrix element is described by diagram (a) of Figure 5-15 along with a symmetric diagram where the photon attaches to particle 1 and particle 2 is placed on mass shell. Because of the symmetry of the matrix element, the contribution of the second diagram is equivalent to diagram (a) of Figure 5-15. Thus, this approximation is equivalent to simply calculating 2×diagram (a) of Figure 5-15. Since the form of this approximation looks like a matrix element of a single-nucleon current between spectator wave functions, it is referred to as the relativistic impulse approximation. Since the combination of diagrams (a), (b) and (c) of Figure 5-15 are related to the relativistic impulse approximation but represent a complete gauge-invariant description of the Gross one-body current matrix elements, the Van Orden *et al.* calculations are referred to as the complete impulse approximation (CIA).

The structure functions calculated in the CIA with the dipole parameterization of the single-nucleon form factors of Galster [88] and the RIA of Hummel and Tjon [3] with

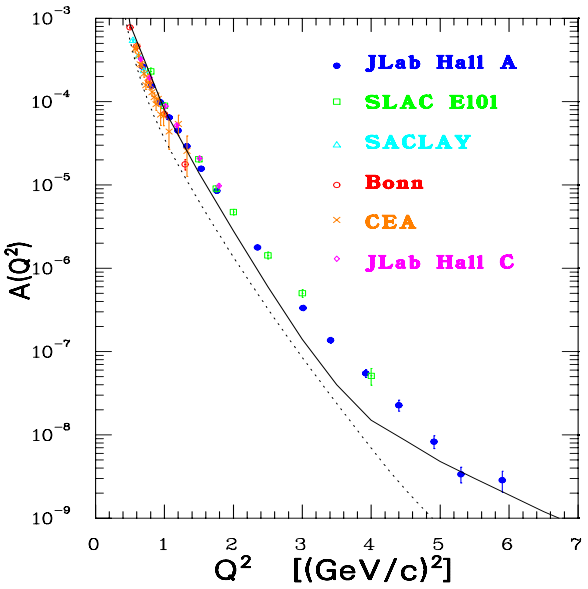

Fig. 5-16: The electric structure function $A(Q^2)$. The solid line is the CIA of Van Orden *et al.* [66] and the dotted line is the RIA of Hummel and Tjon [3].

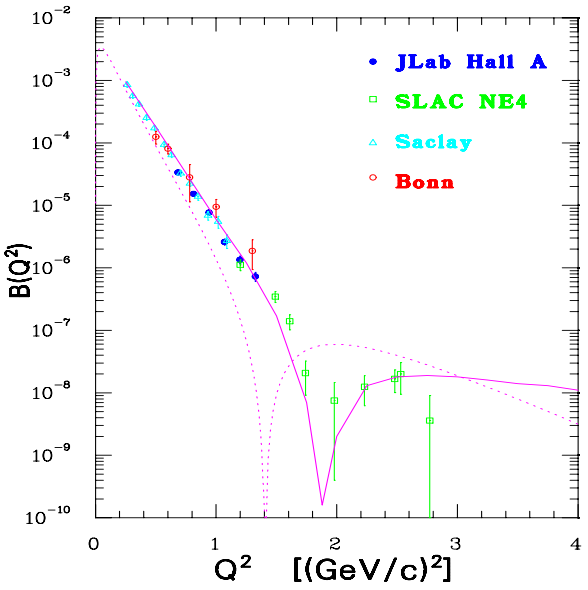

Fig. 5-17: The magnetic structure function $B(Q^2)$. The solid line is the CIA of Van Orden *et al.* [66] and the dotted line is the RIA of Hummel and Tjon [3].

Höhler single-nucleon electromagnetic form factors [48] are shown in Figures 5-16 and 5-17. The RIA calculation, as described above, uses an on-shell form of the single nucleon current operator obtained by setting $f_0 = h_0 = 1$ and $g_0 = 0$ in Equation 5-45. Only small contributions from the exchange currents are required to bring the CIA into good agreement with the data. Note that for the CIA calculation, the minimum of $B(Q^2)$ is at larger Q^2 than in the calculation of Hummel and Tjon. This appears to be the result of dynamical differences in the interaction models used.

The low-Q^2 limit for the RIA can be obtained to first order in $(Q/M_N)^2$ following the standard style of IA. The electromagnetic form factors of the deuteron can be decomposed as:

$$\begin{aligned} F_C &= G_E^S D_C + (2G_M^S - G_E^S) D_C^{so} \ , \\ F_Q &= G_E^S D_Q + (2G_M^S - G_E^S) D_Q^{so} \ , \\ F_M &= G_E^S D_M^E + G_M^S D_M^M \ , \end{aligned} \tag{5-48}$$

where:

$$\begin{aligned} D_C &= \int_0^\infty dr j_0(\tau)(u^2+w^2) - \left(\frac{Q^2}{8M_N^2} + \frac{Q^4}{16M_N^2}\frac{d}{dQ^2}\right)\int_0^\infty dr j_0(\tau)(u^2+w^2) \\ &\quad + \frac{Q^2}{M_N^2}\frac{d^2}{dQ^2}\int_0^\infty dr j_0(\tau)\Big[u\Big(-\frac{d^2}{dr^2}+\alpha^2\Big)u + w\Big(-\frac{d^2}{dr^2}+\frac{6}{r^2}+\alpha^2\Big)w\Big] \ , \end{aligned} \tag{5-49}$$

$$\begin{aligned} D_C^{so} &= \frac{Q^2}{12M_N^2}\int_0^\infty dr[j_0(\tau)+j_2(\tau)]\left(\frac{2}{3}w^2 - \sqrt{\frac{2}{3}}M_N r v_t(u+\frac{1}{\sqrt{2}}w) + \right. \\ &\quad \left. \frac{1}{\sqrt{3}}M_N r v_s(u-\sqrt{2}w)\right) \ , \end{aligned} \tag{5-50}$$

$$\begin{aligned} D_Q &= \frac{6\sqrt{2}M_d^2}{Q^2}\left[\int_0^\infty dr[j_0(\tau)+j_2(\tau)]\left(uw - \frac{w^2}{2\sqrt{2}}\right) - \left(\frac{Q^2}{8M_N^2} + \frac{Q^4}{16M_N^2}\frac{d^2}{dQ^2}\right)\times \right. \\ &\quad \left. \int_0^\infty dr j_2(\tau)\left(uw - \frac{w^2}{2\sqrt{2}}\right)\right. \end{aligned}$$

$$+\frac{Q^2}{2M_N^2}\frac{d^2}{dQ^2}\int_0^\infty dr j_2(\tau)\Big[w\Big(-\frac{d^2}{dr^2}+\alpha^2\Big)u+u\Big(-\frac{d^2}{dr^2}+\frac{6}{r^2}+\alpha^2\Big)w-$$
$$\frac{w}{\sqrt{2}}\Big(-\frac{d^2}{dr^2}+\frac{6}{r^2}+\alpha^2\Big)w\Big]\Big]\ , \tag{5-51}$$

$$D_Q^{so} = \int_0^\infty dr\Bigg((\sqrt{2}rwu'-\sqrt{2}rww')\Big\{\frac{3}{5}[j_0(\tau)+j_2(\tau)]\Big\}$$
$$+M_N r\frac{2}{\sqrt{3}}u\Big[v_s+\frac{1}{\sqrt{2}}v_t\Big][j_0(\tau)+j_2(\tau)]-M_N r[\sqrt{3}wv_t]\times$$
$$\Big\{\frac{9}{35}[j_2(\tau)+j_4(\tau)]+\frac{4}{15}[j_0(\tau)+j_2(\tau)]\Big\}$$
$$+M_N r[\sqrt{\frac{3}{2}}wv_s]\left\{\frac{18}{35}[j_2(\tau)+j_4(\tau)]-\frac{2}{15}[j_0(\tau)+j_2(\tau)]\right\}\Bigg)\ , \tag{5-52}$$

$$D_M^E = \int_0^\infty dr\left\{\frac{3}{2}w^2+\frac{2M_N r}{\sqrt{3}}\left[v_t\left(\frac{1}{\sqrt{2}}u-w\right)\right.\right.$$
$$\left.\left.-v_s\left(u+\frac{1}{\sqrt{2}}w\right)\right]\right\}[j_0(\tau)+j_2(\tau)]\ , \tag{5-53}$$

$$D_M^M = \int_0^\infty dr\left[\left(2u^2-w^2\right)j_0(\tau)+\left(\sqrt{2}uw+w^2\right)j_2(\tau)\right]\ , \tag{5-54}$$

with $\tau=\frac{Qr}{2}$ and $\alpha=M_N\epsilon$, where ϵ is the binding energy of the deuteron and M_N the nucleon mass. Here u, w, v_t and v_s are the S-, D-, triplet P- and singlet P-state wave functions. All terms quadratic in the P-states are very small in this region.

Van Orden *et al.* found that the structure function $B(Q^2)$ is extremely sensitive to the presence of small P-state components of the deuteron wave function of relativistic origin. In particular the position of the minimum of $B(Q^2)$ is very sensitive to the sign of the singlet P-state v_s. This last observation is very surprising, because the probability of the v_s state is only 0.009%. The reason such a small component can have such a large effect is due to a double interference between the small P-states and the larger S- and D-state components. Note the additional terms in D_M^E where the small components of the deuteron wave function interfere with the large components, enhancing the overall effect of the small components. A second interference will occur if the sign of the v_t component is opposite to v_s. In this case, the two separate interference terms, which are individually small, will add coherently giving the large effect.

5.3.2.2 Equal Time Approximation

A basic flaw exists in the quasipotential formalism that is based on a form of a propagator, g, which contains a delta function. It is generally impossible to systematically correct the lowest-order approximation by the use of Equation 5-39 because unphysical singularities arise. Phillips and Wallace [89] derived a systematic procedure for obtaining three-dimensional bound-state equations from the Bethe-Salpeter one. Unlike the quasipotential formalism this procedure does not involve the use of δ-function constraints on the relative four-momentum. The three-dimensional reduction is obtained by integrating out relative energies. For the propagator of the theory, this produces a form corresponding to zero relative time of the two particles. In configuration space, this action is equivalent to considering the propagator in which the two particles involved are considered only on equal-time (ET) slices. Thus, this is referred to as the ET propagator. Phillips, Wallace, and Devine [67] derived a refined version of the ET formalism of Wallace and Mandelzweig [90, 91] to avoid the unphysical singularities which otherwise occur in the three-dimensional ET interaction with retardations when it is evaluated in a frame where the bound state has a large three-momentum.

The deuteron elastic structure functions were calculated using an instant approximation for the electromagnetic current, in which the time component of photon momentum vanishes, *i.e.* $q^0 = 0$. In the center-of-mass frame, the equally off-shell constraint is equivalent to an instant formalism because the constraint causes the interactions to have zero time component of momentum transfer. This current satisfies current conservation when used with deuteron vertex functions that are obtained with instant one-boson-exchange interaction. Also this simple current has been used with vertex functions calculated with the full retarded OBE interaction obtained in the systematic ET formalism. Two-body currents were included, such as the one shown in Figure 5-18, which become necessary in order to satisfy current conservation when retardation effects are included. The wave functions were

those from the Bonn-B version of the Bonn potential [92], but with a small adjustment to the σ-meson coupling.

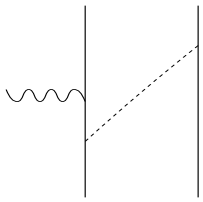

Fig. 5-18: One example of a two-body current which becomes necessary in order to satisfy current conservation when retardation effects are included.

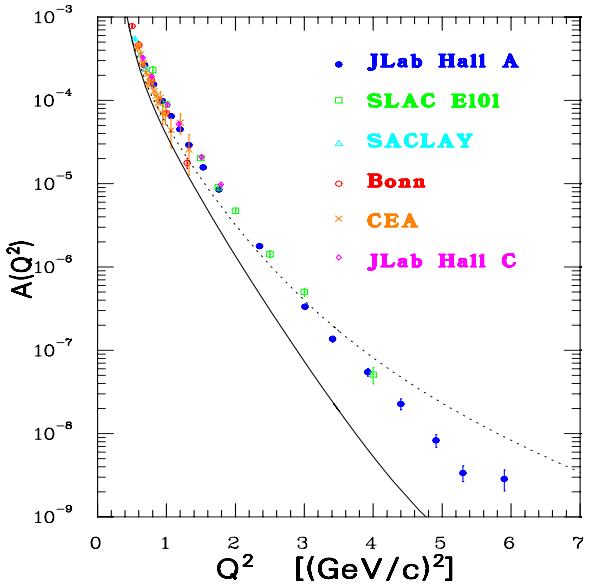

Fig. 5-19: The electric structure function $A(Q^2)$. The solid line is the ET calculation of Phillips *et al.* [67]. The dotted line is the calculation when the $\rho\pi\gamma$ MEC contribution is added using the $f_{\rho\pi\gamma}$ form factor given by vector-meson dominance. The single-nucleon form factors used are from the parameterization of Mergell *et al.* [76].

The results are shown in Figures 5-19 and 5-20. The single-nucleon form factors used are from the parameterization of Mergell *et al.* [76]. Impulse approximation results fall below experimental data. The $\rho\pi\gamma$ MEC contribution was added using the $f_{\rho\pi\gamma}$ form factor given by vector-meson dominance.

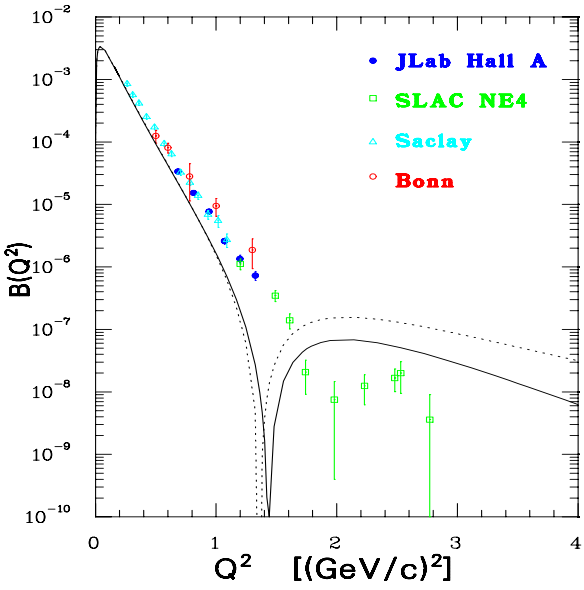

Fig. 5-20: The magnetic structure function $B(Q^2)$. The solid line is the ET calculation of Phillips *et al.* [67]. The dotted line is the calculation when the $\rho\pi\gamma$ MEC contribution is added using the $f_{\rho\pi\gamma}$ form factor given by vector-meson dominance. The single-nucleon form factors used are from the parameterization of Mergell *et al.* [76].

Comparison of the RIA calculations with those of the NRIA for the same observables strengthens the conclusion that neither the consideration of relativistic kinematics for the nucleons and mesons nor the inclusion of negative-energy state effects improves the agreement with the experimental data. By definition, such a non-relativistic impulse approximation calculation neglects both relativistic effects and two-body current contributions. Indeed, we see here that, as already found by Arnold *et al.* [93] and Zuilhof and Tjon [94], that inclusion of relativistic effects actually worsens the agreement with the experimental data. The inclusion of these effects to all orders in a Q/M_N expansion does not lead to a small correction which brings the theory into closer agreement with the experimental data. This suggests that the comparative success of a simple non-relativistic impulse approximation calculation is fortuitous. Dynamical mechanisms beyond the impulse approximation appear to play a more important role in this reaction than one would conclude from the

non-relativistic calculation. The RIA results above imply that once Q^2 gets above about 0.5 $(\mathrm{GeV/c})^2$ two-body current contributions become important. One example of such a two-body current would be the meson-exchange current contributions.

5.4 Meson-Exchange Currents

Both the non-relativistic impulse and relativistic impulse approximations underestimate the measured deuteron structure functions, $A(Q^2)$ and $B(Q^2)$. The discrepancy between theory and experiment increases with increasing Q^2. Even the RIA with inclusion of terms to all order in $(Q/M_N)^2$ fails to describe the data and suggests the possibility that this extra cross section comes from meson-exchange currents. In the NRIA, the contribution of MEC was discussed at the end of section 5.2. Figure 5-1 shows the first order MEC diagrams. In the RIA, the diagrams in which the photon insertion is on the nucleon are included automatically and the only MEC contribution is coming from diagram (b) in Figure 5-21.

In the context of a Bethe-Salpeter one-boson-exchange model of the nuclear force, the deuteron structure functions can be calculated from only two contributions: the RIA in which the photon couples directly to one of the bound nucleons (shown in Figure 5-21-a), and the MEC contribution in which the photon couples to the exchanged mesons (shown in Figure 5-21-b). Because the deuteron is an isospin-zero target, only isoscalar MEC can contribute because of G-parity conservation, and in the context of the OBE model the $\rho\pi\gamma$, $\omega\eta\gamma$ and $\omega\sigma\gamma$ currents are three likely candidates. The properties of these mesons are given in Table 5-3. Note that σ (Hummel and Tjon referred to it in their paper as ϵ) is a phenomenological meson introduced in the one-boson-exchange model of the NN potential to account for the intermediate-range interaction.

A number of experimental measurements, the most famous being the electrodisintegration of the deuteron at threshold [95], have established the existence of isovector meson-exchange currents [96]. In contrast, the nature and size of isoscalar exchange currents is still

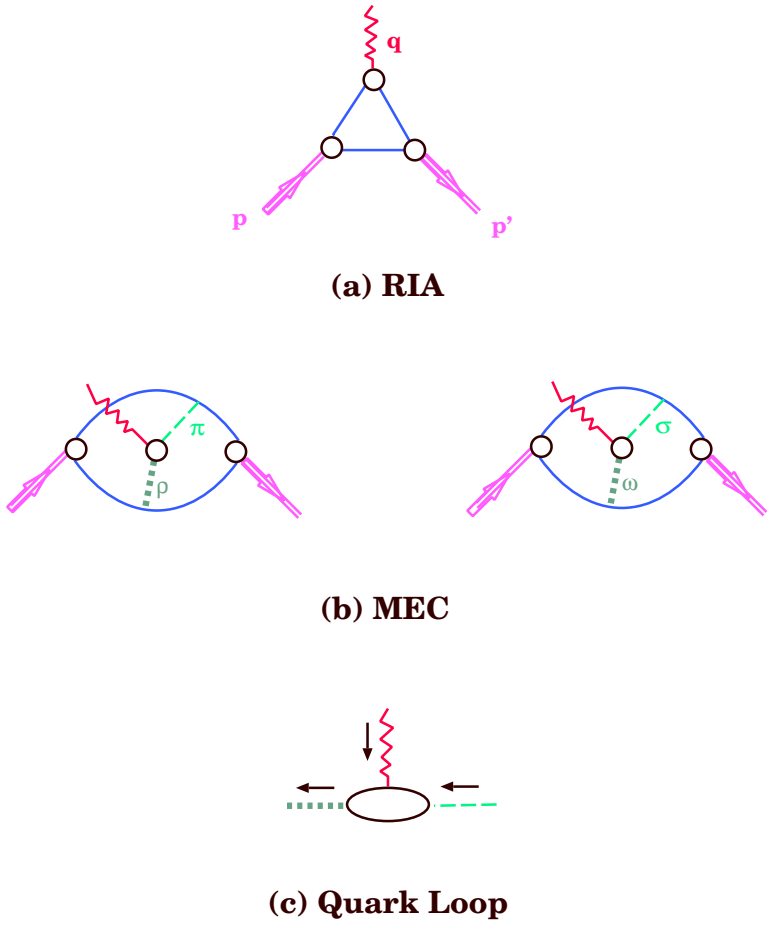

Fig. 5-21: (a) The relativistic Feynman diagram which describes the impulse approximation. (b) The $\rho\pi\gamma$ and $\omega\sigma\gamma$ meson-exchange current contribution. (c) The quark-loop contribution to the $\rho\pi\gamma$ and $\omega\sigma\gamma$ vertices.

an issue of some controversy. The simplest system in which to look for isoscalar exchange currents is the deuteron.

The $\rho\pi\gamma$ and $\omega\sigma\gamma$ exchange currents make small (less than 0.5% [3]) contributions to the magnetic and quadrupole moments. They are therefore masked by the significantly larger (and uncertain) relativistic corrections, which are about 5% for the magnetic moment and 1.5% for the quadrupole moment [97]. The possibility of seeing the effects of MEC is more favorable at large Q^2, where these MEC contributions are expected to be large (because they provide a mechanism for sharing the incoming photon momentum equally between the two nucleons) [98, 99], and where previous calculations of the RIA [93, 100, 3] have underestimated $A(Q^2)$ by an order of magnitude at $Q^2 = 4$ (GeV/c)^2 and have failed to predict the correct location for the minimum in $B(Q^2)$. The form factor for the $\rho\pi\gamma$ or $\omega\sigma\gamma$ vertex is not known experimentally and is a source of uncertainty in the calculations. The coupling constant $g_{\rho\pi\gamma}$ can be extracted from the radiative decay width of $\rho \rightarrow \pi\gamma$. This constant is not well known. Experiments performed by Berg *et al.* [101] give $g_{\rho\pi\gamma} = 0.56$. The value of the coupling constant follows from the decay width:

$$g^2_{\rho\pi\gamma} = \left[\frac{4\pi}{e^2}\right] \frac{24\Gamma(\rho \rightarrow \pi\gamma)}{m_\rho(1 - m^2_\pi/m^2_\rho)^3} \ . \tag{5-55}$$

However, nothing can be said about the sign of the coupling constant. The couplings and form factors for other possible exchange currents can be predicted by quark models, but are not otherwise constrained.

The size of the $\rho\pi\gamma$ isoscalar MEC depends critically on the Q^2 dependence of the form factor associated with the $\rho\pi\gamma$ vertex; if no form factor is used, the result from the $\rho\pi\gamma$ exchange current alone would overestimate $A(Q^2)$ by two orders of magnitude [102] at $Q^2 = 4.0$ (GeV/c)^2. In their calculation, Hummel and Tjon used a simple monopole form factor:

$$f_{\rho\pi\gamma}(Q^2) = \frac{m_\omega^2}{(m_\omega^2 + Q^2)} \ , \tag{5-56}$$

where m_ω is the mass of the ω meson. Such a form factor is justified by the vector-meson dominance (VMD) hypothesis [98], where the interaction between the virtual photon and the meson is mediated by two vector mesons with similar masses and opposite phases. The applicability of VMD is a controversial topic in particle physics and using it to estimate the $\rho\pi\gamma$ form factor is particularly questionable if the photon momentum is large and space-like. To calculate a more reliable estimate of the Q^2 dependence of the form factor at the $\rho\pi\gamma$ vertex, Ito and Gross [102] used a relativistic quark model of the π and the ρ. The Quark-Loop (QL) calculated form factor falls off much more rapidly at large Q^2 than the monopole based on VMD used by Hummel and Tjon; it is about a factor of 3 times smaller at $Q^2 = 8.0$ (GeV/c)^2.

Electromagnetic form factors for the $\rho\pi\gamma$ vertex, estimated from the quark-loop diagram shown in Figure 5-21-c, differ considerably from the monopole form factors obtained from VMD and significantly alter the predictions for the elastic electromagnetic form factors of the deuteron. The $f_{\rho\pi\gamma}(Q^2)$ form factor obtained with the VMD model is shown by the solid curve in Figure 5-22. Also shown, are the quark-based results of Ito and Gross [102], Mitchel and Tandy [103], and Cardarelli and Simula *et al.* [104]. The quark-based results produce a much softer form factor than is produced by the VMD assumption. Using asymptotic power counting based on perturbative QCD, Chernyak and Zhitnitsky [105] have shown that $f_{\rho\pi\gamma}(Q^2) \sim Q^{-4}$, where the extra power in the fall off (the typical asymptotic meson form factor is $\sim Q^{-2}$) is due to the helicity-flip of a quark. Apparently, at some momentum scale, the form factor must start to deviate from the monopole function. Estimates based on quark-loop calculations give a similar result.

The contributions of the exchange currents to the elastic structure functions of the

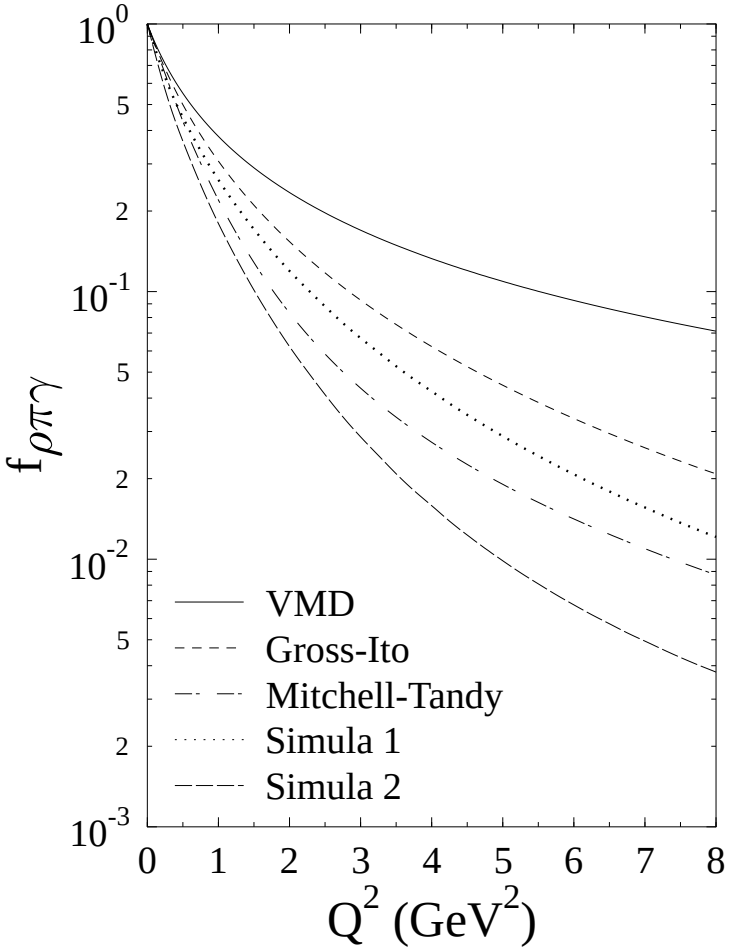

Fig. 5-22: Theoretical predictions [102, 103, 104] of the $\rho\pi\gamma$ meson-exchange current form factor.

deuteron have been calculated in a fully relativistic covariant way by Van Orden, Devine and Gross [66] using the Gross or Spectator equation, and by Hummel and Tjon [3] using the Blankenbecler-Sugar equation. These calculations for $A(Q^2)$ are shown in Figure 5-23. When Hummel and Tjon used a VMD form factor, their $\rho\pi\gamma$ exchange current was too large at high Q^2, and they needed another exchange current to cancel it. The $\omega\sigma\gamma$ MEC has the opposite sign, and assuming factorization, $f_{\omega\sigma\gamma}(Q^2) \sim f_{\rho\sigma\gamma}(Q^2)$, and $g_{\omega\sigma\gamma} = -g_{\rho\pi\gamma} = -0.56$, as suggested from a study of a relativistic quark model by Chemtob, Moniz and Rho [98], a cancellation results from these MECs, as shown in Figure 5-23. Nevertheless, their prediction for $A(Q^2)$ is much larger than the data for $Q^2 > 3.0$ (GeV/c)^2. The contributions of the $\omega\eta\gamma$ exchange currents were small. The CIA calculations are also shown. The contributions of the $\rho\pi\gamma$ exchange current calculated with the Mitchell-Tandy [103] $\rho\pi\gamma$ form factor is remarkably close to the data.

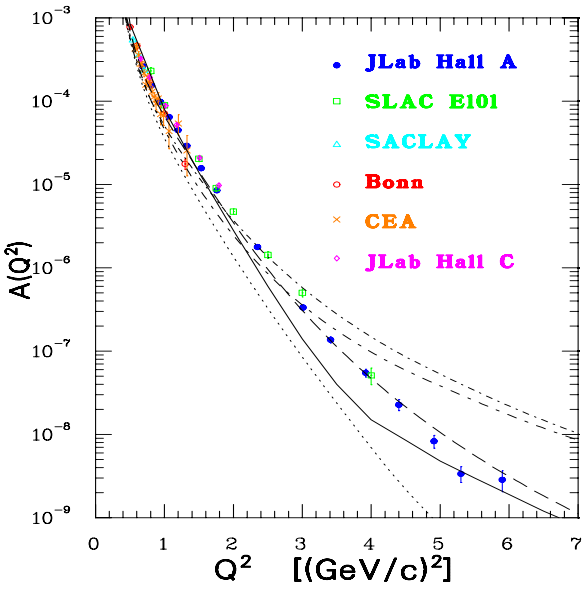

Fig. 5-23: The electric structure function $A(Q^2)$. The solid line is the CIA of Van Orden *et al.* [66]. The dashed line is the CIA plus $\rho\pi\gamma$ meson-exchange current. The dotted line is the RIA of Hummel and Tjon [3]. The dotted short dashed line is the RIA plus $\rho\pi\gamma$ meson-exchange current. The dotted long dashed line is the RIA plus $\rho\pi\gamma$ and $\omega\sigma\gamma$ meson-exchange currents.

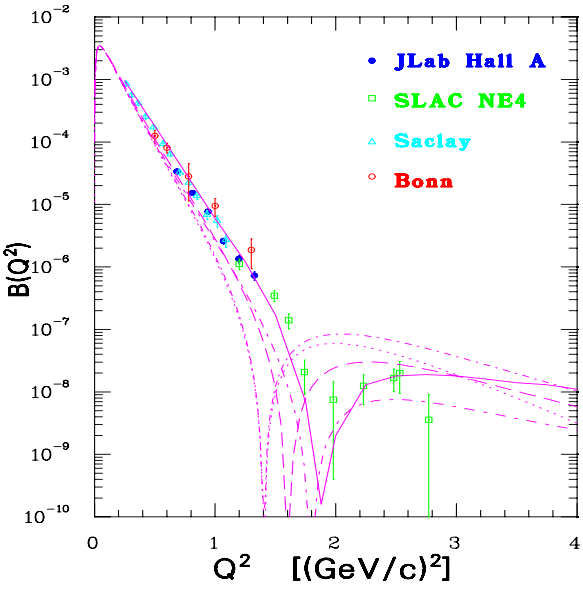

Fig. 5-24: The magnetic structure function $B(Q^2)$. The solid line is the CIA of Van Orden *et al.* [66]. The dashed line is the CIA plus $\rho\pi\gamma$ meson-exchange current. The dotted line is the RIA of Hummel and Tjon [3]. The dotted short dashed line is the RIA plus $\rho\pi\gamma$ meson-exchange current. The dotted long dashed line is the RIA plus $\rho\pi\gamma$ and $\omega\sigma\gamma$ meson-exchange currents.

As can be seen in Figure 5-24, the $\rho\pi\gamma$ MEC makes only a small contribution to the RIA calculation of $B(Q^2)$, and Hummel and Tjon found that they could obtain agreement with the data [2] only by introducing the $\omega\sigma\gamma$ MEC. However, the position of the diffraction minimum is very sensitive to the choice of the $\omega\sigma\gamma$ form factor, and while good agreement was obtained with the VMD model, the more realistic QL model does not succeed in describing the data. Attempts to use an $\omega\sigma\gamma$ exchange current to describe $B(Q^2)$ are not successful unless an unrealistically hard form factor is used. Thus, one concludes that $B(Q^2)$ is not described by the Hummel and Tjon calculations. The effect of adding the contributions of the $\rho\pi\gamma$ exchange current calculated with the Mitchell-Tandy form factor to the CIA calculation is to move the minimum of $B(Q^2)$ to lower Q^2 and worsen the agreement with the data.

The $\rho\pi\gamma$ exchange current tends to increase the size of $A(Q^2)$ and to move the minimum

of $B(Q^2)$ to lower Q^2. In both cases the VMD form factors produce much too large an effect while the softer quark model form factors give smaller effects.

5.5 Dimensional Scaling Laws

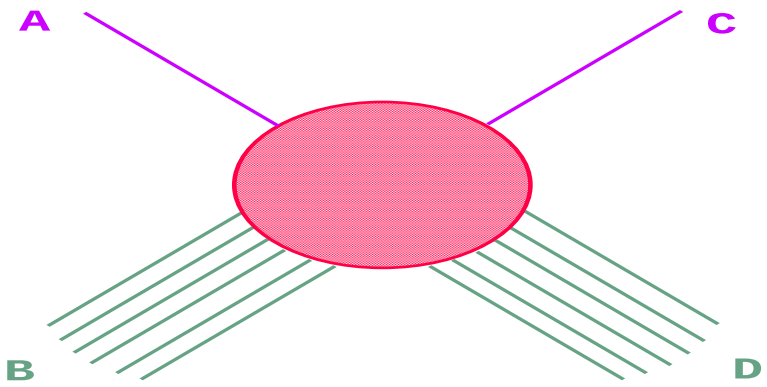

Fig. 5-25: n-point "decomposition" of $AB \longrightarrow CD$ (in this example $n = 14$).

The dimensional scaling laws (also known as the constituent counting rules) were derived by Brodsky and Farrar [106] and Matveev, Muradyan and Tavhelidze [107]. For the exclusive two-body process $AB \longrightarrow CD$, as shown in Figure 5-25, the scaling laws simply state that the asymptotic behavior at large s and t, where s and t are the Mandelstam variables, while keeping t/s fixed is:

$$\frac{d\sigma}{dt}(AB \longrightarrow CD) = \frac{1}{t^{n-2}} f\left(\frac{t}{s}\right) . \tag{5-57}$$

Here n is the total number of leptons, photons, and quark components (*i.e.* elementary fields) in A, B, C, and D. For elastic electron-deuteron scattering, $e\ d \longrightarrow e\ d$, $n = 14$. The scaling laws represent, in the simplest possible manner, the connection between the degree of complexity of a hadron and its dynamical behavior.

One of the most important consequences of Equation 5-57 is its application to elastic electron-hadron scattering. The cross section for elastic electron-hadron scattering can be

written as ($Q^2 = -t$):

$$\frac{d\sigma}{dt}(eH \longrightarrow eH) = \frac{1}{(Q^2)^{(2n_H+2)-2}} f\Big(\frac{t}{s}\Big) = \frac{4\pi\alpha^2 \mid F(Q^2) \mid^2}{(Q^2)^2} f\Big(\frac{t}{s}\Big) \ . \tag{5-58}$$

This formula immediately connects the asymptotic dependence of the spin-averaged electromagnetic form factor to the minimum number of fields n_H in the hadron:

$$F(Q^2) \sim \frac{1}{(Q^2)^{n_H-1}} \ . \tag{5-59}$$

Thus, using the quark model, we have $F(Q^2) \sim 1/Q^2$ for mesons ($n_H = 2$) and $F_1(Q^2) \sim 1/(Q^2)^2$ for baryons ($n_H = 3$). We also find that the Pauli form factor $F_2(Q^2)$ is suppressed by an extra power of Q^2: $F_2(Q^2) \sim 1/(Q^2)^3$. For the elastic deuteron structure functions, $A(Q^2)$ and $B(Q^2)$:

$$\begin{aligned} A(Q^2) &\sim \frac{1}{(Q^2)^{10}} \ , \\ B(Q^2) &\sim \frac{1}{(Q^2)^{12}} \ . \end{aligned} \tag{5-60}$$

Note that the deuteron magnetic form factor, $F_M(Q^2)$, is also suppressed by an extra power of Q^2 because a helicity-flip of one quark is required. This suppresses $B(Q^2)$ by two powers of Q^2. In terms of the charge monopole, magnetic dipole, and charge quadrupole form factors, one has F_C falling like Q^{-10}, and both F_M and F_Q falling like Q^{-12}, with:

$$\lim_{Q^2\to\infty} F_C(Q^2) = \frac{Q^2}{6M_d^2} F_Q(Q^2) \ . \tag{5-61}$$

The experimental data seem to follow this prediction for the pion and proton, as Figure 5-26 indicates. Perturbative quantum chromodynamics, discussed in the next section, substantiated this prediction and introduced logarithmic corrections.

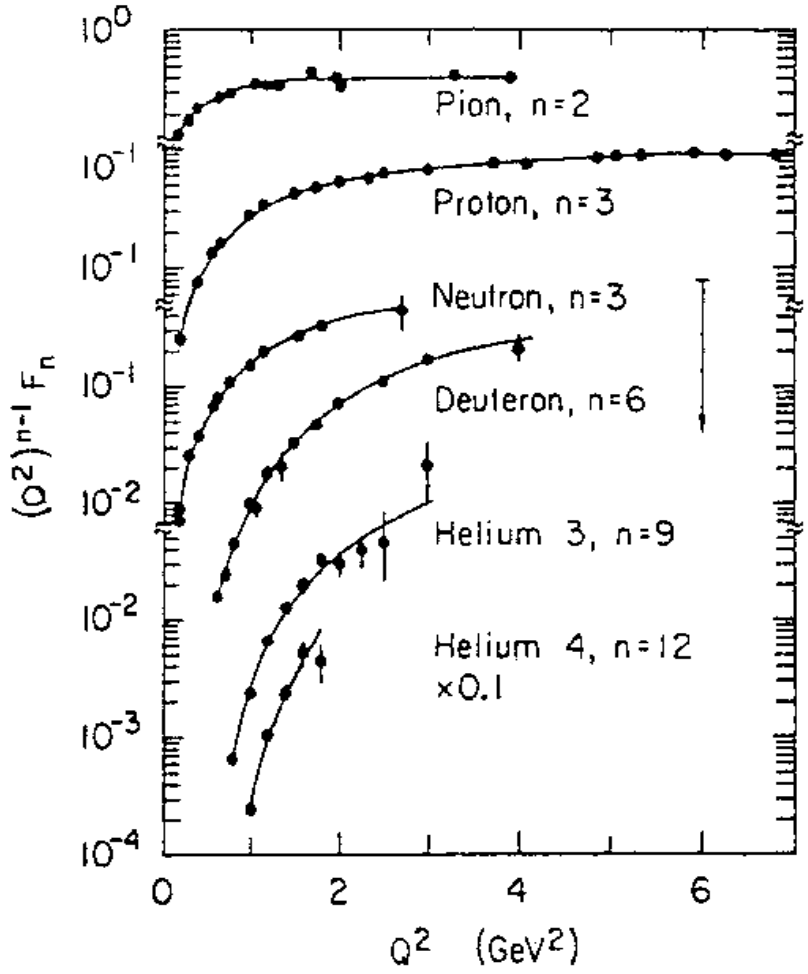

Fig. 5-26: Elastic electromagnetic form factors F_n of hadrons at large Q^2 in the dimensional scaling quark model. Here n represents the number of quarks in the hadron.

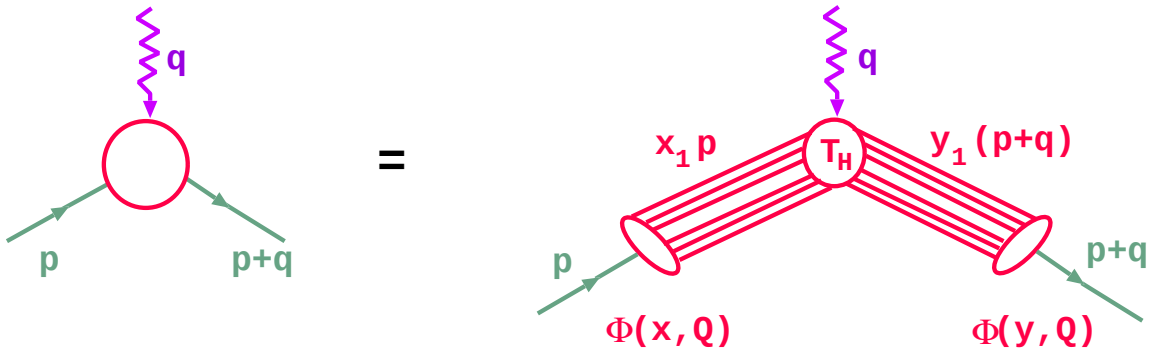

Fig. 5-27: The general structure of the deuteron form factor at large Q^2 in QCD.

5.6 Perturbative Quantum Chromodynamics

If quantum chromodynamics is the theory of the strong interactions, then by extension it must also provide a fundamental description of the nuclear force and nuclear physics. Since the basic scale of QCD, Λ_{QCD}, is of order of a few hundred MeV or less, one expects a transition from the traditional meson and nucleon degrees of freedom of nuclear physics to quark and gluon degrees of freedom of QCD at internucleon separations of 1 fm or less.

For $Q^2 \gg 2M_d\Lambda_{QCD} \sim 0.8$ (GeV/c)^2, or equivalently $\eta \gg \Lambda_{QCD}/2M_d \sim 0.05$, the dominant deuteron form factor $F_d(Q^2) \equiv \sqrt{A(Q^2)}$ can be written in the light-cone frame, defined by [110] $q^+ = 0$, $q_y = 0$, $q_x = Q$, as a convolution (see Figure 5-27) [108, 109]:

$$F_d(Q^2) = \int_0^1 [dx][dy]\Phi^\dagger(y_j, Q)T_H^{6q+\gamma^*\to 6q}(x_i, y_j, Q)\Phi(x_j, Q) \ , \tag{5-62}$$

where the hard-scattering amplitude:

$$T_H^{6q+\gamma^*\to 6q} = \Big[\frac{\alpha_s(Q^2)}{Q^2}\Big]^5 t(x,y)[1 + O(\alpha_s(Q^2)] \tag{5-63}$$

gives the probability amplitude for scattering six collinear quarks in the initial deuteron state to six collinear quarks in the final deuteron state. Here $\alpha_s(Q^2)$ is the QCD strong coupling constant and x and y are the initial and final light-cone longitudinal momentum

fractions. The distribution amplitude $\Phi_d(x_i, Q)$ is defined by [110]:

$$\Phi_d(x_i, Q) = \int^Q [d^2\mathbf{k}_\perp] \Psi_{6q/d}(x_i, \mathbf{k}_{\perp i}) \ . \tag{5-64}$$

The notation $[dx]$ and $[d^2\mathbf{k}_\perp]$ represents:

$$[dx] \equiv \delta(1 - \sum_{i=1}^{n} x_i) \prod_{i=1}^{n} dx_i \ , \tag{5-65}$$

$$[d^2\mathbf{k}_\perp] \equiv 16\pi^3 \delta(\sum_{i=1}^{n} \mathbf{k}_{\perp i}) \prod_{i=1}^{n} \frac{d^2\mathbf{k}_{\perp i}}{16\pi^3} \ . \tag{5-66}$$

The QCD prediction for the leading helicity-zero deuteron form factor takes the form:

$$F_d(Q^2) = \Big[\frac{\alpha_s(Q^2)}{Q^2}\Big]^5 \sum_{m,n} d_{mn} \Big[\ln(Q^2/\Lambda^2_{QCD})\Big]^{-\gamma_n - \gamma_m} \ , \tag{5-67}$$

where $\gamma_{m,n}$ and d_{mn} are QCD anomalous dimensions and constants. Here the main dependence $[\alpha_s(Q^2)/Q^2]^5$ comes from the hard-gluon exchange amplitude T_H. This prediction agrees with the data (see Figure 5-28). The crucial point is that $\eta \gg 1$ appears to be unnecessary for the application of pQCD.

In order to make more detailed and experimentally accessible predictions and to include non-perturbative corrections, reduced amplitude analysis [111] was invoked, in which experimentally determined nucleonic form factors F_N are used to describe the structure of the neutron and the proton. A reduced nuclear form factor is directly related to the probability for the two nucleon system to remain intact. The reduced deuteron form factor is defined as:

$$f_d(Q^2) \equiv \frac{F_d(Q^2)}{F_N^2(Q^2/4)} \ , \tag{5-68}$$

where the two powers of the nucleon form factor $F_N(Q^2) = (1 + Q^2/0.71)^{-2}$ remove in a minimal and approximate way the effects of nucleon compositeness. The argument for the

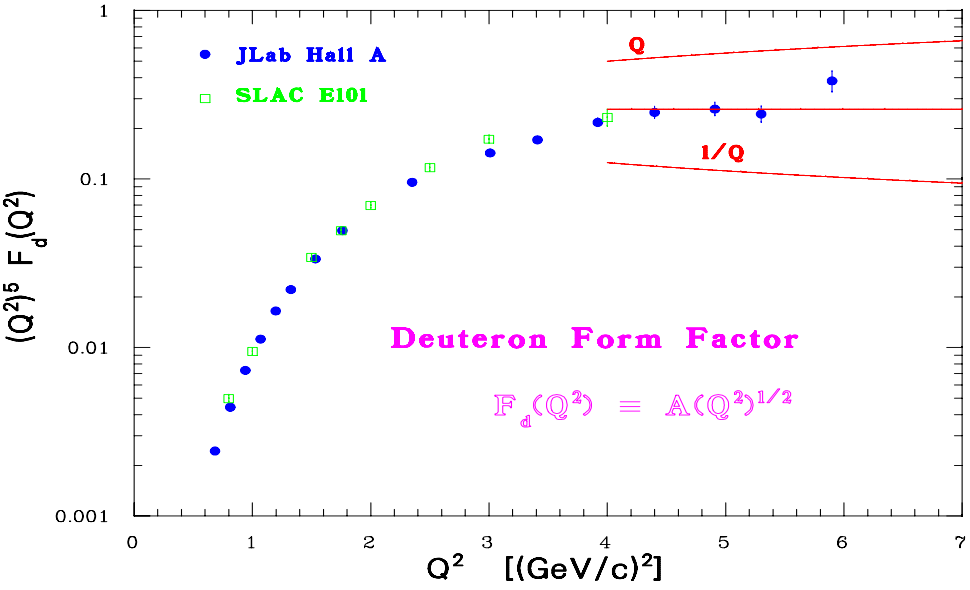

Fig. 5-28: The deuteron form factor $F_d(Q^2)$ times $(Q^2)^5$. The line labeled Q shows how the data should scale for $F_d(Q^2) \sim 1/Q^9$; the line labeled $1/Q$ shows how the data should scale for $F_d(Q^2) \sim 1/Q^{11}$, the straight line is the predicted $1/Q^{10}$ scaling.

nucleon form factor F_N is $Q^2/4$ since, in the limit of zero binding energy, each nucleon must change its momentum from $p/2$ to $(p+q)/2$. Equation 5-68 indicates that the deuteron form factor $F_d(Q^2)$ can be factorized into two parts and the reduced form factor $f_d(Q^2)$ can be regarded as the form factor of a composite of two point-like nucleons. This factorization was obtained by assuming:

$$\Psi_d = \psi_d^{\rm body} \times \psi_N \times \psi_N \tag{5-69}$$

in a simple covariant model [112]. ψ_N is the nucleon wave function and $\psi_d^{\rm body}$ is the usual two-body wave function of the deuteron. The equation of motion for $\Psi_d(x_i, \mathbf{k}_{\perp i})$ in the light-cone frame is given by:

$$[M_d^2 - \sum_{i=1}^{6} \frac{\mathbf{k}_{\perp i}^2 + m_i^2}{x_i}]\Psi_d(x_i, \mathbf{k}_{\perp i}) = \int [dy][d^2\mathbf{j}_\perp] V(x_i, \mathbf{k}_{\perp i}; y_j, \mathbf{j}_{\perp j})\Psi_d(y_j, \mathbf{j}_{\perp j}) \ . \tag{5-70}$$

The factorized form of the deuteron form factor can be obtained by substituting Equation 5-70 into the Drell-Yan formula [110]:

$$F_d(Q^2) = \sum_{a=1}^{6} e_a \int [dx][d^2\mathbf{k}_{\perp i}] \Psi_d^*(x_i, \mathbf{k}_{\perp i} + (\delta_{ia} - x_i)\mathbf{q}_\perp) \Psi_d(x_i, \mathbf{k}_{\perp i}) \ , \tag{5-71}$$

where $\mathbf{q}_\perp$ is absorbed by the a-th quark, $q = (0, q^-, \mathbf{q}_\perp)$ and $Q^2 = \mathbf{q}_\perp^2$. Since the gluon is a color octet in the SU(3) color group, the single-gluon exchange between two color-singlet nucleons is forbidden. Thus, the real kernel calculation requires the inclusion of other components rather than two-nucleons. Brodsky and Ji [112] suggested a simple covariant model to incorporate the quark structure of the nucleon. The hard kernel at large Q^2 was assumed to be the perturbative amplitude for the six quarks to scatter from collinear in the initial two nucleon configuration to collinear in the final two-nucleon configuration, where each nucleon has roughly equal momentum. They argued that the dominant configuration for this recombination is the quark-interchange plus one-gluon exchange between two nucleons as shown in Figure 5-29b. Thus, roughly speaking, we can divide the kernel into two parts: One represents the interchange of quarks and the gluon exchange between two nucleons, which transfer about half of the transverse momentum of the virtual photon from the struck nucleon to the spectator nucleon. Another part is the inner evolution of two nucleons. The first part leads to the reduced form factor of the deuteron and the latter leads to the form factors of two nucleons together with the factorized wave function mentioned above.

From dimensional counting one obtains $f_d(Q^2) \sim 1/Q^2$. In pQCD there are computable logarithmic corrections associated with the running coupling and the Q^2 evolution of the deuteron distribution amplitude. Inclusion of these corrections yields the asymptotic scaling behavior:

$$f_d(Q^2) \sim \Big[\frac{\alpha_s(Q^2)}{Q^2}\Big]\Big[\ln(Q^2/\Lambda_{QCD}^2)\Big]^{-\Gamma} \ . \tag{5-72}$$

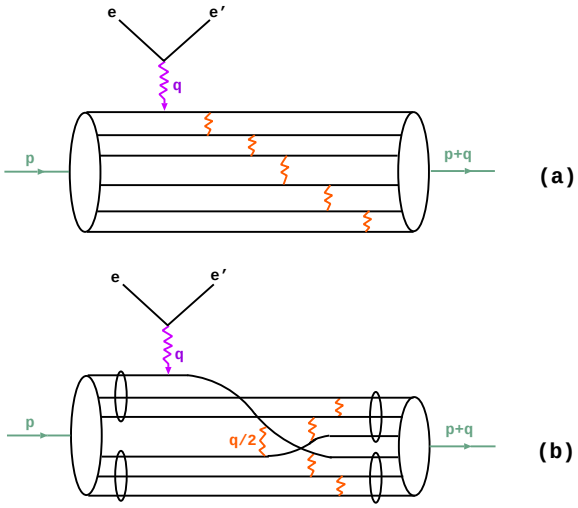

Fig. 5-29: Two possible quark-constituent views of elastic e-d scattering (a) the democratic (cascade) chain model and (b) the quark interchange model.

Here $\Gamma = -(2C_F/5\beta)$, where $C_F = (n_c^2 - 1)/2n_c$, $\beta = 11 - (2/3)n_f$, with $n_c = 3$ and $n_f = 2$ being the numbers of QCD colors and effective flavors. Assuming

$$\alpha_s(Q^2) \sim \frac{1}{\ln(Q^2/\Lambda^2_{QCD})} \tag{5-73}$$

the reduced deuteron form factor becomes:

$$f_d(Q^2) = \frac{a}{Q^2}\left[\ln\frac{Q^2}{\Lambda^2_{QCD}}\right]^{\frac{8}{145}-1}, \tag{5-74}$$

where a is a normalization constant. Figure 5-30 shows the asymptotic QCD prediction compared with the data. Our $f_d(Q^2)$ data seem to follow this prediction for $Q^2 > 2.0$ $(\mathrm{GeV/c})^2$.

Brodsky and Hiller [113] have made a general analysis of the electromagnetic properties of spin-one systems proceeding from gauge theory: in the analysis of high energy elastic e-d cross sections at least two momentum scales must be distinguished. The first scale is given by the deuteron mass M_d and has a purely kinematical origin. The second one is given by the QCD scale $\Lambda_{QCD} \simeq 200$ MeV/c and determines the perturbative QCD regime. In

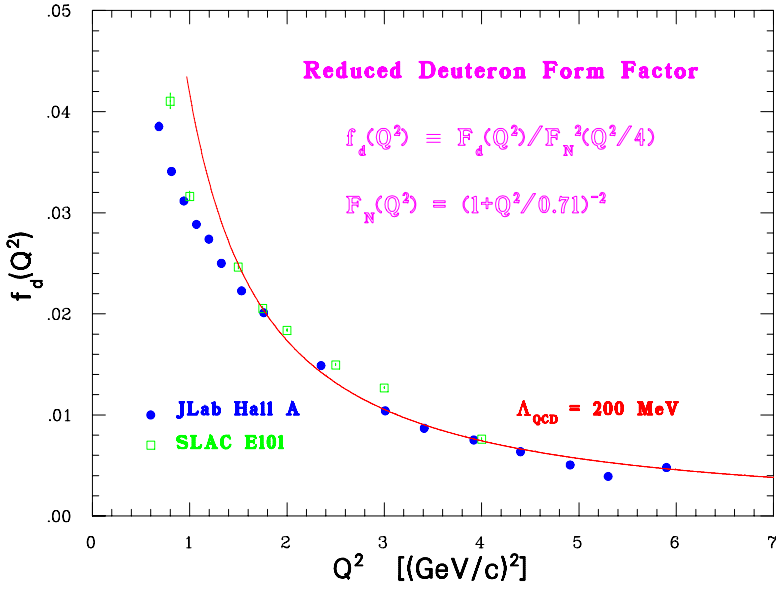

Fig. 5-30: The reduced deuteron form factor $f_d(Q^2)$. The curve is the asymptotic QCD prediction of Brodsky *et al.* [108] for $\Lambda_{QCD} = 200$ MeV, arbitrarily normalized to the data at $Q^2 = 4.0$ GeV/c)^2.

particular, according to arguments of [114], this scale controls a high-Q^2 suppression of the LFC helicity-flip matrix elements of the deuteron electromagnetic current:

$$\begin{aligned} J^+_{10} &\sim a\left(\frac{\Lambda_{QCD}}{Q}\right) J^+_{00}\ , \\ J^+_{1-1} &\sim b\left(\frac{\Lambda_{QCD}}{Q}\right)^2 J^+_{00}\ , \end{aligned} \tag{5-75}$$

where:

$$J^+_{h'h} \equiv \langle p'h' \mid J^+ \mid ph \rangle \tag{5-76}$$

are the matrix elements of the electromagnetic plus component $J^+ = J^o + J^z$, $\mid ph >$ is an eigenstate of momentum p and helicity h, and a and b are some constants. Brodsky and Hiller used the following triplet of matrix elements: J^+_{10}, J^+_{00}, J^+_{1-1}. Taking this triplet and solving the system of Equations 5-24, 5-25, and 5-26 relative to $\mathcal{F}_1$, $\mathcal{F}_2$ and $\mathcal{G}_1$, one finds:

$$\begin{aligned}
\mathcal{F}_1 &= \frac{-1}{(2\eta+1)}\left[2\sqrt{2\eta}J_{10}^{+} + J_{00}^{+} + 2\eta J_{1-1}^{+}\right] , \\
\mathcal{F}_2 &= \frac{-1}{\eta}J_{1-1}^{+} , \\
\mathcal{G}_1 &= \frac{2}{(2\eta+1)}\left[(2\eta-1)\frac{J_{10}^{+}}{\sqrt{2\eta}} + J_{00}^{+} - J_{1-1}^{+}\right] .
\end{aligned} \tag{5-77}$$

As Karmanov [70] pointed out, the triplet matrix elements: J_{10}^{+}, J_{00}^{+}, and J_{1-1}^{+} should be calculated using Equation 5-28 instead of Equations 5-24, 5-25, and 5-26. Thus, the above set of form factors contain non-physical contributions and are related to the correct $\mathcal{F}_1$, $\mathcal{F}_2$ and $\mathcal{G}_1$ by:

$$\begin{aligned}
\mathcal{F}_1 &= \mathcal{F}_1 + \frac{2}{1+2\eta}\Delta , \\
\mathcal{F}_2 &= \mathcal{F}_2 , \\
\mathcal{G}_1 &= \mathcal{G}_1 - B_6 - \frac{1}{1+2\eta}\Delta ,
\end{aligned} \tag{5-78}$$

where Δ is given by Equation 5-29. In the following discussion, the non-physical contributions should not affect the result because it is an investigation of asymptotic behavior rather than a model calculation.

The charge monopole, the magnetic dipole, and the charge quadrupole form factors can be obtained from the above set of Equations 5-77 using Equation 5-14:

$$\begin{aligned}
F_C &= \frac{1}{3(2\eta+1)}\left[8\sqrt{2\eta}J_{10}^{+} + (3-2\eta)J_{00}^{+} + 2(2\eta-1)J_{1-1}^{+}\right] , \\
F_M &= \frac{2}{(2\eta+1)}\left[\frac{1}{\sqrt{2\eta}}(2\eta-1)J_{10}^{+} + J_{00}^{+} - J_{1-1}^{+}\right] , \\
F_Q &= \frac{1}{(2\eta+1)}\left[2\frac{J_{10}^{+}}{\sqrt{2\eta}} - J_{00}^{+} - \frac{\eta+1}{\eta}J_{1-1}^{+}\right] .
\end{aligned} \tag{5-79}$$

It was argued in [108] that the helicity-conserving matrix element J_{00}^{+} will be the dominant amplitude in the region $Q^2 \gg 2M_d\Lambda_{QCD}^2 \sim 0.8$ (GeV/c)^2. Corrections are of order

Λ_{QCD}/Q and Λ_{QCD}/M_d. Neglecting the helicity-flip matrix elements J^+_{10} and J^+_{1-1}, the following ratios for the charge monopole, the magnetic dipole, and the charge quadrapole form factors were derived:

$$F_C : F_M : F_Q = 1 - \frac{2}{3}\eta : 2 : -1 \ . \tag{5-80}$$

This leads to:

$$\frac{B}{A} = \frac{4\eta(\eta+1)}{\eta^2+\eta+\frac{3}{4}} \ . \tag{5-81}$$

Kobushkin and Syamtomov argued that the helicity-one-flip matrix element J^+_{10} can not be neglected [115]. For example in F_M, J^+_{10} is enhanced by kinematical factor $-\sqrt{\frac{1}{2\eta}}$ when $\eta \ll \frac{1}{2}$ and the factor $\sqrt{2\eta}$ when $\eta \gg \frac{1}{2}$. At very high Q^2, the ratios in Equation 5-80 are modified to:

$$F_C : F_M : F_Q = \left(\frac{6M^2+5Q_0^2}{6M^2-3Q_0^2} - \frac{2}{3}\eta\right) : 2\left(\frac{2\eta-1}{2\eta}\frac{Q_0^2}{2M^2-Q_0^2}+1\right) : \left(\frac{1}{\eta}\frac{Q_0^2}{2M^2-Q_0^2}-1\right) , \tag{5-82}$$

where Q_0^2 is chosen to be 1.93 $(\mathrm{GeV/c})^2$, the position of the minimum of $B(Q^2)$. The ratio of the deuteron elastic structure functions can be calculated from Equation 5-82. This ratio is in reasonable agreement with the experimental data, as shown in Figure 5-31.

The models described above are believed to be valid for large momentum transfer processes. Several authors have questioned the validity of dimensional scaling laws and pQCD at the momentum transfers of this experiment. Isgur and Llewellyn Smith [116] concluded that at the available momentum transfers, soft non-perturbative contributions dominate the form factors and pQCD is inapplicable until much larger Q^2 ($\sim$100 $(\mathrm{GeV/c})^2$) are reached. Farrar *et al.* [117] obtained the pQCD prediction for the absolute normalization of the reduced deuteron form factor (constant a in Equation 5-74). Their theoretical value is $< 10^{-3}$

times the experimental value at $Q^2 = 4.0$ (GeV/c)^2, suggesting that pQCD is not relevant to deuteron from factor at present values of Q^2. They concluded that there is no reasonable wave function which can give a pQCD calculated normalization of the form factor, and that the agreement with the pQCD scaling behavior is just fortuitous.

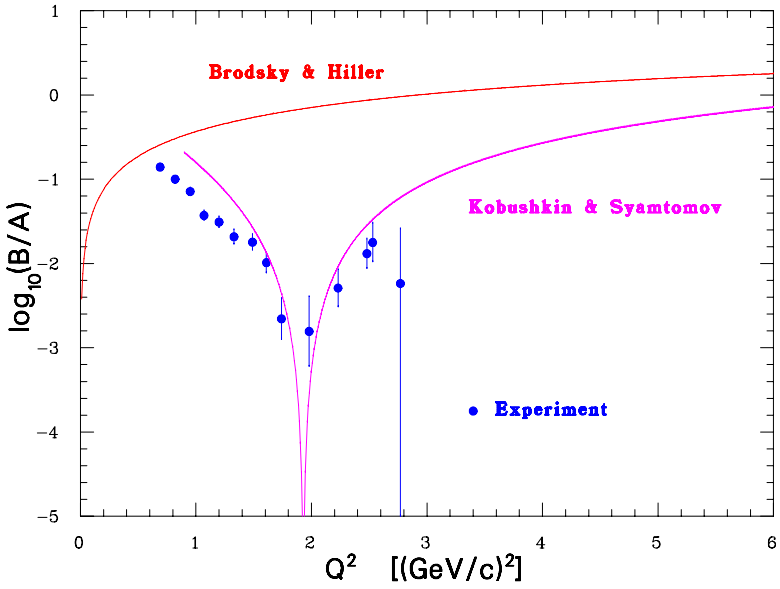

Fig. 5-31: Perturbative QCD predictions for the ratio B/A compared with experiment. The experimental data for $A(Q^2)$ are from this experiment. The experimental data for $B(Q^2)$ at low Q^2 are from this experiment while at high Q^2 are from SLAC [2]. The dashed line is the ratio obtained by Brodsky and Hiller [113]. The solid line is the ratio obtained by Kobushkin and Syamtomov [115].

Chapter 6

Summary and Outlook

We have performed precise measurements of the deuteron elastic structure functions $A(Q^2)$ and $B(Q^2)$, in the momentum transfer ranges of $0.684 \leq Q^2 \leq 5.90$ $(\mathrm{GeV/c})^2$ and $0.684 \leq Q^2 \leq 1.325$ $(\mathrm{GeV/c})^2$, respectively. The measurements took place in Hall A at Jefferson Laboratory. The structure functions were measured by means of coincidence elastic electron-deuteron scattering using the JLab electron beam and a high-power liquid deuterium target. More than 700 W of power was deposited on the target by the electron beam, enabling a cross section measurement at the level of 10^{-41} $\mathrm{cm}^2/\mathrm{sr}$. This is a record low cross section for electron scattering.

The structure function data have been compared to non-relativistic and relativistic impulse approximation predictions, both with and without the inclusion of meson-exchange currents. Both NRIA and RIA predictions generally underestimate the structure functions without the inclusion of MEC contributions. The effect of meson-exchange current contributions to the elastic structure functions depend on the model used for the vertex form factors and coupling constants.

The $A(Q^2)$ data have also been compared to predictions of the dimensional scaling quark model and of perturbative quantum chromodynamics. These models predict that, at large momentum transfers, $A(Q^2)$ should fall off as $1/(Q^2)^{10}$ implying that the product $A(Q^2) \times (Q^2)^{10}$ should be independent of Q^2. Our data seem to exhibit a scaling behavior consistent with this prediction for $Q^2 > 3$ $(\mathrm{GeV/c})^2$.

There are plans to extend both $A(Q^2)$ and $B(Q^2)$ measurements to even higher momentum transfers [118]. Figures 6-1, 6-2, and 6-3 show projected data from such measurements.

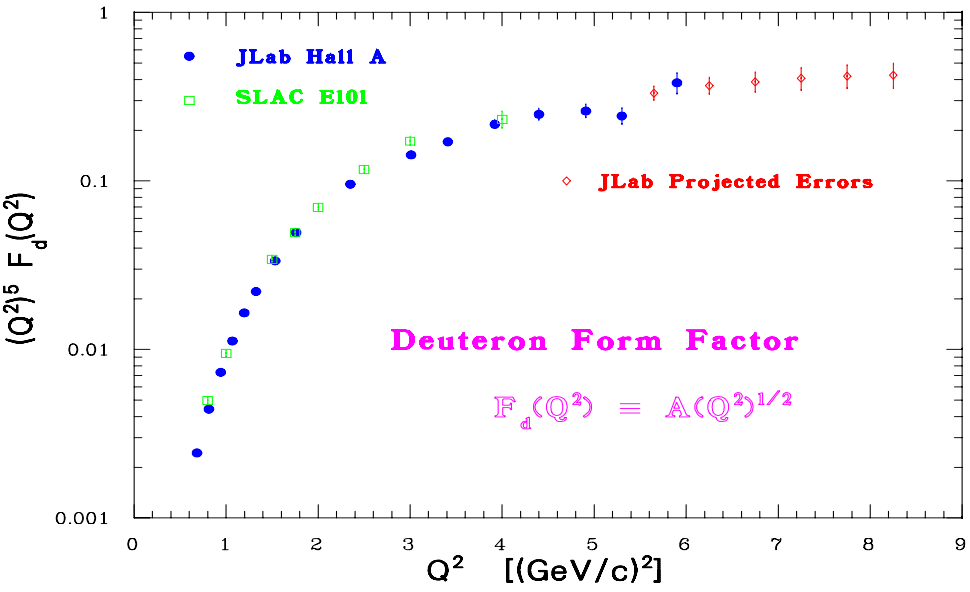

Fig. 6-1: Existing and projected data from a planned $A(Q^2)$ JLab experiment [118] with a 10 GeV beam.

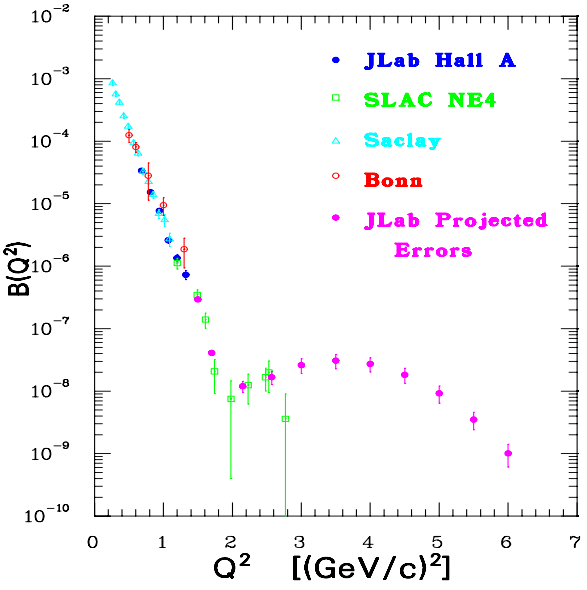

Fig. 6-2: Existing and projected data from a planned $B(Q^2)$ JLab experiment [118].

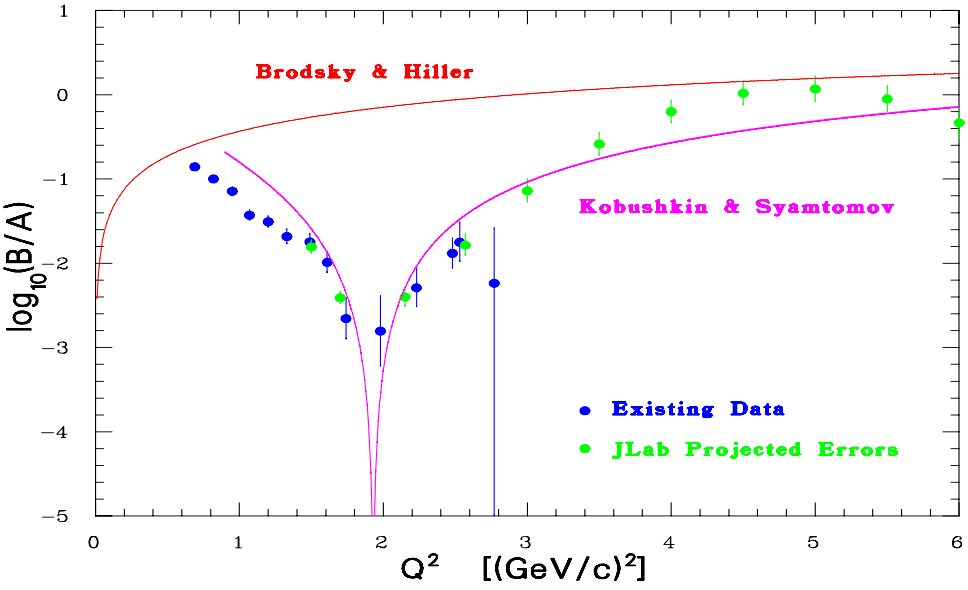

Fig. 6-3: Present and projected data from a planned $B(Q^2)$ JLab experiment [118] compared to pQCD predictions [113, 115] The existing experimental data are from this experiment and SLAC NE4 experiment [2].

The $A(Q^2)$ measurements will use the energy upgraded JLab beam (10 GeV), the High Momentum Spectrometer (HMS) of Hall C as recoil spectrometer, and the proposed Super High Momentum Spectrometer (SHMS) [119] of Hall C as electron spectrometer. The $B(Q^2)$ measurements will use the two Hall A HRS spectrometers coupled to two septum magnets to detect recoil deuterons at $\sim 3^\circ$, and two electron detection systems at $\sim 170^\circ$.

APPENDIX A

Full Trigger Electronics Diagrams

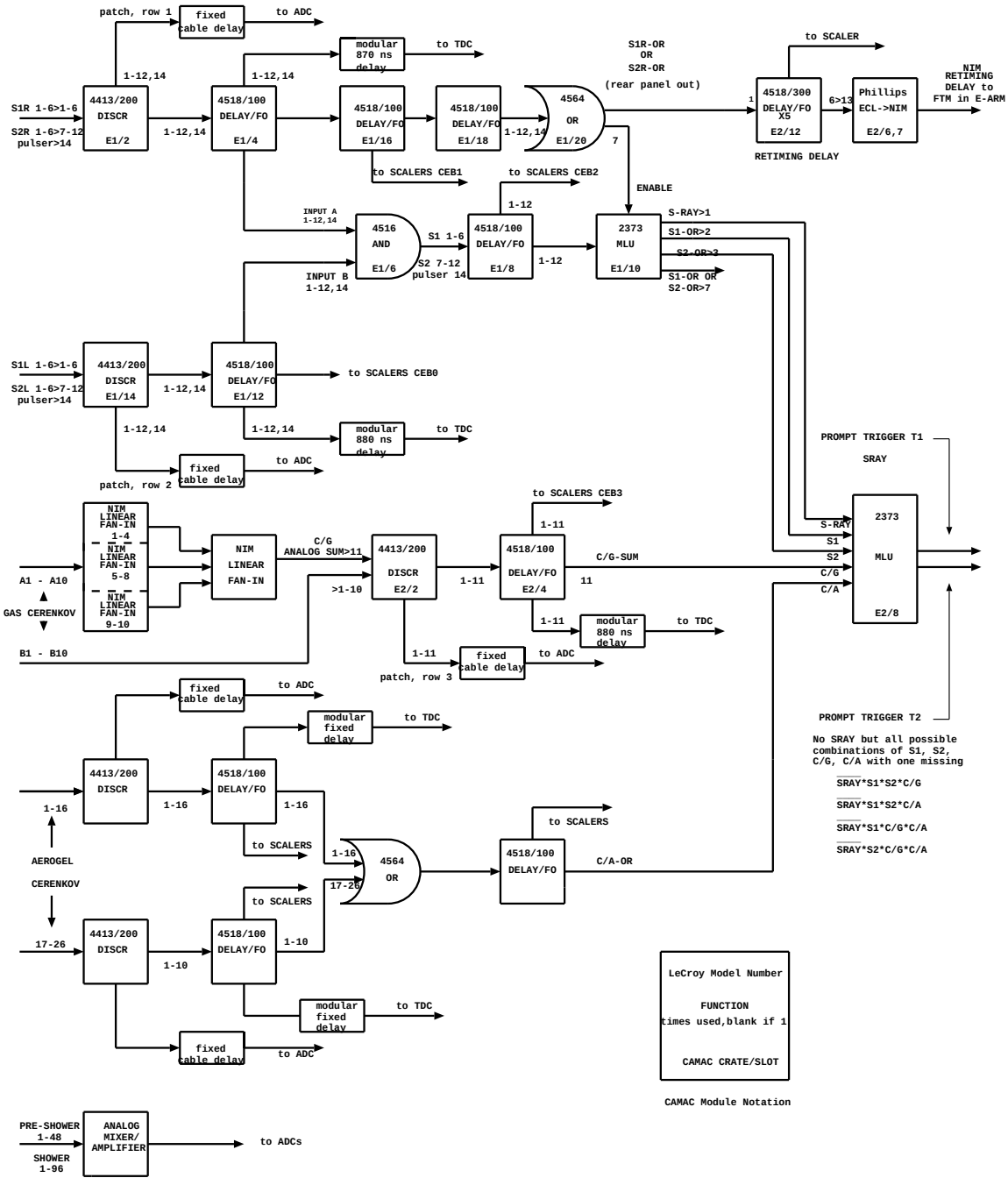

Fig. A-1: Diagram of the Electron arm trigger.

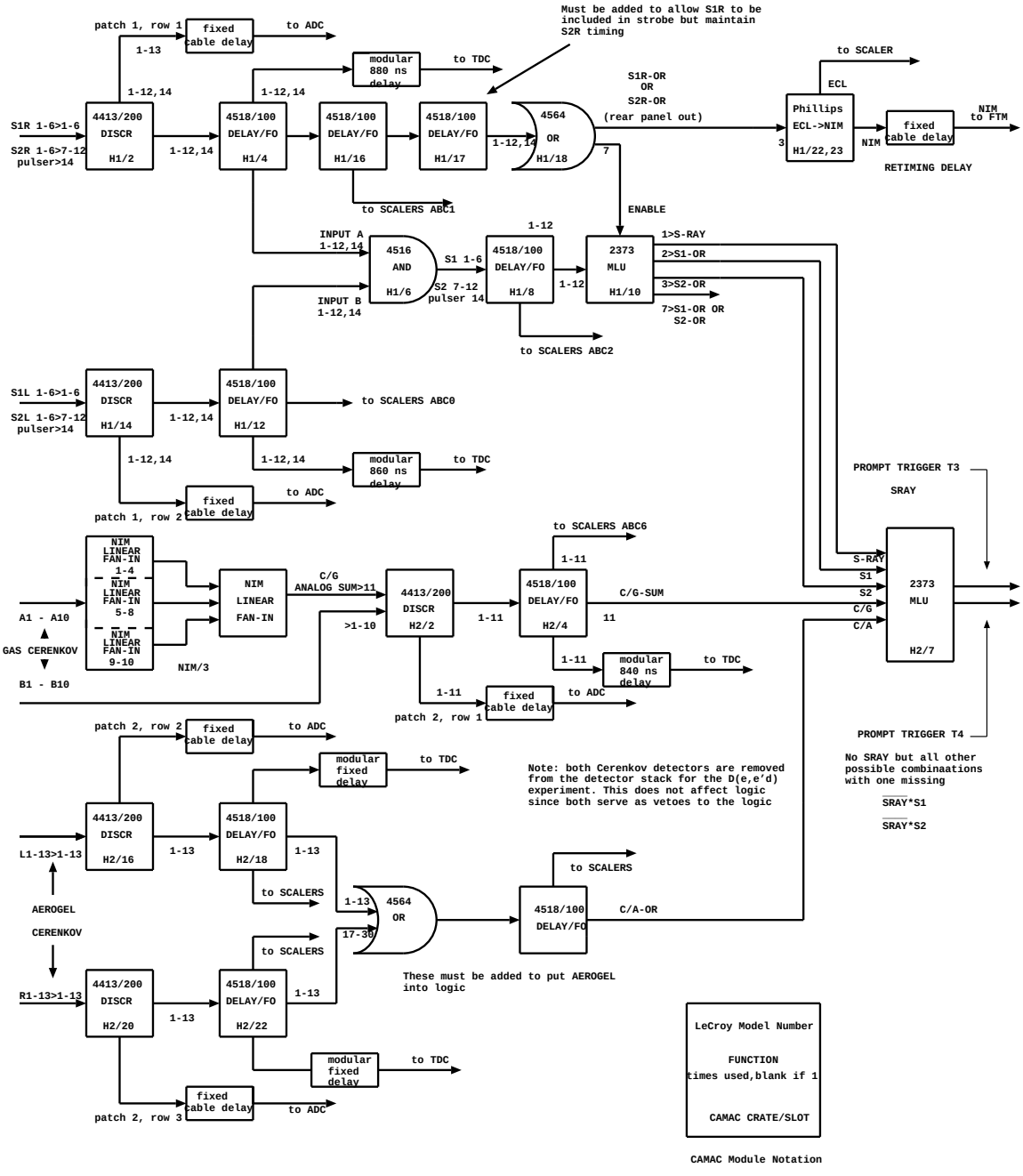

Fig. A-2: Diagram of the Hadron arm trigger.

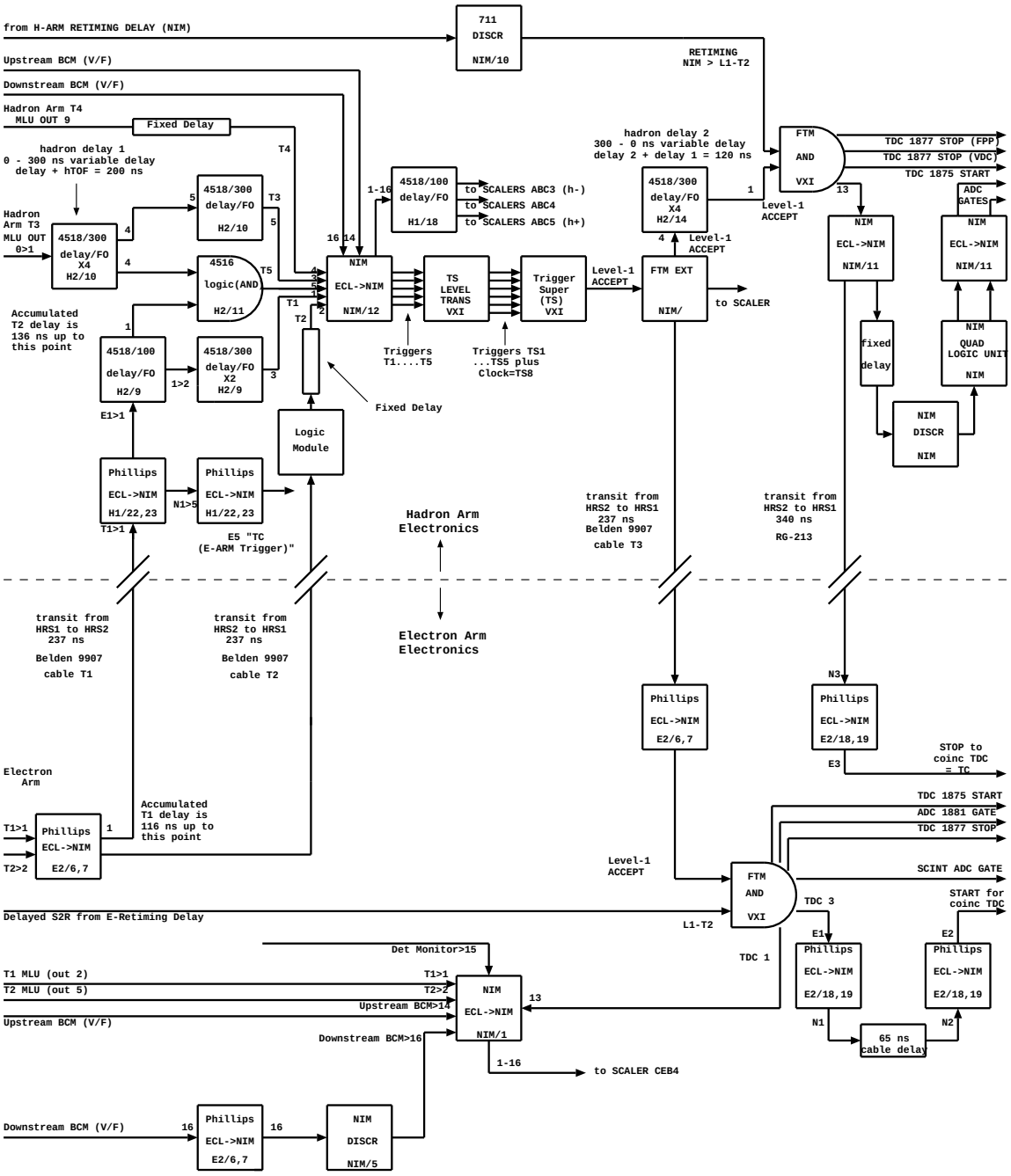

Fig. A-3: Diagram of the coincidence trigger.

APPENDIX B

Spectrometer Setup Kinematics

$\theta_e = 90.0^\circ$

E	E'	P_E	P_p	P_H	θ_p	$\Delta\Omega_e/\Delta\Omega_p$
GeV	GeV	GeV/c	GeV/c	GeV/c	deg.	
0.5423	0.3437	0.3386	0.6420	0.6315	32.37	4.13
0.6015	0.3666	0.3613	0.7043	0.6952	31.36	4.32
0.6580	0.3868	0.3812	0.7632	0.7549	30.45	4.52
0.7122	0.4049	0.3993	0.8192	0.8116	29.62	4.71
0.7649	0.4214	0.4156	0.8732	0.8661	28.85	4.90
0.8159	0.4364	0.4306	0.9252	0.9184	28.15	5.10

Table B-1: e-p elastic kinematics used to setup the spectrometers for the backward angle calibration. E is the nominal (uncorrected) beam energy. E' and P_p correspond to this beam energy. P_E and θ_e are the momentum and angle settings of HRSE. P_E was corrected for ionization energy loss in the target and lowered by 1.0% in order to get more of the radiative tail into the HRSE acceptance. P_H and θ_p are the momentum and angle settings of HRSH. P_H was corrected for ionization energy loss in the target. The Jacobian, $J \equiv \Delta\Omega_e/\Delta\Omega_p$, is given in the lab frame.

$\theta_e = 144.5^\circ$

E	E'	P_E	P_d	P_H	θ_d	$\Delta\Omega_e/\Delta\Omega_d$
GeV	GeV	GeV/c	GeV/c	GeV/c	deg.	
0.5423	0.3558	0.3495	0.8572	0.8254	13.95	5.98
0.6015	0.3803	0.3739	0.9375	0.9117	13.63	6.25
0.6580	0.4021	0.3955	1.0127	0.9908	13.33	6.52
0.7122	0.4218	0.4150	1.0836	1.0650	13.06	6.78
0.7649	0.4397	0.4328	1.1515	1.1350	12.81	7.03
0.8159	0.4561	0.4491	1.2164	1.2010	12.58	7.29

Table B-2: e-d elastic kinematics used to setup the spectrometers for $B(Q^2)$. E is the nominal (uncorrected) beam energy. E' and P_d correspond to this beam energy. P_E and θ_e are the momentum and angle settings of HRSE. P_E was corrected for ionization energy loss in the target and lowered by 1.0% in order to get more of the radiative tail into the HRSE acceptance. P_H and θ_d are the momentum and angle settings of HRSH. P_H was corrected for ionization energy loss in the target. The Jacobian, $J \equiv \Delta\Omega_e/\Delta\Omega_d$, is given in the lab frame.

E	E'	P_E	θ_e	P_p	P_H	θ_p	$\Delta\Omega_e/\Delta\Omega_p$
GeV	GeV	GeV/c	deg.	GeV/c	GeV/c	deg.	
3.245	2.808	2.804	17.26	1.006	1.003	55.91	0.229
3.245	2.759	2.756	18.37	1.072	1.069	54.21	0.258
3.245	2.712	2.709	19.41	1.133	1.130	52.67	0.288
3.245	2.668	2.665	20.37	1.190	1.187	51.30	0.318
3.245	2.626	2.623	21.28	1.243	1.240	50.05	0.349
3.245	2.585	2.582	22.15	1.294	1.291	48.89	0.381
3.245	2.519	2.516	23.55	1.374	1.371	47.10	0.437
3.245	2.453	2.450	24.95	1.454	1.451	45.39	0.500
3.245	2.291	2.288	28.40	1.643	1.640	41.55	0.687
4.045	2.851	2.848	25.46	1.914	1.912	39.81	0.587
3.746	2.473	2.470	29.42	2.003	2.000	37.34	0.825
3.746	2.350	2.347	31.66	2.138	2.135	35.24	1.013
4.045	2.502	2.499	31.02	2.297	2.294	34.16	1.018
4.045	2.382	2.379	33.07	2.427	2.424	32.38	1.229
4.424	2.634	2.627	31.15	2.562	2.560	32.12	1.118
4.045	2.286	2.284	34.76	2.529	2.525	31.03	1.428
4.424	2.490	2.484	33.36	2.715	2.712	30.28	1.377

Table B-3: *e-p* elastic kinematics used to setup the spectrometers for the forward angle calibration. E is the nominal (uncorrected) beam energy. E' and P_p correspond to this beam energy. P_E and θ_e are the momentum and angle settings of HRSE. P_E was corrected for ionization energy loss in the target. P_H and θ_p are the momentum and angle settings of HRSH. P_H was corrected for ionization energy loss in the target.

E	E'	P_E	θ_e	P_d	P_H	θ_d	$\Delta\Omega_e/\Delta\Omega_d$
GeV	GeV	GeV/c	deg.	GeV/c	GeV/c	deg.	
3.245	3.058	3.054	15.26	0.857	0.842	69.91	0.229
3.245	3.024	3.020	16.72	0.938	0.925	68.14	0.258
3.245	2.989	2.985	18.10	1.013	1.002	66.50	0.288
3.245	2.955	2.951	19.41	1.084	1.074	64.97	0.318
3.245	2.920	2.916	20.67	1.151	1.143	63.54	0.349
3.245	2.885	2.881	21.89	1.216	1.209	62.17	0.381
3.245	2.827	2.822	23.88	1.321	1.315	60.01	0.437
3.245	2.765	2.761	25.88	1.425	1.419	57.90	0.500
3.245	2.605	2.602	30.90	1.676	1.671	52.97	0.687
4.045	3.219	3.215	28.24	1.945	1.940	51.55	0.587
3.746	2.813	2.810	33.49	2.090	2.086	47.96	0.825
3.746	2.680	2.677	36.80	2.266	2.262	45.09	1.013
4.045	2.846	2.842	36.43	2.437	2.433	43.91	1.018
4.045	2.712	2.709	39.45	2.603	2.599	41.47	1.229
4.424	2.985	2.978	37.29	2.733	2.730	41.43	1.118
4.045	2.606	2.603	41.94	2.733	2.730	39.58	1.428
4.424	2.825	2.818	40.54	2.925	2.921	38.88	1.377
4.045	2.446	2.444	45.83	2.925	2.921	36.85	1.787

Table B-4: *e-d* elastic kinematics used to setup the spectrometers for $A(Q^2)$. E is the nominal (uncorrected) beam energy. E' and P_d correspond to this beam energy. P_E and θ_e are the momentum and angle settings of HRSE. P_E was corrected for ionization energy loss in the target. P_H and θ_d are the momentum and angle settings of HRSH. P_H was corrected for ionization energy loss in the target.

APPENDIX C

Input for Cross Section Calculations

E	Run No.	I_{ave}	Charge	Live Time	$F(Q^2,T)$	N_{ep}	$(\Delta\Omega)_{MC}$	$\overline{Q^2}$	$\overline{\theta}$	$\overline{x}$	C_{rni}
GeV		μA	μC	$1/C_{cdt}$			msr	$(\mathrm{GeV/c})^2$	deg.	cm	
0.5392	474	10.38	18938	0.2453	1.079	428599	1.581	0.366	90.02	6.14	1.007
0.5392	475	10.24	13502	0.0324	1.079	40255	1.581	0.366	90.02	6.14	1.007
0.5980	520	10.03	12615	0.0942	1.080	78618	1.596	0.433	90.01	6.27	1.008
0.6542	547	10.23	25853	0.1325	1.080	159268	1.618	0.500	89.99	6.40	1.008
0.6542	548	10.53	10220	0.1461	1.080	69626	1.618	0.500	89.99	6.40	1.008
0.7081	549	10.08	28389	0.1636	1.081	164413	1.625	0.567	90.01	6.52	1.008
0.7605	575	8.99	11256	0.3838	1.081	116437	1.634	0.634	90.01	6.63	1.008
0.7605	577	8.89	2255	0.5523	1.081	34344	1.634	0.634	90.01	6.63	1.008
0.8112	684	10.66	11195	0.3925	1.082	88950	1.649	0.701	90.01	6.74	1.008
0.8112	685	10.61	9353	0.6861	1.082	130420	1.649	0.701	90.01	6.74	1.008
0.8112	760	10.44	5461	0.7001	1.082	77212	1.649	0.701	90.01	6.74	1.008
0.8112	761	10.45	2650	0.6687	1.082	35733	1.649	0.701	90.01	6.74	1.008

Table C-1: Input for *e-p* elastic cross section calculations for the backward angle calibration. E is the corrected accelerator beam energy. Data were taken with the acceptance-defining collimators in front of the spectrometers. $\overline{Q^2}$, $\overline{\theta}$, and $\overline{x}$ are from the Monte Carlo simulation, where the variation of the cross section over the spectrometer acceptance is taken into account. $\overline{x}$ is the average distance the recoil protons travel in the target material and is used to calculate the correction for losses of recoil protons due to nuclear interactions.

E	Time	Charge	N_{ed}	$t5$	$s5$	$\overline{Q^2}$	$\overline{\theta}$	$(\Delta\Omega)_{MC}$	$F(Q^2,T)$	$\overline{x}$	C_{rni}
GeV	hour	mC				$(\mathrm{GeV/c})^2$	deg.	msr		cm	
0.5392	2.137	258.4	1895	2846	3080	0.684	144.55	2.24	1.085	7.23	1.084
0.5980	7.125	1738.7	5275	10275	10802	0.813	144.55	2.24	1.086	7.28	1.074
0.6542	7.693	1865.3	2378	6201	7206	0.941	144.53	2.24	1.087	7.30	1.067
0.7081	15.542	3685.4	2276	9278	9635	1.069	144.52	2.25	1.087	7.28	1.061
0.7605	25.302	7933.7	2283	16248	19819	1.197	144.52	2.26	1.088	7.30	1.057
0.8112	42.690	14676.8	2195	22012	27534	1.325	144.51	2.26	1.088	7.32	1.054

Table C-2: Input for e-d elastic cross section calculations for $B(Q^2)$. E is the corrected accelerator beam energy. Data were taken with the acceptance-defining collimators in front of the spectrometers. The C_{cdt} correction is equal to $s5/t5$. $\overline{Q^2}$, $\overline{\theta}$, and $\overline{x}$ are from the Monte Carlo simulation, where the variation of the cross section over the spectrometer acceptance is taken into account. $\overline{x}$ is the average distance the recoil deuterons travel in the target material and is used to calculate the correction for losses of recoil deuterons due to nuclear interactions.

E	Collimator Configuration	Run No.	I_{ave}	Charge	Live Time	$F(Q^2,T)$	N_{ep}	$(\Delta\Omega)_{MC}$	$\overline{Q^2}$	$\overline{\theta}$	$\overline{x}$	C_{rni}
GeV			μA	μC	$1/C_{cdt}$			msr	$(\mathrm{GeV/c})^2$	deg.	cm	
3.227	ii	835	10.45	7168	0.0545	1.085	55200	0.366	0.803	17.20	4.06	1.006
3.227	oo	846	10.79	5048	0.0488	1.085	72253	0.717	0.803	17.19	3.91	1.006
3.227	oo	1027	4.38	3664	0.0943	1.086	77660	0.832	0.892	18.29	3.92	1.006
3.227	ii	1029	4.42	5098	0.1883	1.086	103154	0.422	0.894	18.31	4.11	1.006
3.227	ii	1015	10.13	11951	0.1170	1.086	115234	0.483	0.979	19.34	4.20	1.007
3.227	oo	1016	10.15	6392	0.1048	1.086	115835	0.953	0.977	19.31	3.97	1.007
3.227	ii	989	10.24	6262	0.1495	1.087	60469	0.537	1.061	20.31	4.28	1.008
3.227	oo	990	10.20	5896	0.0851	1.087	68967	1.080	1.058	20.27	4.01	1.008
3.227	oo	966	8.92	7450	0.2011	1.087	168953	1.212	1.136	21.18	4.06	1.008
3.227	ii	967	9.91	12108	0.2414	1.087	153213	0.597	1.139	21.22	4.35	1.009
3.227	ii	968	9.70	9142	0.2240	1.087	107345	0.597	1.139	21.22	4.35	1.009
3.227	ii	960	3.92	2228	0.4808	1.087	45630	0.655	1.216	22.11	4.42	1.010
3.227	oo	961	8.32	2787	0.2829	1.087	74356	1.335	1.211	22.04	4.09	1.009
3.227	oo	962	10.08	19791	0.0972	1.087	177605	1.335	1.211	22.04	4.09	1.009
3.227	ii	1064	8.70	4930	0.6671	1.088	103575	0.750	1.338	23.51	4.54	1.011
3.227	ii	946	8.77	15703	0.6336	1.088	226435	0.842	1.463	24.93	4.66	1.011
3.227	oo	948	4.11	3753	0.6652	1.088	129649	1.841	1.453	24.81	4.25	1.010
3.227	ii	892	10.51	19126	0.7096	1.089	156039	1.109	1.764	28.39	4.97	1.012

Continued

E	Collimator Configuration	Run No.	I_{ave}	Charge	Live Time	$F(Q^2,T)$	N_{ep}	$(\Delta\Omega)_{MC}$	$\overline{Q^2}$	$\overline{\theta}$	$\overline{x}$	C_{rni}
GeV			μA	μC	$1/C_{cdt}$			msr	$(\mathrm{GeV/c})^2$	deg.	cm	
4.022	ii	1658	11.58	16884	0.8684	1.090	88633	1.055	2.203	25.41	5.13	1.013
4.022	oo	1604	9.99	13060	0.8001	1.090	140053	2.230	2.193	25.31	4.61	1.011
4.022	oo	1605	9.89	10354	0.7845	1.090	110419	2.230	2.193	25.31	4.61	1.011
3.725	oo	1331	10.68	15132	0.8241	1.091	125360	3.050	2.342	29.27	4.84	1.012
3.725	ii	1332	8.89	4367	0.8955	1.091	16876	1.370	2.352	29.38	5.41	1.013
3.725	ii	1334	10.41	9383	0.8909	1.091	35326	1.370	2.352	29.38	5.41	1.013
3.729	ii	1371	10.55	16048	0.8527	1.091	37596	1.563	2.593	31.70	5.58	1.013
3.729	oo	1372	10.60	12752	0.8785	1.091	73285	3.510	2.579	31.55	5.03	1.012
4.022	oo	1389	11.06	19783	0.8805	1.091	80944	3.550	2.846	30.92	5.13	1.012
4.022	ii	1390	11.16	19860	0.9196	1.091	36605	1.597	2.860	31.05	5.67	1.013
4.022	oo	1470	10.17	19372	0.8999	1.092	55540	3.908	3.074	33.00	5.39	1.013
4.022	ii	1475	29.12	21404	0.8298	1.092	24093	1.840	3.080	33.06	5.98	1.014

Continued

E	Collimator Configuration	Run No.	I_{ave}	Charge	Live Time	$F(Q^2,T)$	N_{ep}	$(\Delta\Omega)_{MC}$	$\overline{Q^2}$	$\overline{\theta}$	$\overline{x}$	C_{rni}
GeV			μA	μC	$1/C_{cdt}$			msr	$(\mathrm{GeV/c})^2$	deg.	cm	
4.399	oo	1077	8.91	21063	0.9170	1.092	49565	3.730	3.312	31.11	5.37	1.013
4.399	ii	1078	9.24	29751	0.9352	1.092	31549	1.746	3.327	31.24	5.91	1.014
4.399	oo	1081	8.70	14163	0.9256	1.092	33480	3.730	3.312	31.11	5.37	1.013
4.399	oo	1082	10.20	8855	0.9272	1.092	20810	3.730	3.312	31.11	5.37	1.013
4.399	oo	1083	9.59	6523	0.9293	1.092	15354	3.730	3.312	31.11	5.37	1.013
4.399	ii	1084	10.31	34745	0.9479	1.092	37144	1.746	3.327	31.24	5.91	1.014
4.399	oo	1159	9.50	17516	0.9252	1.092	41090	3.730	3.312	31.11	5.37	1.013
4.399	ii	1160	10.18	19409	0.9458	1.092	20652	1.746	3.327	31.24	5.91	1.014
4.022	oo	1542	15.53	14550	0.9294	1.092	30556	4.020	3.256	34.73	5.51	1.013
4.022	ii	1545	15.65	34049	0.9548	1.092	33092	1.925	3.257	34.75	6.15	1.014
4.397	oo	1187	13.14	19328	0.9015	1.092	27471	4.020	3.579	33.35	5.59	1.013
4.397	ii	1188	28.91	43429	0.8506	1.092	26004	1.884	3.594	33.46	6.07	1.014
4.397	oo	1262	13.57	19539	0.8898	1.092	27695	4.020	3.579	33.35	5.59	1.013

Table C-3: Input for *e-p* elastic cross section calculations for the forward angle calibration. E is the corrected accelerator beam energy. "ii" indicates that data were taken with the acceptance-defining collimators in front of the spectrometers. "oo" indicates that data were taken without the acceptance-defining collimators in front of the spectrometers. $\overline{Q^2}$, $\overline{\theta}$, and $\overline{x}$ are from the Monte Carlo simulation, where the variation of the cross section over the spectrometer acceptance is taken into account. $\overline{x}$ is the average distance the recoil protons travel in the target material and is used to calculate the correction for losses of recoil protons due to nuclear interactions.

E	Collimator Configuration	Time	Charge	N_{ed}	$t5$	$s5$	$\overline{Q^2}$	$\overline{\theta_e}$	$(\Delta\Omega)_{MC}$	$F(Q^2,T)$	$\overline{x}$	C_{rni}
GeV		hour	mC				$(\mathrm{GeV/c})^2$	deg.	msr		cm	
3.227	oo	0.889	19.00	17361	25716	26648	0.685	15.22	0.514	1.087	3.51	1.042
3.227	oo	0.672	42.87	18278	27520	30659	0.811	16.66	0.634	1.087	3.56	1.038
3.227	oo	0.390	41.11	10132	14101	14942	0.938	18.02	0.758	1.088	3.60	1.034
3.227	oo	0.942	112.8	15436	19629	21763	1.063	19.31	0.888	1.089	3.64	1.032
3.227	oo	0.949	158.3	13633	16239	17867	1.188	20.55	1.030	1.089	3.67	1.030
3.227	oo	1.261	298.6	14564	16767	18815	1.314	21.75	1.166	1.090	3.71	1.029
3.227	ii	2.936	471.0	4376	4771	5284	1.533	23.76	0.628	1.091	3.88	1.028
3.227	ii	4.766	1382.8	5612	6136	6757	1.761	25.79	0.717	1.091	3.97	1.027
3.227	ii	10.639	3587.4	1787	2078	2406	2.350	30.82	0.964	1.093	4.21	1.026

Continued

E	Collimator Configuration	Time	Charge	N_{ed}	$t5$	$s5$	$\overline{Q^2}$	$\overline{\theta_e}$	$(\Delta\Omega)_{MC}$	$F(Q^2,T)$	$\overline{x}$	C_{rni}
GeV		hour	mC				$(\mathrm{GeV/c})^2$	deg.	msr		cm	
4.022	oo	4.377	1638.6	378	616	664	3.01	27.96	2.26	1.094	4.07	1.027
3.725	oo	14.296	3693.9	252	459	509	3.41	33.25	3.06	1.095	4.24	1.029
3.729	oo	15.877	5306.1	109	374	410	3.92	36.61	3.56	1.095	4.40	1.034
4.022	oo	22.848	6729.3	50	384	430	4.40	36.24	3.61	1.096	4.46	1.037
4.022	oo	51.604	17117.4	35	1155	1251	4.91	39.32	3.88	1.096	4.65	1.041
4.399	oo	53.031	14608.2	11	852	880	5.30	37.18	3.76	1.097	4.64	1.043
4.022	oo	51.618	15870.1	12	890	989	5.30	41.82	4.02	1.097	4.80	1.044
4.397	oo	66.344	19189.5	12	1127	1165	5.90	40.47	3.98	1.097	4.87	1.046
4.022	oo	20.699	7705.2	1	460	525	5.90	45.74	4.01	1.097	5.11	1.049

Table C-4: Input for *e-d* elastic cross section calculations for $A(Q^2)$. E is the corrected accelerator beam energy. "ii" indicates that data were taken with the acceptance-defining collimators in front of the spectrometers. "oo" indicates that data were taken without the acceptance-defining collimators in front of the spectrometers. The C_{cdt} correction is equal to $s5/t5$. $\overline{Q^2}$, $\overline{\theta_e}$, and $\overline{x}$ are from the Monte Carlo simulation, where the variation of the cross section over the spectrometer acceptance is taken into account. $\overline{x}$ is the average distance the recoil deuterons travel in the target material and is used to calculate the correction for losses of recoil deuterons due to nuclear interactions.

References

[1] R.G. Arnold *et al.*, Phys. Rev. Lett. **35**, 776 (1975).

[2] R.G. Arnold *et al.*, Phys. Rev. Lett. **58**, 1723 (1987); P.E. Bosted *et al.*, Phys. Rev. **C42**, 38 (1990).

[3] E. Hummel and J.A. Tjon, Phys. Rev. Lett. **63**, 1788 (1989); Phys. Rev. **C42**, 423 (1990).

[4] L.C. Alexa *et al.*, Phys. Rev. Lett. **82**, 1374 (1999).

[5] S. Platchkov *et al.*, Nucl. Phys. **A510**, 740 (1990).

[6] J.E. Elias *et al.*, Phys. Rev. **177**, 2075 (1969).

[7] R. Cramer *et al.*, Z. Phys. **C29**, 513 (1985).

[8] S. Auffret *et al.*, Phys. Rev. Lett. **54**, 649 (1985).

[9] World Wide Web page of JLab Hall A, http://www.jlab.org/Hall-A (1999).

[10] C. Hyde-Wright and L. Todor , Event-by-Event Calibration of Beam Positions during VCS Experiment E93-050, JLab internal report, 1998 (unpublished).

[11] K. Unser, IEEE Trans. Nucl. Sci. **16**, 934 (1969); K. Unser, IEEE Trans. Nucl. Sci. **28**, 2344 (1981); K.B. Unser, CERN report CERN-SL-91-42-BI, 1991 (unpublished).

[12] S. Nanda, ed., Hall A Experimental Equipment Operations Manual, http://www.jlab.org/Hall-A/document/OPMAN/index.html (April 1997).

[13] L. Ewell, Charge and Current Measurements for Experiment E91-026 at TJNAF, JLab internal report, 1998 (unpublished).

[14] A. Deur, La cible cryogenique du hall A du Thomas Jefferson National Accelerator Facility, Universite Blaise Pascal internal report, 1998 (unpublished).

[15] R. Suleiman, Hall A Cryogenic and Dummy Targets Information, JLab internal report TN-98-007, 1998 (unpublished).

[16] D. Margaziotis, private communication.

[17] B. Dalesio, Experimental Physics and Industrial Control System (EPICS) Overview, http://www.atdiv.lanl.gov/aot8/epics/training/New/EPICS_Overview/index.htm (May 1998).

[18] P. Ulmer, Beam Charge Measurements: Hall A Experiment E89-003 at Jefferson Laboratory, JLab internal report, 1998 (unpublished).

[19] K. McCormick, TJNAF Hall A Cryotarget Density Dependence on Beam Current, JLab internal report, 1999 (unpublished).

[20] Conceptual Design Report CEBAF Basic Experimental Equipment, 1990 (unpublished).

[21] K.L. Brown *et al.*, SLAC report #91, 1977 (unpublished).

[22] N. Liyanage *et al.*, Optics Commissioning of the Hall A High Resolution Spectrometers, MIT-LNS internal report #04, 1998 (unpublished).

[23] J. LeRose, Latest Best Estimate of Target to Collimator/Sieve Distance, http://www.jlab.org/Hall-A/news/minutes/collimator-distance.html (March 1999).

[24] J. LeRose, private communication.

[25] J. Gomez, private communication.

[26] K.G. Fissum *et al.*, VDC Manual V2.1, MIT-LNS internal report #03, 1997 (unpublished).

[27] CODA: CEBAF On-line Data Acquisition User's Manual, JLab internal report, 1997 (unpublished).

[28] E. Jastrezembski, The CEBAF Trigger Supervisor, JLab internal report, 1997 (unpublished).

[29] R. Michaels, private communication.

[30] R. Michaels, Online Codes Dataspy and Dhist for Hall A Spectrometers, http://www.jlab.org/Hall-A/equipment/daq/dplot.html (January 1999).

[31] R. Michaels, Hall A Raw Data Structure, http://www.jlab.org/Hall-A/equipment/daq/dstruct.html (January 1999).

[32] M. Iodice *et al.*, Nucl. Instrum. Meth. **A411**, 223 (1998).

[33] E.A.J.M. Offermann and M. Kuss, ESPACE Manual Version 2.7.0, 1998 (unpublished).

[34] N. Liyanage, Ph.D. Thesis, MIT, 1999 (unpublished); J. Gao, Ph.D. Thesis, MIT, 1999 (unpublished).

[35] A. Ketikyan, H. Voskanyan and B. Wojtsekhowski, About Shower Detector Software, JLab internal report, 1997 (unpublished).

[36] 1998 Review of Particle Physics, C. Caso *et al.*, The European Physical Journal **C3**, 1 (1998).

[37] A.T. Katramatou *et al.*, Nucl. Instr. Meth. **A267**, 448 (1988); A.T. Katramatou, SLAC report SLAC-NPAS-TN-86-08, 1986 (unpublished).

[38] L.W. Mo and Y.S. Tsai, Rev. Mod. Phys. **41**, 205 (1969); Y.S. Tsai, Radiative Corrections to Electron Scattering, SLAC-PUB-848, 1971 (unpublished).

[39] L. Andivahis *et al.*, Phys. Rev. **D50**, 5491 (1994); and references therein.

[40] D. Abbot *et al.*, Phys. Rev. Lett. **82**, 1379 (1999).

[41] E.L. Lomon, Ann. Phys. (N.Y.) **125**, 309 (1980).

[42] J. Carlson and R. Schiavilla, Rev. Mod. Phys. **70**, 743 (1998); and references therein.

[43] R.B. Wiringa, V.G.J. Stoks and R. Schiavilla, Phys. Rev. **C51**, 38 (1995);

[44] R. Schiavilla, V.R. Pandharipande, and D.O. Riska, Phys. Rev. **C40**, 2294 (1989).

[45] R. Schiavilla and D.O. Riska, Phys. Rev. **C43**, 437 (1991).

[46] R. Schiavilla, V.R. Pandharipande, and D.O. Riska, Phys. Rev. **C41**, 309 (1990).

[47] J. Carlson, D.O. Riska, R. Schiavilla, and R.B. Wiringa, Phys. Rev. **C42**, 830 (1990).

[48] G. Höhler *et al.*, Nucl. Phys. **B114**, 505 (1976).

[49] W.P. Sitarski, P.G. Blunden, and E.L. Lomon, Phys. Rev. **C36**, 2479 (1987).

[50] P.G. Blunden, W.R. Greenberg and E.L. Lomon, Phys. Rev. **C40**, 1541 (1989); and private communication.

[51] E.L. Lomon and H. Feshbach, Ann. Phys. (N.Y.) **48**, 94 (1968).

[52] E.L. Lomon, Nucl. Phys. **A434**, 139c (1985); P. LaFrance and E.L. Lomon, Phys. Rev. **D34**, 1341 (1986); P. González, P. LaFrance, and E.L. Lomon, Phys. Rev. **D35**, 2142 (1987).

[53] D. Allasia *et al.*, Phys. Lett. **B174** 450 (1986).

[54] M. Gari and W. Krümpelmann, Z. Phys. **A322**, 689 (1985); Phys. Lett. **B173**, 10 (1986).

[55] R. Dymarz and F.C. Khanna, Nucl. Phys. **A516**, 549 (1990).

[56] R. Dymarz and F.C. Khanna, Phys. Rev. **C41**, 2438 (1990).

[57] R. Dymarz, C.J. Morningstar, R. Gourishankar, and F.C. Khanna, Nucl. Phys. **A507**, 530 (1990).

[58] R. Dymarz and F.C. Khanna, Nucl. Phys. **A507**, 560 (1990).

[59] P.L. Chung, F. Coester, B.D. Keister and W.N. Polyzou, Phys. Rev. **C37**, 2000 (1988).

[60] B.D. Keister, W.N. Polyzou, Advances in Nuclear Physics, vol. **20**, J.W. Negegle and E.W. Vogt (Eds.), Plenum Press, New York, 1991, p. 225.

[61] L.L. Frankfurt, T. Frederico and M. Strikman, Phys. Rev. **C48**, 2182 (1993).

[62] M.G. Fuda and Y. Zhang, Phys. Rev. **C51**, 23 (1995).

[63] J. Carbonell, B. Desplanques, V.A. Karmanov and J.-F. Mathiot, Phys. Rep. **300**, 215 (1998).

[64] E.E. Salpeter and H.A. Bethe, Phys. Rev. **84**, 1232 (1951).

[65] For an introduction to quasipotential equations see, G.E. Brown and A.D. Jackson, *The Nucleon–Nucleon Interaction*, Amsterdam , North–Holland (1976).

[66] J.W. Van Orden, N. Devine and F. Gross, Phys. Rev. Lett. **75**, 4369 (1995).

[67] D.R. Phillips, S.J. Wallace, and N.K. Devine, Phys. Rev. **C58**, 2261 (1998); and private communication.

[68] M. Chemtob, Nucl. Phys. **A382**, 317 (1982).

[69] I.L. Grach and L.A. Kondratyuk, Sov. J. Nucl. Phys. **39**, 198 (1984).

[70] V.A. Karmanov, Nucl. Phys. **A608**, 316 (1996).

[71] L.L. Frankfurt, I.L. Grach, L.A. Kondratyuk, and M.I. Strikman, Phys. Rev. Lett. **62**, 387 (1989).

[72] V.A. Karmanov and A.V. Smirnov, Nucl. Phys. **A546**, 691 (1992).

[73] V.A. Karmanov and A.V. Smirnov, Nucl. Phys. **A575**, 520 (1994).

[74] J. Carbonell and V.A. Karmanov, Nucl. Phys. **A581**, 625 (1995).

[75] V.A. Karmanov, Nucl. Phys. **A362**, 331 (1981).

[76] P. Mergell, U-G. Meissner, D. Dreshcel, Nucl. Phys. **A596**, 367 (1996).

[77] J. Carbonell and V.A. Karmanov, nucl-th/9902053; and private communication.

[78] B. Desplanques, V.A. Karmanov and J.-F. Mathiot, Nucl. Phys. **A589**, 697 (1995).

[79] F. Gross, Phys. Rev. **186**, 1448 (1969); Phys. Rev. **D10**, 223 (1974); Phys. Rev. **C26**, 2203 (1982).

[80] F. Gross, J. W. Van Orden and K. Holinde, Phys. Rev. **C41**, R1909 (1990); Phys. Rev. **C45**, 2094 (1992).

[81] F. Gross and D.O. Riska, Phys. Rev. **C36**, 1928 (1987).

[82] R.A. Arndt and L.D. Roper, Scattering Analysis and Interactive Dial-in (SAID) program, Virginia Polytechnic Institute and State University (1992).

[83] V.G.J. Stoks *et al.*, Phys. Rev. **C48**, 792 (1993).

[84] J.C. Ward, Phys. Rev. **78**, 182 (1950); Y. Takahashi, Nuovo Cimento **6**, 371 (1957).

[85] Y. Surya and F. Gross, Phys. Rev. **C53**, 2422 (1996).

[86] R. Blankenbecler and R. Sugar, Phys. Rev. **142**, 1051 (1966).

[87] A.A. Logunov and A.N. Tavkhelidze, Nouvo Cimento **29**, 380 (1963).

[88] S. Galster *et al.*, Nucl. Phys. **B32**, 221 (1971).

[89] D.R. Phillips and S.J. Wallace, Phys. Rev. **C54**, 507 (1996).

[90] V.B. Mandelzweig and S.J. Wallace, Phys. Lett. **B197**, 469 (1987).

[91] S.J. Wallace and V.B. Mandelzweig, Nucl. Phys. **A503**, 673 (1989).

[92] R. Machleidt, K. Holinde and C. Elster, Phys. Rep. **149**, 1 (1987).

[93] R.G. Arnold, C.E. Carlson and F. Gross, Phys. Rev. **C21**, 1426 (1980).

[94] M.J. Zuilhof and J.A. Tjon, Phys. Rev. **C24**, 736 (1981).

[95] S. Auffret *et al.*, Phys. Rev. Lett. **55**, 1362 (1985).

[96] D.O. Riska and G.E. Brown, Phys. Lett. **38B**, 193 (1972); M. Bernheim *et al.*, Nucl. Phys. **A365**, 349 (1981).

[97] F. Gross, J.W. Van Orden and K. Holinde, Phys. Rev. **C45**, 2094 (1992).

[98] M. Chemtob, E. Moniz and M. Rho, Phys. Rev. **C10**, 344 (1974).

[99] M. Gari and H. Hyuga, Nucl. Phys. **A264**, 409 (1976).

[100] J.A. Tjon and M.J. Zuilhof, Phys. Lett. **B84**, 31 (1979); M.J. Zuilhof and J.A. Tjon, Phys. Rev. **C22**, 2369 (1980).

[101] D. Berg *et al.*, Phys. Rev. Lett. **44**, 706 (1980).

[102] H. Ito and F. Gross, Phys. Rev. Lett. **71**, 2555 (1993).

[103] K.L. Mitchell, Ph.D. Thesis, Kent State University, 1995 (unpublished); P.C. Tandy, Prog. Part. Nucl. Phys. **36**, 97 (1996).

[104] F. Cardarelli, I. Grach, I. Narodetskii, G. Salmé and S. Simula, Phys. Lett. **B359**, 1 (1995).

[105] V. Chernyak and A. Zhitnitsky, Phys. Rep. **112**, 173 (1984).

[106] S.J. Brodsky and G.R. Farrar, Phys. Rev. Lett. **31**, 1153 (1973).

[107] V.A. Matveev, R.M. Muradyan and A.N. Tavkhelidze, Lett. Nuovo Cimento **7**, 719 (1973).

[108] S.J. Brodsky, C-R. Ji and G.P. Lepage, Phys. Rev. Lett. **51**, 83 (1983).

[109] C.E. Carlson, J.R. Hiller, R.J. Holt, Annu. Rev. Nucl. Part. Sci. **47**, 395 (1997).

[110] S.D. Drell and T.M. Yan, Phys. Rev. Lett. **24**, 181 (1970).

[111] S.J. Brodsky and B.T. Chertok, Phys. Rev. Lett. **37**, 269 (1976); Phys. Rev. **D14**, 3003 (1976).

[112] S.J. Brodsky and C.R. Ji, Phys. Rev. **D33**, 2653(1986).

[113] S.J. Brodsky and J.R. Hiller, Phys. Rev. **D46**, 2141 (1992).

[114] C.E. Carlson, and F. Gross, Phys. Rev. Lett. **53**, 127 (1984).

[115] A. Kobushkin and A. Syamtomov, Phys. Rev. **D49**, 1637 (1994).

[116] N. Isgur and C.H. Llewellyn Smith, Phys. Rev. Lett. **52**, 1080 (1984); Phys. Lett. **B217**, 535 (1989).

[117] G.R. Farrar, K. Huleihel and H. Zhang, Phys. Rev. Lett. **74**, 650 (1995).

[118] R. Suleiman and G. Petratos, Deuteron and Helium Form Factor Measurements at JLab, to appear in Proceedings of Exclusive and Semi-Exclusive Workshop at Jefferson Lab (Newport News, May 1999).

[119] C. Yan, The Super HMS, in Proceedings of JLab Workshop on Physics and Instrumentation with 6-12 GeV Beams, S. Dytman, H. Fenker, and P. Roos editors (June 1998).